



Durham E-Theses

Lattice Boltzmann Modelling of Droplet Dynamics on Fibres and Meshed Surfaces

CHRISTIANO, RAYMOND

How to cite:

CHRISTIANO, RAYMOND (2024) *Lattice Boltzmann Modelling of Droplet Dynamics on Fibres and Meshed Surfaces*, Durham theses, Durham University. Available at Durham E-Theses Online:
<http://etheses.dur.ac.uk/15334/>

Use policy

The full-text may be used and/or reproduced, and given to third parties in any format or medium, without prior permission or charge, for personal research or study, educational, or not-for-profit purposes provided that:

- a full bibliographic reference is made to the original source
- a [link](#) is made to the metadata record in Durham E-Theses
- the full-text is not changed in any way

The full-text must not be sold in any format or medium without the formal permission of the copyright holders.

Please consult the [full Durham E-Theses policy](#) for further details.

Lattice Boltzmann Modelling of Droplet Dynamics on Fibres and Meshed Surfaces

Raymond Christianto



Department of Physics
Durham University

*Thesis submitted in partial fulfilment of the requirements for the degree of
Doctor of Philosophy in Durham University*

· 2023 ·

Lattice Boltzmann Modelling of Droplet Dynamics on Fibres and Meshed Surfaces

Raymond Christiano
Department of Physics
Durham University

*Thesis submitted in partial fulfilment of the requirements for the degree of
Doctor of Philosophy in Durham University*

· 2023 ·

ABSTRACT

Fibres and fibrous materials are ubiquitous in nature and industry, and their interactions with liquid droplets are often key for their use and functions. These structures can be employed as-is or combined to construct more complex mesh structures. Therefore, to optimise the effectiveness of these structures, the study of the wetting interactions between droplets and solids is essential. In this work, I use the numerical solver lattice Boltzmann method (LBM) to systematically study three different cases of droplet wetting, spreading, and moving across fibres, and droplets impacting mesh structures.

First, I focus on partially wetting droplets moving along a fibre. For the so-called clamshell morphology, I find three possible dynamic regimes upon varying the droplet Bond number and the fibre radius: compact, breakup, and oscillation. For small Bond numbers, in the compact regime, the droplet reaches a steady state, and its velocity scales linearly with the driving body force. For higher Bond numbers, in the breakup regime, satellite droplets are formed trailing the initial moving droplet, which is easier with smaller fibre radii. Finally, in the oscillation regime (favoured in the midrange of fibre radius), the droplet shape periodically extends and contracts along the fibre.

Outside of the commonly known fully wetting and partial wetting states, there exists the pseudo-partial wetting state (where both the spherical cap and the thin film can coexist together), which few numerical methods are able to simulate. I implement long-range interactions between the fluid and solid in LBM to realise this wetting state. The robustness of this approach is shown by simulating a number of scenarios. I start by simulating droplets in fully, partial, and pseudo-partial wetting states on flat surfaces, followed by pseudo-partially wetting droplets spreading on grooved surfaces and fibre structures. I also explore the effects of key parameters in long-range interactions. For the dynamics demonstration, I simulate droplets in the pseudo-partial wetting state moving along a fibre in both the barrel and clamshell morphologies at different droplet volumes and fibre radii.

Finally, I focus on the dynamics of droplets impacting square mesh structures. I systematically vary the impact point, trajectory, and velocity. To rationalise the results, I find it useful to consider whether the droplet trajectory is dominated by orthogonal or diagonal movement. The former leads to a lower incident rate and a more uniform interaction time distribution, while the latter is typically characterised by more complex droplet trajectories with less predictability. Then, focussing on an impact point, I compare the droplet dynamics impacting a single-layer structure and equivalent double-layer structures. From a water-capturing capability perspective (given the same effective pore size), a double-layer structure performs slightly worse. A double-layer structure also generally leads to shorter interaction time compared to a single-layer structure.

CONTENTS

Acknowledgments	x
Declaration	xi
Contributions	xii
Publications	xiii
1 Background	1
1.1 Motivation	1
1.2 Open Questions	2
1.3 Thesis Structure	3
2 Introduction	5
2.1 Wetting on Flat, Homogenous Surface	5
2.2 The Effect of Long-Range Potential	7
2.3 Wetting on Structured Surfaces	9
2.4 Wetting on Fibre	11
2.5 Key Dimensionless Parameters	13
2.6 Dynamic Wetting	14
2.6.1 Contact Angle Hysteresis	14
2.6.2 Dynamic Contact Angle: The Cox-Voinov Law	15
3 Methods	18
3.1 Introduction	18
3.2 The Lattice Boltzmann Method	19
3.2.1 The Boltzmann Equation	19
3.2.2 The Lattice Boltzmann Equation	20
3.2.3 Discretisation: Velocity Set	22
3.2.4 Free Energy Approach	22
3.3 Two-Phase Fluid	25
3.3.1 Continuum Equations of Motion	25
3.3.2 Free Energy Lattice Boltzmann Model	26
3.3.3 The Lattice Boltzmann Implementation	27
3.4 Two-component Fluid	31
3.4.1 Continuum Equations of Motion	31
3.4.2 Free Energy Lattice Boltzmann	32
3.4.3 The Lattice Boltzmann Implementation	33

4	Modelling the Dynamics of Partially Wetting Droplets on Fibres	37
4.1	Introduction	37
4.2	Simulation Setup Using the Lattice Boltzmann Method	39
4.3	Dynamic Regimes for Clamshell Morphology	42
4.4	Dynamics of Compact Droplets	44
4.5	Dynamics of Droplet Breakup	49
4.6	Dynamics of Droplet Oscillation	51
4.7	Conclusion	53
5	Long-Range Fluid-Solid Interactions in Lattice Boltzmann Simulations	55
5.1	Introduction	55
5.2	Long-Range Interaction in Free-Energy Lattice Boltzmann	56
5.3	Fully Wetting Case: Analytical Integration for Flat Surfaces	58
5.4	Fully Wetting Case: Numerical Integration for Flat Surfaces	61
5.5	Pseudo-partial Wetting Case	67
5.6	Droplet on Pseudo-partial Wetting Fibre	73
5.7	Conclusion	79
6	Droplet Impact on Meshed Surfaces	81
6.1	Introduction	81
6.2	Methods	83
6.2.1	The Continuum Model and the Lattice Boltzmann Model	83
6.2.2	The Meshed Surfaces	84
6.2.3	The Droplet Impact Parameters	85
6.3	Results – Single Layer	86
6.3.1	Orthogonal Direction	88
6.3.2	Diagonal Direction	90
6.4	Results – Double Layer	93
6.5	Conclusion and Future Works	99
7	Conclusions and Future Works	101
7.1	Conclusion	101
7.2	Future Works	103
7.2.1	Pseudo-partial Wetting for Complex Geometries	103
7.2.2	Meshed Surfaces for Water-Oil Separation	104
A	The Lattice Boltzmann Method - Code Implementation and Validation	107
A.1	Code Implementation	107
A.1.1	Parallelisation	107
A.1.2	Reading input file	107
A.1.3	Initialising the simulation	110
A.1.4	Gradient calculation	113
A.1.5	Force calculation	114
A.1.6	Saving files	117
A.1.7	Collision and Streaming	118
A.1.8	Apply Boundary Conditions	121
A.1.9	Compute Momenta	121
A.2	Typical Simulation Statistics	122
A.3	Results Validation	124
A.3.1	Binary Poiseuille Flow	124
A.3.2	Capillary Filling - Washburn’s Law	126
A.3.3	Droplet Morphology	128

A.4	Grid Invariant Test	130
A.4.1	Modelling the Dynamics of Partially Wetting Droplets on Fibres	130
A.4.2	Long-Range Fluid-Solid Interactions in Lattice Boltzmann Simulations	131
A.4.3	Droplet Impact on Meshed Surfaces	131
	Bibliography	133

LIST OF SYMBOLS

Scalar quantities are denoted with a normal font (e.g. a , b , c), while vector quantities are denoted with a bold font (e.g. \mathbf{a} , \mathbf{b} , \mathbf{c}). In this section, physical constants are written in SI units. During simulations, however, their unitless equivalent is used instead. These unitless values will be defined in the methods chapter.

Constants

\mathbb{H}	Planck constant	$6.626\,070\,15 \times 10^{-24}$	J s
\mathbb{K}_B	Boltzmann constant	$1.380\,649 \times 10^{-23}$	J K ⁻¹
\mathbb{N}_A	Avogadro number	$6.022\,140\,76 \times 10^{23}$	mol ⁻¹
R	Universal gas constant	8.314 462 618 153 24	J K ⁻¹ mol ⁻¹
e	Euler's number	2.718 281 ...	-

Generic indices

		Δt	Time step
α	Generic spatial index (eg x , y , and z for Cartesian)	$\Delta \mathbf{u}$	Velocity correction term
		Δx	Lattice spacing
β	Generic spatial index (eg x , y , and z for Cartesian)	Ω^{lbm}	Collision operator
		Ω_i^{lbm}	Discrete collision operator
χ	Generic spatial index (eg x , y , and z for Cartesian)	α_{ed}	Parameter to tune interface width (two-component)
N	Arbitrary number	α_{hd}	Non-trivial root of the discrete entropy function (two-phase)
i	Arbitrary index	β_{hd}	Parameter to tweak kinematic viscosity (two-phase)
\bar{i}	Opposite index of i	δ	Kronecker delta function
j	Arbitrary index	ϵ	Solid node distance to the fluid-solid interface
k	Arbitrary index		
n	Arbitrary index		
Lattice Boltzmann method		ζ^{lrp}	Interface width of the tanh function to smoothened the pseudo-partial wetting
Γ_ϕ	Tunable parameter related to the equilibrium distribution function (two-component)	η	Dynamic viscosity
Δs	Lattice spacing for solid nodes	η_B	Bulk viscosity

κ_{hd}	Parameter for interface width tuning (two-phase)	ψ_{eos}	Free energy parameter related to the equation of state
κ_n	Parameter to tune fluid n contribution to surface tension (two-component)	C	Prefactor to make sure fluid-solid interaction only applies to one fluid and not the other
κ_w	Fluid-solid interaction intensity	C'	Derivation of C as a function of ϕ
λ_{ed}	Parameter for surface tension tuning (two-phase)	D	System characteristic length
μ_ρ	Chemical potential, minimised to density	E	Total system free energy
μ_ρ^b	Bulk component of μ_ρ	\mathbf{F}	Total body force
μ_ρ^i	Interfacial/surface component of μ_ρ	F_α	Total body force in α direction
μ_ϕ	Chemical potential, minimised to order parameter	$F_{\alpha,s}$	Fluid-solid force (two-phase) in α direction
μ_ϕ^b	Bulk component of μ_ϕ	\mathbb{F}_b	Bulk free energy term
μ_ϕ^i	Interfacial/surface component of μ_ϕ	\mathbf{F}_{chem}	Chemical force
μ_ϕ^{lrp}	Long-range potential component of μ_ϕ	\mathbf{F}_{drag}	Drag force
ν	Kinematic viscosity	F_{drive}	Driving force
ξ	Particle velocity	\mathbf{F}_g	Gravity force
ρ	Density	\mathbb{F}_i	Interface free energy term
ρ_l	Liquid density	\mathbf{F}_{LRP}	Long range fluid-solid interaction force
ρ_g	Gas density	\mathbb{F}_{lrp}	Energy contribution from long-range interaction
ρ_{rel}	Rescaled density	\mathbb{F}_s	Fluid-solid interaction free energy term
$\boldsymbol{\sigma}$	Viscous stress tensor	H_{hd}	Discrete entropy function
$\sigma_{\alpha\beta}$	α - β component of viscous stress tensor	\mathcal{M}	Transformation matrix from velocity space into momentum space (two-component)
σ^{lrp}	Prescribed film thickness	M_ϕ	Mobility parameter
τ	Relaxation time	N	Amount of solid nodes
τ_ϕ	Relaxation time related to the mobility parameter (two-component)	P	Interaction between one fluid molecule/node and one solid molecule/node
τ_{MRT}	Relaxation time related to the dynamic viscosity (two-component)	\mathcal{S}	Relaxation matrix containing each moment relaxation rate (two-component)
τ_n	Relaxation time for fluid n	S_i^{Guo}	Guo forcing term
ϕ	Order parameter	\mathcal{T}	A function whose value depends on the sign of \mathcal{V}
ψ_0	A constant chosen such as $\psi_{eos}(\rho_g) = \psi_{eos}(\rho_l)$		

T	Temperature	\mathbf{r}	Coordinate of one liquid molecule or node
T_c	Critical temperature	r_n	Distance between liquid node and solid node of interest
\mathcal{V}	Potential acting on a liquid at position \mathbf{r}	\mathbf{r}_s	Coordinate of solid node or molecule
V_0	Liquid node unit volume	$\mathbf{r}_s^{(i,j,k)}$	Interpolated solid coordinates
V_s	Solid node unit volume	s	A function whose value depends on the location of the neighbouring solid
$V_{s,0}$	Total solid volume	t	Time
a_n^{lrp}	Fitting parameters for pseudo-partial wetting on fibre	\mathbf{u}	Bare fluid velocity
$\mathbf{c}_{i\alpha}$	Discrete velocity vector	\mathbf{v}	Actual fluid velocity
c_s	Speed of sound in fluid	v_α	α -component of the actual fluid velocity
f	Particle distribution function	w_i	Weighting factor
f_a	Attractive interaction	\mathbf{x}	Position
$f_{a,s}$	Smoothened attractive interaction	Wetting	
f^{eq}	Equilibrium distribution function	ΔG	Molar activation energy
f_i	Discrete velocity distribution function	Δp	Laplace pressure
f_i^*	Distribution function after collision	Λ	Mean molecular distance
f_i^{eq}	Discrete equilibrium distribution function	Π	Disjoining pressure
f_r	Repulsive interaction	Φ_s	Fractional area of solid underneath droplet
$f_{r,s}$	Smoothened repulsive interaction	γ	Surface tension
f_s	Prefactor to control the strength of repulsive interaction	γ_{lg}	Surface tension between liquid-gas interface
\mathbf{g}	Gravitational acceleration	γ_{sg}	Surface tension between solid-gas interface
g_α	Gravitational acceleration in α direction	γ_{sl}	Surface tension between solid-liquid interface
g_i	Discrete velocity function (two-component)	θ_a	Advancing angle
g_i^{eq}	Discrete equilibrium distribution function (two-component)	θ_c	Sliding angle
p	Pressure	θ_{cb}^*	Apparent contact angle during Cassie-Baxter state
p_c	Critical pressure	θ_d	Dynamic contact angle
q	Amount of velocity vectors	θ_e	Equilibrium contact angle
$qlrp$	Interpolation degree	θ_{inc}	Inclination angle

θ_m	Microscopic contact angle	ΔT_s	Distance between layers
θ_r	Receding angle	Ω_{rear}	Satellite droplet volume
θ_w	Effective wedge angle	θ_s	Angle between the surface normal and the z -axis
θ_w^*	Apparent contact angle during Wenzel state	ϕ_s	Direction of droplet impact at a given impact point
A	Hamaker constant	\mathcal{A}	Unique impact point on mesh
A_w	Contact area between droplet and surface	\mathcal{B}	Unique impact point on mesh
\mathbb{E}_{xz}	x - z component of strain rate tensor	\mathcal{C}	Unique impact point on mesh
\mathbb{E}_{zx}	z - x component of strain rate tensor	\mathcal{D}	Unique impact point on mesh
\mathbb{K}_0	Equilibrium frequency of the molecular activity	\mathcal{E}	Unique impact point on mesh
\mathcal{P}	Free energy contribution of a film with thickness of e_f	\mathcal{F}	Unique impact point on mesh
\mathcal{R}	Surface roughness	H	Height of droplet perpendicular to fibre
$1/R_1$	Surface first principal curvature	L	Length of droplet along fibre axis
$1/R_2$	Surface second principal curvature	L_{\perp}	Projection of the drop contact perimeter in the direction orthogonal to the motion
S	Spreading parameter	L_F	Filament length
\dot{W}_{diss}	Dissipated energy per unit length and unit time	L_R	Relative droplet size
a	Attractive parameter	LX	Simulation window size in the x direction
b	Repulsive parameter	LY	Simulation window size in the y direction
e_f	Film thickness	LZ	Simulation window size in the z direction
h_m	Microscopic cut-off value	S_s	Pore size
l	Unit length	T_s	Solid thickness
v_{cl}	Contact line velocity	\tilde{V}	Reduced volume
Other symbols		W_F	Filament width
Bo	Bond number	a_n^f	Prefactor fitted to Ca-Bo relation
Ca	Capillary number	m_n^f	Exponent fitted to the Ca-Bo relation
Oh	Ohnesorge number	myPE	Local processor index during parallel processing
Re	Reynolds number	nbPE	Number of processors used in parallel processing
We	Weber number	r	Distance
ΔS_s	Width of solid bar		

r_d	Droplet radius	y_s^j	y -coordinate of the interpolated solid
r_f	Fibre radius	yk	Node index in y direction
t_{sim}	Total simulation time	z_0	Normalised coordinate for system with different T_s
\bar{t}_{sim}	Average simulation time	z_s^k	z -coordinate of the interpolated solid
x_s^i	x -coordinate of the interpolated solid	zk	Node index in z direction
xk	Node index in x direction	z_{fs}	Fluid-solid node interface location

ACKNOWLEDGMENTS

First of all, I would like to express my deepest gratitude to my supervisors, Prof Halim Kusumaatmaja, Dr Yudi Rachmawan, and Prof Jas Pal Badyal; also to my ‘unofficial’ supervisor, Dr Ciro Semprebon. Thank you for all your patience, kindness, and guidance through these four and a half years. I do not think that I could have finished my PhD studies if not for your endless support. I am also extremely grateful to the people who often helped me during my study: Dr M Subkhi Sadullah, Dr Alvin Shek, Dr Samuel Avis, Dr Jack R Panter, Fandi Oktasendra, Dr Abhinav Naga, and Michael Rennick. Thank you for all the interesting and useful discussions during these years.

On a more personal note, I want to thank other people in the Simulation of Soft Matter Group. I also want to thank the people in the Global Challenge Research Fund (GCRF) CDT, especially Prof Douglas Halliday and Abir van Hunen. Thank you to the Durham Indonesian Student Society. Special thanks to the Kings Church Durham, the members of the Ustinov cell group, and the members of the Mischpocha house group.

Finally, I’m deeply indebted to Dr Gea OF Parikesit and Dr Indraswari Kusumaningtyas for introducing me to Prof Halim Kusumaamatja and for their support during my preparation to study in Durham. I will never forget the day when Pak Gea sent me an email about the PhD advertisement. I would like to thank Filipus Gilang Wicaksono and Timothy Agung Wibisono for being my primary supporters and my good friends since our time together as undergraduates. Also thank you to all of my other friends back in Indonesia, especially during the lockdown period. I am extremely grateful to both of my parents for their continuous support, in every sense of the word. Thank you to my little brother, Joshua Justin Nathaniel, for being patient with his always-missing older brother. And thank you to my God because only due to His grace, I can live my current life.

DECLARATION

The work presented in this thesis has been developed by the author under the supervision of Prof Halim Kusumaatmaja of the Department of Physics at Durham University and Prof Jas Pal Badyal of the Department of Chemistry at Durham University. All text and figures are the work of the author unless otherwise stated.

Copyright © 2024 Raymond Christianto

The copyright of this thesis rests with the author. No quotation from it should be published without the author's prior written consent and information derived from it should be acknowledged.

CONTRIBUTIONS

The work presented in this thesis has been developed by the author under the supervision of Prof Halim Kusumaatmaja of the Department of Physics at Durham University and Prof Jas Pal Badyal of the Department of Chemistry at Durham University. The author has also benefited from guidance from Dr Ciro Semprebon of the Mathematics, Physics and Electrical Engineering at Northumbria University.

The work presented in Chapter 5 is a collaborative work between the author and Fandi Oktasendra. Fandi Oktasendra developed the decaying potentials for fully and partial wetting states, the step function for pseudo-partial wetting state, and the numerical integration for arbitrary surfaces using the phase field method. The author adapted these into the lattice Boltzmann models.

- Figure 5.1. Fandi Oktasendra originally derived the analytical expression to compute the $\mathcal{V}(\mathbf{r})$ for flat surfaces.

PUBLICATIONS

The work that is presented in Chapter 3 has been submitted for journal articles.

- R. Christiano, Y. Rahmawan, C. Semprebon, and H. Kusumaatmaja, “Modeling the Dynamics of Partially Wetting Droplets on Fibres”, *Physical Review Fluids* 7, 103606 (2022).

CHAPTER 1

Background

1.1 Motivation

Fibres and fibrous materials are ubiquitous in nature and industry, and their interactions with liquid droplets are often vital for their use and functions. In nature, numerous plants and animals, such as cacti and spider silk, have unique fibre-like features, able to efficiently condense and collect water droplets [1, 2]. Mammalian hair fibres have a series of axially symmetric serrations on their cylindrical main structure, directing water droplets to move parallel to the fibre [3]. Fibrous elements are also widely used for small-scale (laboratory) and large-scale (industrial) applications. For example, the tips of atomic force microscopes can be fabricated by dipping a fibre in an acid bath to etch the fibre material away, taking advantage of the formation of liquid meniscus [4, 5]. Textile fibres and yarns need to be treated with spin finishes, necessitating fast and uniform adsorption during the treatment [6]. Wetting properties of steel wires are key for coating with zinc-aluminium [7] or polymers [8] to prevent corrosion.

Fibres can also be harnessed to construct more complex structures, such as meshed surfaces. Different fibre materials, such as stainless steel [9], copper [10], nylon [11, 12], or acrylic [13], can be employed. For example, one way to prepare a compound droplet (microdroplets encapsulated by a larger droplet) is by using fibre junctions [12]. Fibre networks have been suggested as a possible open droplet microfluidic design [14]. Meshed surfaces mimic nature for improved designs of water collecting and fog harvesting devices [9, 13, 15]. Meshed surfaces are also used for spray generation [16, 17], inkjet printing [18], and oil-water separation [19, 20].

1.2 Open Questions

Drop dynamics on fibres are highly influenced by wetting. In general, there are three different wetting regimes that liquid on a surface can adopt. These are fully wetting when the liquid spreads into a film with no observable contact angle, partial wetting when the liquid will form a spherical cap droplet, and pseudo-partial wetting when the droplet and the film can coexist together [5, 21]. To date, most studies on droplet dynamics on fibre have focussed on the fully wetting regime [11, 22, 23, 24, 25, 26], few on the partial wetting regime [27, 28, 29], while to the best of my knowledge, none for the pseudo-partial wetting regime.

Here, there are several questions of interest. First, studies show that in the fully wetting regime, at the low-velocity range, the droplet velocity scales proportionally to the driving force (e.g. gravity), with a prefactor related to the droplet aspect ratio [11, 22]. How do drop dynamics fibres change going from the fully wetting, to the partial wetting, and to the pseudo-partial wetting regime? Furthermore, the aforementioned dynamic laws were derived for the so-called barrel morphology. Depending on the droplet volume and the contact angle, a droplet on fibre can adopt either the barrel morphology (where the droplet encapsulates the fibre) [30] or the clamshell morphology (where the droplet is perched on one side of the fibre) [31]. Are these dynamic laws still valid for the clamshell morphology? It has also been found that on a flat surface, the receding contact line will develop a corner that later will break into smaller droplets (i.e. the so-called pearling transition) [32, 33, 34]. Can this transition be observed on a fibre?

Research on droplet dynamics on meshed surfaces has also mainly considered the fully and partial wetting regimes. Moreover, droplet impact dynamics on meshed surfaces focussed on very low velocity (e.g. for fog harvesting) [9, 15, 35, 36] or very high velocity (e.g. for spray generation) [37, 38, 39, 40]. Only a few studies have been carried out for velocity ranges in-between these two extremes. Inspired by *Thuja plicata*, von Spreckelsen et al. [13] proposed a 3D-printed mesh with a diamond-like pore as a tool to collect rainwater. Experiments show that this structure has great water-collecting ability; however, no explanation has been given as to why. Numerical simulations can systematically study this structure to characterise the droplet impact characteristics. Are there any advantages or disadvantages to using multiple layers of the meshed surfaces?

Based on these open questions, in this thesis, I will address on three problems related

to fibrous materials and meshed surfaces employing the numerical solver named the lattice Boltzmann method (LBM), which has been proven to be able to computationally model such systems [41, 42, 43, 44]. First, I will investigate the motion of a droplet on a partially wetting cylindrical fibre. Specifically, I will study the relation between the body force and the droplet velocity and how it is affected by the fibre curvature. I will also consider the possible formation of satellites when the droplet is moving at a high velocity.

To date, LBM has been extensively used to study partial and fully wetting regimes [45, 46, 47, 48]. However, the case of the pseudo-partial wetting regime [49] has received much less attention. For the second problem, I developed a method to model such a wetting regime with LBM. Here, I report extensive details and benchmarks of the model development. I start from a simple flat homogeneous surface before moving to more complex grooved surfaces and cylindrical fibre structures. Finally, I consider both quasi-static and dynamic examples.

For the third problem, I simulate droplet impact on meshed surfaces. I focus on investigating the dynamics of millimetre-sized droplets impacting mesh-like structures with dimensions comparable to the droplet size. I systematically analyse the penetration, capture, and bouncing behaviour of impacting droplets based on the impact point, trajectory, and velocity. Next, to further characterise the system, I choose an impact point and compare the behaviour of two-layer structures to a single-layer structure with equivalent pore size.

1.3 Thesis Structure

This thesis is structured as follows. In Chapter 2, I introduce several basic concepts of wetting. I start describing wetting on a flat homogeneous surface and then introduce the effect of the long-range potential. Next, I discuss structured surfaces in general, prior to focussing on fibres. At the end of the chapter, I summarise relevant dimensionless numbers involved in droplet dynamics.

Chapter 3 introduces the lattice Boltzmann models (LBM) used in this thesis. I begin by summarising the basic concepts of LBM, such as the continuous lattice Boltzmann equation, the lattice Boltzmann equation, and the free-energy-based LBM. Then, I discuss in detail the two implementations that I employed in this thesis: the two-phase model and the two-component model.

In Chapter 4, I discuss the dynamics of a droplet on partially wetted fibre. Numerical results

show the existence of three regimes: compact, breakup, and oscillation. Both the effects of the Bond number (i.e. body force), the Capillary number (i.e. velocity), and the fibre radius are considered.

Chapter 5 reports the implementation and benchmark studies of fully wetting and pseudo-partial wetting in LBM. I simulate flat surfaces, grooved surfaces, and fibre structures. I also show the results for both quasi-static and dynamic examples.

Chapter 6 contains the study of droplet impact on meshed surfaces with square pores. I characterise the outcomes of different impact points based on their trajectory and velocity. I discuss why droplets that move orthogonally to the square mesh have fewer cases of droplets passing through. I also compare the difference between two-layer structures and a single-layer structure with an equivalent pore size.

Finally, in Chapter 7, I summarise the main results of this thesis and discuss ideas for future work.

CHAPTER 2

Introduction

2.1 Wetting on Flat, Homogenous Surface

At the molecular level, a molecule at an interface between different phases or immiscible components will lose its cohesive interactions as illustrated in Figure 2.1(a). Depending on our point of view, this can lead to both (1) an excess of energy at the interface and (2) an imbalance of cohesive (intra-molecular) and adhesive (inter-molecular) forces [5]. This phenomenon leads to a key concept known as interfacial or surface tension (γ). Surface tension can be thought of as the energy to increase a unit area of the interface, with the SI unit being $[\text{J}/\text{m}^2]$. Following the geometry in Figure 2.1(b), surface tension can also be defined as the amount of force per unit length, with the SI unit being $[\text{N}/\text{m}]$.

Surface tension will minimise the interface area between phases. In the absence of any other forces or interaction energies, it will lead to a spherical shape. Some common examples are free-falling droplets from faucets, floating soap bubbles, and water drops on plant leaves or petals [50]. Surface tension is the cause of the overpressure inside the interior of a droplet or bubble. This overpressure is called Laplace pressure (Δp). For a three-dimensional surface with principal curvatures of $1/R_1$ and $1/R_2$, the Laplace pressure is [5]:

$$\Delta p = \gamma \left(\frac{1}{R_1} + \frac{1}{R_2} \right). \quad (2.1)$$

A small droplet has a higher Δp compared to a larger droplet, which makes a smaller droplet has higher free energy [5]. Therefore, to minimise the free energy, smaller droplets will coalesce into larger droplets through the process known as Ostwald's ripening [51].

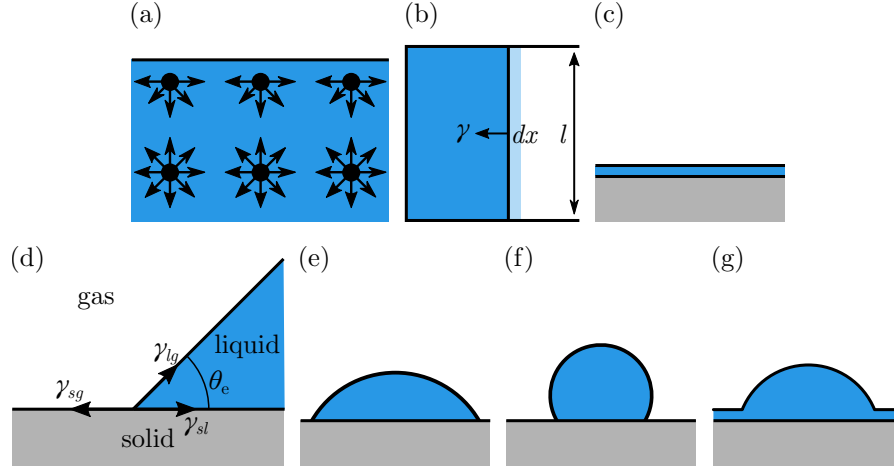


Figure 2.1: (a) An illustration of molecules that lose half of their interaction because of an interface. (b) Surface tension (γ) is defined as the amount of force per unit length (l) needed to increase the film length by dx . (c) A film in a fully wetting state. (d) An illustration of the triple contact line between solid, liquid, and gas interface. (e) A partially wetting droplet in a ‘mostly wetting’ state. (f) A partially wetting droplet in a ‘mostly non-wetting’ state. (g) A droplet and a film coexist together in a pseudo-partial wetting state.

When we put a liquid droplet on a solid surface, the final shape of the droplet is determined by the surface wettability. Qualitatively, a system is more wetting if the droplet spreads further on the surface. The spreading parameter (S) quantifies the degree of surface wettability. S is defined as the difference in surface tension between dry and wet conditions and mathematically is written as [5]:

$$S = \gamma_{sg} - [\gamma_{sl} + \gamma_{lg}], \quad (2.2)$$

where γ_{sg} , γ_{sl} , and γ_{lg} are the surface tensions between solid-gas, solid-liquid, and liquid-gas interface, respectively. If $S > 0$, the liquid will fully spread on the solid surface, leading to a fully wetting scenario (Figure 2.1(c)).

If S is negative, the liquid will form a spherical cap on the solid. This state is called partially wetting and the droplet shape is defined by its equilibrium contact angle (θ_e). This angle is measured at the triple contact line (Figure 2.1(d)) [5]. For a liquid-gas-solid system, usually, this angle is measured tangentially to the liquid surface made with the solid surface at the point of contact [50]. The relation between them is calculated using Young’s equation [5]:

$$\cos \theta_e = \frac{\gamma_{sg} - \gamma_{sl}}{\gamma_{lg}}. \quad (2.3)$$

When $\theta_e < 90^\circ$ (Figure 2.1(e)) the system is “mostly wetting”. If $\theta_e > 90^\circ$ (Figure 2.1(f)), the system is “mostly non-wetting”. Finally, we have a neutral wetting system if $\theta_e = 90^\circ$.

2.2 The Effect of Long-Range Potential

In addition to fully and partial wetting states, there is also a case where both droplet and film can co-exist together, which is called pseudo-partial wetting (Figure 2.1(g)). The presence of a pseudo-partial wetting state requires complex long-range interactions between the liquid and solid molecules.

To better illustrate the rules of long-range interactions, let us consider a liquid film spreading on an ideally smooth surface. Suppose we write the total system free energy per unit area as E . The free energy contribution of a film of thickness e_f can be written as $\mathcal{P}(e_f)$ [21]:

$$E(e_f) = \gamma_{sl} + \gamma_{lg} + \mathcal{P}(e_f). \quad (2.4)$$

When the film is very thick ($e_f \rightarrow \infty$), the total free energy should only come from the solid-liquid and liquid-gas interfaces and therefore we can conclude $\mathcal{P}(\infty) = 0$ [5]. At the limit of a very thin film ($e_f \rightarrow 0$), the total free energy should be equivalent to the dry surface energy (γ_{sg}), therefore $\mathcal{P}(0)$ is equivalent to the spreading parameter S [21]:

$$\mathcal{P}(0) = S = \gamma_{sg} - (\gamma_{sl} + \gamma_{lg}). \quad (2.5)$$

The form of how $\mathcal{P}(e_f)$ changes is related to the interactions between different molecules (i.e. intermolecular interactions). In general, there are two types of intermolecular interactions: short-range and long-range interactions [51]. The former is typically in the order of interatomic separations (less than 1.0 nm). Typically, short-range interactions will affect the bulk properties of gas, liquid, or solid phases. Long-range interactions are typically in the order of ~ 100 nm. There are three common contributors to long-range interactions [52]. The first is the Keesom interaction, which is the interaction between identical dipolar molecules. The second is the Debye interaction, which is the interaction between dipolar molecules and induced dipolar molecules. Finally, we have the London dispersion interaction which is caused when two adjacent atoms occupy positions that make the atoms form temporary dipoles. Collectively, these interactions are called the van der Waals interaction [5]. The van der Waals interaction potential goes with the inverse sixth power of the distance ($1/r^6$). For a spreading

thin film, the excess free-energy contributions from the film is modelled as [5]:

$$\mathcal{P}(e_f) = \frac{A}{12\pi e_f^2}, \quad (2.6)$$

where A is the Hamaker constant which describes the molecular characteristics of the solid and liquid molecules. It is to be noted that even though in general the contribution of $\mathcal{P}(e_f)$ is dominated by the long-range interaction, for a few special cases, the short-range interaction can also contribute to $\mathcal{P}(e_f)$ [21]. Figure 2.2(a) shows the value of E as a function of e_f for fully wetting condition with $S > 0$ and $A > 0$.

A concept related to the excess free energy is the so-called disjoining pressure which was first introduced by Derjaguin [53, 54]. Disjoining pressure can be thought of as the excess pressure that must be applied to a fluid film by two confining surfaces to counter the film's tendency to separate these confining surfaces [55]. It can also be thought of as the amount of 'mechanical' pressure needed to transform a bulk substance into an equilibrium film of the same substance [56]. Mathematically, it is the negative derivative of the free-energy contribution of the thin film, with respect to the film thickness [21]:

$$\Pi(e_f) = -\frac{d\mathcal{P}}{de_f}. \quad (2.7)$$

A positive disjoining pressure $\Pi(e_f) > 0$ will increase the film thickness [55].

Next, let us consider a case when $A < 0$, but with $S > 0$ and $S < 0$ shown in Figures 2.2(b) and (c), respectively. In both cases, there exists a minimum value of E at e_m , leading to a preferred film thickness corresponding to e_m . If $S > 0$, such film will extend indefinitely, while for $S < 0$, the film has a finite contact area. Here, the thin film also co-exists with a spherical cap with a finite contact angle [21]. These cases correspond to the pseudo-partial wetting scenario.

Finally, Figures 2.2(d) and (e) show the cases of $S < 0$ with $A > 0$ and $A < 0$. In both cases, $E(e_f)$ does not have a minimum at finite thickness. The droplet will adopt the partially wetting condition, with an equilibrium contact angle of θ_e . The difference between these two is in the shape of the droplet wedge. When $A > 0$, the profile is curved inward, while when $A < 0$, it is curved outward [21].

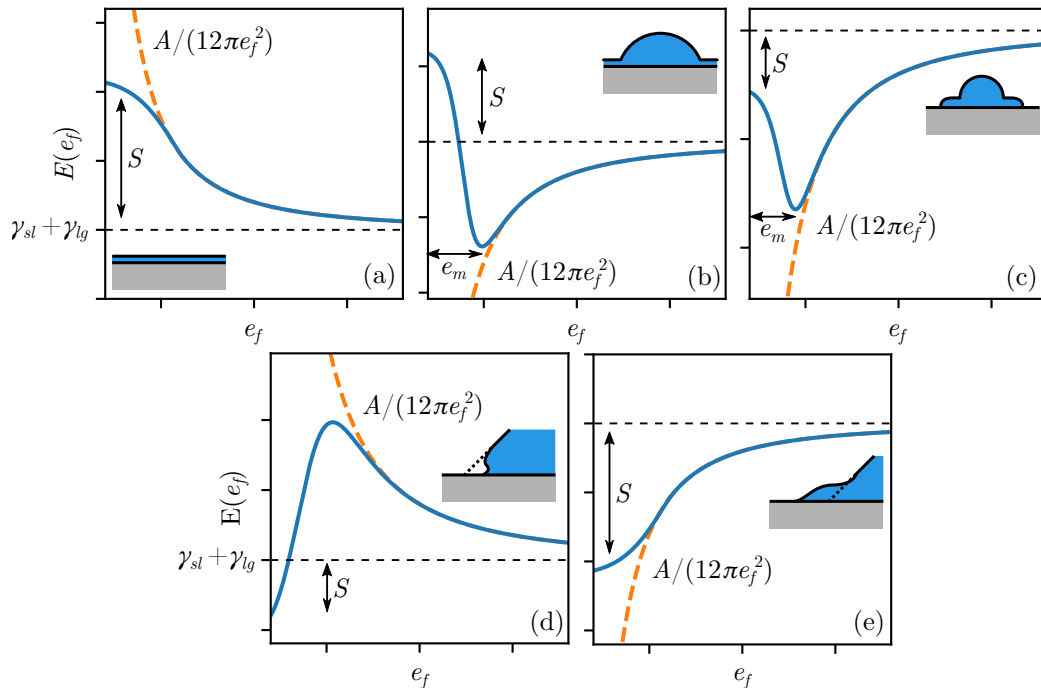


Figure 2.2: Qualitative figures showing different effects of S and A . The dashed line represents the free-energy contribution of the solid-liquid interface (γ_{sl}) and the liquid-gas interface (γ_{lg}). The blue solid line represents $E(e_f)$ while the orange dashed line is the function $A/(12\pi e_f^2)$. (a) A system in fully wetting condition with $S > 0$ and $A > 0$ with monotonically decreasing $E(e_f)$. Pseudo-partial wetting cases with $A < 0$ and (b) $S > 0$ and (c) $S < 0$. Partially wetting system with $S < 0$ and (d) $A > 0$ and (e) $A < 0$. These figures are adapted from [21].

2.3 Wetting on Structured Surfaces

In the previous sub-section, we defined the spreading parameter and the contact angle to describe the wetting characteristics of a surface. For example, metallic surfaces have large chemical binding energy causing a high surface energy (in the order of 1 eV), while plastics have a much lower surface energy. However, there are numerous ways to modify the wetting behaviours of a surface.

One way is to do a chemical treatment on the surface. For example, silicon wafers coated with chromium and gold can be treated to be both hydrophilic ($\theta_e = 80^\circ$) [57] and hydrophobic (95°) [58]. Another method called plasma chemical functionalisation employs plasma to deposit gas molecules into substrates, which can be used to modify neutral surfaces into both hydrophilic (65°) and hydrophobic (132°) surfaces [13]. Poly-dimethylsiloxane or more commonly known as PDMS is naturally hydrophobic (109°), but can be made hydrophilic (45°) by using ultraviolet light to induce graft polymerisation [59].

Another versatile way to modify surface wetting is to introduce roughness. Roughness can

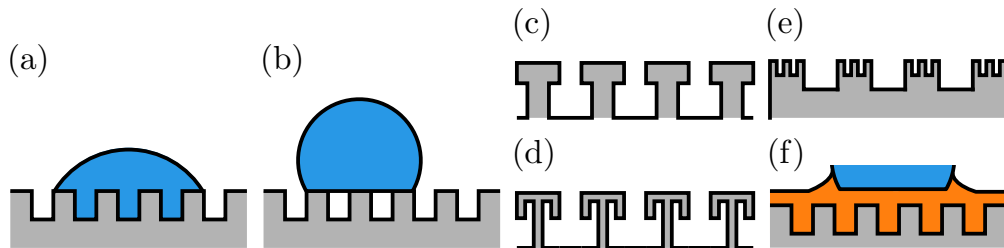


Figure 2.3: Illustrations of a droplet in (a) the Wenzel and (b) the Cassie-Baxter states. (c) Single and (d) double reentrant structures. (e) Surface with hierarchical structures. (f) A droplet on a liquid-infused surface.

enhance the wetting characteristics of a structure. When the droplet fills the grooves, the droplet is in the Wenzel state (Figure 2.3(a)). Mathematically, the apparent contact angle during the Wenzel state (θ_w^*) can be predicted by:

$$\cos \theta_w^* = \mathcal{R} \cos \theta_e, \quad (2.8)$$

where \mathcal{R} is the ratio between the real surface area and the apparent surface area whose value is ≥ 1 (increasing with roughness). Since the value of $\cos \theta_w^*$ increases with \mathcal{R} , a rough hydrophilic surface will be more hydrophilic and vice versa. Another possible state is when air gaps can be trapped underneath the droplet: the Cassie-Baxter state (Figure 2.3(b)). At this state, θ_e^* can reach $>150^\circ$ causing the droplet to reach the so-called superhydrophobic state. For the Cassie-Baxter state, the apparent contact angle (θ_{cb}^*) is expressed by [5]:

$$\cos \theta_{cb}^* = -1 + \Phi_s (\cos \theta_e + 1), \quad (2.9)$$

where Φ_s is the fractional area of the solid underneath the drop.

In reality, real solid surfaces are not smooth and have defects or irregularities on their surface, unless polishing has been employed to smoothen the roughness [51]. However, we can also intentionally introduce regular features. Simpler shapes can be grooves [60, 61] and pillars [62, 63, 64]. Both shapes can induce both Wenzel and Cassie-Baxter shapes, depending on their arrangement. A more complex shape is the so-called reentrant structures, which have overhang box caps [65] or mushroom caps on the top of the pillars [66] (Figures 2.3(c) and (d), respectively). The additional contact area introduced by the reentrant structure can be used to prevent a collapse from the Cassie-Baxter state to the Wenzel state. Carefully designed overhang structures can also be used to introduce directional fluid navigation, where liquid can

move in one direction but not the other [67].

The surface roughness can also be hierarchical (Figure 2.3(e)). For example, it has been proven that Lotus leaves have microstructures formed by papillose epidermal cells, which are covered with epicuticular wax tubules on the surface as its nanostructures lead to a large water droplet contact angle to be higher than 150° [68]. Banana leaves also have both micro and nanostructures [69]. However, the nanostructures on the top have a cone shape with large gaps, while on the bottom they are spherical with small gaps. These differences in structures cause a difference in the observed contact angle: hydrophilic (76°) at the top and hydrophobic (94°) at the bottom. This phenomenon is called Janus wettability [70].

Another type of surface structure which is actively researched is obtained by introducing another liquid to function as a lubricant, known as liquid-infused surface (LIS) [71] or slippery liquid-infused porous surfaces (SLIPS) [72]. Inspired by *Nepenthes* pitcher plants [73], a rough or porous solid substrate can be infused with a lubricant (Figure 2.3(f)). The lubricant film will separate the droplet from the solid structure, which can introduce a smoother surface, less friction, and less pinning [74, 75].

2.4 Wetting on Fibre

Other than planar substrates, fibres and fibrous materials are ubiquitous in nature, and they are the focus of this thesis. Two prominent examples of fibrous structures in nature are cactus and spider silk. Cactus have an integrated multi-level surface structure of conical spines comprising multiple barbs with microgrooves which are designed to efficiently harvest water from fog [1]. Spider silk also has been observed to have a similar multi-scale surface structure, with a periodic spindle-knot and joint structure at the micron scale and random and ordered fibre structures in the nanoscale, respectively [2].

A droplet sitting on a fibre free of external force typically can adopt two different morphologies. The first is called the barrel morphology (Figure 2.4(a)), which is axisymmetric and the droplet fully encapsulates the fibre. Lord Rayleigh in his seminal paper [30] is one of the earliest observers of the barrel configuration. When a water jet encapsulates a fibre (i.e. a fibre sheathed by a liquid film), the jet surface will instead break up into numerous droplets in a barrel shape because of Rayleigh-Plateau instability. Another morphology, the so-called clamshell configuration (Figure 2.4(b)) has been noted by Adams [31]. It is characterised by

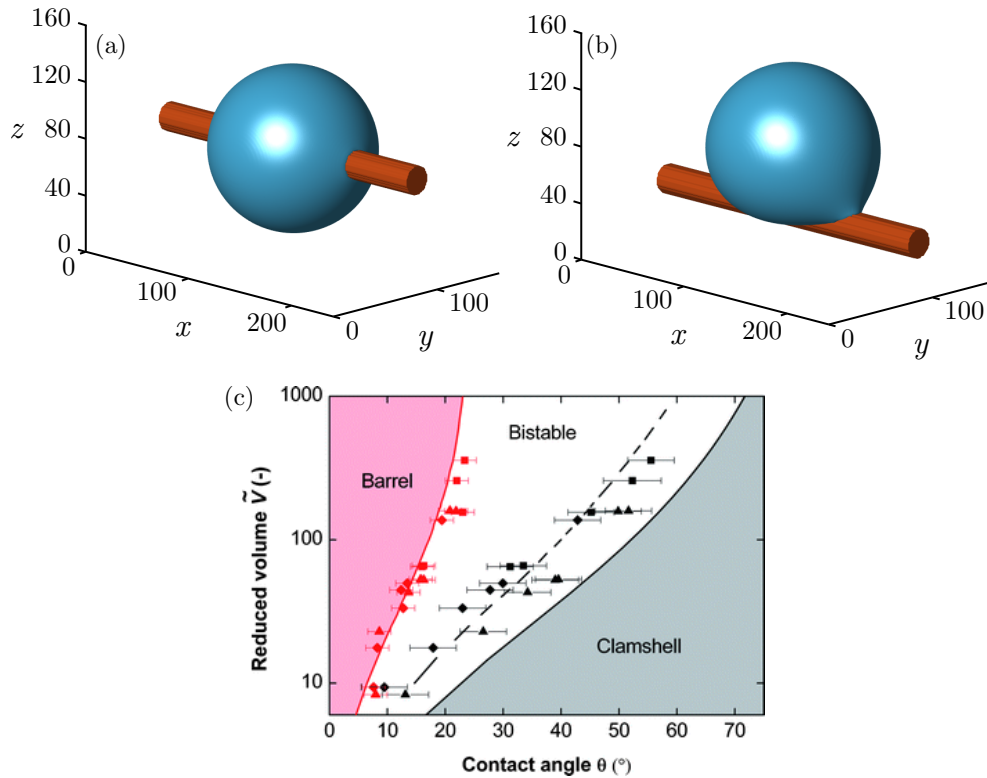


Figure 2.4: (a,b) Three-dimensional view of a droplet in the barrel and clamshell morphologies, respectively. (c) Morphology diagram of a droplet on fibre as a function of contact angle θ and the reduced volume $\tilde{V} = \Omega/(r_f)^3$, where Ω is the droplet volume and r_f is the fibre radius. Black and red symbols denote experimental results of barrel-to-clamshell and clamshell-to-barrel transitions, respectively. Different shapes denote different fibre diameters: (\square) 0.2, (\triangle) 0.3, and (\diamond) 0.5 mm. The solid lines indicate the stability limit for each morphology which is determined using numerical calculation, while the dashed line indicates the condition where both morphologies have equal energy. Figure (c) is reproduced with permission from [76].

an asymmetric shape, where the droplet is perched on one side of the fibre. Adams noted that by adding surfactant (i.e. detergent) to an aqueous medium, an oil droplet will increase its contact angle and transforms into the clamshell morphology.

The research on the transition between the barrel and clamshell morphologies has been done extensively. McHale, Newton, and Carroll used a finite element approach to predict the stability of both morphologies [77]. In another work, McHale and Newton introduce an absolute stability curve for clamshell, where the total free energy of the clamshell is lower than the barrel [78]. Eral, et al. used electrowetting and finite element calculations to demonstrate the reversibility of this transition and they identified a morphology diagram as a function of reduced volume and droplet contact angle (Figure 2.4(c)) [76]. De Ruiter, et al. studied the difference between the barrel-to-clamshell and the clamshell-to-barrel transition mechanisms [79]. Amrei, et al. investigated the effect of surface roughness on the equilibrium shape and

contact angle of a droplet on fibre [80]. They found that surface roughness delays the barrel-to-clamshell transition. On a conical fibre, the change in fibre radius can induce spontaneous movement from the cone tip to the base, followed by a transition from the barrel morphology to the clamshell morphology [24].

2.5 Key Dimensionless Parameters

There are a number of physical properties that influence the droplet equilibrium shapes and dynamics. These include the droplet density (ρ), characteristic length (D), surface tension (γ), dynamic viscosity (η), gravitational acceleration (g), and velocity (v). To compare different physical effects, dimensionless numbers obtained from these properties are employed. In general, dimensionless numbers can be grouped into independent and dependent dimensionless numbers. Below are examples of independent dimensionless numbers:

$$\text{We} = \frac{\rho D v^2}{\gamma}, \quad (2.10)$$

$$\text{Re} = \frac{\rho D v}{\eta}, \quad (2.11)$$

$$\text{Bo} = \frac{\rho g D^2}{\gamma}, \quad (2.12)$$

$$\text{Ca} = \frac{\eta v}{\gamma}. \quad (2.13)$$

The Weber number (We) compares inertial and capillary effects [81]. The Reynolds number (Re) compares inertia and viscosity effects [5]. The Bond number (Bo) compares the pressure contributed by gravity and surface tension. The capillary number (Ca) compares the relative effect of viscosity and surface tension [5] and is also often used to represent non-dimensionalised velocity. An example of a dependent dimensionless number is the Ohnesorge number (Oh) which compares inertial, viscous, and capillary forces [82]. It is mathematically described as:

$$\text{Oh} = \frac{\eta}{\sqrt{\rho \gamma D}} = \frac{\sqrt{\text{We}}}{\text{Re}}. \quad (2.14)$$

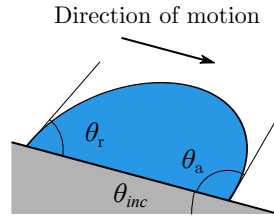


Figure 2.5: The advancing (θ_a) and the receding (θ_r) angle of a moving droplet on a tilted surface with inclination θ_{inc} .

2.6 Dynamic Wetting

2.6.1 Contact Angle Hysteresis

So far, we have only discussed the equilibrium or Young's contact angle. In reality, this is only accurate on a homogeneous (smooth) surface. On most surfaces, there exist defects that can pin the droplet at the onset of movement. For example, let us put a partially wetting droplet on a tilted surface with an inclination angle (θ_{inc}). Let us assume that initially, the droplet is not moving. Then, as we keep increasing θ_{inc} , the front contact angle will increase and the rear contact angle will decrease. The critical tilt angle on the onset of movement (θ_c) is called the sliding angle [52]. The maximum front contact angle when the droplet starts moving is called the advancing angle (θ_a), while the minimum rear angle is called the receding angle (θ_r) (Figure 2.5(a)). The difference between the advancing and the receding contact angle is called the contact angle hysteresis ($CAH = \theta_a - \theta_r$). Typically, the relation between the advancing, the receding, and the equilibrium (Young's) contact angle is $\theta_r \leq \theta_e \leq \theta_a$. Therefore, on a real surface, the stationary contact angle will be between the advancing and the receding contact angle.

A large CAH causes pinning, where a droplet will not move until the driving force is sufficient to overcome such pinning. For example, CAH is the cause of liquid columns being captured in a vertical tube. The difference in contact angle of upward and downward pulls will balance the weight of the liquid column [5]. CAH is also one of the factors that contributed to the so-called coffee-ring effect, which is an exemplar of evaporation-driven capillary flow. During evaporation, a pinned contact line has a higher evaporation rate compared to its bulk part, therefore causing a capillary flow into the contact line which causes an accumulation of solid particles near the contact line [83]. CAH can also introduce pressure drop in slug flow within mini and macro channels [84].

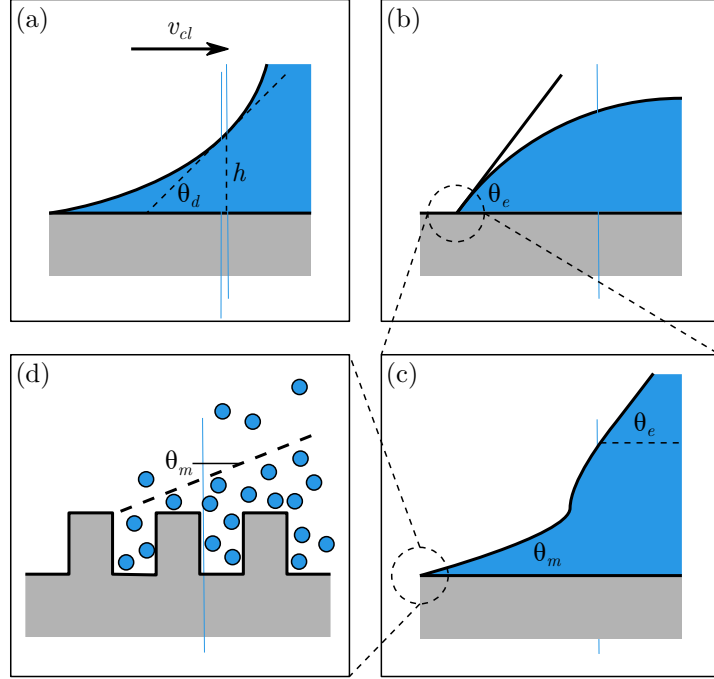


Figure 2.6: (a) Illustration showing the dynamic contact angle (θ_d) during movement with velocity v_{cl} . (b,c,d) Illustrations of three different regimes showing local contact angles: outer, intermediate, and inner regimes, respectively. θ_e is the equilibrium or Young's contact angle while θ_m is the microscopic contact angle. Figures are adapted from [87].

2.6.2 Dynamic Contact Angle: The Cox-Voinov Law

Once the droplet has started moving, the dynamic contact angle (θ_d) will deviate from its stationary value (Figure 2.6(a)). A popular framework to describe the dynamic contact angle is given by the so-called Cox-Voinov law [85, 86]. Mathematically, it is written as:

$$\theta_d(h) = \left[\theta_m^3 \pm \left(\frac{9\eta v_{cl}}{\gamma} \right) \ln \left(\frac{h}{h_m} \right) \right]^{1/3}, \quad (2.15)$$

where v_{cl} is the contact line velocity, θ_m is the microscopic contact angle, and h_m is called the cut-off value, and the \pm sign represents the advancing and receding motion, respectively. An important point to be made is this equation is only valid when $\theta_d < 135^\circ$.

In the Cox-Voinov law, we are introduced to a new concept called the microscopic contact angle. In reality, the so-called 'local contact angle' has a less clear definition depending on which length scale we use to measure it [87]. Generally speaking, three regimes are showing three distinct 'contact angles'. The first region is the so-called outer regime. This region is roughly in the length scale of the droplet radius r_d , located far from the contact line, and defined as what we previously called the equilibrium or Young's contact angle (θ_e) (Figure 2.6(b)). The

second regime is called the intermediate regime, whose characteristic is a change of drop profile from convex to concave (Figure 2.6(c)). Roughly speaking, the length scale is approximately on the order of $3 \text{Ca} r_d / \theta_e$. The final regime is the inner regime, usually in the nanometre scale, where the liquid molecules constantly fluctuate (Figure 2.6(d)).

Unfortunately, θ_m and h_m values are difficult to measure due to the fact that the h_m scale is in the nanometre range [87]. The existence of h_m , however, shows that pure macroscopic hydrodynamics cannot explain all the phenomena in the dynamic regime. In the triple contact line, the dissipation of energy per unit length and unit time (\dot{W}_{diss}) can be hydrodynamically computed by using this formula [52, 88]:

$$\dot{W}_{\text{diss}} = \frac{\eta v^2}{\theta_d} \int_{h_m}^D \frac{dh}{h} = \frac{\eta v^2}{\theta_d} \ln \left(\frac{D}{h_m} \right). \quad (2.16)$$

Assuming a full macroscopic hydrodynamics phenomenon, h_m is set to 0 (i.e. from the triple contact line) while D is set to the relevant length scale (e.g. the droplet radius r_d). However, using this boundary will cause the rate of energy dissipation to become infinity (i.e. Huh-Scriven paradox [85, 89]). To solve this, we have to combine both hydrodynamics and microscopic details by introducing a microscopic cut-off h_m [52, 87].

Several models have tried to relate both hydrodynamics and microscopic details [90]. Usually, these models start from the so-called molecular kinetic theory [91], where we assume that a substrate can contain multiple adsorption sites (e.g. the corrugation on the surfaces (Figure 2.6(d))) and the molecular activity of the fluid interface depends on the strength of these potential wells. Two examples of such models are by Petrov and Petrov [92]:

$$\theta_m(v_{cl}) = \cos^{-1} \left[\theta_e \pm \left(\frac{2 \mathbb{K}_B T}{\gamma \Lambda^2} \right) \sinh^{-1} \left(\frac{v_{cl}}{2 \mathbb{K}_0 \Lambda} \right) \right], \quad (2.17)$$

and by Brochard-Wyart and de Gennes [93]:

$$v_{cl} = \frac{\gamma (\cos \theta_m - \cos \theta_e)}{\frac{\mathbb{K}_B T}{\mathbb{K}_0 \Lambda^3} + \frac{6 \eta}{\theta_d} \ln \left(\frac{D}{h_m} \right)}, \quad (2.18)$$

where \mathbb{K}_B is the Boltzmann constant, T is the temperature, Λ is the mean molecular distance,

and \mathbb{K}_0 is the equilibrium frequency of the molecular activity, which is defined as [90]:

$$\mathbb{K}_0 = \frac{\mathbb{K}_B T}{\mathbb{H}} \exp\left(\frac{-\Delta G}{\mathbb{N}_A \mathbb{K}_B T}\right), \quad (2.19)$$

where \mathbb{H} is the Planck constant, ΔG is the molar activation energy, and \mathbb{N}_A is the Avogadro number. A more comprehensive overview of the contact line dynamics can be found in [90].

CHAPTER 3

Methods

3.1 Introduction

To mathematically describe the state of moving fluid we need variables which describe the fluid velocity (\mathbf{u}), pressure (p), and density (ρ) [88]. These quantities evolve in macroscopic fluid equations of motion that conserve mass and momentum. Unfortunately, these equations can have complex solutions, such as analytical solutions are only available for a small subset of cases [94]. Therefore, for more complex cases, we instead have to numerically solve these equations by using computational fluid dynamics (CFD).

Broadly speaking, there are two main categories of CFD. The first category is the so-called conventional methods. In conventional methods, the macroscopic fluid equations are directly discretised and solved by using numerical approximations. Some examples are finite differences (FD) [95, 96], finite volume (FV) [96, 97], and finite elements method (FEM) [98, 99]. These methods are reasonably simple in principle and directly solve the macroscopic variables of the fluid (i.e. \mathbf{u} , p , and ρ) [94]. However, because the macroscopic fluid equations are typically non-linear and simultaneous, they need highly complex and computationally expensive iterative algorithms to solve properly. Furthermore, conventional methods are usually used at macroscopic scales, therefore it is difficult or cumbersome to account for coarse-grained molecular information.

The second category of CFD is the particle-based methods. Using these methods, we can either track the particle positions, mass and momentum directly, or we can track the distributions of the particles themselves. Molecular dynamics (MD) [100, 101], direct simulation Monte Carlo (DSMC) [102, 103], dissipative particle dynamics (DPD) [104, 105], multiparticle

collision dynamics (MPCD) [106, 107], and lattice Boltzmann method (LBM) [94, 108] are examples of particle-based CFD. Because particle-based methods can be used to track a wide range of particles, different methods are favourable for different purposes. For example, MD tracks the position of atoms and molecules directly. These particles interact through intermolecular forces, whose positions are updated numerically by integrating Newton's equation of motion [94, 100]. This means that MD is suitable for microscale phenomena (where atomistic details are pertinent) but is often too computationally expensive for macroscale phenomena. With the so-called mesoscopic models, we instead track the distributions or the representative collections of molecules [94]. DPD and LBM are two examples of this class of models. With mesoscopic models, we can simulate systems with larger lengths and time scales than microscopic models. Mesoscopic models are also able to incorporate microscopic or mesoscopic physics that are hard to describe macroscopically [109]. A more detailed comparison between the conventional and the particle-based methods can be found in [94, 108, 110, 111].

In this project, I am using the LBM as my numerical solver. LBM is based on Boltzmann's kinetic theory. In LBM, instead of dealing with the interaction between individual molecules, we focus on the collective evolution of the ensembles of the molecules [109]. Compared to other methods, LBM has several advantages for the problem of interest in this thesis. First, it is able to capture both complex multiphase flows with a high-density ratio between the liquid and gas phases. Second, I can easily incorporate complex geometries, as well as changes in the interface topology. Third, the LBM algorithm is suitable for parallel computation, which makes it appropriate for the demanding problems addressed here. In the following sections, I will discuss the LBM in general and the specific models that I am using: the two-phase fluid model and the two-component fluid model.

3.2 The Lattice Boltzmann Method

3.2.1 The Boltzmann Equation

The fundamental variable in kinetic theory is the probability density or the particle distribution function [94]. The particle distribution function can be denoted as $f(\mathbf{x}, \boldsymbol{\xi}, t)$. We can say f represents the density of particles with velocity ($\boldsymbol{\xi}$) at position (\mathbf{x}) and time (t). More explicitly, with the Boltzmann equation, we are working in both physical and velocity spaces.

We can relate f to macroscopic variables from its moments which are obtained by inte-

grating f over the entire velocity space. Some salient examples of these macroscopic values are [94]:

1. Mass density:

$$\rho(\mathbf{x}, t) = \int f(\mathbf{x}, \boldsymbol{\xi}, t) d^3\xi. \quad (3.1)$$

2. Momentum density:

$$\rho(\mathbf{x}, t) \mathbf{u}(\mathbf{x}, t) = \int \boldsymbol{\xi} f(\mathbf{x}, \boldsymbol{\xi}, t) d^3\xi. \quad (3.2)$$

The distribution function evolves over time via the Boltzmann equation. Its form is:

$$\frac{\partial f}{\partial t} + \boldsymbol{\xi} \frac{\partial f}{\partial \mathbf{x}} + \frac{\mathbf{F}}{\rho} \frac{\partial f}{\partial \boldsymbol{\xi}} = \Omega^{lbm}(f). \quad (3.3)$$

The left-hand side represents the streaming of the distribution function, while the right-hand side represents the effects of intermolecular collisions [109]. On the left-hand side, the streaming is affected by advection due to the velocity associated with the particle distribution function and acceleration due to any force present [94].

3.2.2 The Lattice Boltzmann Equation

In LBM, instead of using particle distribution function in continuous velocity space, we use the discrete velocity distribution function $f_i(\mathbf{x}, t)$, which represents the density of particles with discrete velocity $\mathbf{c}_{i\alpha} = (c_{ix}, c_{iy}, c_{iz})$ at position \mathbf{x} and time t [94]. The velocity discretisation alongside its weighting factor will form a velocity set $\{\mathbf{c}_{i\alpha}, w_i\}$. $f_i(\mathbf{x}, t)$ is not only discrete in the velocity space but also in the spatial and time space. Typically, we use a square lattice (2D) or a cubic lattice (3D) with spacing Δx , while time is divided into a time step Δt . From this discretisation, we obtain the lattice Boltzmann equation (LBE) as [94]:

$$f_i(\mathbf{x} + \mathbf{c}_i \Delta t, t + \Delta t) - f_i(\mathbf{x}, t) = \Omega_i^{lbm}(\mathbf{x}, t). \quad (3.4)$$

Here, Ω_i^{lbm} is called the discrete collision operator and has many different forms. The simplest and the most popular is the Bhatnagar-Gross-Krook (BGK) operator [112]:

$$\Omega_i^{lbm}(f) = -\frac{f_i - f_i^{eq}}{\tau} \Delta t, \quad (3.5)$$

which will relax f_i into f_i^{eq} at relaxation time τ . More complex collision operators are available, which provide better stability and accuracy. Indeed, in Sections 3.3 and 3.4, we will use the so-called entropic and multiple relaxation time lattice Boltzmann schemes. Combining these equations, we can rewrite them into the so-called lattice BGK (LBGK) equation:

$$f_i(\mathbf{x} + \mathbf{c}_i \Delta t, t + \Delta t) = f_i(\mathbf{x}, t) - \frac{\Delta t}{\tau} \left(f_i(\mathbf{x}, t) - f_i^{eq}(\mathbf{x}, t) \right). \quad (3.6)$$

Typically, the LBM algorithm is divided into two parts: the collision step and the streaming step. The collision step applies the intermolecular collisions:

$$f_i^*(\mathbf{x}, t) = f_i(\mathbf{x}, t) - \frac{\Delta t}{\tau} \left[f_i(\mathbf{x}, t) - f_i^{eq}(\mathbf{x}, t) \right], \quad (3.7)$$

where $f_i^*(\mathbf{x}, t)$ represents the distribution function after collision. Next, in the streaming step, f_i^* is propagated to its neighbouring node:

$$f_i(\mathbf{x} + \mathbf{c}_i \Delta t, t + \Delta t) = f_i^*(\mathbf{x}, t). \quad (3.8)$$

The equilibrium distribution functions as employed in Equations (3.5), (3.6), and (3.7) is usually taken to be the Maxwell-Boltzmann distribution function [94]:

$$\begin{aligned} f_i^{eq}(\mathbf{x}, |\mathbf{v}|, t) &= \rho \left(\frac{3}{4\pi e} \right)^{3/2} e^{-3|\mathbf{v}|^2/(4e)} = \rho \left(\frac{\rho}{2\pi p} \right)^{3/2} e^{-p|\mathbf{v}|^2/(2\rho)} \\ &= \rho \left(\frac{1}{2\pi RT} \right)^{3/2} e^{-p|\mathbf{v}|^2/(2RT)}. \end{aligned} \quad (3.9)$$

When expanded to second order in the fluid velocity and written in the discretised form, it is given by [94]:

$$f_i^{eq}(\rho, \mathbf{u}) = w_i \rho \left(1 + \frac{u_\alpha \mathbf{c}_{i\alpha}}{c_s^2} + \frac{u_\alpha u_\beta (\mathbf{c}_{i\alpha} \mathbf{c}_{i\beta} - c_s^2 \delta_{\alpha\beta})}{2c_s^4} \right), \quad (3.10)$$

where c_s is the speed of the sound in the system. This form is valid for an isothermal, weakly compressible fluid assumption, and employed in most LBM models [94].

Just like the continuous version, the macroscopic parameters can be computed from the moment of the f_i :

1. Mass density:

$$\rho(\mathbf{x}, t) = \sum f_i(\mathbf{x}, t). \quad (3.11)$$

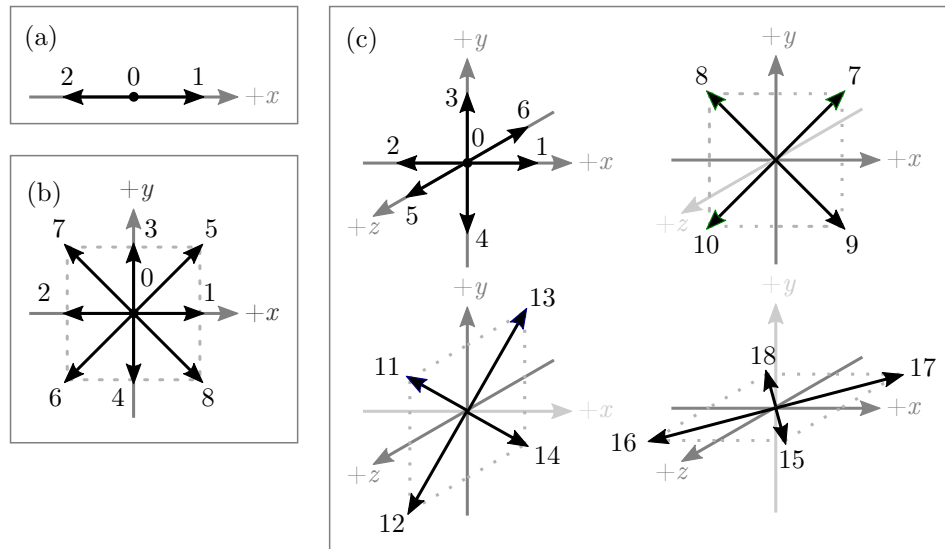


Figure 3.1: Illustrations for (a) D1Q3, (b) D2Q9, and (c) D3Q19 velocity sets.

2. Momentum density:

$$\rho \mathbf{u}(\mathbf{x}, t) = \sum \mathbf{c}_i f_i(\mathbf{x}, t). \quad (3.12)$$

3.2.3 Discretisation: Velocity Set

As discussed in the previous subsection, we need to do a discretisation in the velocity, spatial, and time-space. From discretisation in the velocity space, we will obtain a velocity set $\{\mathbf{c}_{i\alpha}, w_i\}$. A family of possible velocity sets was proposed by Qian, Humières, and Lallemand [113]. They proposed a simple cubic lattice with d spatial dimensions and q velocity vectors, denoted as $DdQq$. In most cases, the so-called D1Q3, D2Q9, and D3Q19 are sufficient for a one-dimensional, two-dimensional, and three-dimensional simulation, respectively. In this thesis, unless noted otherwise, I use the D3Q19 velocity set. Figure 3.1 shows these velocity sets, while Tables 3.1, 3.2, and 3.3 show their detailed properties.

3.2.4 Free Energy Approach

One popular application of CFD is for multiphase and multicomponent flows. Here, a system with different phases (e.g. liquid, gas) and/or components (e.g. water, oil) can coexist together. One of the biggest challenges in such systems is to track the shape and position of moving interfacial boundaries because such an interface can be very complex and unsteady. There are broadly two approaches to model these interfaces. The first one is the so-called interface tracking, where the interface is assumed to have zero thickness [114] and needs to be explicitly

Table 3.1: D1Q3 velocity set [113].

i	0	1	2
w_i	$\frac{2}{3}$	$\frac{1}{6}$	$\frac{1}{6}$
c_{ix}	0	1	-1

Table 3.2: D2Q9 velocity set [113].

i	0	1	2	3	4	5	6	7	8
w_i	$\frac{4}{9}$	$\frac{1}{9}$	$\frac{1}{9}$	$\frac{1}{9}$	$\frac{1}{9}$	$\frac{1}{36}$	$\frac{1}{36}$	$\frac{1}{36}$	$\frac{1}{36}$
c_{ix}	0	+1	-1	0	0	+1	-1	-1	+1
c_{iy}	0	0	0	+1	-1	+1	-1	+1	-1

Table 3.3: D3Q19 velocity set [113].

i	0	1	2	3	4	5	6
w_i	$\frac{1}{3}$	$\frac{1}{18}$	$\frac{1}{18}$	$\frac{1}{18}$	$\frac{1}{18}$	$\frac{1}{18}$	$\frac{1}{18}$
c_{ix}	0	+1	-1	0	0	0	0
c_{iy}	0	0	0	+1	-1	0	0
c_{iz}	0	0	0	0	0	+1	-1

i	7	8	9	10	11	12	13	14	15	16	17	18
w_i	$\frac{1}{36}$											
c_{ix}	+1	-1	+1	-1	0	0	0	0	+1	-1	+1	-1
c_{iy}	+1	+1	-1	-1	+1	-1	+1	-1	0	0	0	0
c_{iz}	0	0	0	0	+1	+1	-1	-1	+1	+1	-1	-1

tracked by a 2D mesh. This mesh needs to be updated and refined every single time step [115]. Because of the discontinuity between both phases or components, additional boundary conditions are needed such as a continuous velocity profile inside the boundary and a stress jump normal to the interface corresponding to the surface tension [94, 114]. Examples of this approach are front tracking [116, 117, 118] and marker-and-cell (MAC) [119, 120, 121].

On the other hand, LBM uses the so-called interface capturing method. Instead of using a moving mesh, we introduce an order parameter to differentiate different phases or components [109, 122]. There are no explicit elements that represent the interface; the interface is treated as a high variation region of the order parameter [123]. The order parameter evolves via another partial differential equation, typically using the so-called Allen-Cahn [124, 125, 126] or Cahn-Hilliard [127, 128, 129] equations, and no special boundary conditions are required. The fluid material parameters, such as density and viscosity are functions of the parameters. Interface properties such as surface tension can be represented through body force or gradients in the fluid pressure tensor in the Navier-Stokes equation [44, 122]. One potential disadvantage of the interface capturing methods is that the interface has a finite thickness which, for computational limitations, is often larger than the actual size in experiments. Other examples of front-capturing methods are volume-of-fluid (VOF) [130, 131, 132], and level-set formulations [133, 134, 135].

In general, there are four basic LBM multiphase/multicomponent methods: the colour-gradient model, the interparticle-potential model, the free-energy model, and the mean-field theory model [136]. In the free-energy-based model, we start with a free-energy functional that contains the thermodynamics of the system. From this functional, we can derive other relevant physical quantities that we are interested in. Also, the free-energy model has an advantage as a thermodynamically consistent model. If the system is in equilibrium, the free energy of the system will be minimised. In case the system is not in equilibrium, a thermodynamic force will drive the system towards equilibrium [44].

In general, the free energy of a multiphase or multicomponent system can be written as [44]:

$$E = \int_{V_0} [\mathbb{F}_b + \mathbb{F}_i] dV + \int_{A_0} \mathbb{F}_s dS, \quad (3.13)$$

where \mathbb{F}_b is the bulk term, \mathbb{F}_i is the interface term, and \mathbb{F}_s is the fluid-solid interaction term. The bulk term contains the equation of state which allows the coexistence of several fluid phases or

components. The interface term will penalise any variation in our order parameter. Finally, the fluid-solid interaction term describes how favourable the different fluid phases or components interact with the solid. I will discuss the specific forms of the free energy employed in this thesis in Sections 3.3 and 3.4. From the variation of E with regards to the order parameter (see Equations 3.30 and 3.61), we can obtain the so-called chemical forces (\mathbf{F}_{chem}) that drive the phase separation and determine the shape of the interfaces between phases and/or components.

3.3 Two-Phase Fluid

3.3.1 Continuum Equations of Motion

As has been described in Section 3.1, we need macroscopic fluid equations that conserve mass and momentum to describe the state of moving fluid. The continuity equation expresses the conservation of mass: the total mass flowing out of a volume element per unit time is equal to the decrease per unit time of the mass in the volume element. It is mathematically defined as [94]:

$$\frac{\partial \rho}{\partial t} + \nabla \cdot (\rho \mathbf{u}) = 0. \quad (3.14)$$

Next, the Navier-Stokes equation expresses the conservation of momentum. The change of net momentum is affected by the flow of momentum in and out of the volume unit, the difference in pressure, as well as the viscous and body forces acting on the fluid. Mathematically, it is written as [94]:

$$\frac{\partial(\rho u_\alpha)}{\partial t} + \frac{\partial(\rho u_\alpha u_\beta)}{\partial x_\beta} = -\frac{\partial p}{\partial x_\alpha} + \frac{\partial}{\partial x_\beta} \left[\eta \left(\frac{\partial u_\alpha}{\partial x_\beta} + \frac{\partial u_\beta}{\partial x_\alpha} \right) + \left(\eta_B - \frac{2\eta}{3} \right) \frac{\partial u_\chi}{\partial x_\chi} \delta_{\alpha\beta} \right] + F_\alpha, \quad (3.15)$$

where η is the dynamic viscosity, η_B is the bulk viscosity, and F_α is the body force. The body force here is not only limited to gravity, but can also include the fluid-solid interaction, electric or magnetic fields, etc. α , β , and χ denote generic spatial indices. Using Cartesian coordinates, this means that each index member is $\{x, y, z\}$.

Typically, fluid velocity has three spatial components. Combined with pressure and density, we have five different variables to describe fluid motion. However, we only have four equations to solve these variables: one from the continuity equation and three from the Navier-Stokes equation (one for each spatial direction). We can add another equation, the so-called equation of state (EOS), which relates variables describing the local thermodynamic state of the fluid.

The most common example of EOS is the ideal gas law [94]:

$$p = \rho RT, \quad (3.16)$$

which relates pressure to the density and temperature through the specific gas constant R . The ideal gas EOS is often conveniently chosen to model single fluid systems. However, to account for the coexistence between a high density phase (i.e. liquid) and a low density phase (i.e. gas), a more sophisticated EOS is required. A popular example is the van der Waals (vdW) EOS which is based on the vdW fluid theory [137]. In the vdW fluid, we assume that the interactions between neutral molecules are approximated by Lennard-Jones potential energy, where the force between molecules will be repulsive if the distance between them is less than a given distance and attractive otherwise [138]. Using the assumption that two molecules cannot overlap (hard-core repulsion), one can tune the interaction between the molecules by tuning the attractive (a) and the repulsive (b) parameter. Mathematically, the vdW EOS can be written as [137]:

$$p = \frac{\rho RT}{1 - b\rho} - a\rho^2. \quad (3.17)$$

To match experimental observations more accurately, different forms of EOS have been proposed. For example, the Carnahan-Starling (CS) EOS is obtained by modifying the repulsion term of the vdW EOS [137]:

$$p = \rho RT \frac{1 + (b\rho/4) + (b\rho/4)^2 - (b\rho/4)^3}{(1 - b\rho/4)^3} - a\rho^2, \quad (3.18)$$

where the parameters $a = 0.4963R^2T_c^2/p_c$ and $b = 0.18727RT_c/p_c$ are computed by fitting experimental data. Here, p_c and T_c represent the critical pressure and temperature, respectively.

3.3.2 Free Energy Lattice Boltzmann Model

In this thesis, I employ different free energy models to suitably capture different phenomena of interest. In Chapters 4 and 6, I need to model a two-phase (binary), single-component, high-density ratio system. Therefore, the free energy functional that I use is [42, 44]:

$$E = \int_{V_0} [\mathbb{F}_b + \mathbb{F}_i] dV, \quad (3.19)$$

where:

$$\mathbb{F}_b = \frac{\lambda_{hd}}{2} [\psi_{eos} - \psi_0], \quad (3.20)$$

$$\mathbb{F}_i = \frac{\kappa_{hd}}{2} \nabla^2 \rho, \quad (3.21)$$

and the parameters λ_{hd} and κ_{hd} are used to tune the surface tension and the interface width.

Next, ψ_{eos} is obtained by integrating the equation of state:

$$p = \rho \left[\frac{d\psi_{eos}}{d\rho} \right] - \psi_{eos}, \quad (3.22)$$

whose form depends on the EOS used. For Carnahan-Starling [44]:

$$\psi_{eos} = \rho \left[C - a\rho - \frac{8RT(-6 + b\rho)}{(-4 + b\rho)^2} + RT \log \rho \right], \quad (3.23)$$

$$\frac{d\psi_{eos}}{d\rho} = C - 2a\rho - \frac{16RT(-12 + b\rho)}{(-4 + b\rho)^3} + RT(1 + \log \rho). \quad (3.24)$$

Following Wöhrgang, et al. [44], I choose $a = 0.037$, $b = 0.2$, $R = 1$, and $T_c = 0.3773a/(bR)$, while C is chosen such that $\psi_{eos}(\rho_g) = \psi_{eos}(\rho_l) = \psi_0$.

3.3.3 The Lattice Boltzmann Implementation

3.3.3.1 Entropic Lattice Boltzmann Method with Exact Difference Forcing Methods

The entropic Lattice Boltzmann method (ELBM) is developed by Mazloomi, Chikatamarla, and Karlin in 2014 [42]. In the entropic LBM, instead of using a constant relaxation time τ for the collision operator, Mazloomi, Chikatamarla, and Karlin use two parameters, α_{hd} and β_{hd} . The lattice Boltzmann equation is then rewritten as [42]:

$$\begin{aligned} f_i(\mathbf{x} + \mathbf{c}_i \Delta t, t + \Delta t) - f_i(\mathbf{x}, t) &= \alpha_{hd} \beta_{hd} [f_i^{eq}(\mathbf{x}, t) - f_i(\mathbf{x}, t)] \\ &+ [f_i^{eq}(\rho, \mathbf{u} + \Delta \mathbf{u}) - f_i^{eq}(\rho, \mathbf{u})], \end{aligned} \quad (3.25)$$

where f_i^{eq} is defined as Equation (3.10). Here, parameter β_{hd} is related to the kinematic viscosity ν through:

$$\nu = \frac{(\beta_{hd}^{-1} - 1) c_s^2}{2}, \quad (3.26)$$

and its value varies between 0 and 1. Next, α_{hd} is the non-trivial root for the discrete entropic equation H_{hd} [44]:

$$H_{hd}(f' + \alpha_{hd}[f^{eq}(\rho, \mathbf{u} + \Delta\mathbf{u}) - f']) = H_{hd}(f'), \quad (3.27)$$

where:

$$]f'_i = f_i + [f_i^{eq}(\rho, \mathbf{u} + \Delta\mathbf{u}) - f_i^{eq}(\rho, \mathbf{u})]. \quad (3.28)$$

The core idea behind ELBM is to ensure that every LBM time step obeys the second law of thermodynamics, where the entropy never decreases. Mazloomi, Chikatamarla, and Karlin mathematically describe H_{hd} as:

$$H_{hd} = \sum_i f_i \ln \left(\frac{f_i}{w_i} \right), \quad (3.29)$$

where w_i is the weighting factor of the velocity vectors.

One main property of entropic LBM is α_{hd} 's ability to vary. For bulk cases, the value of α_{hd} converges to 2 which corresponds to the BGK scheme. However, at the interface between two phases with a high density ratio, the BGK is often inadequate. For a density ratio of more than 10, the surface tension force leads to instability [94]. The α_{hd} factor from Equation (3.27) helps stabilise the large density gradient at the liquid-vapour interface. The use of entropic LBM allows us to achieve a density ratio of 1000, which is typical for a two-phase liquid-gas system [42].

In ELBM, the thermodynamic parameters will enter the lattice Boltzmann equation through the forcing term, which is the second term on the right-hand side of Equation (3.25). To describe this, I need to introduce the concept of the chemical potential (μ_ρ). The chemical potential is defined as the free energy cost of adding materials to the system [94]. Mathematically, it is obtained by minimising the free energy functional as a function of the order parameter. Using

Equation (3.19) and Equation (3.23), we can obtain [44]:

$$\mu_\rho = \mu_\rho^b + \mu_\rho^i = \frac{\delta E}{\delta \rho}, \quad (3.30)$$

$$\mu_\rho^b = \frac{\lambda_{hd}}{2} \frac{d\psi_{eos}}{d\rho}, \quad (3.31)$$

$$\mu_\rho^i = -\kappa_{hd} \nabla^2 \rho. \quad (3.32)$$

Differences in the chemical potential lead to \mathbf{F}_{chem} which takes into account both the deviation from ideal gas law and the surface tension effects [42]. Mathematically, it is defined as [94]:

$$\mathbf{F}_{\text{chem}} = \nabla c_s^2 \rho - \rho \nabla \mu_\rho. \quad (3.33)$$

Next, I describe how \mathbf{F}_{chem} and other body forces such as gravity (\mathbf{F}_g) enter through ELBM. We define the velocity correction term $\Delta \mathbf{u}$ [139]:

$$\Delta \mathbf{u} = \frac{\mathbf{F} \Delta t}{\rho}, \quad (3.34)$$

where the total force $\mathbf{F} = \mathbf{F}_{\text{chem}} + \mathbf{F}_g$. This velocity correction is used both in the forcing term in Equation (3.25) and in the calculation of α in Equation (3.27). It is important to emphasise that the real fluid velocity should be calculated at half time step (the average between before and after the step). In ELBM, \mathbf{u} is called the bare fluid velocity and is calculated via [44]:

$$\rho \mathbf{u}(\mathbf{x}, t) = \sum \mathbf{c}_i f_i(\mathbf{x}, t), \quad (3.35)$$

and related to the actual fluid velocity \mathbf{v} via [44]:

$$\mathbf{v} = \mathbf{u} + \frac{\Delta \mathbf{u}}{2}. \quad (3.36)$$

3.3.3.2 Bounce-Back Boundary Conditions

In this work, I am assuming a no-slip condition between the fluid and the solid phase. To impose this in LBM, I use the so-called half-way bounce-back boundary condition (BBBC) [140, 141]. The idea is simple: populations that leave the boundary node \mathbf{x}_b meet the wall surface at $t + (\Delta t/2)$. These populations with direction i and velocity \mathbf{c}_i are then reflected to their

opposite direction \bar{i} and velocity $\mathbf{c}_{\bar{i}} = -\mathbf{c}_i$, arriving back at position \mathbf{x}_b and time $t + \Delta t$ [94]. Therefore, the streaming step is replaced by:

$$f_{\bar{i}}(\mathbf{x}_b, t + \Delta t) = f_i^*(\mathbf{x}_b, t), \quad (3.37)$$

where $f_i^*(\mathbf{x}_b, t)$ is the population that is going into the solid boundary and $f_{\bar{i}}(\mathbf{x}_b, t + \Delta t)$ is the population that has been reflected. The BBBC is illustrated in Figure 3.2 for a two-dimensional system using a D2Q9 velocity set and with a planar fluid-solid boundary. Populations \mathbf{c}_6 , \mathbf{c}_4 , and \mathbf{c}_8 are reflected into populations \mathbf{c}_5 , \mathbf{c}_3 , and \mathbf{c}_7 , respectively.

3.3.3.3 Fluid-Solid Interaction: The Forcing Method

To introduce the droplet contact angle, I use the so-called forcing method which is originally proposed by Huang, et al. for the pseudo-potential LBM [45], adapted by Mazloomi, Chikata-marla, and Karlin for their entropic LBM [42], and then further benchmarked by Bala, et al. [81]. Here, a forcing term ($F_{\alpha,s}$) is introduced with tunable fluid-solid interaction intensity. For a single component, two-phase fluid-solid interaction, the forcing term can be written as:

$$F_{\alpha,s} = \kappa_w \rho_{rel}(\mathbf{x}) \sum_i w_i s(\mathbf{x} + \mathbf{c}_i \delta t) \mathbf{c}_i. \quad (3.38)$$

In Equation (3.38), κ_w is the fluid-solid interaction intensity with values that can vary from negative (non-wetting) to positive (wetting). $\rho_{rel}(\mathbf{x})$ is called the rescaled density, written as:

$$\rho_{rel}(\mathbf{x}) = \frac{\rho(\mathbf{x}) - \rho_g}{\rho_l - \rho_g}. \quad (3.39)$$

$\rho_{rel}(\mathbf{x})$ is 0 if $\rho(\mathbf{x}) = \rho_g$ (bulk gas) and 1 if $\rho(\mathbf{x}) = \rho_l$ (bulk liquid). The rescaled density is essential to prevent large $F_{\alpha,s}$ to be applied in the gas phase since this will cause strong deviations of the gas density and instability in the simulation. Finally, $s(\mathbf{x} + \mathbf{c}_i \delta t)$ is a function which takes the value of 1 if the fluid node is located two lattice units away from the solid node and 0 everywhere else (Figure 3.3).

The forcing method is implemented as follows:

1. Copy the ρ value from fluid layer 1 to the solid layer.
2. Calculate $F_{\alpha,s}$ from Equation (3.38).
3. Add $F_{\alpha,s}$ to the corrected velocity calculation (Equation (3.34)).

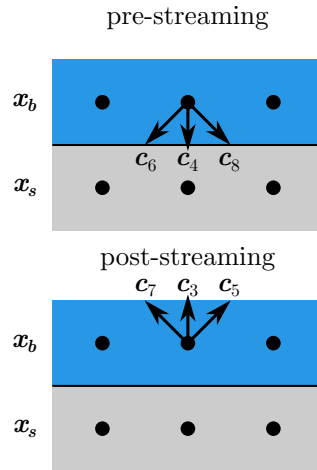


Figure 3.2: An illustration of half-way bounce-back boundary condition for D2Q9 velocity set. With this boundary condition, populations c_6 , c_4 , and c_8 are reflected into populations c_5 , c_3 , and c_7 , respectively. This figure is adapted from [94].

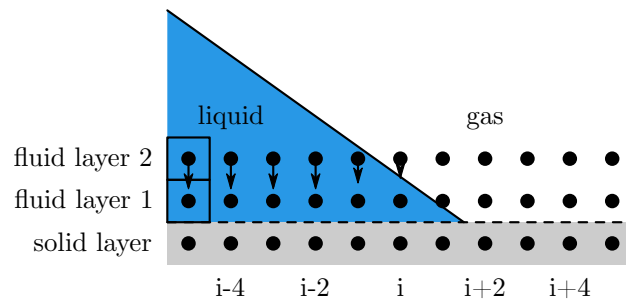


Figure 3.3: A sketch of the forcing terms acting on the second layer of fluid above the solid. The arrows show the magnitude of the forcing term (Equation (3.38)). The figure is adapted from [81].

4. Use the corrected velocity calculation to calculate the distribution function after the collision.

3.4 Two-component Fluid

For the work carried out in Chapter 5, instead of using a two-phase model, I will employ a two-component fluid model. This choice was made because a two-component fluid with the same density is more stable, as I explore to develop a fluid-solid interaction with long-range potential.

3.4.1 Continuum Equations of Motion

Similar to the two-phase model, for the two-component model, I employ the continuity equation (Equation (3.14)), the Navier-Stokes equation (Equation (3.15)), and the equation of state

(EOS). For the latter, here I use the ideal gas law (Equation (3.16)), whose form in lattice Boltzmann is [142]:

$$p = \rho c_s^2, \quad (3.40)$$

where c_s^2 is the speed of sound whose value is $1/3$.

Furthermore, I use the relative concentration ϕ as the order parameter to differentiate the two fluid components. Here, I use $\phi = 1$ for fluid 1 and $\phi = -1$ for fluid 2. ϕ is evolved using the so-called advection-diffusion (Cahn-Hilliard) equation [143]:

$$\partial_t \phi + \partial_\alpha (\phi \mathbf{v}) = M_\phi \nabla^2 \mu_\phi. \quad (3.41)$$

The second term on the left-hand side is called the advection term, where ϕ moves along with the fluid [94]. The right-hand side is the diffusive term, where the evolution of ϕ is driven by chemical potential inhomogeneities. M_ϕ is the so-called mobility parameter. Its value can either be constant or a function ϕ .

3.4.2 Free Energy Lattice Boltzmann

The model I employ here was originally developed by Briant and Yeomans [142]. However, I use the notation from the work by Semperebon, et al [143], who have extended Briant and Yeomans model into a ternary system. The free energy functional is written as:

$$E = \int_{V_0} [\mathbb{F}_b + \mathbb{F}_i] dV, \quad (3.42)$$

where:

$$\mathbb{F}_b = \frac{1}{32} [\kappa_1 + \kappa_2] (1 + \phi)^2 (1 - \phi)^2 + c_s^2 \rho \ln \rho, \quad (3.43)$$

$$\mathbb{F}_i = \frac{\alpha_{ed}^2}{8} [\kappa_1 + \kappa_2] \nabla^2 \phi, \quad (3.44)$$

where κ_1 and κ_2 are parameters used to tune the surface tension between fluids 1 and 2, while α_{ed} is used to tune the interface width. These parameters are related to the surface tension (γ_{12}) by [143]:

$$\gamma_{12} = \frac{\alpha_{ed} (\kappa_1 + \kappa_2)}{6}. \quad (3.45)$$

3.4.3 The Lattice Boltzmann Implementation

3.4.3.1 Multiple Relaxation Time Lattice Boltzmann Method

Briant and Yeomans have developed a lattice Boltzmann model for a two-component system [142]. In this model, they used two distribution functions f_i and g_i to evolve ρ and ϕ , respectively. For a velocity set with q velocity vectors, the physical variables are related to the distribution function by [144]:

$$\rho(\mathbf{x}, t) = \sum_i^q f_i(\mathbf{x}, t) = 1, \quad (3.46)$$

$$\rho(\mathbf{x}, t) u_\alpha(\mathbf{x}, t) = \sum_i^q f_i(\mathbf{x}, t) c_{i,\alpha}(\mathbf{x}, t), \quad (3.47)$$

$$\phi(\mathbf{x}, t) = \sum_i^q g_i(\mathbf{x}, t). \quad (3.48)$$

Here, the lattice Boltzmann equation is defined as [144]:

$$f_i(\mathbf{x} + \mathbf{c}_i \Delta t, t + \Delta t) - f_i(\mathbf{x}, t) = -\mathcal{M}^{-1} \mathcal{S} \mathcal{M} [f_i(\mathbf{x}, t) - f_i^{eq}(\mathbf{x}, t)] + S_i^{\text{Guo}}, \quad (3.49)$$

$$g_i(\mathbf{x} + \mathbf{c}_i \Delta t, t + \Delta t) - g_i(\mathbf{x}, t) = -\frac{\Delta t}{\tau_\phi} [g_i(\mathbf{x}, t) - g_i^{eq}(\mathbf{x}, t)]. \quad (3.50)$$

I use the so-called multiple-relaxation-time (MRT) collision operator to evolve f_i . The basic idea behind MRT is instead of relaxing the population (f_i) with a single relaxation time, we instead use the so-called transformation matrix (\mathcal{M}) and relaxation matrix (\mathcal{S}) to relax different moments individually [94]. The transformation matrix \mathcal{M} has a shape of $q \times q$, where q is the number of velocity vectors for that particular set. Here, I specifically use the D3Q19

velocity set with matrix \mathcal{M} [145]:

$$\mathcal{M} = \begin{bmatrix} 1 & 1 & 1 & 1 & 1 & 1 & 1 & 1 & 1 & 1 & 1 & 1 & 1 & 1 & 1 & 1 & 1 & 1 \\ -30 & -11 & -11 & -11 & -11 & -11 & -11 & 8 & 8 & 8 & 8 & 8 & 8 & 8 & 8 & 8 & 8 & 8 \\ 12 & -4 & -4 & -4 & -4 & -4 & -4 & 1 & 1 & 1 & 1 & 1 & 1 & 1 & 1 & 1 & 1 & 1 \\ 0 & 1 & -1 & 0 & 0 & 0 & 0 & 1 & -1 & 1 & -1 & 1 & -1 & 1 & -1 & 0 & 0 & 0 \\ 0 & -4 & 4 & 0 & 0 & 0 & 0 & 1 & -1 & 1 & -1 & 1 & -1 & 1 & -1 & 0 & 0 & 0 \\ 0 & 0 & 0 & 1 & -1 & 0 & 0 & 1 & 1 & -1 & -1 & 0 & 0 & 0 & 0 & 1 & -1 & 1 & -1 \\ 0 & 0 & 0 & -4 & 4 & 0 & 0 & 1 & 1 & -1 & -1 & 0 & 0 & 0 & 0 & 1 & -1 & 1 & -1 \\ 0 & 0 & 0 & 0 & 0 & 1 & -1 & 0 & 0 & 0 & 0 & 1 & 1 & -1 & -1 & 1 & 1 & -1 & -1 \\ 0 & 0 & 0 & 0 & 0 & -4 & 4 & 0 & 0 & 0 & 0 & 1 & 1 & -1 & -1 & 1 & 1 & -1 & -1 \\ 0 & 2 & 2 & -1 & -1 & -1 & -1 & 1 & 1 & 1 & 1 & 1 & 1 & 1 & 1 & -2 & -2 & -2 & -2 \\ 0 & -4 & -4 & 2 & 2 & 2 & 2 & 1 & 1 & 1 & 1 & 1 & 1 & 1 & 1 & -2 & -2 & -2 & -2 \\ 0 & 0 & 0 & 1 & 1 & -1 & -1 & 1 & 1 & 1 & 1 & -1 & -1 & -1 & -1 & 0 & 0 & 0 & 0 \\ 0 & 0 & 0 & -2 & -2 & 2 & 2 & 1 & 1 & 1 & 1 & -1 & -1 & -1 & -1 & 0 & 0 & 0 & 0 \\ 0 & 0 & 0 & 0 & 0 & 0 & 0 & 1 & -1 & -1 & 1 & 0 & 0 & 0 & 0 & 0 & 0 & 0 & 0 \\ 0 & 0 & 0 & 0 & 0 & 0 & 0 & 0 & 0 & 0 & 0 & 0 & 0 & 0 & 0 & 1 & -1 & -1 & 1 \\ 0 & 0 & 0 & 0 & 0 & 0 & 0 & 0 & 0 & 0 & 0 & 1 & -1 & -1 & 1 & 0 & 0 & 0 & 0 \\ 0 & 0 & 0 & 0 & 0 & 0 & 0 & 1 & -1 & 1 & -1 & -1 & 1 & -1 & 1 & 0 & 0 & 0 & 0 \\ 0 & 0 & 0 & 0 & 0 & 0 & 0 & -1 & -1 & 1 & 1 & 0 & 0 & 0 & 0 & 1 & -1 & 1 & -1 \\ 0 & 0 & 0 & 0 & 0 & 0 & 0 & 0 & 0 & 0 & 0 & 1 & 1 & -1 & -1 & -1 & -1 & 1 & 1 \end{bmatrix} \quad (3.51)$$

This matrix transforms the nineteen velocity distribution functions (f_i) into nineteen moments, $m_j = \mathcal{M}_{ji} f_i$. These moments consisted of both hydrodynamic (i.e. macroscopic and affect NSE) and non-hydrodynamic moments (i.e. do not affect NSE) [94, 146, 147]. For this work, the relevant moments are: density ρ (row one); momentum density ρu_x , ρu_y , ρu_z (rows four, six, eight); and viscous stress tensor components $3\sigma_{xx}$, $\sigma_{yy} - \sigma_{zz}$, σ_{xy} , σ_{yz} , σ_{xz} (rows ten, twelve, fourteen, fifteen, sixteen) [148].

The relaxation matrix \mathcal{S} contains the relaxation rate for each moment. The form of \mathcal{S} depends on which method we used to construct \mathcal{M} [94]. In this work, the form of the matrix \mathcal{S} is:

$$\mathcal{S} = \text{diag}\{0, 1, 1, 0, 1, 0, 1, 0, 1, (1/\tau_{\text{MRT}}), 1, (1/\tau_{\text{MRT}}), 1, (1/\tau_{\text{MRT}}), (1/\tau_{\text{MRT}}), (1/\tau_{\text{MRT}}), 1, 1, 1\}. \quad (3.52)$$

where τ_{MRT} is the relaxation time, which is related to the dynamic viscosity (η) via [74]:

$$\eta = \rho c_s^2 \left[\tau_{\text{MRT}} - \frac{\Delta t}{2} \right]. \quad (3.53)$$

τ_{MRT} is a function of ϕ . At the bulk phase, this is simply equal to τ_1 (when $\phi = +1$) or τ_2 (when $\phi = -1$). At intermediate values of ϕ , we linearly interpolate between τ_1 and τ_2 .

g_i is evolved using the BGK collision operator with relaxation time τ_ϕ , which is related to the mobility parameter (M_ϕ) via [143, 144]:

$$M_\phi = \Gamma_\phi \left(\tau_\phi - \frac{\Delta t}{2} \right), \quad (3.54)$$

where Γ_ϕ is a tunable parameter that will appear in the equilibrium distribution function.

The equilibrium distribution function for this model is defined as follows. For $i > 0$ [143]:

$$f_i^{eq} = w_i \left(\frac{p_b}{c_s^2} + \frac{u_\alpha \mathbf{c}_i \boldsymbol{\alpha}}{c_s^2} + \frac{u_\alpha u_\beta (\mathbf{c}_i \boldsymbol{\alpha} \mathbf{c}_i \boldsymbol{\beta} - c_s^2 \delta_{\alpha\beta})}{2c_s^4} \right), \quad (3.55)$$

$$g_i^{eq} = w_i \left(\frac{\Gamma_\phi \mu_\phi}{c_s^2} + \frac{\phi u_\alpha \mathbf{c}_i \boldsymbol{\alpha}}{c_s^2} + \frac{\phi u_\alpha u_\beta (\mathbf{c}_i \boldsymbol{\alpha} \mathbf{c}_i \boldsymbol{\beta} - c_s^2 \delta_{\alpha\beta})}{2c_s^4} \right), \quad (3.56)$$

where w_i is the weighting coefficient whose value depends on the velocity sets that we are using. For D3Q19, w_i is tabulated in Table 3.3. f_0^{eq} and g_0^{eq} are calculated by imposing the constraints given in Equations (3.46) and (3.48):

$$f_0^{eq}(\mathbf{x}, t) = 1 - \sum_1^q f_i^{eq}(\mathbf{x}, t), \quad (3.57)$$

$$g_0^{eq}(\mathbf{x}, t) = \phi(\mathbf{x}, t) - \sum_1^q g_i^{eq}(\mathbf{x}, t). \quad (3.58)$$

S_i^{Guo} in Equation (3.49) is the so-called Guo forcing term which is used to include chemical (or thermodynamic) forces from an imbalance in chemical potential (\mathbf{F}_{chem}) and external forces such as gravity (\mathbf{F}_g) and long-range fluid-solid interaction (\mathbf{F}_{LRP}). I will discuss the Guo forcing term in more detail in the next section.

3.4.3.2 Guo Forcing

One of the most popular methods to include forces in lattice Boltzmann models is the so-called Guo forcing [149]. The forcing term is written as follows [94]:

$$S_i^{\text{Guo}} = \left(1 - \frac{\Delta t}{2\tau_{MRT}}\right) w_i \left(\frac{\mathbf{c}_{i\alpha}}{c_s^2} + \frac{(\mathbf{c}_{i\alpha}\mathbf{c}_{i\beta} - c_s^2\delta_{\alpha\beta})u_\beta}{c_s^4}\right) F_\alpha, \quad (3.59)$$

where $F_\alpha = \mathbf{F} = \mathbf{F}_{\text{chem}} + \mathbf{F}_g + \mathbf{F}_{\text{LRP}}$ and the other parameters take their usual meaning.

For a two-component fluid model, \mathbf{F}_{chem} is defined as:

$$\mathbf{F}_{\text{chem}} = \nabla c_s^2 \rho - \phi \nabla \mu_\phi, \quad (3.60)$$

where μ_ϕ [143]:

$$\mu_\phi = \mu_\phi^b + \mu_\phi^i = \frac{\delta E}{\delta \phi}, \quad (3.61)$$

$$\mu_\phi^b = \frac{1}{8} (\kappa_1 + \kappa_2) (\phi + 1)(\phi - 1)(\phi), \quad (3.62)$$

$$\mu_\phi^i = -\frac{\alpha^2}{4} (\kappa_1 + \kappa_2) (\nabla^2 \phi). \quad (3.63)$$

I will discuss the formulation of \mathbf{F}_{LRP} in Chapter 5.

Similar to EDM forcing method, the real fluid velocity is calculated at the half-time step. However, since Guo forcing does not differentiate the bare and the real fluid velocity, the momentum density is calculated via [94]:

$$\rho \mathbf{u}(\mathbf{x}, t) = \sum \mathbf{c}_i f_i(\mathbf{x}, t) + \frac{\mathbf{F} \Delta t}{2}. \quad (3.64)$$

The accuracy of EDM and Guo forcing for single or multiphase systems is similar [150], so the choice of using either one is entirely up to the user.

CHAPTER 4

Modelling the Dynamics of Partially Wetting

Droplets on Fibres

4.1 Introduction

Fibre and fibrous materials have been used extensively both in nature [1, 2, 3] and industry [4, 5, 6, 7, 8]. Therefore, given their wide-ranging interest, droplet studies on fibres have a long history. In a seminal paper, Lord Rayleigh has observed that a thin film encapsulating a fibre can break up because of capillary instability [30], resulting in a string of droplets with barrel morphology, where the droplet is axisymmetric and encapsulates the fibre completely. Adams noted another morphology, clamshell, which is favoured by the droplet when the contact angle of the droplet increases [31]. Clamshell is characterised by its asymmetric shape, where the droplet is only perched on one side of the fibre. More recent studies have systematically investigated the transition and the stability of these two morphologies [76, 77, 78, 79, 80], which depend on the contact angle of the droplet, the droplet volume, and the fibre radius.

Beyond equilibrium properties, droplet dynamics on fibres have also generated significant interest. Several groups have deduced the scaling laws for droplet velocity along the fibre by balancing the viscous forces experienced by the droplet against the driving force [11, 22]. Typically, the droplet weight due to gravity is the driving force in the experiments. Other external driving forces, both parallel and perpendicular to the fibre, have also been considered to generate droplet motion, including subjecting the droplet to airflow [26, 29] or using a centrifugal force by rotating the fibre support [27]. In addition, more complex fibre geometries have been investigated. These include conical fibres [28, 151, 152, 153], where the curvature

asymmetry can be exploited to drive self-propulsion; fibre cross-junctions [23, 154], where the droplet trajectory can be tuned, for example, as the droplet size and orientation of the driving force is varied; and multiple parallel fibres, both when the fibres are rigid and flexible [155, 156, 157].

To date, the majority of works on droplet dynamics have focussed on the case where the droplet is perfectly wetting the solid fibres. In contrast, here I will primarily consider the dynamics of partially wetting droplets. I will investigate the complex shape and velocity of such droplets as I vary the fibre curvature and the droplet body force (correspondingly, velocity). When the droplet remains compact, I identify scaling laws for both the barrel and clamshell morphologies. Compared to known results for fully wetting droplets [11, 22], a key difference is in how the loss of symmetry and corresponding variation of the droplet shape and aspect ratio affects the dynamics of droplets with clamshell morphology. Focussing on the clamshell morphology, I then demonstrate that the droplet dynamics are affected by the fibre curvature. On flat surfaces, it has been observed that, with increasing velocity, the receding contact line becomes unstable leading to the formation of trailing satellite droplets. This phenomenon, the so-called pearling instability, has been extensively studied on flat surfaces [32, 33, 158, 159]. Interestingly, I find satellite droplet formation occurs on fibres as well, and it is favoured with increasing fibre curvature. Moreover, I find a region of the parameter space in which the droplet oscillates as it moves along the fibre. A similar observation was made by Yang et al. [160] for droplets on an inclined flat surface.

This chapter is organised as follows. In Section 4.2, I discuss the simulation setup based on the lattice Boltzmann method [94]. The lattice Boltzmann method has been successfully harnessed to study a wide range of interfacial flows, including droplet collisions [44, 161], capillary filling, self-propelled droplet slugs [81], and droplet impact on textured superhydrophobic surfaces [162]. The results are divided into four sections. In Section 4.3, I identify three dynamic regimes for droplets in the clamshell morphology. I systematically vary the Bond number and the size ratio between the droplet and the fibre radius. Then, in turn, I focus on the dynamical behaviour of clamshell droplets on fibre for each regime (compact droplet, droplet breakup, and oscillating droplet) in Sections 4.4, 4.5, and 4.6, respectively. For comparison, the compact droplet dynamics for barrel morphology is also discussed in Section 4.4. Finally, I summarise the key results and provide an outlook for future work in Section 4.7.

4.2 Simulation Setup Using the Lattice Boltzmann Method

In this chapter, I simulate the droplet-fibre system using the entropic lattice Boltzmann method (ELBM) and the forcing method to simulate the solid-liquid interaction. The details of this implementation can be found in Section 3.3.

At equilibrium, it is well-known that a droplet on fibre can adopt both barrel and clamshell morphologies, depending on the contact angle (θ_e) and its volume (Ω) relative to fibre radius (r_f) [76, 77, 78, 79, 80]. Typically, the barrel and clamshell morphologies are favoured for small contact angles with large volumes and large contact angles with small volumes, respectively. A bistable region is also observed where both morphologies are mechanically stable. Using ELBM, I am able to simulate both barrel and clamshell morphologies, as depicted in Figure 4.1. Figure 4.1(a) shows the cross-sections of droplets in the barrel morphology, while Figure 4.1(b) shows the cross-sections in the clamshell morphology. The different lines for the cross-sections in Figures 4.1(a) and (b) correspond to several values of contact angle formed by the droplet on the fibre surface. To characterise the droplet shape, I denote with L the length of the droplet along the fibre axis, and with H the height of the droplet perpendicular to the fibre.

In this work, I am mainly interested in the droplet dynamics as a body force is introduced parallel to the fibre. I identify three nondimensional control parameters. The first one is the contact angle θ_e formed by the droplet with the fibre surface. The second one is the relative droplet size (to the fibre radius), defined as:

$$L_R = \frac{\Omega^{1/3}}{r_f}, \quad (4.1)$$

where Ω is the droplet volume and r_f is the fibre radius. The third control parameter is the nondimensional body force, represented by the Bond number (Bo), which has been described in Equation (2.12). Here, the characteristic droplet length is defined as $D = \Omega^{1/3}$. Finally, in addition to the three non-dimensional control parameters, the main observable considered in this work is the non-dimensional droplet velocity, represented by the Capillary number (Ca) seen in Equation (2.13).

There are two main sets of simulation data that I generate. First, I focus on the clamshell morphology and study its stability against satellite droplet formation as I vary the Bond number and relative droplet size. To vary Bo I keep the droplet volume fixed to $\Omega = 8 \times 10^6$ lattice units (l.u.), and tune the value of g_x , obtaining Bo values ranging between 0.842 and 2.221. For

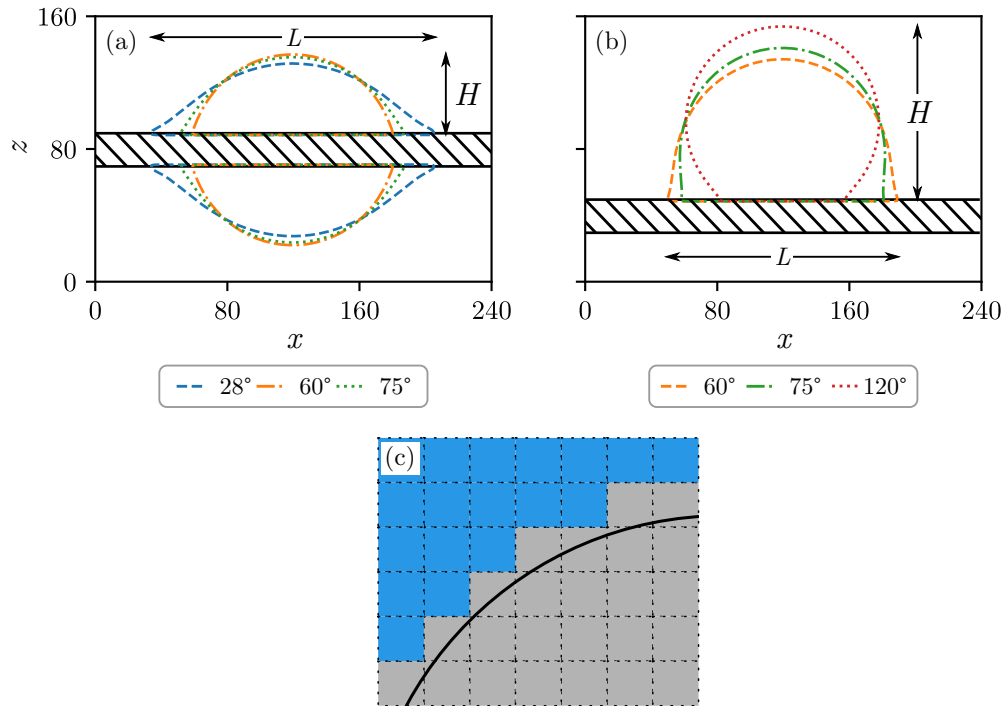


Figure 4.1: (a,b) The cross-sections of droplets with the same volume L_R (defined in Equation (4.1)) but different contact angles (θ_e) for the barrel and clamshell morphologies. L denotes the droplet length along the fibre, while H denotes the height of the droplet perpendicular to the fibre. (c) A staircase approximation of a curved surface in the lattice Boltzmann method. The blue lattices denote fluid nodes, while the grey lattices denote solid nodes.

simplicity, I set g_y and g_z to 0. To vary the relative droplet size, I keep the volume constant and vary the fibre radius employing the following values: $r_f = 10, 12, 16, 20, 24, 30, 40,$ and 60 l.u.. This leads to relative droplet size values L_R of 9.28, 7.74, 5.80, 4.64, 3.87, 3.09, 2.32, and 1.55, respectively. For the droplet contact angle, I choose the value of κ^w in Equation (3.38) that leads to $\theta_e = 75^\circ$ on a flat surface. I do not have equivalent Reynolds numbers due to the system not reaching steady-state for most cases. However, since the Bond number of this set is similar to the next data set, it can be argued that the Reynolds number will not differ significantly.

In the second set of data, I investigate the scaling law between the droplet velocity and its driving force, comparing barrel and clamshell morphologies. In this case, I vary the relative droplet size by fixing the fibre radius to $r_f = 10$ l.u., and vary the droplet volume, leading to $L_R = 9.28, 8.43, 6.69, 5.31$. For these values, both the barrel and clamshell morphologies are mechanically stable when the contact angle θ_e is 60° and 75° [76]. I also simulate barrel morphologies with $\theta_e = 28^\circ$ and clamshell morphologies with $\theta_e = 120^\circ$. For these combinations of volume and contact angles, only one morphology, respectively barrel and clamshell, is stable.

Furthermore, the gravitational acceleration g_x is varied such that I obtain values of Bo ranging between 3.969×10^{-3} and 3.793. The Reynolds number range is between 5.206×10^{-3} and 12.66.

As is common in lattice Boltzmann simulations, I use the so-called staircase approximation [163, 164] to model the fibre circular cross-section. In this approach, a curved or inclined surface is approximated by piecewise facets that follow the structure of the underlying cubic lattice (Figure 4.1(e)). This staircase approximation introduces roughness to the fibre cross-section and this will modify the effective contact angle. Such roughness due to the staircase approximation is not constant along the fibre cross-section. However, as a simple estimate, I can apply the Wenzel contact angle equation [165], and given a typical roughness of 1.2-1.3, the deviation is $< 10^\circ$ for all the cases considered here.

Here, the roles of contact angle hysteresis during droplet motion are ignored for simplicity. Previous works on flat surfaces have shown that the pearling transition is driven by contact angle hysteresis [32, 33, 160]. Since no similar works have been done on fibres, I want to focus on the contribution of the fibre curvature by itself. In addition, it is difficult to implement contact angle hysteresis on complex surfaces. The currently existing models are primarily developed for flat surfaces, where the density gradient normal to the surface is constrained [162] or a geometrical interpolation is done on the triple contact line to estimate the local contact angle [166, 167].

These assumptions will affect the dynamics in several ways. First, there is no critical sliding angle. This means that for all values of g_x , the droplet will always slide. The staircase approximation does not lead to contact line pinning when considering droplet sliding along the fibre. It only becomes important when the contact line transverses the corners of the surface resulting from the staircase approximation. Second, this will affect the neck dynamics when a satellite droplet separates from the main droplet. Without hysteresis, the onset of the breakup will happen at higher Bo and L_R . Finally, while not a focus of this work, it also has an effect on the shape transition between clamshell and barrel morphology when bistability exists, since in the transient states contact line motion occurs across the fibre.

In the simulations, I first initialise the droplet on a fibre setting $g_x = 0$ and let it equilibrate until it reaches its static equilibrium shape. Then, a constant gravitational acceleration $g_x > 0$ corresponding to the target Bond number is applied instantaneously to the droplet, and the resulting droplet dynamics are monitored. This can lead to steady moving droplets corre-

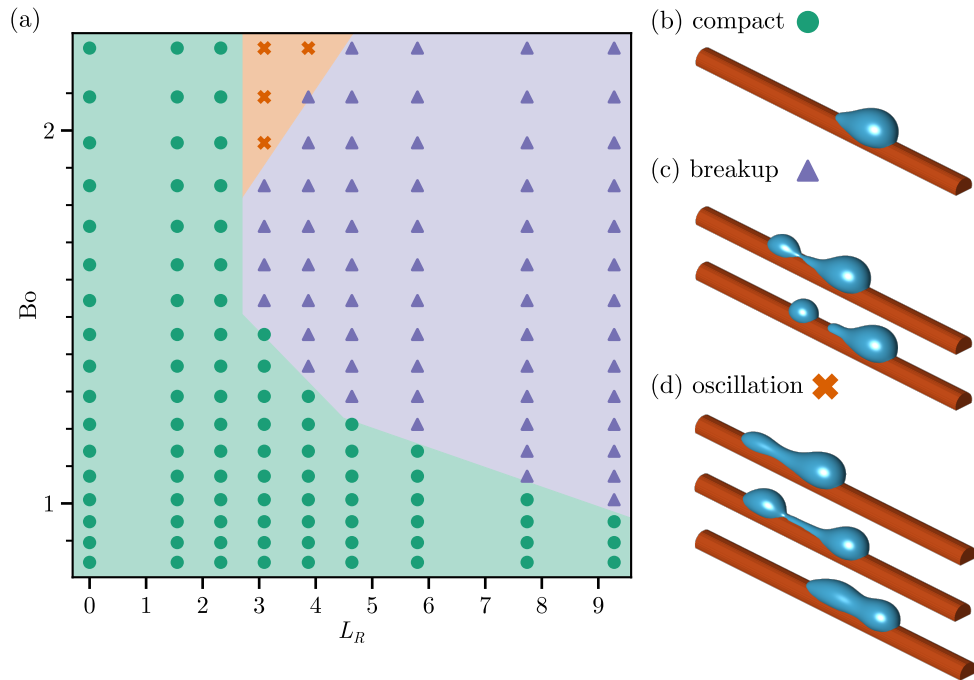


Figure 4.2: (a) The dynamic phase diagram for a droplet in a clamshell configuration for varying Bond number (Bo) and size ratio between the droplet and the fibre radius (L_R). There are three different possible outcomes, and they are illustrated in the subsequent panels for (b) compact droplet, (c) droplet breakup, and (d) oscillating droplet.

sponding to the deformed barrel and clamshell morphologies, and also non-steady state shapes with periodic shape oscillations or the formation of satellite droplets. Since the instantaneous application of the body force is expected to affect the transient dynamics, I also selectively simulated an incremental increase of the body force, obtaining qualitatively similar results, though quantitative differences are observed for the regime with satellite droplet formation.

4.3 Dynamic Regimes for Clamshell Morphology

Figure 4.2(a) illustrates three dynamic regimes detected in the simulations of a droplet in the clamshell configuration. They form a phase diagram in the parameter space of the Bond number (Bo) and the size ratio between the droplet and the fibre radius, L_R . I denominate the three regimes referring to the droplet shape as (i) compact droplet (Figure 4.2(b)), (ii) droplet breakup (Figure 4.2(c)), and (iii) oscillating droplet (Figure 4.2(d)).

The compact droplet regime is highlighted with the circle symbols and a green background. Here, the droplet first undergoes a transient state where it is accelerated, and some shape oscillations are triggered. However, after the oscillations are damped, the droplet will eventually move along the fibre with a steady state shape. In practice, for the classification done in this

work, I identify a droplet in the compact regime when: (a) there are no satellite droplets produced by the main droplet, and (b) the residual oscillation triggered by the transient state is damped with a maximum variation of 1% within the simulation time window. As expected, this regime is found at a low Bo number when the droplet is only weakly deformed when compared to its equilibrium shape. In this case, the droplet receding contact line has a rounded shape without any tail. With increasing Bo, and correspondingly the droplet velocity, a visible tail can be observed in the steady state, as illustrated in Figure 4.2(b). This is reminiscent of previous works on pearling stability on flat surfaces [33, 158, 159].

The droplet breakup regime is highlighted by the triangle symbols and a blue background. Here, during the transient state, the droplet breaks up leaving behind one or several satellite droplets. The satellite droplets are considerably larger than that observed for the pearling instability studied on flat surfaces [33, 158, 159]. However, due to the demanding computational resources, I am limited to a relatively small droplet size and simulation domain. It will be interesting to study larger systems in the future. A key observation in the work is that the stability of the compact droplet regime depends on the relative size of the droplet and fibre radius. As observed in Figure 4.2(a), at parity of droplet volume, when the fibre has a large radius of curvature r_f (alternatively, low curvature), the droplet can reach a steady state shape without forming satellite droplets for the entire range of the Bo number explored in this phase diagram. For smaller fibre radius, in contrast, the droplet becomes unstable, leading to the formation of satellite droplets, as shown in Figure 4.2(c). Interestingly, the onset of this instability shifts to lower Bo as the fibre radius r_f becomes smaller. It is worth noting that, in this work, I assume an idealised fibre where there is no contact angle hysteresis along the droplet. A previous simulation study by Yang et al. [160] on a flat surface also highlighted satellite droplet formation, but correlated it with increasing contact angle hysteresis.

In the oscillating droplet regime, the droplet oscillates regularly as it moves along the fibre. Over the range of parameters explored in Figure 4.2(a), this is observed for the intermediate range of relative droplet sizes. Initially, the droplet dynamics is akin to that for droplet breakup, where the trailing edge bulges and a neck is formed connecting the rear and the front of the droplet, see e.g. Figure 4.2(d). However, unlike the droplet breakup regime, the neck does not rupture and the rear portion of the droplet merges with its front. Furthermore, I observe the droplet oscillation is not damped and can repeat over multiple cycles in the simulations. Indeed, it appears to continue indefinitely, suggesting that the energy provided by the body

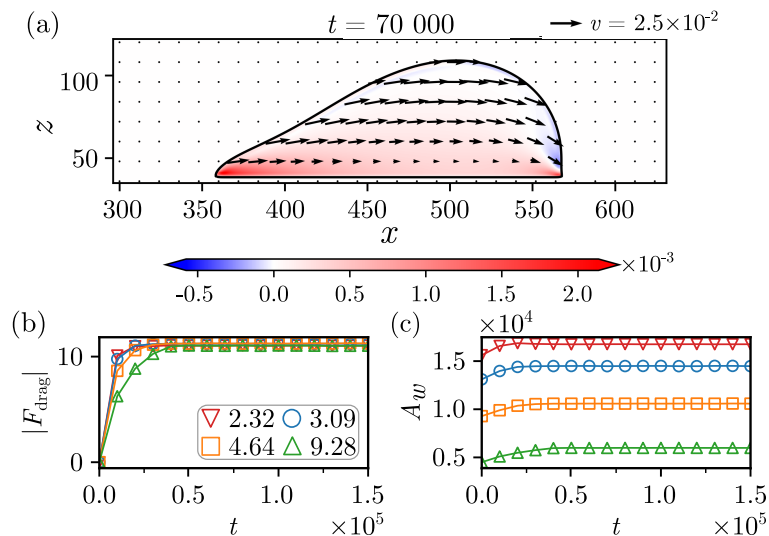


Figure 4.3: (a) Typical droplet flow profile in a compact configuration. The colour map corresponds to the x - z component of the strain-rate tensor. Here, I use $L_R = 3.09$ and $Bo = 1.453$. (b) The time evolution of the solid-liquid friction in the x direction, F_{drag} . Different colours denote different values of $L_R = \Omega^{1/3}/r_f$. (c) shows the contact area between the droplet and the fibre (A_w) as a function of time for different normalised fibre curvature. For panels (b) and (c), $Bo = 0.842$.

force at a constant rate feeds the droplet oscillation as well as the motion of the centre of mass.

4.4 Dynamics of Compact Droplets

In this and the next sections, I will discuss the droplet dynamics for each dynamic regime in turn, starting with the compact droplet case. In Figure 4.3(a) I inspect the middle cross-section of the droplet along the fibre and illustrate its typical flow profile (see the arrows). At steady state, the internal velocity is dominated by the positive x -component with clear variations in the z direction. To characterise this, in Figure 4.3(a), I have also shown the x - z component of the strain-rate tensor in the plane of the droplet cross-section, defined as $\mathbb{E}_{xz} = \mathbb{E}_{zx} = (\partial_x v_z + \partial_z v_x)/2$. In the case here, the second term is much larger compared to the first term.

From the strain-rate colour map, I can infer that viscous dissipation is dominated by shear close to the solid substrate. Correspondingly, the primary friction force arising at the liquid-solid interface opposes the external body force due to gravity. The liquid-solid friction force in the x direction, $F_{\text{drag},x}$, can be estimated as:

$$F_{\text{drag},x} = \int_A \eta_l \nabla_{\perp} v_x dA, \quad (4.2)$$

where the integral is over the solid-liquid contact area, η_l is the dynamic viscosity of the liquid, and $\nabla_{\perp} v_x$ is the velocity gradient normal to the solid surface. Figure 4.3(b) shows the time evolution of the drag force, F_{drag} , for several different fibre curvatures. Here, I have chosen $\text{Bo} = 0.842$ where the droplet is in the compact regime for all values of L_R considered in the phase diagram in Figure 4.2(a). I find that, at steady state, the friction force approaches the same value for all L_R cases. This is expected because I have used the same droplet volume, and at steady state, the friction force must balance the driving force due to gravity. There are, however, two clear variations as I study fibres of different radii. First, the relaxation time to steady state: fibres with smaller curvatures (i.e. larger fibre radii) reach steady state faster than fibres with larger curvatures (smaller fibre radii). Second, the liquid-solid contact area: as shown in Figure 4.3(c), the contact area is larger for a fibre with smaller curvature (larger fibre radius). Moreover, since the total friction force is the same, as a corollary, the shear stress must be smaller with decreasing curvature (increasing fibre radius).

Next, I investigate in the relation between the droplet velocity and the driving force. Lorenceau and Quéré [22] have previously investigated the spontaneous motion of a perfectly wetting droplet in a barrel configuration on a conical fibre. They argued that, at steady state, the viscous force in the droplet scales as

$$F_{\text{drag}} \sim \eta_l \frac{v r_f}{\theta_w}, \quad (4.3)$$

where η_l is the droplet viscosity, v is the droplet velocity, r_f is the fibre radius, and θ_w is the effective wedge angle at the contact line. If the wedge angle θ_w is small ($< 30^\circ$ or when $H/L < 0.5$) and the droplet moves slowly such that it does not drastically change the shape of the droplet, they further estimated that θ_w is in the order of the droplet aspect ratio H/L , where H is the droplet height perpendicular to the fibre and L is the droplet length along with the fibre. Balancing the viscous friction with the driving force F_{drive} , then I obtain

$$v \sim \frac{H}{L} \frac{F_{\text{drive}}}{\eta_l r_f}. \quad (4.4)$$

A similar scaling argument has also been derived by Gilet et al. [11]. If the driving force is due to gravity, as is the case here, the scaling law above can be rewritten in terms of two dimensionless numbers, the Capillary and Bond numbers. Substituting $F_{\text{drive}} = \rho_l g_x \Omega$, I can

write

$$\begin{aligned}\frac{\eta v}{\gamma l_g} &\sim \frac{H}{L} \frac{\rho l g_x \Omega^{2/3}}{\gamma l_g} \frac{\Omega^{1/3}}{r_f}, \\ \text{Ca} &\sim \frac{H}{L} \frac{\Omega^{1/3}}{r_f} \text{Bo}, \\ \text{Ca} &\sim \frac{H}{L} L_R \text{Bo}.\end{aligned}\tag{4.5}$$

To check the validity of the derived scaling law for partially wetting droplets, I will therefore fit the simulation data against the corresponding equations:

$$\text{Ca} = a_1^f (L_R \text{Bo})^{m_1^f},\tag{4.6}$$

$$\text{Ca} = a_2^f \left(\frac{H}{L} L_R \text{Bo} \right)^{m_2^f},\tag{4.7}$$

where a_1^f , a_2^f , m_1^f , and m_2^f are numerical constants. The two equations above differ in whether the droplet aspect ratio, H/L , is taken into account in the scaling law, as Lorenceau and Queré argued it should only be valid when $\theta_w \sim H/L$ is small.

Figures 4.4(a) and (b) show how the simulation data fit against the proposed scaling laws for the barrel morphology. To ensure the scaling law is tested robustly, I have varied the droplet contact angle, the droplet volume, and the applied body force. The fibre radius is fixed at $r_f = 10$. The different colours denote different contact angles (θ_e), while different symbols correspond to different reduced volumes (L_R). I find that the exponents (m_1^f and m_2^f) are always very close to 1 (between 0.944 to 1.012) for the range of Bo considered. Deviations from 1 can be observed for larger Bo (typically when $\text{Bo} > 0.3$, though it depends on droplet morphology and contact angle), accompanied by clear deformations of the droplet shape. In this low Bo regime, adding or removing the H/L prefactor does not make the exponents change significantly. Therefore, for a partially wet fibre, the relationship between the velocity and the external force is linear. However, by incorporating the aspect ratio prefactor, all the results collapse into a single line, including fibres with different wettabilities. This observation is well aligned with the argument by Lorenceau and Queré that the use of $\theta_w \sim H/L$ in the scaling law is reasonable only if $H/L < 0.5$ [22]. The inset in Figure 4.4(b) shows that for barrel morphology, H/L is below 0.5.

The linear relation between Ca and $L_R \times \text{Bo}$ can also be observed for the clamshell mor-

phology, as demonstrated in Figures 4.4(c) and (d). However, unlike the barrel morphology, I am unable to collapse all the data points for different contact angles into a single master curve irrespective of whether I include the aspect ratio H/L prefactor or not. Indeed, the aspect ratio H/L is typically larger than 0.5 for the clamshell morphology, compared to the barrel morphology. Furthermore, in Figures 4.4(c) and (d), the coefficients a_1^f and a_2^f increase monotonically with θ_e . With increasing contact angle, the droplet contact area (see the inset) is smaller, and the droplet centre of mass is further away from the fibre surface, and as a result, the liquid-solid friction is smaller and droplet velocity is faster. The same argument applies when comparing the barrel and clamshell morphologies. At parity of contact angle and driving force, the clamshell is faster than the barrel because the wet area is smaller.

The data shown in Figure 4.4(c) correspond to cases where the droplet size is large compared to the fibre radius. I expect that, in the limit where the droplet is small compared to the fibre, I should recover the scaling law proposed for a droplet moving on an inclined flat surface [32, 168, 169]. By balancing the driving gravitational force and dissipative viscous force, Kim et al. derived a relation for the droplet steady state velocity [168]:

$$v \sim \frac{\rho g_x \Omega}{\eta_l L_\perp}, \quad (4.8)$$

where L_\perp is the projection of the drop contact perimeter in the direction orthogonal to the motion. Equation (4.8) can further be rewritten into:

$$\begin{aligned} \frac{\eta_l v}{\gamma l_g} &\sim \frac{\Omega^{1/3}}{L_\perp} \frac{\rho g_x \Omega^{2/3}}{\gamma l_g}, \\ \text{Ca} &\sim \frac{\Omega^{1/3}}{L_\perp} \text{Bo}. \end{aligned} \quad (4.9)$$

The key term to consider is the ratio $(\Omega^{1/3}/L_\perp)$ as I vary the size ratio between the droplet and the fibre. When this ratio is small, corresponding to the flat surface limit, for a given contact angle θ_e , L_\perp scales with $\Omega^{1/3}$. This leads to an expected linear scaling between Ca and Bo, without any dependency on the fibre radius. In contrast, when this ratio is large, I expect L_\perp to scale as the radius of the fibre r_f , which explains the linear scaling between Ca and $L_R \times \text{Bo}$ observed in Figure 4.4(c).

To verify the crossover, in Figure 4.4(d), I systematically vary the fibre radius r_f (corresponding to L_R values from 0.05 to 10.0) for four different droplet volumes (indicated by the

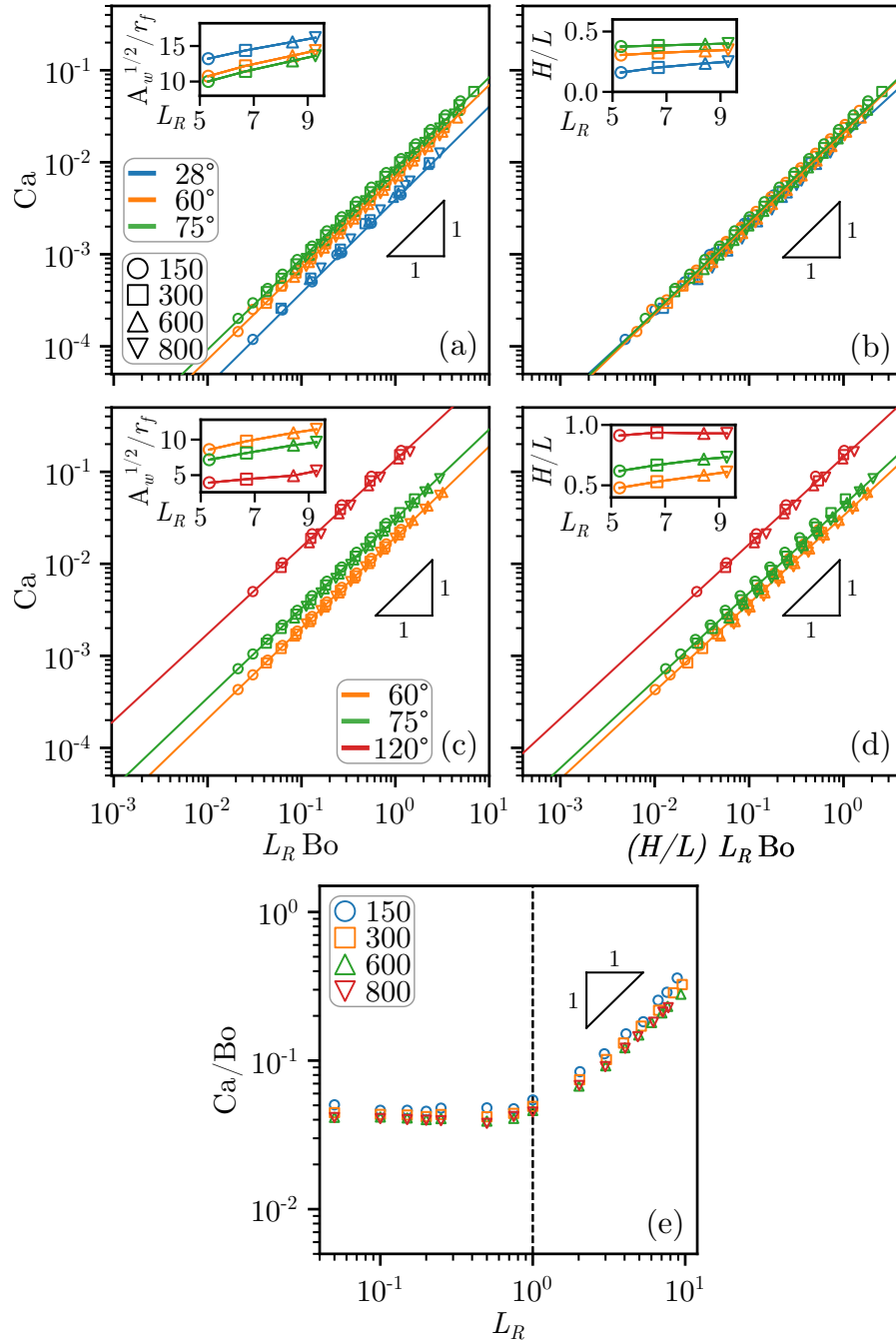


Figure 4.4: (a,b,c,d) Scaling laws between the droplet Capillary (Ca) and Bond (Bo) numbers. The markers are the simulation data points (all panels), while the lines are the best fits based on Equation (4.6) (for panels (a) and (c)) and (4.7) (for panels (b) and (d)). Panels (a) and (b) are for the barrel morphology, while panels (c) and (d) are for the clamshell morphology. Insets in panels (a) and (c) show the wetted area normalised to the fibre radius ($A_w^{1/2}/r_f$) as a function of the reduced volume L_R . Inset in panels (b) and (d) show the droplet aspect ratio (H/L) as a function of the reduced volume L_R . All the data shown in the insets are taken for $Bo = 0$, and their values do not change significantly with varying Bo across the range considered here. In panel (e), I plot Ca/Bo as a function of reduced volume $L_R = \Omega^{1/3}/r_f$. The dashed line shows $L_R = 1.0$. For each value of the droplet volume Ω , the fibre radius is varied such that L_R ranges from 0.05 to 10.0.

different colours and symbols), while fixing the gravitational acceleration and droplet contact angle. At low L_R values, I clearly observe a plateau in the ratio between Ca and Bo, while for large L_R values, I again find an additional linear dependence on L_R . The latter is the regime where the fibre curvature significantly affects the droplet dynamics. Furthermore, as expected the crossover occurs around $L_R = 1.0$, indicated by the dashed vertical line, where the droplet size becomes comparable to the fibre.

4.5 Dynamics of Droplet Breakup

During breakup the droplet can be considered as a compound of three main parts: (i) the main droplet body at the front, (ii) a satellite droplet at the rear, and (iii) a liquid filament connecting the main body and the satellite droplet that eventually ruptures. When breakup takes place, the rear side of the droplet starts to bulge (see $t = 65,000$ l.u., Figure 4.5(a)), but the fluid flow is predominantly in the x direction, akin to that in the compact droplet regime. As in the previous case, the viscous force is at the largest close to the solid boundary, as indicated by the colour map illustrating the x - z component of the strain rate. Once the satellite droplet is formed, its volume is typically smaller than the main droplet, so it is subjected to the smaller driving force, and its centre of mass moves at a smaller velocity than the main droplet. As breakup proceeds, the liquid filament becomes increasingly thinner and more elongated, as illustrated in the snapshot for $t = 85,000$ l.u.. Close to the rupture point in the filament region, I can see a clear downward fluid velocity. This effectively squeezes the neck region leading to droplet breakup, as shown in the snapshot for $t = 90,000$ l.u..

In the previous sub-section, I observed that the value of the drag force converges to the same value for a given Bo, as I vary the fibre radius. Here, when droplet breakup occurs, I find that F_{drag} overshoots the value for a steady state compact droplet. Figures 4.5(b) and (c) show the drag force F_{drag} and the droplet contact area A_w at Bo = 1.073 for two cases: $L_R = 5.80$ when the droplet has a compact shape, and $L_R = 7.74$ when the droplet breaks up. Since the droplet contact area is smaller when the curvature is high, I argue the amount of energy which can be dissipated is lower. To compensate for this, the droplet will stretch (increasing A_w) before the main and satellite droplets separate. After the separation, the total drag force, F_{drag} , for those two droplets approaches that of a compact droplet.

The droplet breakup mechanism can be characterised by the filament length and the satellite

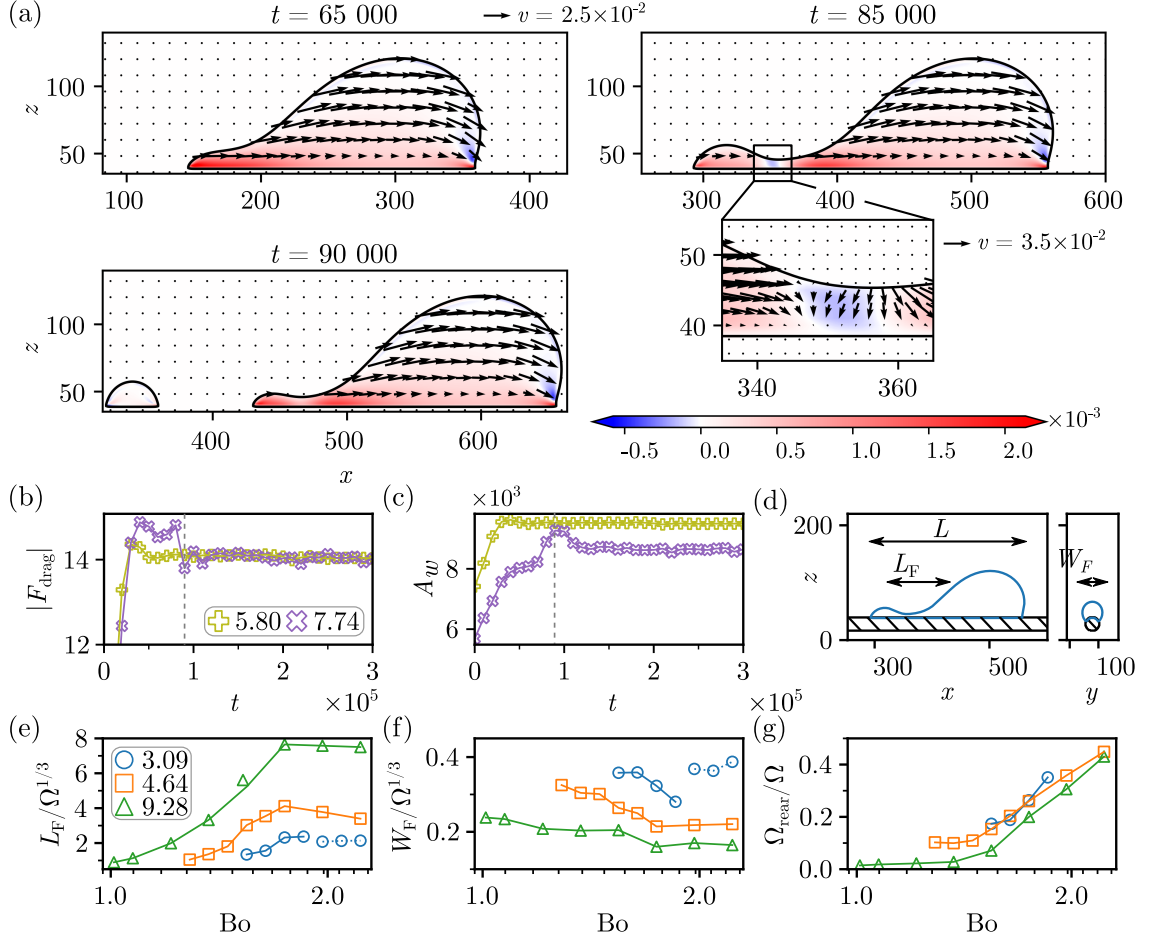


Figure 4.5: (a) The droplet flow profile during breakup. The colour map shows the x - z component of the strain-rate tensor. Here, $Bo = 1.073$ and $L_R = 7.74$. (b) The drag force (F_{drag}) and (c) the contact area (A_w) between the droplet and the fibre as a function of time for different normalised fibre curvature and $Bo = 1.073$. For $L_R = 5.80$, this leads to a compact configuration, while for $L_R = 7.74$, it leads to droplet breakup. The grey dashed line shows the breakup point. (d) The typical cross-section of the droplet upon breakup, where L denotes the droplet length alongside the fibre, L_F denotes the filament length, and W_F denotes the filament width. (e) L_F normalised by the droplet characteristic length ($\Omega^{1/3}$), (f) W_F normalised by $\Omega^{1/3}$, and (g) the rear droplet volume (Ω_{rear}) normalised by initial droplet volume (Ω) as a function of Bond number. In panels (e-g), different colours correspond to different L_R , with solid lines for droplet breakup cases and dotted lines for droplet oscillation cases.

droplet size. Figure 4.5(d) shows the cross-section of a typical droplet on the verge of breakup. L denotes the droplet length alongside the fibre, while L_F denotes the filament length. I define the filament boundary as the point where the curvature changes from convex (droplet) to concave (filament). In Figures 4.5(e) and (f), I compare L_F and W_F at the verge of breakup as a function of Bo for three values of L_R : 3.09 ($r_f = 30$), 4.64 ($r_f = 20$), and 9.28 ($r_f = 10$). In general, with decreasing fibre radius, the filament length increases and its width decreases. As the filament elongates over time, it eventually breaks up. Finally, Figure 4.5(g) shows the satellite droplet volume (Ω_{rear}), measured on the first frame of breakup. I find that the volume of the satellite droplet increases with the Bond number. At the same time, for the same Bond number, higher curvature surface ($1/r_f$) will induce a smaller satellite droplet volume.

4.6 Dynamics of Droplet Oscillation

In addition to droplet breakup, I also find another dynamic regime at a higher Bond number that I term droplet oscillation. This regime is similar to the one described by Yang et al. [160] on a flat surface, as illustrated in Figure 4.6(a). Here, in the time range between $t = 40,000$ l.u. and $t = 50,000$ l.u., I observe droplet dynamics similar to the one leading to droplet breakup, where the filament stretches and a downward fluid displacement in the neck region is initiated. However, a breakup is not triggered, and the filament survives for a much longer time until eventually, the filament shortens ($t = 110,000$ l.u.), the two parts of the droplet recombine, and the cycle is repeated.

In the analysis of the breakup mechanism, I find that smaller fibre curvature (larger fibre radius) will lead to a shorter filament (L_F), wider filament (W_F), and a larger satellite droplet volume (Ω_{rear}) (see Figures 4.5(e)–(g)). In Figures 4.5(e) and (f), I also include data points for the oscillation cases, which are denoted by dotted lines. Compared to the breakup cases (see the full and dashed blue lines), I find that L_F does not differ significantly, while W_F is clearly larger. In general, filaments with a higher aspect ratio (W_F/L_F) are more stable. Furthermore, when the satellite and main droplets are of similar size, they are affected by a similar driving force, and consequently, the velocity difference between them is small. Taken together, these limit the extension of the filament region, and the short separation makes it easier for the satellite droplet to recombine with the main droplet in the droplet oscillation cases. This consideration also qualitatively explains why droplet oscillation is detected in a

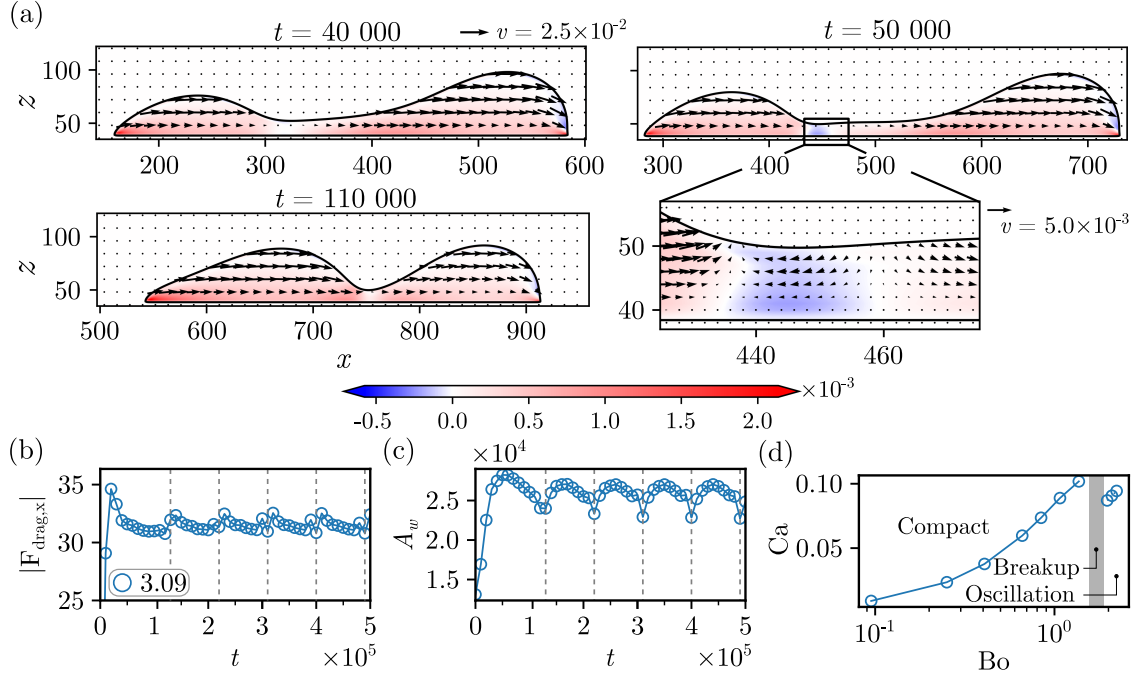


Figure 4.6: (a) The typical droplet flow profile in the droplet oscillation regime. The colour map shows the x - z component of the strain-rate tensor. (b) The wetted area and (c) the drag force as a function of time for $L_R = 3.09$ and $Bo = 2.221$. (d) Ca as a function of Bo for $L_R = 3.09$. For the compact cases, the velocity is measured at steady state conditions. For the droplet oscillation cases, the velocity is averaged over one cycle of stretching and contraction.

narrow boundary region between compact and breakup in the phase diagram of Figure 4.2(a). If the fibre curvature is too small, filament formation is suppressed, leading to a stable compact droplet. However, if the fibre curvature is too large, (1) the rear droplet volume will be too small, (2) the filament will be too long, and (3) the contact area will also be too small for the filament to be stable; leading to droplet breakup.

In Figures 4.6(b) and (c), I also show the time evolution of the drag force, F_{drag} , and the droplet contact area, A_w . A period in these curves corresponds to one cycle of droplet stretching and contraction, and I observe that the droplet oscillation indefinitely repeats over multiple cycles in the simulation. The minimum contact area coincides with the maximum drag force, as shown by the dashed grey lines in Figures 4.6(b) and (c).

Finally, Figure 4.6(d) shows the droplet centre of mass velocity (nondimensionalised into Ca) as a function of Bo when $L_R = 3.09$. For the droplet oscillation cases, I plot the average centre of mass velocity over one cycle of stretching and contraction. As I have previously shown in Figure 4.4, Ca increases proportionally with Bo (for $Bo < 1.4$) when the droplet has a compact shape. However, as I enter the droplet oscillation regime, I observe that the average Ca is lower even though the external driving force is larger. This reflects the fact that

the droplet shape oscillation leads to extra dissipation during droplet motion. With the same droplet oscillation regime, the average Ca increases monotonically again with Bo.

4.7 Conclusion

In this work, I have used the lattice Boltzmann method to investigate the dynamics of droplets moving along a fibre, focussing in particular on the clamshell morphology and the partially wetting droplet case. By systematically varying the droplet Bond number and fibre radius, I observed three regimes in the droplet dynamics. First, at a low Bond number, the droplet maintains a compact shape. Here, the driving force is balanced by viscous force such that the droplet reaches a steady state. The viscous dissipation is dominated by shear close to the solid substrate, and for a smaller fibre radius, the shear stress is larger while the liquid-solid contact area decreases. Analysing the droplet velocity in the low Bond number regime, I further identified a scaling law relating the Capillary number, the Bond number and the size ratio between the droplet and the fibre: $Ca \propto Bo \times L_R$ when the fibre curvature is dominant, $L_R > 1.0$; and $Ca \propto Bo$ when $L_R < 1.0$ as I approach the flat surface limit. A similar scaling law was further observed for a droplet in the barrel morphology. In fact, for barrel configuration, all the data can be collapsed into a single line by including a droplet geometrical factor, such that $Ca \propto Bo (L_R) (H/L)$.

For large Bond numbers, the droplet shape becomes unsteady. The dominant unsteady regime is droplet breakup, where satellite droplets are formed at the rear of the moving droplet. Importantly, the transition to the droplet breakup regime strongly depends on the fibre curvature. The larger the curvature (the smaller the fibre radius), the lower the Bond number for the transition between compact droplet and droplet breakup regimes. I rationalised this by characterising the filament prior to satellite formation. The filament is longer and narrower with increasing fibre curvature, which suggests it becomes less stable. Another unsteady regime is droplet oscillation whereby the droplet extends and contracts periodically. This regime was observed in the mid-range of fibre radius explored in this work, indicating subtle dynamics are at play. Compared to the droplet breakup regime, the rear bulge is larger and the filament is wider during the extension phase. As a result, the rear bulge can catch up with the filament and the droplet as a whole contracts. Furthermore, compared to the compact droplet regime, the shape oscillation leads to extra dissipation during droplet motion. Correspondingly, the

droplet moves slower in this regime.

This work highlights several avenues for further investigation. First, I have idealised the fibre geometry in that there is no contact line pinning and contact angle hysteresis along the fibre. In contrast, real fibres unavoidably have some roughness, and previous works on flat surfaces suggest contact angle hysteresis is an important factor in satellite droplet formation [158, 160]. Second, I have demonstrated that the substrate curvature can have a strong effect on the resulting droplet dynamics. It will be interesting to explore this concept further on more complex curved geometries, such as a conical fibre or an undulating egg-box substrate [151, 153]. Third, I currently limit the work to an external force (e.g. gravity) parallel to the fibre axis. In many practical applications, it will be relevant to consider a driving force that acts on different angles with respect to the fibre axis. It will also be valuable to consider other types of driving forces, such as due to an imposed air flow [26, 154, 170].

CHAPTER 5

Long-Range Fluid-Solid Interactions in Lattice

Boltzmann Simulations

5.1 Introduction

In general, there are three different wetting states that a droplet on a surface can adopt [5, 21]. The first is a partial wetting condition where in the absence of gravity the droplet will form a spherical cap shape with an equilibrium contact angle given by the Young equation (θ_e). The second is the fully wetting condition, where the droplet will spread into a film with no observable contact angle. The third possible state is less frequent and is called pseudo-partial wetting. It is characterised by a film and droplet that can coexist together. The pseudo-partial wetting state arises from long-range interactions between the fluid and solid molecules, whereby the interactions are attractive at short distances and repulsive at large distances. These are needed to stabilise the existence of both thin film and droplets on the top of it [171, 172]. It cannot occur on surfaces that have either an attractive interaction or repulsive interaction only.

The existence of the pseudo-partial wetting state has been proved experimentally. Amongst others, it has been reported for systems of air-octane-silicone [171], deuterated water-alkane-air [173], dodecane-silicone oils-grafted glass [174], and air-polystyrene-oxidised silicon [175]. However, most of the experimental studies on this topic are focussing on the spreading dynamics of the precursor film and not on the dynamics of the supported droplet [171, 175, 176, 177]. Numerical studies have also been performed using different numerical solvers, including (but not limited to) asymptotic analytical models [178, 179], the finite elements method (FEM) [180], the volume of fluid (VOF) method [181], the molecular dynamics (MD) method [182, 183],

the phase field (PF) method [184], and the lattice Boltzmann method (LBM) [49]. Analogue to the experimental works, most simulation studies have mainly focused on the quasi-static morphologies or on the droplet spreading mechanism.

LBM is a mesoscopic-scale method that has been used extensively to model complex fluid interactions. Previously, I have discussed the main strengths and weaknesses of LBM compared to other numerical methods in Section 3.1. Here, I emphasise that within free-energy-based LBM, new free-energy functionals that represent long-range fluid-solid interaction can be introduced without the need for extensive rework. Furthermore, the resulting equation of motion can be derived starting from the free energy functionals [94]. LBM is also able to describe both quasi-static and dynamic features, therefore allowing investigation of both cases within the same framework.

This chapter is divided into the following sections. In Section 5.2, I elucidate how we update the free-energy functional to include the long-range interactions. I also discuss in detail the steps to derive the corresponding chemical potential, reprised by the lattice Boltzmann equation (LBE). In Sections 5.3 and 5.4, I show droplet spreading driven by long-range interactions considering both attractive and repulsive cases. I will compare two ways of obtaining the long-range interaction: using both analytical and numerical integration of a potential on a flat surface. This comparison is done to ensure that the numerical integration is accurate for flat surfaces before it is used for arbitrary surfaces. Using the analytical and numerical integration, the wetting state will be both partial and fully wetting states. In Section 5.5, I then introduce a more complex potential which has both attractive and repulsive contributions. I investigate how different parameters affect the droplet's steady-state shape. Here, I use both flat surfaces and those patterned with ridges and grooves. Next, in Section 5.6, I simulate droplets on cylindrical fibres, addressing both quasi-static shapes and their motion. Finally, in Section 5.7, I summarise the results of this chapter and also discuss the strengths and weaknesses of the current implementation and possible solutions to improve the methods. I will also discuss further ideas and works that can follow this work.

5.2 Long-Range Interaction in Free-Energy Lattice Boltzmann

In this chapter, I use the two-component lattice Boltzmann model (LBM) which has been described in detail in Section 3.4. In summary, the model can simulate equal-density two-

component systems. It employs the so-called Guo forcing to include the contribution from the chemical forces, gravitational forces, and fluid-solid long-range interaction forces.

To incorporate the long-range interactions within LBM, we start with the free-energy functional:

$$E = \int_{V_0} [\mathbb{F}_b + \mathbb{F}_i + \mathbb{F}_{lrp}] dV, \quad (5.1)$$

where \mathbb{F}_b and \mathbb{F}_i are the bulk and the interface free energy terms which have been defined in Equations (3.43) and (3.44), respectively. \mathbb{F}_{lrp} is the contribution from the fluid-solid long-range interaction, which is defined as:

$$\mathbb{F}_{lrp} = C(\phi) \mathcal{V}(\mathbf{r}). \quad (5.2)$$

\mathcal{V} is the potential acting on the liquid at position \mathbf{r} , obtained by integrating the interaction with all of the solid nodes:

$$\mathcal{V}(\mathbf{r}) = \int_{V_{s,0}} P(\mathbf{r}) dV_s, \quad (5.3)$$

where $V_{s,0}$ is the total solid volume, and P is the effective interaction between one liquid node and one solid node. Different forms of P will be discussed in more detail in the next sections.

C is a prefactor whose purpose is to make sure that the solid interaction only applies to fluid 1 ($\phi = 1$) and not to fluid 2 ($\phi = -1$), where ϕ is the order parameter that will be evolved by the lattice Boltzmann equation (LBE). There are many forms of $C(\phi)$ that can be used. The simplest form of C is:

$$C(\phi) = \frac{\phi + 1}{2}, \quad (5.4)$$

giving $C = 1$ for fluid 1 and $C = 0$ for fluid 2. A more complex form has been developed by Oktasendra, et al [184]:

$$C(\phi) = \frac{3}{4}\phi - \frac{1}{3}\mathcal{T}(\mathbf{r})\phi^2 - \frac{1}{4}\phi^3 + \frac{1}{6}\mathcal{T}(\mathbf{r})\phi^4 + \left(\frac{1}{6}\mathcal{T}(\mathbf{r}) + 3\right), \quad (5.5)$$

where $\mathcal{T}(\mathbf{r})$ is defined as:

$$\mathcal{T}(\mathbf{r}) = \begin{cases} -1, & \text{if } \mathcal{V}(\mathbf{r}) < 0, \\ +1, & \text{otherwise.} \end{cases} \quad (5.6)$$

They have found that this form works better for the phase field method by keeping the simulation numerically stable while also preventing enrichment near the fluid-solid boundaries (i.e. $\phi > 1.0$ or $\phi < -1.0$). In this form, C will be zero in the bulk phase (when $\phi = \pm 1$) but will

have a finite value when $-1 < \phi < +1$. During testing, I did not observe any major difference in behaviour between the simpler and the more complicated form of C in LBM. Therefore, I use the simpler model defined in Equation (5.4) for the rest of this chapter.

From Equation (5.2), we can then derive the chemical potential contribution of the long-range interaction (μ_ϕ^{lrp}):

$$\mu_\phi^{lrp} = \frac{d\mathbb{F}_{lrp}}{d\phi} = C'(\phi) \mathcal{V}(\mathbf{r}), \quad (5.7)$$

where:

$$C'(\phi) = \frac{dC(\phi)}{d\phi} = \frac{1}{2}. \quad (5.8)$$

The chemical potential will enter the Guo forcing term (Equation (3.59)) as \mathbf{F}_{LRP} by using means of:

$$\mathbf{F}_{LRP} = -\phi \nabla \mu_\phi^{lrp}. \quad (5.9)$$

Typically, $\nabla \mu_\phi^{lrp}$ is numerically evaluated using a finite difference method. Together with \mathbf{F}_{chem} (Equation (3.60)) and \mathbf{F}_g , the forcing term will enter LBM via the velocity correction in Equation (3.64).

5.3 Fully Wetting Case: Analytical Integration for Flat Surfaces

I start with a simple form of P . Here, I use Oktasendra et al.'s modified Lennard-Jones interaction to obtain a simple attractive or repulsive interaction [184]:

$$P(\mathbf{r}) = \frac{a}{(b + |\mathbf{r} - \mathbf{r}_s|)^6}. \quad (5.10)$$

Here, \mathbf{r}_s is the coordinate of the solid while a models the effect of the Hamaker constant by controlling the strength and the type of the interaction. The choice $a > 0$ represents a repulsive interaction, while $a < 0$ represents an attractive interaction. The parameter b is a positive constant that is used to prevent a division by 0 when $|\mathbf{r} - \mathbf{r}_s| = 0$. A similar model has also been employed by Di and Wang to model the spreading of a droplet in a fully wetting condition [180].

For a flat surface with an infinite area and a finite thickness, we can derive an analytical expression for \mathbf{F}_{LRP} . Figure 5.1(a) illustrates a thin film on a solid with an infinite area over the x and y directions, with a thickness of T_s . By rewriting the distance between the fluid and

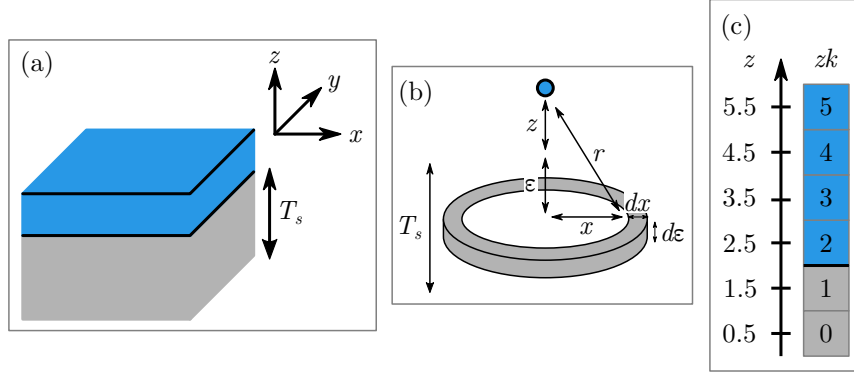


Figure 5.1: (a) A thin film spreading infinitely in the x - y direction, located on top of a solid with a thickness of T_s . (b) A cylindrical shell with an inside radius of x , thickness of dx , and height of dz for the analytical integration of \mathcal{V} . r is the distance between the liquid domain and the cylindrical shell. The illustration and derivation were originally done by Fandi Oktasendra as part of the preparation for [184]. (c) A simple fluid-solid lattice Boltzmann method (LBM) simulation setup. z represents the lattice's real coordinates, while zk represents the node indices. In my LBM implementation, the fluid and solid never mix in the node. Therefore, the fluid-solid interface is always located in between nodes (e.g. between $zk = 1$ and $zk = 2$).

solid as $|\mathbf{r} - \mathbf{r}_s| = r$, the integrated potential can be written as:

$$\mathcal{V}(r) = \int \frac{a}{(b+r)^6} dV_s. \quad (5.11)$$

Since the solid is assumed to have infinite size in the x and y directions, we can simplify the system as a cylindrical shell with a radius of x , a shell thickness of dx , and a height of dz (Figure 5.1(b)). By defining the distance of the fluid node of interest to the fluid-solid interface as z and the solid node's distance to the fluid-solid interface as ϵ , r can be rewritten as:

$$r = \sqrt{x^2 + (z + \epsilon)^2}. \quad (5.12)$$

For a cylindrical shell, we can rewrite $dV_s = (2\pi x) dx dz$. Substituting this and Equation (5.12) into Equation (5.11), \mathcal{V} can be expressed as a function of z , x , and ϵ :

$$\mathcal{V}(z, x, \epsilon) = \int_{\epsilon=0}^{T_s} \int_{x=0}^{\infty} \frac{a}{\left(b + \sqrt{(z + \epsilon)^2 + x^2}\right)^6} 2\pi x dx dz. \quad (5.13)$$

For a flat surface with infinite area ($x \rightarrow \infty$), this can be solved as:

$$\mathcal{V}(z, \epsilon) = \frac{\pi a}{10} \int_{\epsilon=0}^{T_s} \frac{b + 5(z + \epsilon)}{(b + z + \epsilon)^5} d\epsilon, \quad (5.14)$$

$$\mathcal{V}(z) = \frac{\pi a}{10} \frac{2b + 5z}{3(b + z)^4} - \frac{5(T_s + z) + 2b}{3(T_s + z + b)^4}. \quad (5.15)$$

For $T_s \rightarrow \infty$ (i.e. solid with infinite thickness), Equation (5.15) can be further simplified to:

$$\mathcal{V}(z) = \frac{\pi a}{10} \frac{2b + 5z}{3(b + z)^4}. \quad (5.16)$$

Equation (5.15) or (5.16) can be used to calculate \mathbf{F}_{LRP} by using μ_ϕ^{lrp} . Since \mathcal{V} only varies in the z direction, $\nabla \mu_\phi^{\text{lrp}}$ can be written as:

$$\nabla \mu_\phi^{\text{lrp}} = \frac{\partial \mu_\phi^{\text{lrp}}}{\partial z} = \frac{\partial C'(\phi)}{\partial z} \mathcal{V}(z) + C'(\phi) \frac{\partial \mathcal{V}(z)}{\partial z}. \quad (5.17)$$

I note that $\partial C'/\partial z = 0$. From Equation (5.16), I can calculate:

$$\frac{\partial \mathcal{V}(z)}{\partial z} = \frac{-\pi a}{10} \frac{(b + 5z)}{(b + z)^5}. \quad (5.18)$$

An important point to be made here is that in my implementation, z starts from 0.5, not 0.0. This happens because in the LBM implementation that I use, each node cannot be a mixture of fluid and solid. Therefore, the fluid-solid interface is always located between the nodes (e.g. between $zk = 1$ and $zk = 2$ in Figure 5.1(c)). However, there are LBM implementations where the fluid-solid interface is located inside the lattice [185, 186, 187].

In LBM, collision and streaming are typically performed only in the fluid nodes. However, for the purposes of gradient computation, we usually need to update the values at the solid nodes by imposing boundary conditions. For ϕ , I impose $\nabla_\perp \phi(z_{fs}) = 0$, where z_{fs} is the location of the fluid-solid interface. In practice, this can be achieved by simply copying the value of ϕ in the fluid node to its neighbouring solid nodes (e.g. $\phi(1) = \phi(2)$ in (Figure 5.1(c))). For solid nodes with multiple fluid node neighbours, the values of ϕ are averaged. Without any LRP forces, this results in a neutrally wetting droplet (i.e. $\theta_e = 90^\circ$).

For μ_ϕ^{lrp} , I do not impose a specific boundary condition. Instead, I use a combination of forward, backward, and central differences, depending on the location of the solid nodes, to

Table 5.1: Finite different coefficients used to compute $\nabla\mu_\phi^{lrp}$ in the x direction. Similar coefficients apply for the y and the z direction.

	$x - 2$	$x - 1$	\mathbf{r}	$x + 1$	$x + 2$
central	0.0	-0.5	0.0	0.5	0.0
forward	0.0	0.0	-1.5	2.0	-0.5
backwards	0.5	-2.0	1.5	0.0	0.0

compute $\nabla\mu_\phi^{lrp}$. Since LBM is generally accurate to the second order in time and space, the finite difference coefficients are chosen to be accurate to the second order. Table 5.1 shows the finite difference coefficients that I have chosen for computing $\nabla\mu_\phi^{lrp}$ in the x direction. Similar coefficients apply for the y and the z directions.

In Figure 5.2, I have implemented Equation (5.18) to simulate a quasi three-dimensional droplet spreading in the x direction. The value of b is set to 0.5, and I vary the values of a as follows: $a = 10^{-2}$, -10^{-2} , and -10^{-1} . The half-droplet is initialised at $z = 4.5$ with a droplet radius of $r_d = 20$ l.u.. The first column of Figure 5.2 shows the droplet profiles at different time steps, while the second column shows the variation of ϕ as a function of z at $x = 89.5$. The first, second, and third rows correspond to $a = 10^{-2}$, $a = -10^{-2}$, and $a = -10^{-1}$, respectively.

Figure 5.2 shows that at a low value of a , the droplet can adopt a partially wetting condition. Depending on the sign of a , it can be either hydrophobic (Figures 5.2(a) and (b)) or hydrophilic (Figures 5.2(c) and (d)). In the hydrophobic case, there is a slight depletion of ϕ near the solid lattice, while I cannot observe enrichment for the hydrophilic case. When a is set to -1.0×10^{-1} , the attractive interaction is very strong, causing the droplet to be pulled sideways and spread into a thin film. Additionally, a slight enrichment near the fluid-solid interface can be observed at $t = 600,000$ time steps.

5.4 Fully Wetting Case: Numerical Integration for Flat Surfaces

Even though the previous section has shown that the long-range interaction can be implemented in LBM, Equation (5.15) can only be derived if the surface structure is simple enough to be integrated analytically. To derive the form of \mathcal{V} for arbitrary surfaces, Oktasendra et al. introduced a method to integrate \mathcal{V} numerically [184]. Figure 5.3(a) illustrates a simple setup of corrugated surfaces. If the distance between the fluid node of interest and the solid node n is written in a shorthand form as $r_n = |\mathbf{r} - \mathbf{r}_n|$, where $n = \{0, 1, \dots, N - 1\}$, and N is the

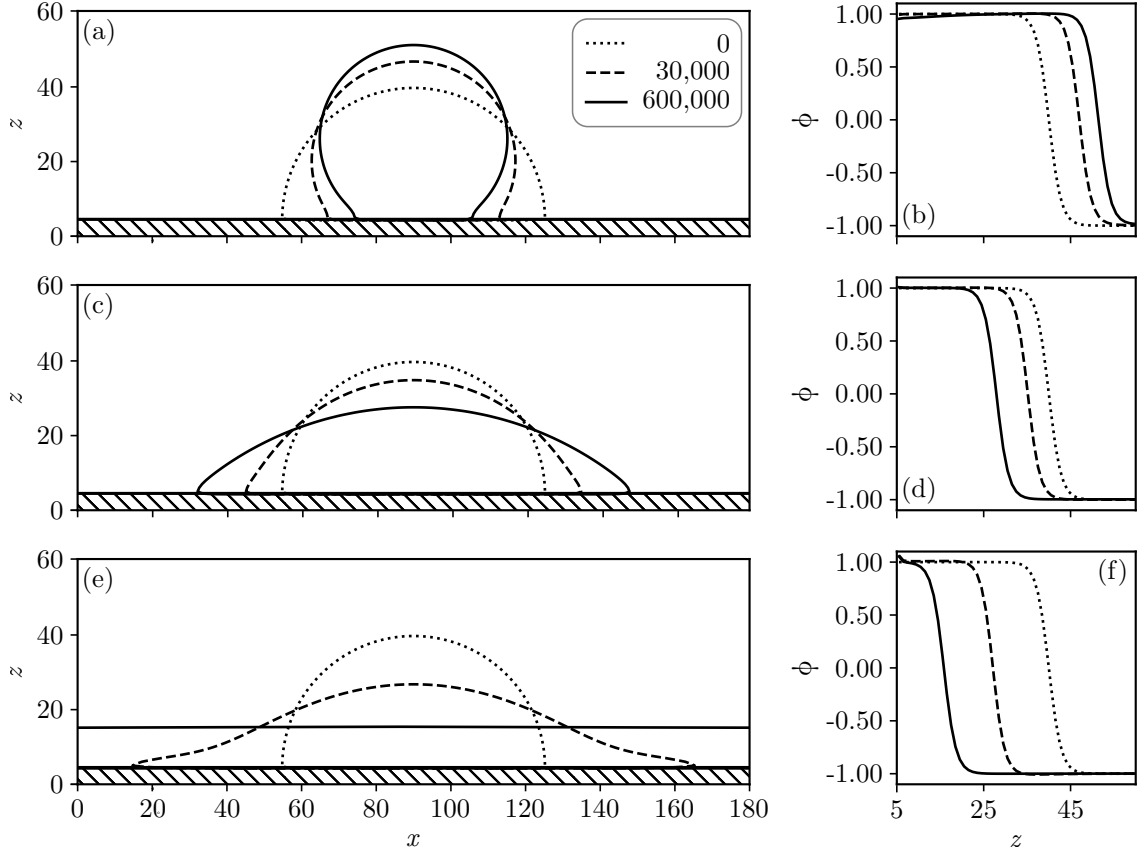


Figure 5.2: (a,c,e) The two-dimensional profile and (b,d,f) the cross-section at $x = 89.5$ of droplets spreading. Rows 1-3 represent $a = 1 \times 10^{-2}$, -1×10^{-2} , and -1×10^{-1} , respectively. $b = 0.5$ for all data. Different line styles represent different time steps. The hatched regions indicate solid.

number of the solid nodes, \mathcal{V} can be computed as:

$$\mathcal{V} = \sum_0^{N-1} P(r_n) \Delta s. \quad (5.19)$$

In LBM, Δs is typically equal to 1 l.u.. This value of Δs causes a severe underestimation of \mathcal{V} . To mitigate this, during the integration, one solid node is instead interpolated into $(2q_{lrp} - 1)$ smaller nodes in each direction, with a new node size of $\Delta s = 1/(2q_{lrp} - 1)$, where q_{lrp} is the so-called degree of interpolation Figure 5.3(b)). Therefore, using this interpolation method, we increase the number of solid nodes from N to $(2q_{lrp} - 1)^3 N$. For solid nodes with coordinates $\mathbf{r}_s = \{x_s, y_s, z_s\}$, the new interpolated coordinates can be computed using:

$$\mathbf{r}_s^{(i,j,k)} = \{x_s^i, y_s^j, z_s^k\}, \quad (5.20)$$

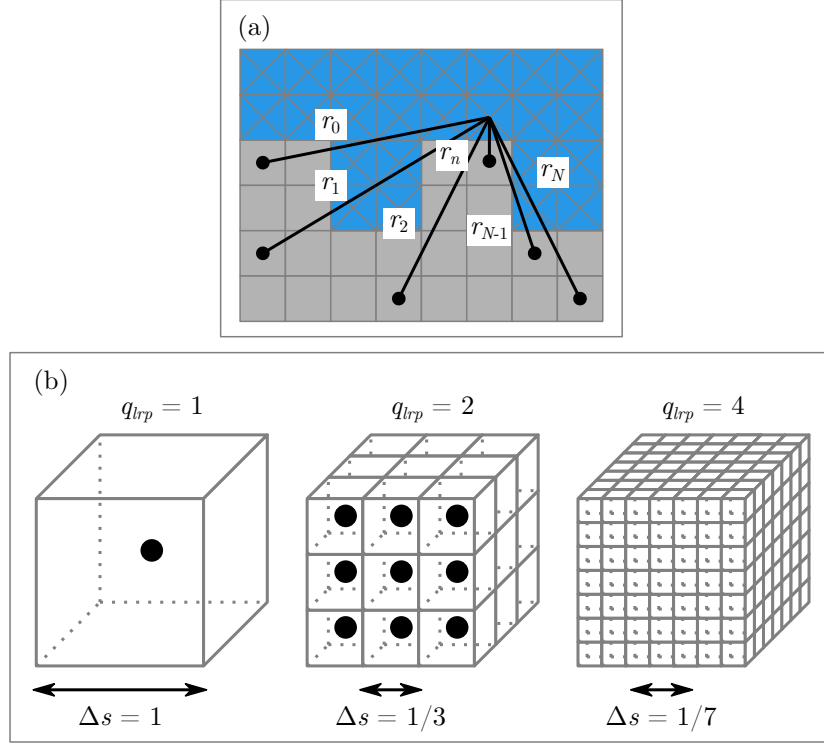


Figure 5.3: (a) A sketch showing the numerical integration for an arbitrary surface. Grey lattices represent solid nodes, while blue lattices represent fluid nodes. r_n represents the distance from the centre of the liquid node to the centre of the solid node. The integrated potential is defined as $\mathcal{V}(\mathbf{r}) = \sum_n^N P(r_n)$. (b) An illustration showing how the interpolation degree (q_{lrp}) works. q_{lrp} divides one lattice node into $(2q_{lrp} - 1)^3$ smaller lattices with a size of Δs , thereby increasing the accuracy of the integration of \mathcal{V} .

where

$$x_s^i = x_s + [i - (q_{lrp} - 1)]\Delta s, \quad (5.21)$$

$$y_s^j = y_s + [j - (q_{lrp} - 1)]\Delta s, \quad (5.22)$$

$$z_s^k = z_s + [k - (q_{lrp} - 1)]\Delta s. \quad (5.23)$$

Here, i , j , and k are indices whose values start at 0 and end at $2(q_{lrp} - 1)$.

For a more concrete example, let us assume a solid node with coordinates $\mathbf{r}_s = \{0, 0, 0\}$, and we want to interpolate it using an interpolation degree of $q_{lrp} = 2$. This means that this node will be interpolated into three nodes in each direction, resulting in a total of twenty-seven nodes with $\Delta s = 1/3$. The interpolated coordinates are as follows:

$$\begin{aligned}
r_s^{(0,0,0)} &= \{-1/3, -1/3, -1/3\}, & r_s^{(1,0,0)} &= \{0, -1/3, -1/3\}, & r_s^{(2,0,0)} &= \{1/3, -1/3, -1/3\}, \\
r_s^{(0,0,1)} &= \{-1/3, -1/3, 0\}, & r_s^{(1,0,1)} &= \{0, -1/3, 0\}, & r_s^{(2,0,1)} &= \{1/3, -1/3, 0\}, \\
r_s^{(0,0,2)} &= \{-1/3, -1/3, 1/3\}, & r_s^{(1,0,2)} &= \{0, -1/3, 1/3\}, & r_s^{(2,0,2)} &= \{1/3, -1/3, 1/3\}, \\
r_s^{(0,1,0)} &= \{-1/3, 0, -1/3\}, & r_s^{(1,1,0)} &= \{0, 0, -1/3\}, & r_s^{(2,1,0)} &= \{1/3, 0, -1/3\}, \\
r_s^{(0,1,1)} &= \{-1/3, 0, 0\}, & r_s^{(1,1,1)} &= \{0, 0, 0\}, & r_s^{(2,1,1)} &= \{1/3, 0, 0\}, \\
r_s^{(0,1,2)} &= \{-1/3, 0, 1/3\}, & r_s^{(1,1,2)} &= \{0, 0, 1/3\}, & r_s^{(2,1,2)} &= \{1/3, 0, 1/3\}, \\
r_s^{(0,2,0)} &= \{-1/3, 1/3, -1/3\}, & r_s^{(1,2,0)} &= \{0, 1/3, -1/3\}, & r_s^{(2,2,0)} &= \{1/3, 1/3, -1/3\}, \\
r_s^{(0,2,1)} &= \{-1/3, 1/3, 0\}, & r_s^{(1,2,1)} &= \{0, 1/3, 0\}, & r_s^{(2,2,1)} &= \{1/3, 1/3, 0\}, \\
r_s^{(0,2,2)} &= \{-1/3, 1/3, 1/3\}, & r_s^{(1,2,2)} &= \{0, 1/3, 1/3\}, & r_s^{(2,2,2)} &= \{1/3, 1/3, 1/3\}.
\end{aligned}$$

The procedure to implement the numerically integrated \mathcal{V} in LBM is relatively simple.

1. Read the solid coordinates generated by LBM and interpolate them using Equation (5.20).
2. For each fluid node, compute each $P(\mathbf{r})$ from the interpolated coordinates. Then, compute \mathcal{V} by using Equation (5.19). Ensure that the new definition of $\Delta s = 1/(2q_{lrp} - 1)$ is used.
3. Save the interpolated coordinates and \mathcal{V} into a file.
4. During the LBM simulation, read the previously generated \mathcal{V} and use it to compute μ_ϕ^{lrp} (Equation (5.7)), $\nabla\mu_\phi^{lrp}$, and \mathbf{F}_{LRP} (Equation (5.9)).
5. Sum the contributions of \mathbf{F}_{LRP} , \mathbf{F}_{chem} , and \mathbf{F}_g to obtain the Guo Forcing term (Equation (3.59)) and the velocity correction term (Equation (3.35)).
6. Evolve this value with the LBE (Equation (3.46)).

In Figure 5.4, the results obtained from numerical integration for a flat surface with a finite thickness of T_s using Equation (5.19) are compared with the analytical expression for a flat surface with infinite thickness using Equation (5.16). Three combinations of $\{T_s, q_{lrp}\}$ are considered: $\{5, 2\}$, $\{5, 4\}$, and $\{10, 2\}$. For both the analytical and numerical integration, $a = -10^{-1}$ and $b = 0.5$. The system is initialised in the same way as the previous subsection.

Figures 5.4(a) and (b) show the value of \mathcal{V} and the relative error of the numerically computed \mathcal{V} . The dashed lines represent the analytical results, while the different markers denote different combinations of $\{T_s, q_{lrp}\}$. In Figure 5.4(a), we can observe that for attractive interaction, \mathcal{V}

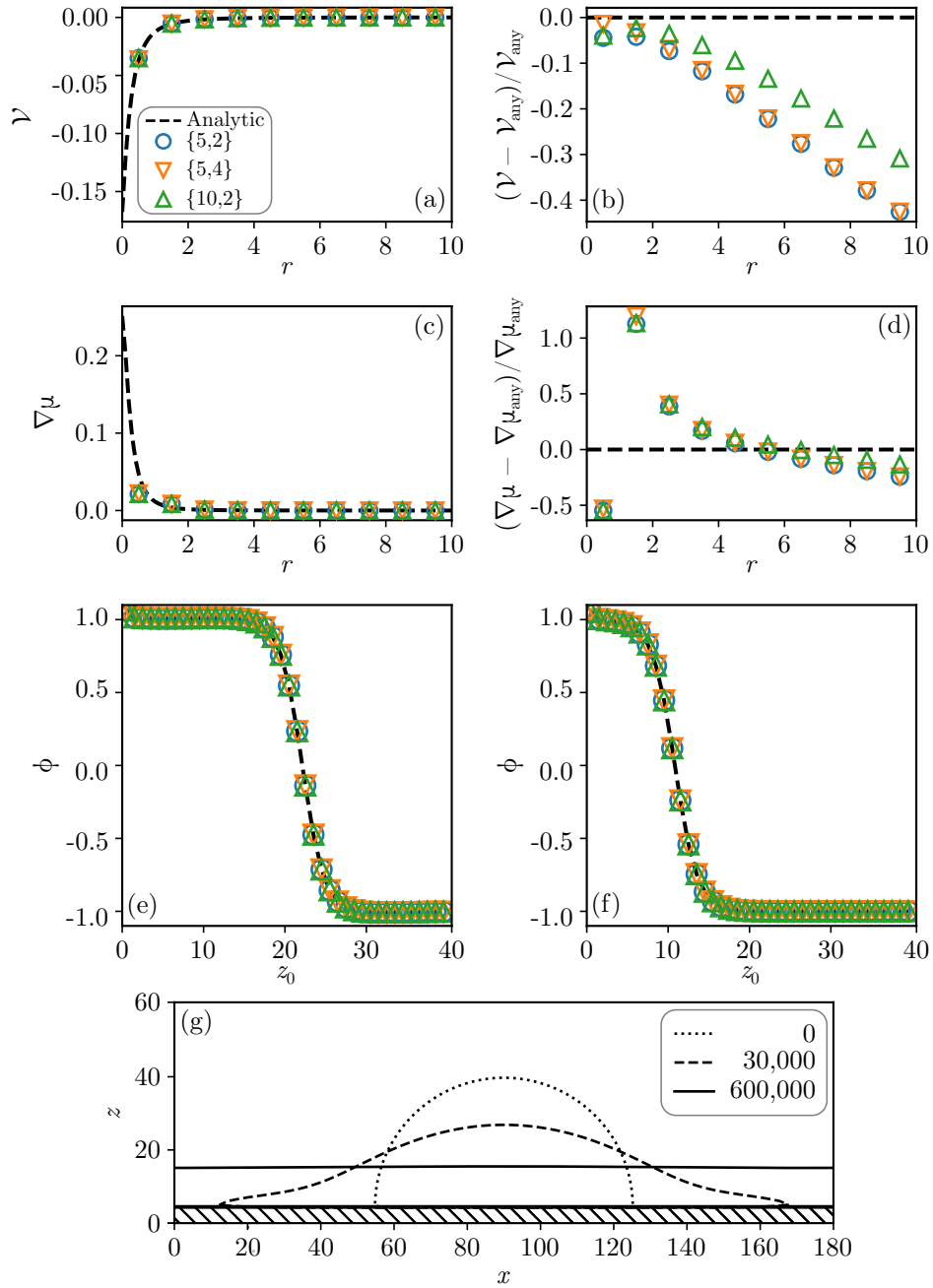


Figure 5.4: (a,b,c,d,ef) The comparison between the analytical and numerical calculations for \mathcal{V} , $\nabla\mu_{\text{LRP}}$, and the droplet cross-section at $x = 89.5$. The dashed lines represent the analytically integrated \mathcal{V} , while the symbols represent the numerically integrated \mathcal{V} . Different symbols denote different combinations of $\{T_s, q_{lrp}\}$, where T_s represents the solid thickness and q_{lrp} is the interpolation degree. (a,b) The value of \mathcal{V} and the relative error compared to the analytical value. (c,d) The value of $\nabla\mu_{\text{LRP}}$ and its relative error. (e,f) The droplet profiles at $x = 89.5$ for $t = 30,000$ and $600,000$ time steps, respectively. The data is normalised such that the first fluid node is located at $z = 0.5$. (g) The two-dimensional profile of a droplet spreading using the numerically integrated \mathcal{V} with the combination of $\{5,2\}$. Different line styles represent different time steps. The hatched regions indicate solid.

values is negative initially, before decaying exponentially to zero.

Qualitatively, the numerical and analytical \mathcal{V} do not differ significantly, especially at lower values of r . This is supported by Figure 5.4(b), which shows an error of less than 10% for $r < 2.5$. At higher values of r , the relative error increases to 40%. However, this deviation is acceptable because the absolute magnitude of $\mathcal{V}(r > 2.5)$ is three orders of magnitude smaller than $\mathcal{V}(r < 2.5)$, indicating that the long-range potential has minimal influence on the fluid at this distance. Figure 5.4(b) shows that increasing q_{lrp} to 4 while keeping $T_s = 5$ significantly reduces the error at lower r , but does not reduce the error at higher r . This suggests that the inaccuracies at lower r mainly come from the solid discretisation. Conversely, increasing the solid thickness to $T_s = 10$ reduces the error at higher r , but does not reduce the error at lower r .

$\nabla\mu_\phi^{lrp}$ exhibits a relatively high error, particularly for smaller values of r . At $r = 1.5$, the error exceeds 100% compared to the analytical value. This significant difference is a numerical artefact which is caused by the structure of the nodes themselves. As previously mentioned, in LBM, the simulation window consists of nodes in a cubic lattice structure, where the distance between each node is always 1 l.u.. On the other hand, Equations (5.16) and (5.15) decay exponentially, causing $\nabla\mu_\phi^{lrp}$ to become very steep as r approaches zero. The numerically computed $\nabla\mu_\phi^{lrp}$ is sparsely sampled, thus causing this error. Increasing the stencil size will not reduce the error significantly because the dominant contribution occurs at small distances, which are not adequately sampled by LBM. One possible approach to fix this is by increasing the simulation resolution, but that would significantly increase the computational cost. Another possible approach is by introducing an alternative form of P with a less steep gradient of \mathcal{V} .

The droplet profiles show that despite the relatively high error of $\nabla\mu_\phi^{lrp}$, the simulation results are representative. Figures 5.4(e) and (f) show the droplet cross-sections at $x = 89.5$ when $t = 30,000$ and $600,000$ time steps, respectively. There is no significant difference in the droplet profile when using analytically and numerically integrated \mathcal{V} . At $t = 30,000$ time steps, the droplet has not spread into a thin film, but its height is already lower than the initial condition. By $600,000$ time steps, the droplet has reached steady state with a slight enrichment at liquid nodes near the surface. Figure 5.4(g) shows that the two-dimensional droplet profile with integration parameter of $\{5, 2\}$ exhibits similar dynamics to those obtained by employing analytical \mathcal{V} (Figure 5.2(e)).

From here, I conclude that the numerical integration of \mathcal{V} is meaningful with only a small

inaccuracy near the fluid-solid interface. However, due to the way LBM treats its lattice structure, there is a high numerical error during the calculation of $\nabla\mu_\phi^{lrp}$ near the fluid-solid interface where the gradient of \mathcal{V} is steep. Although this approximation does not significantly affect the simulation results for numerically integrated \mathcal{V} compared to the analytically integrated \mathcal{V} , when compared with other numerical solvers, it needs to be carefully considered. For example, our results here are qualitatively the same as the work of Oktasendra et al. [184]. Quantitatively (e.g. with equivalent physical parameters), the results are different due to lower numerical error near the solid-fluid interface of the phase-field method.

5.5 Pseudo-partial Wetting Case

The potential P defined in Equation (5.10) can only simulate fully wetting and partially wetting conditions. To simulate a pseudo-partial wetting system, a different form of interaction is required. Again, Oktasendra et al. introduced an alternative form of P [184]:

$$P(\mathbf{r}) = \begin{cases} f_a = \frac{a}{b^6}, & \text{if } r < \sigma^{lrp}, \\ f_r = -f_s f_a \left[\frac{\sigma^{lrp}}{r} \right]^6, & \text{otherwise.} \end{cases} \quad (5.24)$$

Here, f_a represents the attractive interaction, which is applied when the fluid-solid distance ($|\mathbf{r} - \mathbf{r}_s| = r$) is less than a prescribed thin film thickness (σ^{lrp}). Beyond σ^{lrp} , the interaction changes to repulsive interaction (f_r). The prefactor f_s is used to control the strength of the repulsive interaction relative to the attractive interaction. When $f_s = 1.0$, $f_r = -f_a$ at $r = \sigma^{lrp}$. Using this form of P , the attractive interaction is a constant, while the repulsive interaction decays according to a power law.

In LBM, the LRP interaction is introduced through $\nabla\mu_\phi^{lrp}$, therefore a smooth P is needed to ensure differentiability. In the original form introduced by Oktasendra et al. [184], P has a discontinuity at $r = \sigma^{lrp}$, preventing this form to be used as-is. To mitigate this issue, here, I introduced a modified version of Equation (5.24), where the transition from attractive to

repulsive interaction is smoothed by a hyperbolic tangent (tanh) function:

$$P(r) = f_{a,s} + f_{r,s} \quad (5.25)$$

$$f_{a,s} = \frac{1}{2} \left[-\tanh \left(\frac{r - (\sigma^{lrp} - 5\zeta^{lrp})}{2\zeta^{lrp}} \right) + 1 \right] \left[f_a \right] \quad (5.26)$$

$$f_{r,s} = \frac{1}{2} \left[+\tanh \left(\frac{r - (\sigma^{lrp} - 5\zeta^{lrp})}{2\zeta^{lrp}} \right) + 1 \right] \left[-f_s f_a \left(\frac{\sigma^{lrp}}{r} \right)^6 \right] \quad (5.27)$$

Using this modified form, the tanh function in the attractive interaction smoothly transitions $f_{a,s}$ from f_a to 0 as $r \rightarrow \sigma^{lrp}$. Similarly, the tanh function in the repulsive part transitions $f_{r,s}$ from 0 to $-f_s f_a (\sigma^{lrp}/r)^6$. I also introduce the interface width (ζ^{lrp}) to control the width of the tanh function. It is important to note that ζ^{lrp} is distinct from the fluid-fluid interface width. The term $\sigma^{lrp} - 5\zeta^{lrp}$ is used to tweak the centre of the hyperbolic tangent. Using $\sigma^{lrp} - 5\zeta^{lrp}$ instead of σ^{lrp} reduces the relative error at $P(r \approx \sigma^{lrp})$. The term $\sigma^{lrp} - 5\zeta^{lrp}$ component can also be adjusted to match the smooth transition to the step function (e.g. $\sigma^{lrp} - 4\zeta^{lrp}$, $\sigma^{lrp} - 2.5\zeta^{lrp}$, etc.).

Figure 5.5 reports the values of P and the numerically integrated \mathcal{V} for a flat surface with a thickness of $T_s = 5$ and an interpolation degree of $q_{lrp} = 2$. $a = -10^{-6}$, $b = 0.5$, and $\sigma^{lrp} = 5$ for all cases. In the first row, I use $\zeta^{lrp} = 0.075$ and $f_s = 0.15$; the second row uses $\zeta^{lrp} = 0.025$ and $f_s = 0.15$; while the third row employs $\zeta^{lrp} = 0.025$ and $f_s = 0.30$. In general, a smaller ζ^{lrp} will increase the sharpness of P near σ^{lrp} (Figures 5.5(c) and (e)), leading to an increase in $|\mathcal{V}(r \approx 0)|$. Increasing f_s increases the contribution of the repulsive part ($P(r > \sigma^{lrp})$), thereby reducing the maximum value of $|\mathcal{V}(r \approx 0)|$ and makes $\mathcal{V}(r \rightarrow \infty)$ decays faster.

In Figure 5.6, the numerically integrated \mathcal{V} is implemented in the LBM. The left column shows the two-dimensional droplet profiles, while the right column shows the one-dimensional profiles at $x = 89.5$. The droplet is initialised as a half droplet with $r_d = 25$ and film thickness of 10 l.u.. We observe that the droplet and film can coexist. The simulation starts with a half-droplet on the top of a thin film at $t = 0$. By $t = 30,000$, the droplet has spread. However, not all of the volume is transferred into a thin film. Instead, beyond a certain film thickness, the excess volume forms a stable sessile drop on top of the film. After 600,000 time steps, the system has reached steady state where the droplet and the film can coexist. The cross-section shows that there is no significant enrichment of ϕ at $z = 0.5$.

Different combinations of ζ^{lrp} and f_s can tune the apparent contact angle. For the same

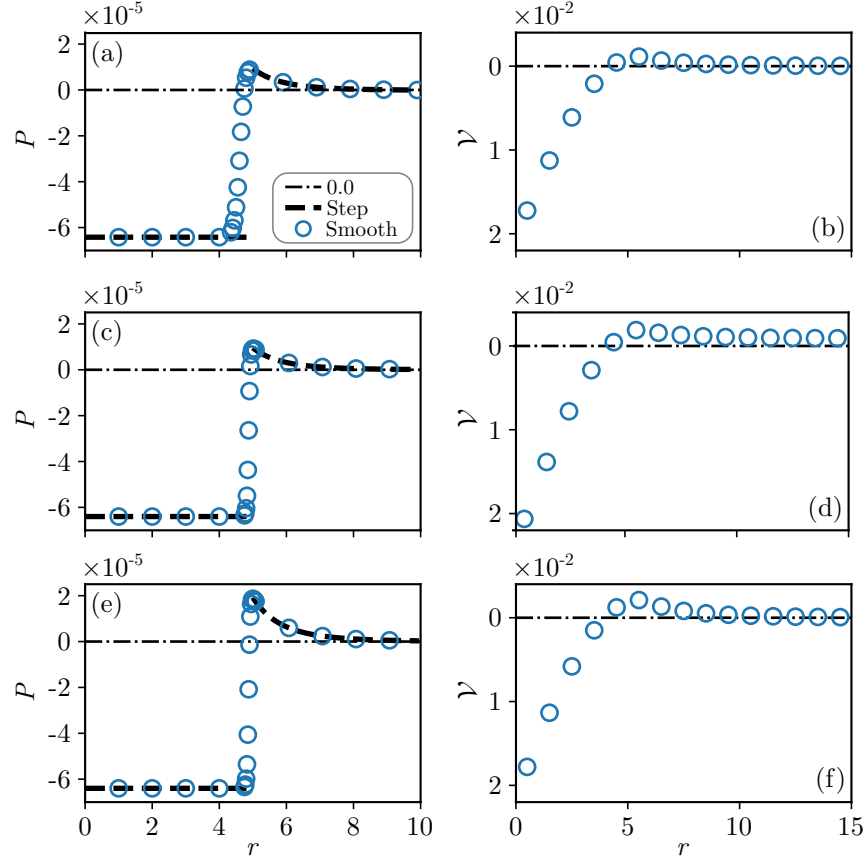


Figure 5.5: (a,c,e) The fluid-solid interaction potential (P) and (b,d,f) the integrated potential (\mathcal{V}) as a position of distance. Rows 1-3 represent $\zeta^{lrp} = 0.075$, $f_s = 0.15$; $\zeta^{lrp} = 0.025$; $f_s = 0.15$, and $\zeta^{lrp} = 0.025$, $f_s = 0.30$, respectively. $a = 10^{-6}$, $b = 0.5$, and $\sigma^{lrp} = 5$ for all cases. Markers denote data that is smoothed using a hyperbolic tangent function. Please note that the markers for P are denser when $r \approx \sigma^{lrp}$ to visualise the effect of the hyperbolic tangent transition.

value of f_s , the apparent contact angle is lower when ζ^{lrp} is smaller (i.e. the tanh function is sharper around σ^{lrp}). This is because with a smaller ζ^{lrp} , $f_{a,s}$ can maintain its maximum value for longer r compared to a larger ζ^{lrp} (compare Figures 5.5(a) with (c) when $r \approx 5$). However, the droplet's apparent contact angle does not differ significantly. On the other hand, by increasing f_s , we increase the repulsive interaction strength relative to the attractive interaction, therefore, making the apparent contact angle higher (Figures 5.6(e) and (f)).

After showing that it is possible to achieve pseudo-partial wetting on a flat surface, I focus on grooved surfaces and compare the results with the work of the authors in [184]. Similar to the fully wetting case, these comparisons are only done qualitatively and not quantitatively, due to the form of P used in LBM being different to the one in the phase-field method. It has been found that for a grooved surface, the liquid can adopt different states depending on the type of fluid-solid wetting interaction. For pseudo-partial wetting, there are three distinct

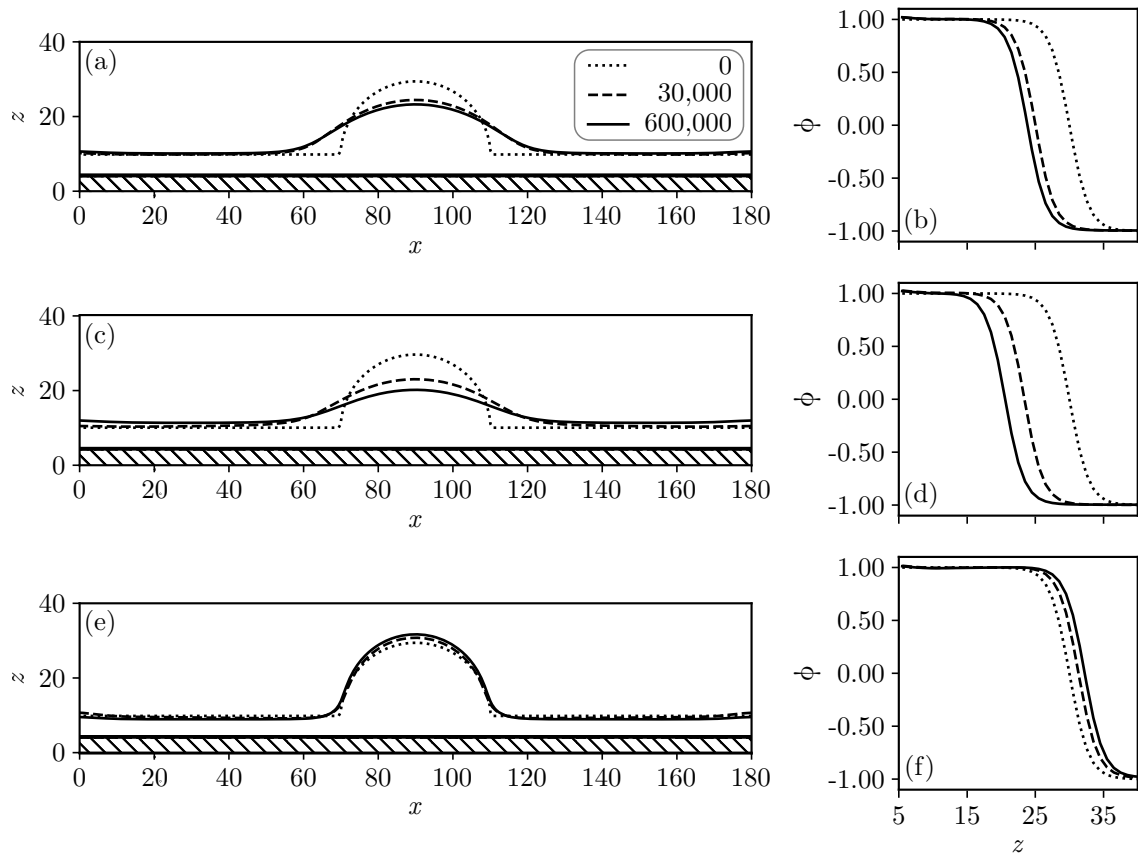


Figure 5.6: (a,c,e) The two-dimensional profile and (b,d,f) the cross-section at $x = 89.5$. Rows 1-3 represent $\zeta^{lrp} = 0.075$, $f_s = 0.15$; $\zeta^{lrp} = 0.025$, $f_s = 0.15$; and $\zeta^{lrp} = 0.025$, $f_s = 0.30$, respectively. $a = 10^{-6}$, $b = 0.5$, and $\sigma^{lrp} = 5$ for all cases. Different line styles represent different time steps. The hatched regions indicate solid.

stages. The first is the so-called pre-filling stage. In this stage, the pressure difference between the liquid and gas is large and negative. Depending on the difference in the liquid and gas pressures, the droplet can either be pinned at the top corner of the ridge, leaving the top of the ridge dry) or can form a continuous film covering the groove, the sidewall, and the top of the ridge. The second stage is called the capillary filling stage. In this stage, the liquid fills the gap between the ridges, before forming a droplet above the groove while the ridge is only covered with thin film. In the last stage, typically when the pressure difference between the liquid and the gas is around zero, the liquid-gas interface collapses, and the liquid fills up the whole simulation domain.

In Figure 5.7(a), I illustrate the grooved surfaces. The structure is repeating in the x and y directions with a finite height in the z direction. Due to this periodicity, we can simulate a unit cell of repeating ridge (Figure 5.7(b)) with periodic boundary conditions in the x and y directions. Figure 5.7(b) also shows the dimension of the structure, which is indicated in lattice

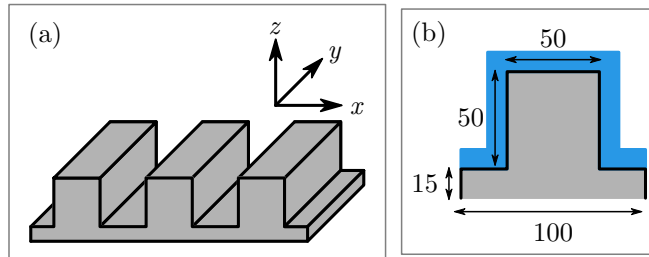


Figure 5.7: (a) A schematic of the grooved surfaces. The structure is repeated in the x and y directions. (b) A single unit cell of a repeating ridge shape. The boundary is periodic in the x and y directions.

units (l.u.). Instead of initialising with different pressure differences, I choose to initialise with different amounts of liquid instead. There are three configurations that I use: (1) a thin film wrapping around the ridge and the groove with a thickness of 5 l.u., (2) a thin film wrapping around the ridge and the groove with a thickness of 10 l.u., and (3) the groove and the ridge submerged in liquid with a thickness of 60 l.u.. Figure 5.8 shows the results of this simulation setup. Here, $q_{lrp} = 2$, $a = 4 \times 10^{-5}$, $b = 1.0$, $\sigma^{lrp} = 6.0$, and $\zeta^{lrp} = 0.025$. The first column in Figure 5.8 shows the results for $f_s = 0.10$ while the second column shows the result for $f_s = 0.25$.

Figures 5.8(a) and (b) show the colour-maps of \mathcal{V} . Lighter colours denote attractive interaction, while darker colours denote repulsive interaction. In general, the attractive region follows the shape of the groove, the sidewall, and the top of the ridge. We can see that the inside corners display brighter colours (i.e. higher concentration of the attractive part) compared to the outer corners near the top of the ridge. This is because, at the inside corners, there is more interaction with solid nodes compared to the outer corners. At higher f_s , the overall interaction is less attractive with smaller regions with bright colours. However, qualitatively, the inside and outside corners still show the same behaviour as for lower f_s .

Figures 5.8(c) and (d) show the configuration after I initialise the system with a thin film with 5 l.u. thickness. After 250,000 time steps, the liquid still does not move. It is stable as the thin film is encapsulating the grooved surface, similar to the pre-filling stage in [184]. The film is slightly thicker at the inside corner compared to the outside corner, but the film thickness does not differ significantly between the grooves, the sidewalls, and the top of the ridge when $f_s = 0.10$. There is a slight depletion on the sidewalls near the inside corner when $f_s = 0.25$, but it is not significant.

When the film thickness is increased to 15 l.u. (Figures 5.8(e) and (f)), we observe different

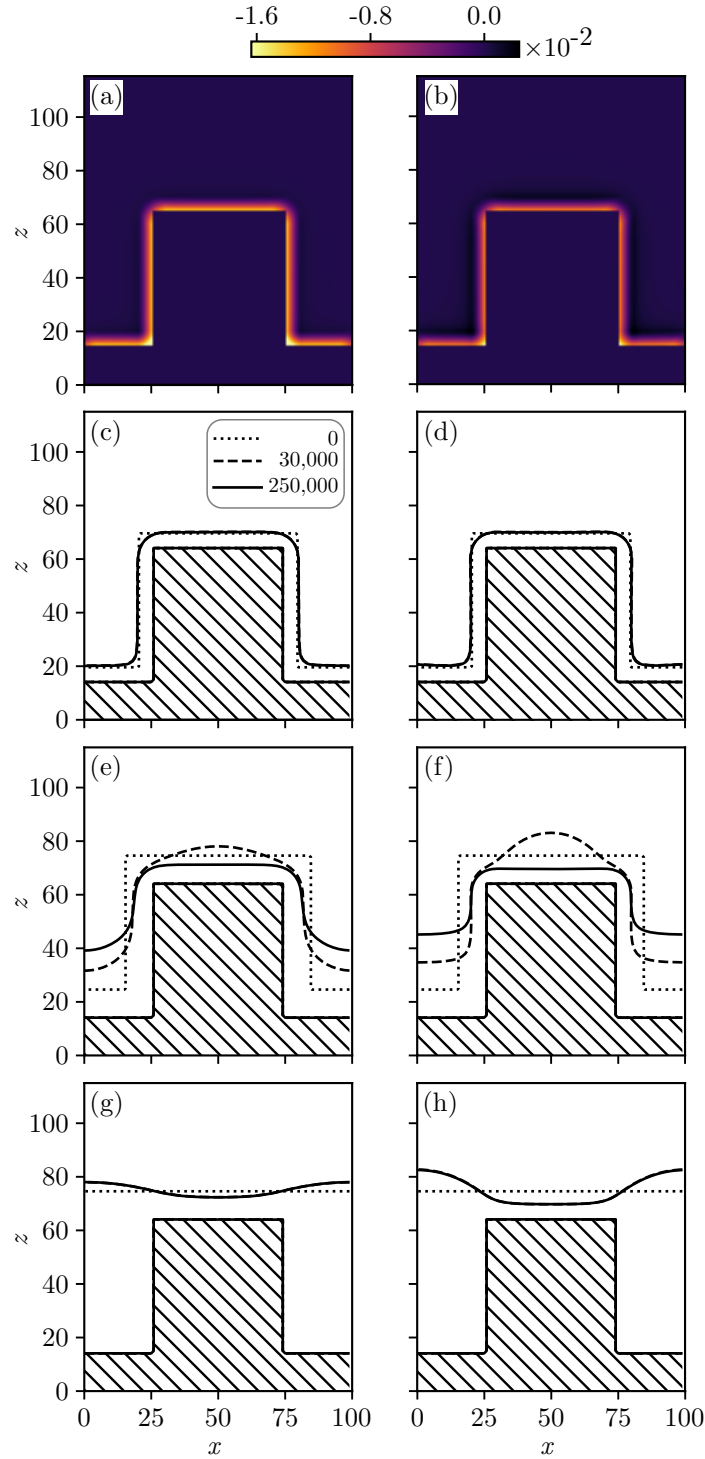


Figure 5.8: (a,b) The distribution of \mathcal{V} around the grooved surfaces. Lighter colours denote regions with attractive interaction. The two-dimensional profiles of (c,d) a thin film with an initial thickness of 5 l.u.; (e,f) a thin film with an initial thickness of 10 l.u.; (g,h) a ridge that is submerged inside liquid with a thickness of 60 l.u. For all cases, $q_{lrp} = 2$, $a = 4 \times 10^{-5}$, $b = 1.0$, $\sigma^{lrp} = 6.0$, and $\zeta^{lrp} = 0.025$. The first column represents $f_s = 0.10$, while the second column represents $f_s = 0.25$. The hatched regions indicate solid.

morphologies. At $t = 30,000$ time steps, the fluid on the sidewall drains into the grooves. There is a bottleneck at the top corner which is causing a bulge on the top of the ridge. However, after 600,000 time steps, the bulge also drains into the grooves, leaving a thin film at the top of the ridge. The system with lower repulsive interaction shows that the liquid can wet the solid more, resulting in a smaller bulge at the top of the ridge during the transient state. The final profile also shows that the film is thicker when $f_s = 0.10$. This stage is similar to the capillary filling stage before the droplet fills the grooves completely.

If the liquid is initialised above the ridge (Figures 5.8(g) and (h)), we can see that the liquid quickly separates into two parts: a thin film at the top of the ridge and a droplet on top of the grooves. This state can only be observed with pseudo-partial wetting, where the droplet will gather inside the groove and leaves the top of the ridge with a thin film. This corresponds to the capillary filling stage in [184]. Lower f_s corresponds to a lower apparent contact angle and a thicker film.

5.6 Droplet on Pseudo-partial Wetting Fibre

So far, I have only shown the quasi-static results even with pseudo-partial wetting states, while the main motivation for implementing the long-range potential is to simulate droplet dynamics. Following the results in Chapter 4, my aim is to see how a droplet on a pseudo-partial wetting state moves alongside a fibre. The geometry is the same fibre model used in Chapter 4, used to numerically integrate \mathcal{V} . Here, I find a problem where the droplet will adopt a squared shape in the steady state condition instead of an axisymmetric barrel morphology. The issue appears more pronounced with a larger fibre radius (r_f) (Figures 5.9(a) and (b)) even though the colour scale indicates that \mathcal{V} is radially distributed around the fibre (Figures 5.9(c) and (d)).

Further investigation shows that the problem is caused by numerical artefacts due to the staircase approximation. In the staircase approximation, a curved or inclined surface is approximated by piecewise facets that follow the structure of the underlying cubic lattices [163, 164]. Previously in Section 5.5, I have shown that the inside corner of grooved surfaces will have a higher \mathcal{V} compared to the outer corner. With the staircase approximation, we basically introduce a solid with alternating inside and outside corners. This means that for the same supposed distance from the fibre surface, \mathcal{V} can have different values depending on whether it

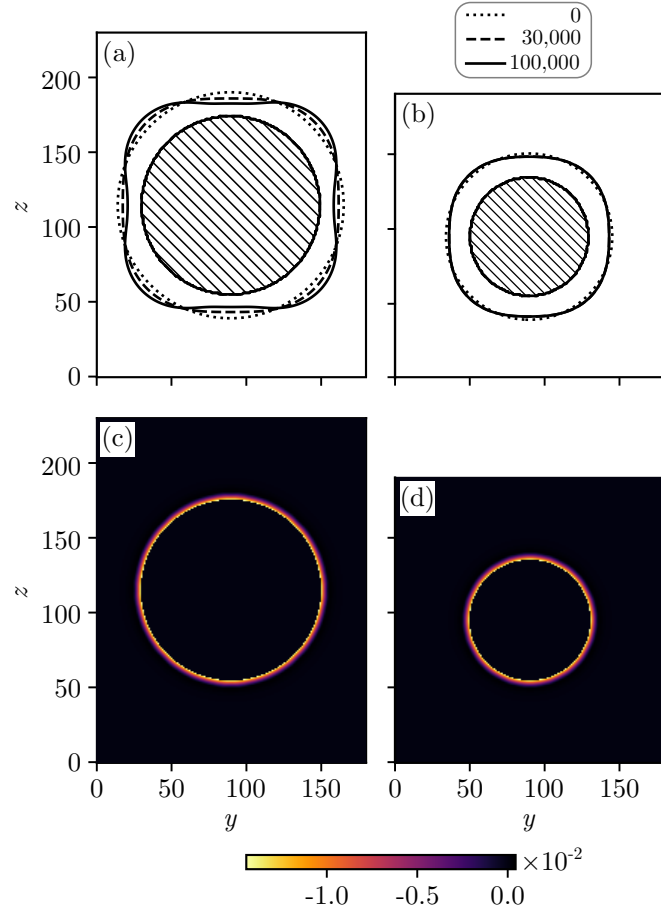


Figure 5.9: (a,b) The two-dimensional profiles of film wrapping around a fibre. Different line styles denote different time steps. The hatched regions indicate solid. (c,d) The distribution of $\mathcal{V}(\mathbf{r})$ around the fibres. lighter colours denote regions with lower \mathcal{V} . The first column denotes results for $r_f = 60$, while the second column denotes $r_f = 40$.

is located on the inside corner, the outside corner, or on the facets of the staircase.

To mitigate this issue, the numerically integrated data is fitted into a smooth curve that varies with r . From Figures 5.5(b), (d), and (f), we know that for pseudo-partial wetting, \mathcal{V} has a characteristic of a steady increase in \mathcal{V} when $r < \sigma^{lrp}$, followed by a smooth decay to 0 when $r > \sigma^{lrp}$. The important feature is that in between the steady increase and the exponential decay, the curve must have a maximum at σ^{lrp} , which is crucial to ensure the pseudo-partial wetting regime. To capture accurately the shape with the maximum, I employ a fourth-order polynomial modulated by exponential decay:

$$\mathcal{V}(r) = (a_0^{lrp} + a_1^{lrp}r + a_2^{lrp}r^2 + a_3^{lrp}r^3 + a_4^{lrp}r^4) \exp(-a_5^{lrp}r), \quad (5.28)$$

where a_n^{lrp} are obtained from data fitting, with $n = \{0, 1, \dots, 5\}$.

The implementation steps are as follows:

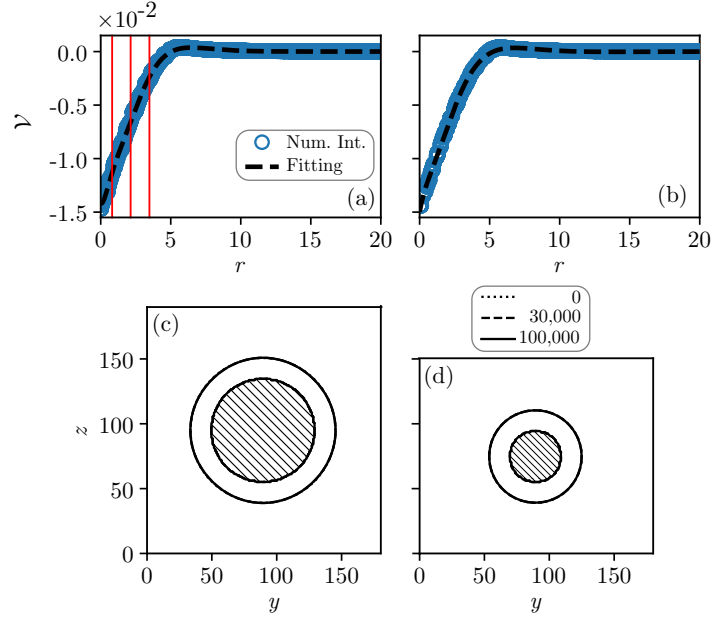


Figure 5.10: (a,b) \mathcal{V} data for a fibre sorted by r . Markers denote numerically integrated data while the dashed lines are Equation (5.28) fitted to the data. Vertical red lines are used to show the locations of some of the fluctuations that can be observed in the attractive regime. These fluctuations are caused by the staircase approximation. (c,d) The two-dimensional profiles of the droplet around the fibre as a function of time. The first column represents data for $r_f = 40$ while the second column for $r_f = 20$. The hatched regions indicate solid.

1. Numerically integrate P of the fibre that is modelled using the staircase approximation.
2. Extract the value of \mathcal{V} and sort them by r , where r is the distance between the liquid nodes and the centre of the fibre, subtracted by the fibre radius ($r = |\mathbf{r} - \mathbf{r}_s| - r_f$).
3. Fit \mathcal{V} to Equation (5.28) to obtain a_n^{lrp} .
4. Use Equation (5.28) to compute \mathcal{V} , μ_ϕ^{lrp} , $\nabla\mu_\phi^{lrp}$, and \mathbf{F}_{LRP} in the LBM code.

In Figures 5.10 (a) and (b), we can see \mathcal{V} for $r_f = 40$ and 20, respectively. Here, $a = -4.0 \times 10^{-6}$, $b = 1.0$, $\sigma^{lrp} = 6.0$, $\zeta^{lrp} = 0.025$, and $f_s = 0.10$. The blue markers represent the data obtained from numerical integration, while the dashed lines are the fitted data using Equation (5.28). The first column shows the results for $r_f = 40$ while the second column shows the results for $r_f = 20$.

At $r_f = 40$, we can see fluctuations on \mathcal{V} when $r < \sigma^{lrp}$ which I note with red lines. This jagged region is caused by the staircase approximation, which introduces more corners. Such jagged edges cannot be seen in $r_f = 20$, which has fewer corners, suggesting why in Figure 5.9 larger r_f gives us worse results. Therefore, unlike a typical LBM simulation where the staircase approximation is improved by increasing the fibre radius, with the current interpolation method, the fluctuations are instead amplified because the number of corners is increased when

Table 5.2: The fitting parameters for fibre with different fibre radius (r_f). $a = -4.0 \times 10^{-6}$, $b = 1.0$, $\sigma^{lrp} = 6.0$, $\zeta^{lrp} = 0.025$, and $f_s = 0.10$.

	$r_f = 40$	$r_f = 20$
a_0^{lrp}	-1.416×10^{-2}	-1.497×10^{-2}
a_1^{lrp}	-1.772×10^{-2}	-3.628×10^{-3}
a_2^{lrp}	5.365×10^{-3}	-4.734×10^{-3}
a_3^{lrp}	-8.746×10^{-3}	1.710×10^{-3}
a_4^{lrp}	-1.679×10^{-3}	-1.097×10^{-4}
a_5^{lrp}	1.158×10^{-0}	7.141×10^{-1}

the fibre radius is increased. By introducing a smooth \mathcal{V} through fitting, therefore, ignoring the number of corners, this artefact is removed.

Table 5.2 shows a_n^{lrp} for $r_f = 40$ and 20. Figures 5.10 (c) and (d) show the two-dimensional droplet profile where \mathcal{V} is computed using Equation (5.28). The droplet is initialised with a film thickness of 6 l.u.. After $t = 100,000$ time steps, we can see that for both small and large fibre radii, the droplet stays axisymmetric, unlike when we are using numerically integrated \mathcal{V} . This proves that the artefact is indeed caused by the staircase approximation.

When a droplet wets a fibre, it can adopt different morphologies. Two of the most common are the clamshell morphology, when the droplet is perched on the side of the fibre, and the barrel morphology when the droplet completely encapsulates the fibre [76]. These morphologies are discussed in more detail in Section 2.4 and Chapter 4. Figures 5.11(a) and (b) show the three-dimensional views of the corresponding droplet in clamshell and barrel morphologies with pseudo-partial wetting. These two morphologies are both mechanically stable and are obtained with different initialisations. For the clamshell morphology (Figures 5.11(c) and (d)), I initialise a half droplet on top of the film-coated fibre and let it settle down naturally. The edge of the droplet will contact the thin film before the rest of the volume spreads out, and the droplet settles into the clamshell morphology. On the other hand, for the barrel morphology, I instead initialise a cylinder that encapsulates the film-coated fibre (Figures 5.11(e) and (f)).

In Figure 5.12, $r_f = 40$ and $r_f = 20$ are used to compare the relation between the Capillary number (Ca) and the Bond number (Bo). Ca is defined in Equation (2.13) and Bo is defined in Equation (2.12). For Bo, I set the lengthscale term to the cubic root of the droplet volume ($\Omega^{1/3}$). I pick three values for Bo: 0.01, 0.1, and 1.0. The system Reynolds numbers are

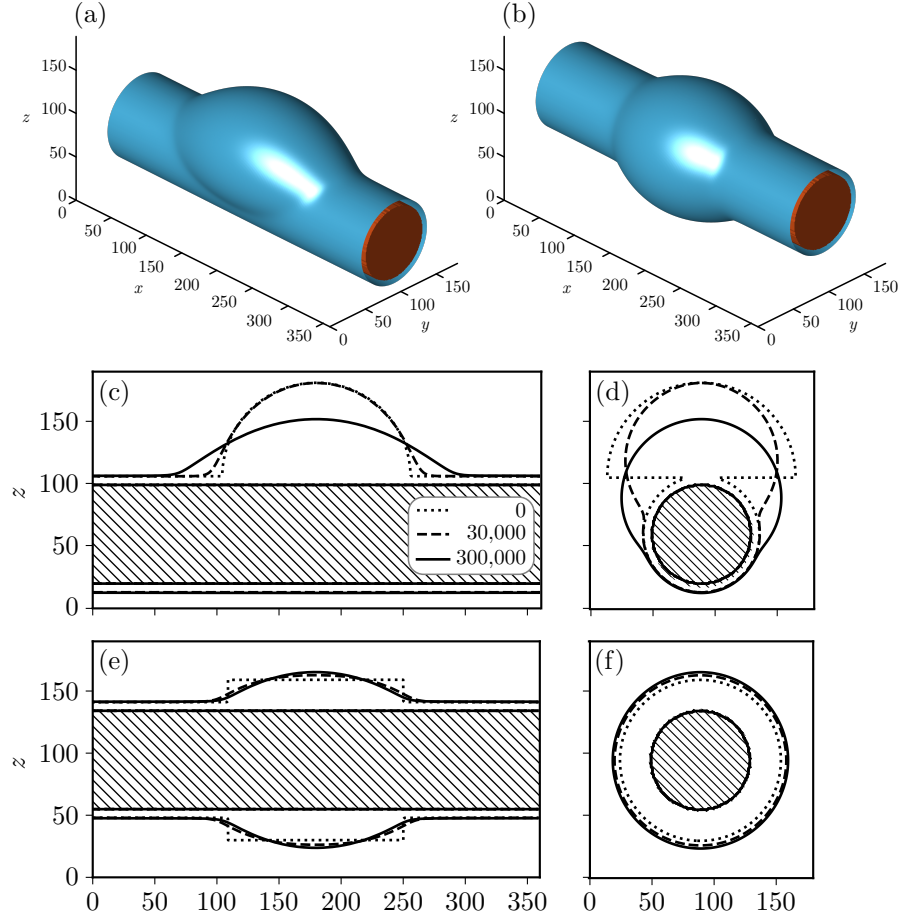


Figure 5.11: (a,b) The three-dimensional picture showing a droplet in clamshell and barrel morphologies sitting on a fibre in pseudo-partial wetting. (c,e) two-dimensional droplet profiles at $y = 89.5$ for clamshell and barrel morphologies. (d,f) The droplet profiles at $x = 179.5$ for clamshell and barrel. Different line styles denote different time steps. The hatched regions indicate solid.

between 2.215×10^{-4} and 36.65. In the pseudo-partial wetting state, one needs to define a criterion to separate the droplet volume and the thin film volume. Here, I define Ω as the total volume of the liquid outside of the thin film that coats the fibre. For $r_f = 40$, $\Omega = 800,000$ and 600,000 l.u., while for $r_f = 20$, $\Omega = 800,000$, 600,000, and 150,000 l.u.. The droplet's acceleration is only in the positive x direction. For the LBM parameters, I set $\tau_1 = 3.0$ and $\tau_2 = 0.505$, which result in a kinematic viscosity ratio of $\nu_1/\nu_2 = 500$. I also use $\alpha_{ed} = 1.414$ and $\kappa_1 = \kappa_2 = 0.008$ which give us the surface tension of $\gamma_{12} = 3.771 \times 10^{-3}$. At first, the system is initialised similarly to the system in Figure 5.11 to obtain the barrel and clamshell morphologies. After the static droplet reaches equilibrium, a constant g_x is assigned and the system is run until the droplet's average velocity does not change.

Figures 5.12(a) and (b) show the droplet flow profile where the colour map shows the x - z component of the strain-rate tensor: $\mathbb{E}_{xz} = \mathbb{E}_{zx} = (\partial v_x/\partial z + \partial v_z/\partial x)/2$. The droplet velocity

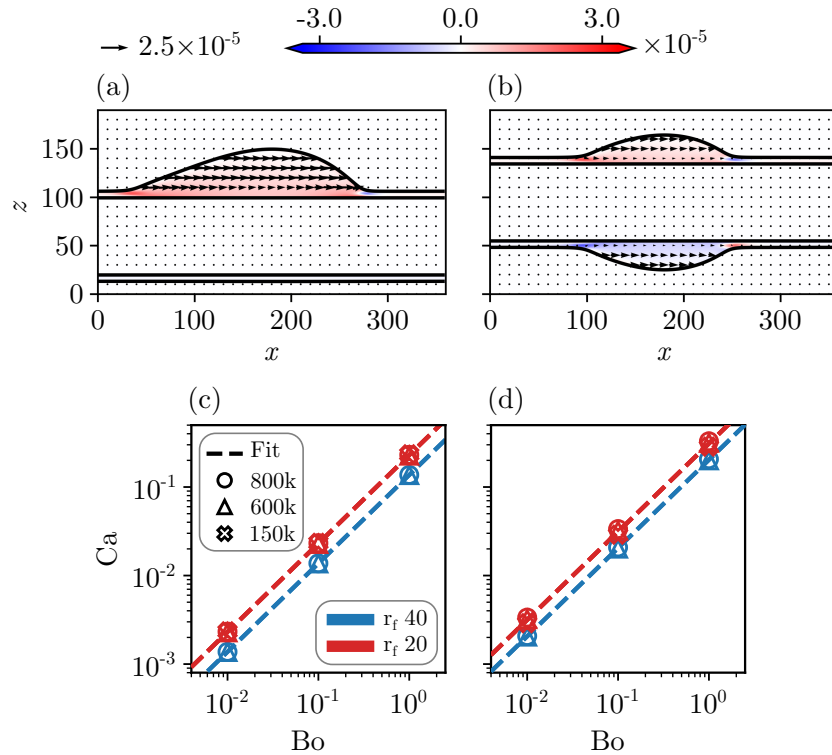


Figure 5.12: Pseudo-partial wetting droplets flow profile on a fibre. The colour map shows the x - z component of the shear-rate tensor. (a,b) Barrel and clamshell morphologies, $Bo = 1.0$. (c,d) Scaling laws between the Capillary number (Ca) and the Bond number (Bo). Different symbols denote different droplet volumes, while different colours denote different fibre radii. Dashed lines are obtained by fitting each fibre radius to Equation (5.29). Both axes are in the logarithmic scale. The first column shows data for clamshell morphology while the second column shows barrel morphology.

profile is dominated by v_x , as indicated by arrows that are uniformly pointing to the right. Similar to the partially wetting case, the dissipation is high around the contact area and the liquid wedge. However, in a pseudo-partial wetting state, the exact shape of the liquid wedge is ambiguous because the droplet contact line merges smoothly with the thin film. Nevertheless, we can qualitatively see that the region with high dissipation is generally larger than the partially wetting state. This is consistent for both morphologies, both fibre radii, and all three Bond numbers.

Figures 5.12(c) and (d) show the relation between Ca and Bo. The dashed lines are obtained by fitting the simulation results to this equation:

$$Ca = a_3^f (Bo)^{m_3^f}. \quad (5.29)$$

Different markers denote different values of Ω , while different colours denote different values of r_f . From these figures, several interesting observations can be made. First, in general, for

both morphologies, the relation between Ca and Bo is proportional for all fibre radii. This is shown by the fitted m_3^f values: 0.997 ($r_f = 40$, clamshell), 0.996 ($r_f = 20$, clamshell), 0.999 ($r_f = 40$, barrel), and 0.999 ($r_f = 20$, barrel). Second, similar to the partially wetting state, clamshell droplets move faster than barrel droplets for all fibre radii. The a_3^f values are 0.203 ($r_f = 40$, clamshell), 0.310 ($r_f = 20$, clamshell), 0.137 ($r_f = 40$, barrel), and 0.230 ($r_f = 20$, barrel). Thirdly, for the same Bond number, a higher volume results in faster-moving droplets. However, this increase is not proportional to Ω . The difference between $\Omega = 150,000$ and $600,000$ is smaller between $600,000$ and $800,000$. Currently, we do not have a detailed explanation for this phenomenon. One hypothesis is that, in a pseudo-partial wetting state, the viscous dissipation itself is not proportional to Ω/r_f , unlike the partially wetting state. Another hypothesis is the arbitrary criterion to compute the droplet volume introduces inaccuracy during the computation of the Bond number. Currently, the criterion assumes that the droplet and the thin film can be treated as two separate entities with their dynamic. However, as can be seen in Figures 5.12(a) and (b), this assumption is slightly inaccurate because the transition between the droplet wedge and thin film is smooth while at the same time, most of the dissipation is concentrated in this transitioning regime.

5.7 Conclusion

To date, the numerical studies of pseudo-partial wetting are limited compared to partial and fully wetting states. In particular, few have tried to simulate complex solid structures. In this work, I have shown that by incorporating long-range interactions between the fluid and solid, we can introduce fully, partial, and pseudo-partial wetting for arbitrary structures. Both quasi-static and dynamic examples have been simulated using LBM. Because of the relatively simple way of implementing the long-range interaction, this work can also be easily adapted to other lattice Boltzmann models.

However, because this work is still in its early stages, there are still a lot of questions that need to be addressed. The first question is related to the method of coupling the long-range interaction to LBE. In the free-energy model, there are three ways to couple the free-energy terms to the LBE. These are via a forcing term, a pressure tensor term, and a mixture between the two [94]. In this work, I have only used the forcing term method because it is relatively simple to implement. It will be interesting to try implementing the long-range interactions via

the pressure tensor and/or the mixed methods and compare the results with the forcing term method.

Another problem is related to the staircase approximation. As mentioned earlier, there are different models of boundary conditions that can take into account a lattice comprising part fluid and part solid [185, 186, 187]. These methods have been designed to approximate a curved surface better than a staircase approximation. With the current limitation of staircase approximation, I need to fit the numerically integrated \mathcal{V} to a polynomial equation to remove the roughness that is caused by the corners of the solids. This means that one set of a_n^{lrp} is only valid for a set of a , b , σ^{lrp} , ζ^{lrp} , and f_s . A new set of a_n^{lrp} needs to be generated every time the parameters are changed. By coupling this method with advanced boundary conditions [185, 186, 187], hopefully, we can simplify the computation of \mathcal{V} without the worry of numerical artefacts that are caused by staircase approximation. It will also be possible to model a moving boundary [188] with pseudo-partial wetting.

Finally, with our current version of the code, the spurious velocity is still relatively high at low Bond numbers. This causes difficulty in computing the viscous dissipation at low Bond and Capillary numbers because of the artificial velocity gradients caused by the spurious velocity. Currently, there are several different LBMs that can reduce spurious velocities by a significant amount [189, 190, 191]. Incorporating the long-range interaction with these LBM, it is possible to better simulate droplet dynamics with lower Bond and Capillary numbers.

CHAPTER 6

Droplet Impact on Meshed Surfaces

6.1 Introduction

Understanding the impact of droplets on structured surfaces is crucial for various phenomena. In nature, insects, plants, and animals have developed remarkable surface features to control liquid behaviour on their surfaces. Examples include hydrophobic and hydrophilic stripe regions on bamboo leaves [192], asymmetric micro-steps on butterfly wings [193], and hierarchical roughness on lotus leaves [194]. These surface features offer advantages such as self-cleaning [195], self-healing [196], anti-fogging [197, 198], and anti-icing properties [199, 200]. Inspired by these observations, engineered structured surfaces have been developed for applications in fields like inkjet printing [201], flat panel displays [202], and printed circuit boards [203]. Droplet impact manipulation is also utilized in aerosol or spray generation [17], for inhibiting ice formation [204], and in heat transfer applications [205, 206]. Recently, water collection has gained significant interest due to the growing demand for clean water [207, 208]. The dynamics of droplet impact on structured surfaces is a key factor in determining the efficiency of many rains [209, 210, 211, 212] and fog harvesting [15, 213] approaches proposed to date.

The outcome of droplet impact depends on various factors such as impact velocity, direction, size, and droplet surface tension, as well as surface texture, roughness, and wettability [25, 214, 215, 216, 217]. Possible outcomes include droplet bouncing, splashing, captive, and penetration. The relationship between these factors is not yet fully understood, leading to extensive research in this field. For instance, Vaikuntanathan and Sivakumar [218] found that grooved surfaces caused anisotropic behaviour of maximum droplet spreading. Liu et al. [219] demonstrated reduced interaction time through pancake bouncing on multiscale superhydrophobic surfaces.

Pearson, Maynes, and Webb [220] showed that anisotropic surfaces can introduce unusual two-pronged water jets during the droplet spreading phase. Xiao et al. [221] studied droplet impact on surfaces with random roughness and found that such surfaces exhibited a larger spreading ratio and lower contact angle. Henman, Smith, and Kiwari [222] investigated droplet impact on liquid-infused surfaces and discovered that splashing effects can be manipulated by varying the surface textures and the infusing lubricant viscosity. Additionally, Alizadeh et al. [223] observed that the wetting of soft surfaces decreased with reduced elastic modulus, and the influence of viscous dissipation was less pronounced on soft surfaces.

Another key characteristic of interest in the droplet impact phenomena is called interaction time. Typically, the interaction time is defined as the amount of time a droplet is in contact with the solid before it leaves off the surface [224]. After striking the surface, the droplet will spread out to a maximum diameter, before recoiling and leaving the surface [225]. The manipulation of interaction time is important for many applications. A shorter interaction time will encourage bouncing, while a longer interaction time will suppress it. Applications such as anti-icing [204], self-cleaning surfaces [226], and heat-transfer control [227] favour a shorter interaction time, while printing [228], spraying [229], or hazardous fluid handling [230] favour a longer interaction time instead. There are several parameters that can be used to control the interaction time duration. For example, larger droplets generally have a longer interaction time compared to smaller droplets [231]. Complex surfaces such as curved surfaces [164] and crater-like surfaces [232] have shown the capability to reduce interaction time, while mesh or grid-like is able to suppress droplet bouncing [10, 16]. Furthermore, superheating a surface can introduce the so-called Leidenfrost effect, where a thin vapour layer can enhance droplet bouncing [233, 234].

In this chapter, I focus on computationally investigating the dynamics of millimetre-sized droplets impacting meshed surfaces with dimensions comparable to the droplet size. This scenario is crucial to understand as it is commonly encountered in various applications due to the simplicity and effectiveness of mesh design. My motivation stems from the work of von Spreckelsen et al. [13], where they created meshed surfaces using 3D printing inspired by coniferous plant leaves and observed impressive water collection ability. Meshed surfaces have also been used in spray generation [12], digital microfluidics [12], inkjet printing [18], and water-oil separation devices [19, 20]. One of the envisaged use for the meshed surfaces by [13] is for roofing purposes. By layering two or more surfaces, the surface effectively becomes waterproof,

breathable, and light transparent.

To simulate this scenario, I employ the entropic lattice Boltzmann method [42], which allows for capturing complex surface geometries and high-density ratios between the liquid and gas phases. I systematically analyze the penetration, capture, and bouncing behaviour of impacting droplets based on the impact point, trajectory, and velocity. I focus on a millimetre-sized droplet with a similar-sized meshed surface. To characterise the interaction between the droplet and the meshed surface quantitatively, I use two parameters. The first is the incident rate: the number of cases where the droplet will pass through the surface compared to the total number of unique cases. The second one is what I call ‘interaction time’. Because the parameters that I have used suppress droplet bouncing, the term interaction time characterises the time difference between the droplet impact and the droplet passing through the surfaces.

For a single-layer surface, generally, droplets that move orthogonally to the meshed surface can be captured more compared to droplets that move diagonally. The former also tends to have a lower interaction time compared to the latter. I then choose an impact point that exhibits complex behaviours and compare droplet dynamics impacting this point to an equivalent double-layer surface. I find that from a water-capturing capability perspective, a double-layer surface performs worse than its single-layer counterpart, given the same effective pore size. A double-layer surface tends to have more than one unique configurations, which may encourage droplets to pass through the surface from a certain direction. Also, a double-layer surface generally leads to a shorter infraction time compared to a single-layer surface.

This chapter is organized as follows: In Section 6.2, I provide details about the simulation setup and parameters used. Section 6.3 discusses the simulation results for droplets impacting a single layer of meshed surfaces, including variations in trajectory, position, velocity, body force, and size. Section 6.4 compares the effectiveness of single-layer and double-layer meshed surfaces in capturing impacting droplets. Finally, in Section 6.5, I summarise the key findings and present future research directions.

6.2 Methods

6.2.1 The Continuum Model and the Lattice Boltzmann Model

To simulate the impact of droplets on the meshed surfaces, I utilise the entropic lattice Boltzmann method (ELBM) along with the forcing method to simulate the interaction between solid

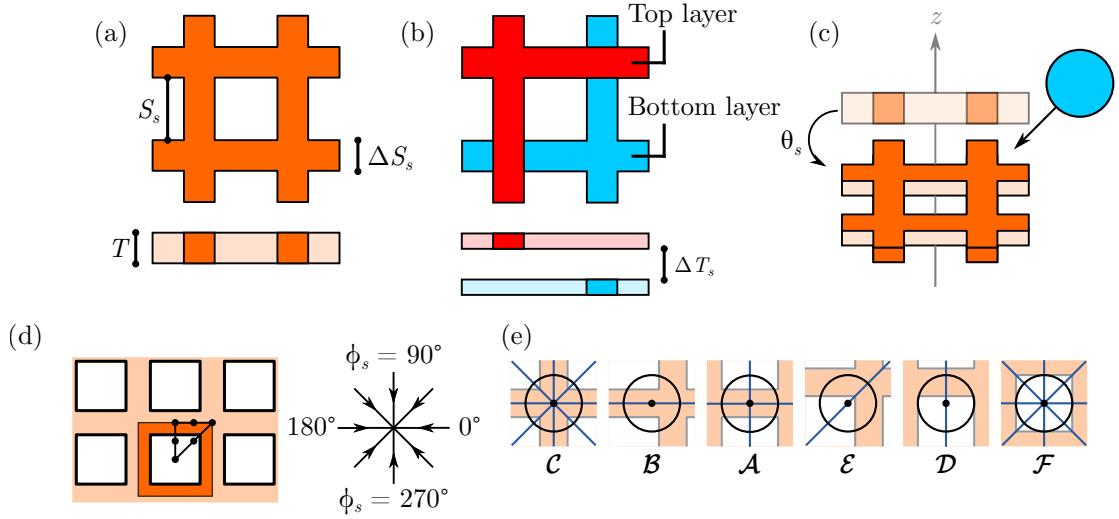


Figure 6.1: (a) A schematic illustration of the single-layer surface with square-shaped pores. S_s represents the pore length, ΔS_s corresponds to the width of the solid bars, and T_s indicates the pore thickness. (b) A double-layer surface designed to be equivalent to (a). ΔT_s represents the separation distance between the top and bottom layers. (c) A schematic of the droplet impacting the surface. θ_s denotes the angle between the surface normal and the z -axis. (d) The top view of the meshed surface. The black dots represent unique impact points that I sample, taking symmetry into account. ϕ_s indicates the direction of droplet impact at a given impact point. (e) Six distinct impact points, ranging from regions with more solid fractions to regions with less solid fractions. The straight lines depict the symmetry axes.

and liquid phases. The detailed methodology can be found in Section 3.3.

6.2.2 The Meshed Surfaces

The meshed surfaces under investigation are depicted in Figure 6.1(a). For simplicity, I assume that the pores are square-shaped with a size of S_s and a thickness of T_s . The width of the solid bars, denoted as ΔS_s , remains constant throughout the surface. In the case of a single-layer surface, I set $S_s = 80$ lattice units (l.u.), $\Delta S_s = 40$ l.u., and $T_s = 10$ l.u., unless otherwise specified. Additionally, I compare the performance of a single-layer surface with that of a double-layer surface, as shown in Figure 6.1(b). For the double-layer surface, I set $S_s = 200$ l.u., $\Delta S_s = 40$ l.u., and $T_s = 5$ l.u. within each layer. These parameter values result in equivalent composite pore size (as observed from the top view) and thickness when compared to the single-layer surface. Furthermore, I introduce another parameter, ΔT_s , which represents the distance between the layers. In the comparative analysis, I consider two ΔT_s values: 20 l.u. and 40 l.u.

6.2.3 The Droplet Impact Parameters

I investigate the impact of droplets on a solid surface at an angle (θ_s, ϕ_s) as illustrated in Figures 6.1(c) and (d). This choice is inspired by experimental observations by von Spreckelsen et al. [13], which revealed diverse and anisotropic dynamics when the impact is at an angle compared to when the impact is parallel ($\theta_s = 0^\circ$) or perpendicular ($\theta_s = 90^\circ$) to the surface. Specifically, I focus on $\theta_s = 30^\circ$ to exemplify the typical behaviours (Figure 6.1(c)). For my analysis, I consider eight values of ϕ_s divided into two sets: the orthogonal set ($\phi_s = \{0^\circ, 90^\circ, 180^\circ, 270^\circ\}$) and the diagonal set ($\phi_s = \{45^\circ, 135^\circ, 225^\circ, 315^\circ\}$).

Taking advantage of the symmetry of the square mesh, I also sample the droplet impact points with respect to the square mesh geometry at six unique locations indicated by the filled circles and labelled as \mathcal{A} – \mathcal{F} in Figures 6.1(d) and (e). Focussing on one unit cell of the surfaces which is indicated by a region with darker colours in Figure 6.1(d), the number of unique directions corresponding to each unique point can be enumerated as follows, where I take into account both the symmetry planes and the number of times each point is repeated in a unit cell.

- \mathcal{A} has three unique directions: 0° (four occurrences), 45° (four occurrences), 90° (four occurrences).
- \mathcal{B} has five unique directions: 0° (eight occurrences), 45° (eight occurrences), 90° (eight occurrences), 135° (eight occurrences), 180° (eight occurrences).
- \mathcal{C} has two unique directions: 0° (eight occurrences) and 45° (four occurrences).
- \mathcal{D} has five unique directions: 0° (eight occurrences), 45° (eight occurrences), 90° (four occurrences), 270° (four occurrences), 315° (eight occurrences).
- \mathcal{E} has five unique directions: 45° (four occurrences), 90° (eight occurrences), 135° (eight occurrences), 180° (eight occurrences), 225° (four occurrences).
- \mathcal{F} has two unique directions: 0° (four occurrences) and 45° (four occurrences).

To quantify the droplet impact velocity and the effect of gravity, I utilise two dimensionless parameters known as the Weber (We) and Bond (Bo) numbers. The Weber number compares the influence of inertia to capillary effects [5], while the Bond number compares the gravitational force to the surface tension force [94]. These quantities are defined by Equations (2.10) and (2.12), respectively. By employing the definition of $D = \Omega^{1/3}$ and considering a droplet radius of 40 l.u., I set We to either 0.542 or 2.169, and vary Bo across the values 0.000, 0.354,

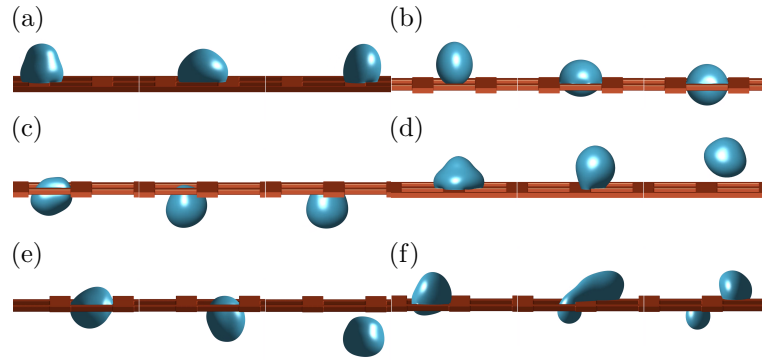


Figure 6.2: The six different outcomes of a droplet impacting a meshed surface: (a) captured on the top of the surface, (b) captured inside the pore, (c) captured underneath the surface, (d) bounce off the surface, (e) passing through the surface, (f) broken up by the surface.

0.707, 1.061, and 1.415. These choices allow me to replicate the typical range of We and Bo values observed in the experiments conducted by von Spreckelsen et al. [13]. For reproduction purposes, the system Reynolds numbers are 392 and 784.

For initialisation, a droplet is equilibrated in a smaller simulation window without any solid for 30,000 time steps to remove any instabilities. It is then transplanted into a new simulation window with a solid structure. Initial velocity and constant acceleration are then assigned such that when the droplet reaches the top of the solid structure, it will have a velocity equivalent to its Weber number.

6.3 Results – Single Layer

When a droplet impacts a flat surface, the resulting behaviour can range from simple deposition to complete rebound [214]. In the case of my meshed surfaces, I have identified six distinct outcomes, which can be categorised into two groups. In the first group, the droplet becomes captured by the surface, either on top, inside a pore, or underneath the surface (Figures 6.2(a), (b), and (c)). The most common scenario is the droplet being captured on the top of the surface, while the other cases are typically observed in zero or low-gravity environments. In the second group, the droplet passes through the surface. The droplet can simply bounce off the surface (Figure 6.2(d)), which is typically observed in zero or low-gravity environments. The droplet can also slide into or pass through a pore (Figure 6.2(e)). If the impact velocity and/or gravity are sufficiently high, the surface can even break the droplet up (Figure 6.2(f)).

Due to limited computational resources, each data point is simulated for a restricted time frame, typically 40,000 time steps. In most cases, the interaction between the droplet and the

Table 6.1: The incident rates of droplets passing through the meshed surfaces.

		Orthogonal	Orthogonal (%)	Diagonal	Diagonal (%)
\mathcal{A}	We = 6.72	12/40	30%	8/20	40%
	We = 26.88	16/40	40%	8/20	40%
\mathcal{B}	We = 6.72	8/120	6.67%	48/80	60%
	We = 26.88	8/120	6.67%	64/80	80%
\mathcal{C}	We = 6.72	0/40	0%	12/20	60%
	We = 26.88	0/40	0%	16/20	80%
\mathcal{D}	We = 6.72	48/80	60%	48/80	60%
	We = 26.88	60/80	75%	40/80	50%
\mathcal{E}	We = 6.72	24/80	30%	48/80	60%
	We = 26.88	24/80	30%	56/80	70%
\mathcal{F}	We = 6.72	16/20	80%	16/20	80%
	We = 26.88	20/20	100%	20/20	100%
	Total	236/760	31.05%	384/600	64.00%

meshed surface could be observed within this time frame. However, for certain scenarios, the interaction required a longer duration. Unless specifically stated, the final observed outcomes are based on the time frame of 40,000 time steps.

In Table 6.1, I have tabulated the outcomes of my simulations, indicating the incident rates of droplets passing through the surfaces and droplets separated into two smaller droplets, relative to all possible cases. The data presented include results for both the orthogonal and diagonal sets, with further categorization based on different impact points and impact velocities (represented by the Weber number). Each velocity data point is obtained for all five different body forces (Bond number).

Overall, it is observed that droplets are more likely to exit the surface when they approach from a diagonal direction. This behaviour is consistent across a number of impact points: \mathcal{C} (where the orthogonal impact always hits the solid bar), \mathcal{B} , and \mathcal{E} . However, at impact point \mathcal{D} , the pattern alternates, where the incident rate is higher when the droplet is approaching from an orthogonal direction. At impact points \mathcal{A} and \mathcal{F} , the difference between the orthogonal and diagonal approaches is not significant.

Figures 6.3(a) and (b) present histograms depicting the duration of droplet interaction with the surfaces before they exited. The x -axis represents the interaction time, while the y -axis

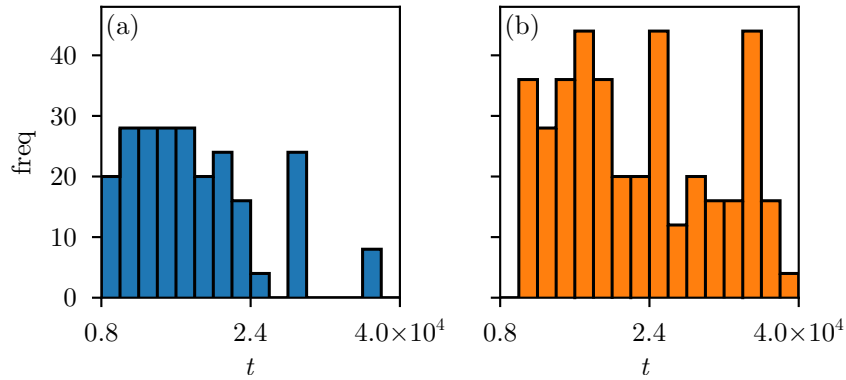


Figure 6.3: (a,b) Histograms for orthogonal and diagonal velocity sets, respectively. The x -axis represents the interaction time between the droplets and the solid surfaces, while the y -axis indicates the frequency of the cases. The bin width is set to 2,000 time steps.

displays the frequency of occurrences. Figure 6.3(a) displays the data for orthogonal sets, while Figure 6.3(b) displays the data for diagonal sets. The bin width is set at 2,000 time steps since the results are recorded every 500 time steps.

In the case of orthogonal sets, the interaction time is primarily concentrated within the range of 8,000 to 24,000 time steps, without any distinct peaks. This indicates that the interaction in orthogonal sets is relatively rapid and can be observed within a comparatively shorter time frame. On the other hand, for diagonal sets, the interaction time spans a wider range from 10,000 to 40,000 time steps, exhibiting peaks at approximately 16,000 to 18,000, 24,000 to 26,000, and 34,000 to 36,000 time steps.

6.3.1 Orthogonal Direction

When ϕ_s belongs to the orthogonal set, the final outcome of the droplet impact is relatively predictable. Let us first define two types of droplet movement: parallel and perpendicular to the solid bar. A droplet exhibits a ‘parallel’ movement when its trajectory aligns with the solid bar beneath it (Figures 6.4(a) and (b)). The droplet may impact the centre of the solid bar (Figure 6.3(a)), or it may be offset from the solid bar (Figure 6.3(b)), but the general direction of the droplet is alongside the solid bar. In contrast, in Figures 6.3(c) and (d), while the droplet impact point is similar to Figures 6.3(a) and (b), the droplet’s direction is perpendicular to the solid bar. I refer to these as a ‘perpendicular’ movement.

For impact point \mathcal{C} , when the droplet hits the centre of the junction, we observe that regardless of the direction ($\phi_s = \{0^\circ, 90^\circ, 180^\circ, 270^\circ\}$), the droplet remains on the solid bar and always moves parallel to the solid bar direction. The capillary force between the droplet

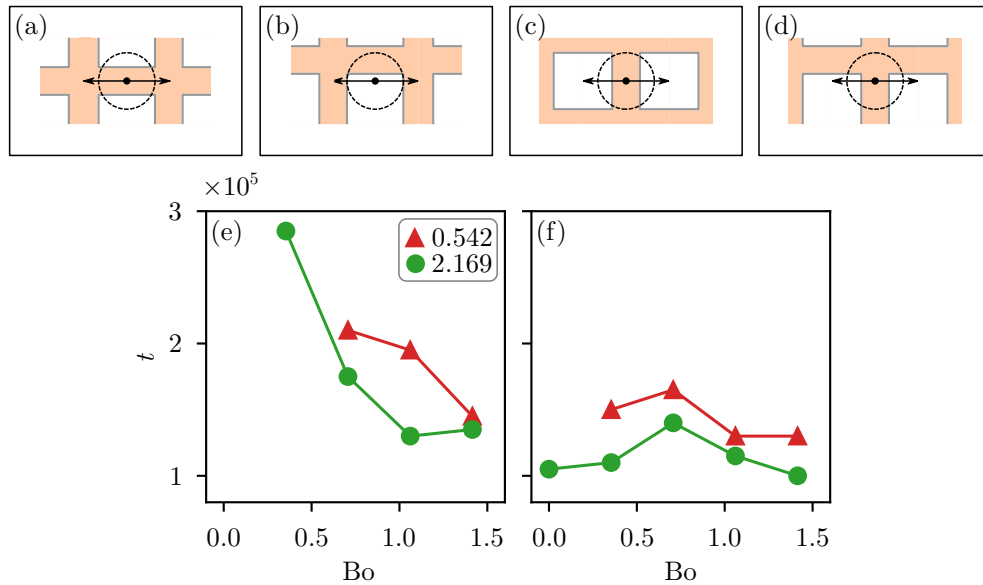


Figure 6.4: (a,b) Illustrations of ‘parallel’ droplet movement. (c,d) Illustrations of ‘perpendicular’ droplet movement. (e,f) Graphs showing interaction time (the duration between the droplet impact and the droplet passing through the surface) as a function of Bond number (Bo) for impact points \mathcal{A} and \mathcal{F} , respectively. The triangle markers correspond to the Weber number (We) of 0.542, while the circle markers correspond to $We = 2.169$.

and the solid bar is sufficiently strong to maintain their contact. As a result, the droplet never leaves the surfaces. This outcome is also observed for impact points \mathcal{A} and \mathcal{B} when $\phi_s = \{0^\circ, 180^\circ\}$. At impact point \mathcal{B} , the droplet movement is a combination of both parallel and perpendicular motion to the solid bar for $\phi_s = \{90^\circ, 270^\circ\}$, but the parallel movement still dominates. The simulation results show that the droplet only leaves the meshed surface at a high Bond number.

For impact point \mathcal{A} when $\phi_s = \{90^\circ, 270^\circ\}$ and impact point \mathcal{F} for all directions, droplet motion perpendicular to the solid bar dominates. Droplets start to pass through the impact point \mathcal{F} at a lower Bond number because the impact point is centred at the pore, instead of a solid bar for impact point \mathcal{A} . Nevertheless, in both cases, increasing the impact velocity decreases the time at which the droplet leaves the surface (Figures 6.4(e) and (f)). The effects of the body force, however, are slightly different. Increasing the body force at \mathcal{A} reduces the interaction time between the droplet and the meshed surface. At \mathcal{F} , the interaction time peaks at $Bo = 0.707$ before decreasing. This is because after the droplet enters the pore, it encounters resistance from the solid bar. At low or middle Bond numbers, the middle of the droplet is pinned by the solid bar. However, at a higher Bond number, the pinning site move to the top half of the droplet, therefore reducing resistance during pinning which also reduces interaction

time.

The impact point \mathcal{E} is dominated by perpendicular droplet motion because the impact point is close to the solid junction. Generally, there are two groups of movement for \mathcal{E} . The first one is when the droplet is moving towards the solid junction, which can be seen for $\phi_s = \{180^\circ, 270^\circ\}$. The second one is droplet movement away from the junction, which can be observed for $\phi_s = \{0^\circ, 90^\circ\}$. The incident rate is zero when the droplet is moving towards the junction, because the junction will increase the droplet-solid contact area, therefore increasing the capillary force between the droplet and the solid and stabilising the droplet movement.

The impact point \mathcal{D} can be treated as the transition between impact positions \mathcal{A} and \mathcal{F} . When the droplet direction is $\phi_s = \{0^\circ, 180^\circ\}$, similar to point \mathcal{A} , the droplet movement is still mostly parallel. However, because there is less solid underneath it, there is less capillary force between the droplet and the solid, therefore lowering the minimum Bo needed to pass through the surface and increasing the incident rate compared to \mathcal{A} . Also, unlike impact point \mathcal{A} , impact point \mathcal{D} is asymmetric when $\phi_s = \{90^\circ, 270^\circ\}$. The droplet is moving away from the solid bar when $\phi_s = 90^\circ$, and moving towards the solid bar when $\phi_s = 270^\circ$. This asymmetry is causing a higher incident rate for $\phi_s = 90^\circ$. Overall, the percentage of the incident rate for impact point \mathcal{D} is located in-between impact points \mathcal{A} and \mathcal{F} .

6.3.2 Diagonal Direction

As demonstrated in Table 6.1 and Figure 6.3(b), the incident rates of droplets entering the surface are generally higher for diagonal trajectories compared to orthogonal trajectories. Furthermore, the interaction time is more widely distributed for diagonal trajectories in comparison to orthogonal trajectories. These contrasting behaviours can be attributed to the inherently more complex nature of droplet movement on a diagonal trajectory as opposed to an orthogonal one. To gain a better understanding, let us examine Figures 6.5(a) and (b), which depict different cross-sectional views of a droplet on top of the solid bar. In this context, the arrow in the y direction represents parallel movement, while the arrow in the x direction represents perpendicular movement. Additionally, there is also droplet motion in the z direction, especially when the droplet passes through into the surface.

In the case of orthogonal trajectories, we only have motion in the x and z directions (i.e. 0° and 180°) or motion in the y and z directions (i.e. 90° and 270°). Consequently, although both parallel and perpendicular movements may initially occur during the impact sequence,

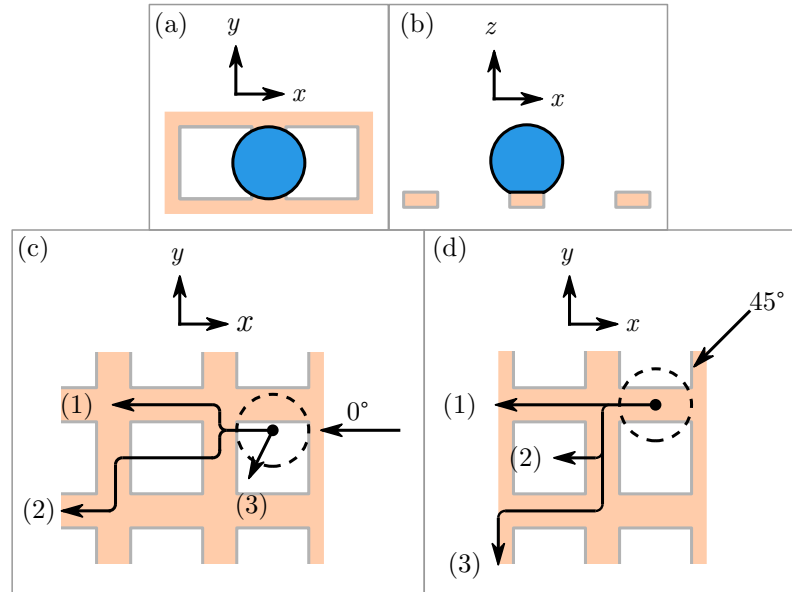


Figure 6.5: (a,b) The cross-sections of droplets in the x - y and x - z planes, respectively. (c) Three possible trajectories of a droplet hitting impact point \mathcal{D} from the direction of 0° . (d) Three possible trajectories of a droplet hitting impact point \mathcal{A} from the direction of 45° .

one of the two tends to be suppressed. For instance, consider Figure 6.5(c), which illustrates three general trajectories of a droplet impacting the \mathcal{D} point at a 0° direction. At low Bond numbers, the droplet follows trajectory (1), striking the vertical bar (parallel to the y -axis) before being pulled towards the horizontal bar (parallel to the x -axis) by the junction. At medium Bond numbers, the droplet moves along the negative y direction along the vertical bar, crosses over the pore, and gets captured by the second horizontal bar (trajectory (2)). At very high Bond numbers, the gravitational acceleration in the z direction is substantial enough to pull the droplets directly down into the pore before they can be intercepted by the surface (trajectory (3)).

For diagonal directions, both parallel and perpendicular movements have an influence on the final trajectory of the droplet, and neither is suppressed. In Figure 6.5(d), I illustrate the typical trajectories of droplets hitting impact point \mathcal{A} from a direction of 45° . At low Bond numbers (trajectory (1)), the droplets can be captured because the component of the gravitational acceleration in the y direction is small enough to suppress the perpendicular movement. However, at medium and high Bond numbers, this force becomes significant, allowing the droplets to move alongside the solid bar. At medium Bond numbers, the droplets are pulled into the pore by the gravitational force in the x direction (trajectory (2)). At high Bond numbers, both force components in the x and y directions are strong enough that the

Table 6.2: Two main groups of interaction time for diagonal movements.

Increasing Bo \rightarrow reducing interaction time					
We	Impact Pos.	ϕ_s	We	Impact Pos.	ϕ_s
0.542	\mathcal{B}	$\{45^\circ, 135^\circ\}$	0.542	\mathcal{E}	$\{45^\circ\}$
2.169	\mathcal{B}	$\{45^\circ, 135^\circ\}$	0.542	\mathcal{E}	$\{135^\circ, 315^\circ\}$
0.542	\mathcal{C}	$\{45^\circ, 135^\circ, 225^\circ, 315^\circ\}$	2.169	\mathcal{E}	$\{45^\circ\}$
0.542	\mathcal{D}	$\{45^\circ, 135^\circ\}$	2.169	\mathcal{E}	$\{225^\circ\}$
2.169	\mathcal{D}	$\{45^\circ, 135^\circ\}$	0.542	\mathcal{F}	$\{45^\circ, 135^\circ, 225^\circ, 315^\circ\}$
			2.169	\mathcal{F}	$\{45^\circ, 135^\circ, 225^\circ, 315^\circ\}$

Increasing Bo \rightarrow increasing interaction time		
We	Impact Pos.	ϕ_s
0.542	\mathcal{B}	$\{135^\circ, 225^\circ\}$
2.169	\mathcal{B}	$\{135^\circ, 225^\circ\}$
0.542	\mathcal{C}	$\{45^\circ, 135^\circ, 225^\circ, 315^\circ\}$

droplets do not enter the first pore and instead skirt around it (trajectory (3)).

Although the droplet trajectories in the diagonal direction are more complex compared to the orthogonal direction, I have observed two main groups of interaction time when the droplet has passed through the surface. The first group is the most common, where the interaction time between the droplet and the surface decreases as the Bond number (Bo) increases. This implies that heavier droplets leave the surfaces faster, which aligns with our general expectation that they are more difficult to be captured by the solid surfaces. In total, I found twenty-five directions with this trend, which I have tabulated in Table 6.2. For example, Figures 6.6(a) and (b) depict the effect of the Bond number on the interaction time with a direction of 45° for impact points \mathcal{B} and \mathcal{D} , respectively.

The second group exhibits the opposite behaviour, where increasing the Bond number also increases the interaction time. This group consists of eight directions. For example, Figure 6.6(c) displays the interaction time versus Bond number for impact point \mathcal{B} at 135° . In this group, the droplets typically enter the pores relatively early. However, due to the trajectory of the droplets, the droplets become pinned inside the pores, before being able to pass through the surfaces. Since the pinning occurs early in the interaction, increasing the Bond number does not alter the droplet trajectory. Instead, the droplets remain pinned for a longer duration

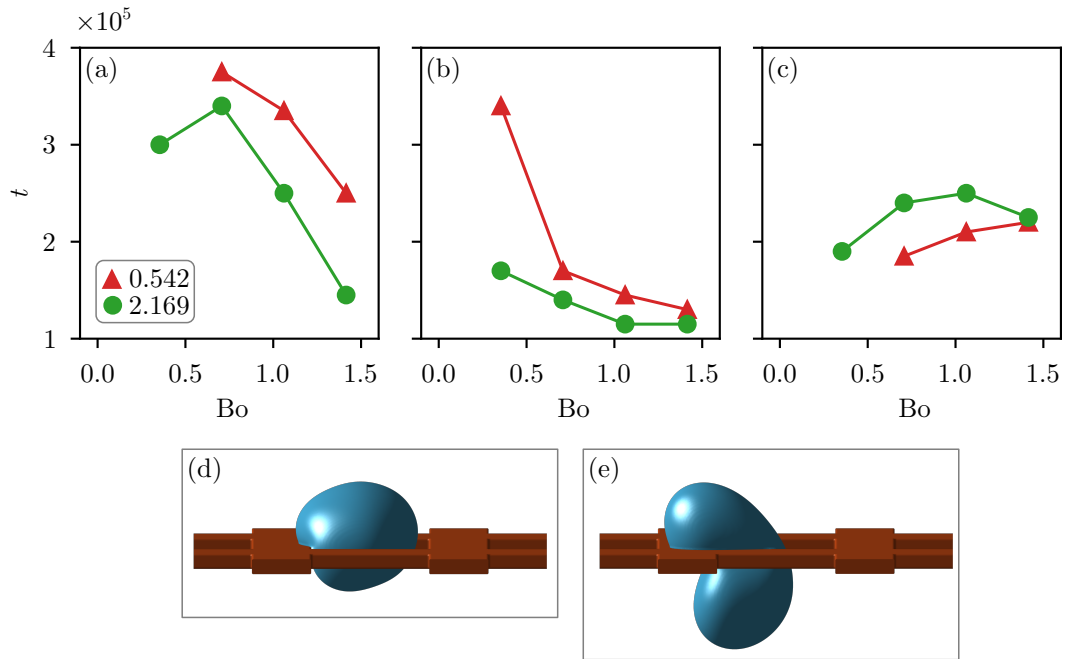


Figure 6.6: (a,b,c) The interaction time as a function of Bond number at impact point \mathcal{B} , $\{45^\circ\}$; \mathcal{D} , $\{45^\circ\}$; and \mathcal{B} $\{135^\circ\}$, respectively. (d,e) Droplets pinned at the inside of the pore when $Bo = 0.354$ and 0.707 , respectively. The impact point is \mathcal{D} with $We = 2.169$.

due to deformation around the surface thickness. Figures 6.6(d) and (e) depict a droplet being pinned for different Bond numbers.

6.4 Results – Double Layer

In this section, I aim to compare the differences between single-layer and double-layer surfaces. Based on the results from Section 6.3, I will focus on impact point \mathcal{D} , which shows a richer behaviour of orthogonal movements compared to other impact points. Compared to impact point \mathcal{E} , the solid junction is relatively far from the impact point, therefore it will have less effect on the initial parallel movement. On the other hand, compared to \mathcal{A} and \mathcal{F} , the perpendicular movement is more complex because the impact point is halfway between the pore and the solid bar. As discussed in Section 6.2, the double-layer surface is designed in such a way that, when viewed from the top, the composite surface is equivalent to its single-layer counterpart (Figure 6.7). I have identified two unique impact points for double-layer surfaces that correspond to the composite of a single-layer \mathcal{D} impact point. I denote these as configuration (1), illustrated in Figure 6.7(a), and configuration (2), illustrated in Figure 6.7(b). Additionally, I have varied the separation distance between the two layers, using $\Delta T_s = 20$ and $\Delta T_s = 40$, which correspond to $r_d/2$ and r_d , respectively. Here, r_d represents the droplet radius.

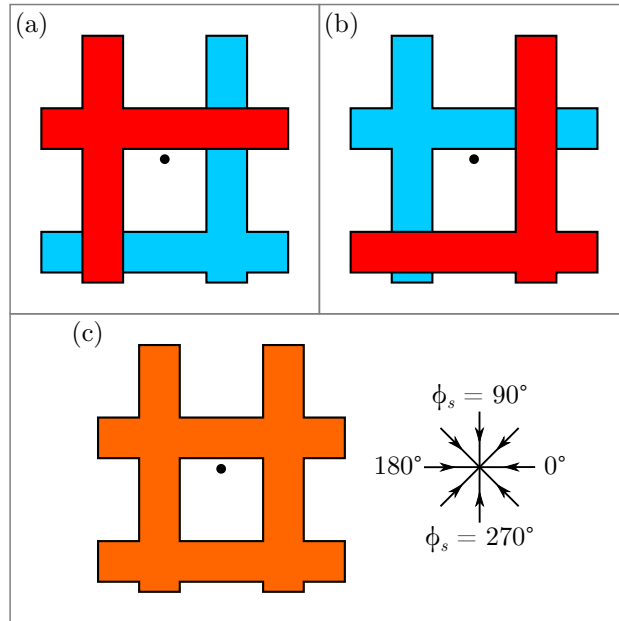


Figure 6.7: (a,b) Double-layer surfaces described as configuration (1) and (2), respectively. The surface coloured in red is located on top of the blue-coloured one. (c) A single-layer surface with an equivalent composite seen from the top.

In Tables 6.3 and 6.4, I provide a summary of the incident rates of the double-layer setup. This includes cases where the droplets pass through the surfaces as well as cases where the droplets are separated into two smaller droplets. The orthogonal and diagonal sets each consist of four members, the same as in the single-layer setup. I also use the same groups of Weber and Bond numbers as in the single-layer setup. I use $We = 0.542$ and 2.169 , and I use $Bo = 0.000, 0.354, 0.707, 1.061,$ and 1.415 . Therefore, taking into account all groups of Bond numbers, each Weber number will have a total of forty possible cases (five $Bo \times$ (four orthogonals + four diagonals)). However, because both configurations have an equal probability to form a similar single-layer composite, I am going to sum the incident cases of both configurations (i.e. eighty probable cases instead of forty) when comparing the effects of ΔT_s .

Overall, the double-layer setup performs slightly worse than its single-layer counterpart. At $We = 0.542$, the incident rates when the droplets are leaving the surface are $24/40$, $50/80$, and $49/80$ for the single-layer configuration, double-layer configuration with $\Delta T_s = 20$, and double-layer configuration with $\Delta T_s = 40$, respectively. At $We = 2.169$, the rates are $28/40$, $54/80$, and $57/80$ for the single-layer configuration, double-layer configuration with $\Delta T_s = 20$, and double-layer configuration with $\Delta T_s = 40$. Comparing each configuration directly, however, shows that configuration (1) is consistently performing better than the single-layer surface. The incident rates are $24/40$ (single), $23/40$ ($\Delta T_s = 20$), and $23/40$ ($\Delta T_s = 40$) for $We =$

0.542; and 28/40 (single), 24/40 ($\Delta T_s = 20$), and 26/40 ($\Delta T_s = 40$) for $We = 2.169$. On the contrary, configuration (2) performs worse for all Weber numbers. These are 27/40 ($\Delta T_s = 20$) and 26/40 ($\Delta T_s = 40$) for $We = 0.542$; and 30/40 ($\Delta T_s = 20$) and 31/40 ($\Delta T_s = 40$) for $We = 2.169$.

Figure 6.8 depicts the distribution of interaction time for $We = 0.54$. A single-layer surface has a more uniform distribution of interaction time compared to a double-layer surface. Interaction time between 16,000 and 18,000 time steps occur the most (four droplets passing through with these interaction times), and the second highest interaction times are 10,000 – 12,000, 12,000 – 14,000, and 14,000 – 16,000 time steps, each with three droplets. For the double-layer surface, configuration (1) at $\Delta T_s = 40$ shows similar behaviour to the single-layer surface, where the interaction time distribution is relatively uniform. For the other cases, the distributions are more biased towards lower interaction time. The maximum frequency of the droplet passing through is also higher for a double-layer surface: five (conf. (1) and (2), $\Delta T_s = 20$) and six (conf. (2), $\Delta T_s = 40$), compared to four for the single-layer surface and the double-layer surface (conf. (1) with $\Delta T_s = 40$).

Figure 6.9 shows the histograms for $We = 2.169$. Compared to the lower Weber number, the single-layer surface has a less uniform interaction time distribution with two peaks. The first peak happens at interaction times of 8,000 – 10,000 time steps with nine droplets passing through, while the second peak happens at interaction times of 28,000 – 30,000 time steps with five droplets. The double-layer surfaces, on the other hand, is keeping the distribution shape while only increasing the amount of the incident rates. Configuration (2) has a higher peak compared to configuration (1): two bins with five cases each ($\Delta T_s = 20$) and one bin with nine cases ($\Delta T_s = 40$). Both are seen at lower interaction time (less than 16,000 time steps). Configuration (1) peaks consist of one bin with five cases for $\Delta T_s = 20$ and one bin with four cases, with three more bins each having three cases, for $\Delta T_s = 40$.

From the tables and histograms, we can conclude that configuration (1) generally performs better than its single-layer counterpart, while configuration (2) shows higher incident rates of droplets passing through the surfaces, and these incidents occur more rapidly compared to the other configuration. The poorer performance of configuration (2) is the primary reason for the overall inferior performance of the double-layer surfaces compared to the single-layer surface.

The poorer performance of configuration (2) compared to configuration (1) can be attributed to the location of the solid bars. In configuration (1), the solid bar is situated near

Table 6.3: The incident rate of droplets passing the meshed surfaces for impact point \mathcal{D} at $We = 0.542$.

		single	$\Delta T_s = 20$ (1)	$\Delta T_s = 20$ (2)	$\Delta T_s = 40$ (1)	$\Delta T_s = 40$ (2)
Bo = 0	ortho.	0/4	0/4	1/4	0/4	1/4
	diag.	0/4	0/4	1/4	0/4	1/4
Bo = 0.354	ortho.	2/4	2/4	1/4	1/4	2/4
	diag.	2/4	1/4	3/4	1/4	2/4
Bo = 0.707	ortho.	2/4	3/4	2/4	2/4	2/4
	diag.	2/4	2/4	4/4	3/4	3/4
Bo = 1.061	ortho.	4/4	3/4	3/4	4/4	3/4
	diag.	4/4	4/4	4/4	4/4	4/4
Bo = 1.415	ortho.	4/4	4/4	4/4	4/4	4/4
	diag.	4/4	4/4	4/4	4/4	4/4
Total		24/40	23/40	27/40	23/40	26/40

Table 6.4: The incident rate of droplets passing the meshed surfaces for impact point \mathcal{D} at $We = 2.169$.

		single	$\Delta T_s = 20$ (1)	$\Delta T_s = 20$ (2)	$\Delta T_s = 40$ (1)	$\Delta T_s = 40$ (2)
Bo = 0	ortho.	1/4	1/4	1/4	1/4	1/4
	diag.	0/4	0/4	2/4	0/4	2/4
Bo = 0.354	ortho.	4/4	2/4	2/4	2/4	2/4
	diag.	3/4	1/4	3/4	1/4	4/4
Bo = 0.707	ortho.	4/4	3/4	3/4	3/4	3/4
	diag.	3/4	3/4	4/4	4/4	4/4
Bo = 1.061	ortho.	2/4	3/4	3/4	3/4	3/4
	diag.	4/4	3/4	4/4	4/4	4/4
Bo = 1.415	ortho.	4/4	4/4	4/4	4/4	4/4
	diag.	3/4	4/4	4/4	4/4	4/4
Total		28/40	24/40	30/40	26/40	31/40

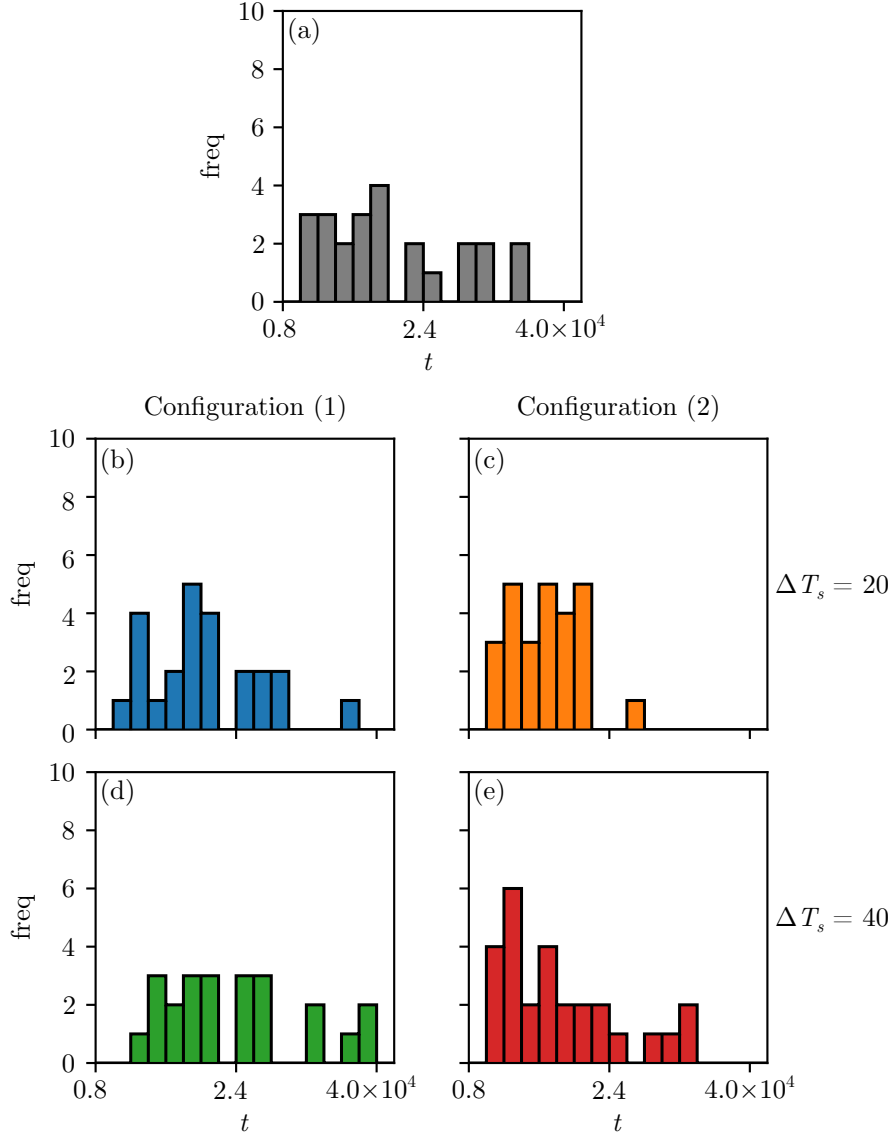


Figure 6.8: Histograms of interaction time for impact point \mathcal{D} and Weber number 0.542. The solid configurations are: (a) single-layer; (b,c) $\Delta T_s = 20$, configuration 1 and 2; (d,e) $\Delta T_s = 40$, configuration 1 and 2.

the impact point, as indicated by the small dot (Figure 6.7(a)). This implies that for most directions, this configuration will behave similarly to the single-layer variant, where the top layer has a chance to capture the droplets whose directions are $\phi_s = \{225^\circ, 270^\circ, 315^\circ\}$. In the second layer, the solid surface is also located in a good position to capture a droplet that has passed through the first layer, specifically when $\phi_s = \{45^\circ, 90^\circ, 135^\circ\}$. These are the reasons why configuration (1) generally performs better than a single-layer surface.

Configuration (2) swaps the solid bar locations of configuration (1). With configuration (2), the second layer is able to capture droplets moving in directions of $\phi_s = \{225^\circ, 270^\circ, 315^\circ\}$ at lower Bond numbers. However, the solid bar in the first layer is located too far from the

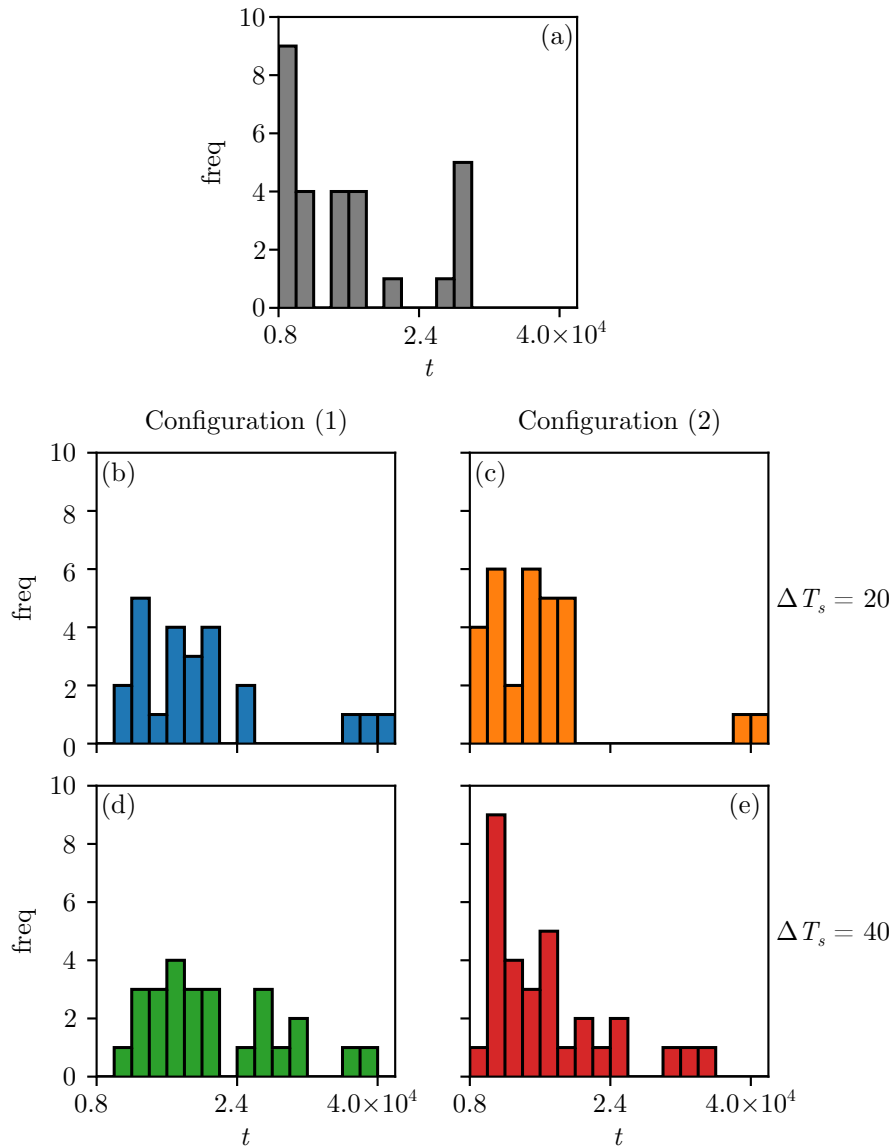


Figure 6.9: Histograms of interaction time for impact point \mathcal{D} and Weber number 2.169. The solid configurations are: (a) single-layer; (b,c) $\Delta T_s = 20$, configuration 1 and 2; (d,e) $\Delta T_s = 40$, configuration 1 and 2.

impact point, therefore offering almost zero resistance for droplets that are moving from $\phi_s = \{45^\circ, 90^\circ, 135^\circ\}$ to pass through the surface even at very low Bond numbers. My simulations suggest this is the main contributor to the worse performance of configuration (2).

Regarding the similarity of outcomes for the two values of ΔT_s , each ΔT_s introduces its unique interactions, such as pinning by the two layers for $\Delta T_s = 20$ (Figure 6.10(a)) and droplet squeezing for $\Delta T_s = 40$ (Figure 6.10(b)). However, neither of these interactions has significantly affected the droplet movement. Pinning can capture a smaller droplet or a droplet moving at a lower velocity, but it can be bypassed by a large droplet or a fast-moving droplet. On the other hand, a larger gap can redirect droplet movement to be captured by the solid

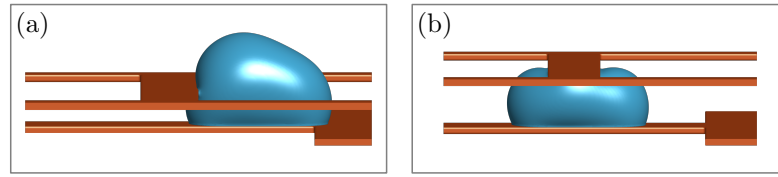


Figure 6.10: (a) A droplet being pinned on a double-layer configuration with $\Delta T_s = 20$. (b) A droplet being squeezed on a double-layer configuration with $\Delta T_s = 40$. For both figures, $\phi_s = 0^\circ$, $Bo = 0.354$, and $We = 0.542$.

surface, but the precise outcome depends on numerous variables. Therefore, on average, the outcome appears to be more similar. This observation aligns with findings by von Spreckelsen et al. [13], where, for relatively small gaps (e.g. they used less than 6 mm, which is close to a raindrop diameter), the increase in droplet penetration is not significant.

6.5 Conclusion and Future Works

In this chapter, the outcomes of droplet impacts on square meshed surfaces were investigated, with a focus on different impact points and droplet trajectories. Two sets of trajectories were considered: orthogonal trajectories when the direction is a multiple of 90° relative to the orientation of the solid bars, and diagonal trajectories when the direction is an odd multiple of 45° . Generally, orthogonal trajectories exhibited a lower rate of droplets leaving the surface compared to diagonal trajectories. This is because, with orthogonal trajectories, the droplet tends to adopt either a parallel movement (alongside the solid bar) or a perpendicular movement (into the pore). Depending on the impact points, both movements can contribute, although one is typically suppressed. When the perpendicular movements dominate, the droplet can pass through the surfaces. In contrast, diagonal trajectories are more unpredictable, as both movements contribute equally and neither is suppressed. We find these result in higher incident rates compared to orthogonal trajectories.

The outcomes of single-layer and double-layer surfaces with equivalent composite shapes were also compared. In terms of water-capturing capability, the double-layer surface performed worse than its single-layer counterpart. Due to its two-layer surface, there are two possible configurations. Even though one configuration can perform better than a single-layer surface, the other one performs worse, therefore reducing the overall performance of double-layer surfaces. The effects of surface separation were found to be minimal within a small range of values considered here ($\Delta T_s = r_d/2$ and $\Delta T_s = r_d$). While it is performing worse, double-layer sur-

faces offer more flexibility with additional parameters that can be tuned such as the separation distance and different wetting states for different layers.

This work opens up several avenues for further investigation. Firstly, the use of smooth meshed surfaces in this study eliminates the effects of contact line pinning on the solid bars. Exploring the impact of surface roughness on the overall behaviour would be interesting. Secondly, varying the pore shape can provide additional insights. For square pores, orthogonal trajectories are preferable, as droplets moving parallel to the solid bar have a higher chance of capture, compared to those with diagonal trajectories. Compared to a square pore, von Spreckelsen et al. [13] found that a rhombus pore with an opening angle of 45° performs better. It is hypothesized that with a 45° pore, it is easier to suppress the contribution of perpendicular movement to a smaller range of angles, thereby increasing the probability of capture. However, this shape does not eliminate penetration, as there is still a window of direction where droplets can enter the surfaces. Exploring the design of pore shapes that significantly narrow this window would be valuable. Finally, the effects of the droplet-to-pore size ratio were not assessed. It would be interesting to investigate how different impact points interact with droplets of varying sizes moving from various directions in both single and double-layer surfaces.

CHAPTER 7

Conclusions and Future Works

7.1 Conclusion

Given their ubiquitous role in nature and industry, fibres and fibrous materials have attracted significant scientific interest. In particular, here, I focussed on their interactions with liquid droplets. In this work, I employ the numerical solver lattice Boltzmann method (LBM) to systematically study the interaction between liquid droplets and different solids. Specifically, I focussed on droplet wetting, spreading, and moving across fibres, as well as droplet impact on meshed surfaces.

In Chapter 4, I have modelled a system of a droplet moving on a fibre where the applied force is parallel to the fibre length. I took into account two droplet morphologies: barrel and clamshell morphologies. By varying the droplet Bond number and the fibre radius, three distinct dynamic regimes can be observed for the clamshell morphology: compact droplet, droplet breakup, and droplet oscillation. The compact droplet regime is characterised by a steady state shape. Depending on the size of the droplet relative to the fibre radius (L_R), there are two distinct regimes related to the Capillary number (Ca , representing the droplet velocity) and the Bond number (Bo , representing the droplet body force). When $L_R < 1.0$ (i.e. when the droplet radius is smaller than the fibre radius), Ca is only proportional to Bo . On the other hand, when $L_R > 1.0$ (i.e. when the droplet radius is larger than the fibre radius), Ca is proportional to both Bo and L_R . When the Bond number is high, the droplet separates into two parts connected by a liquid filament. Smaller fibre radii will increase the filament length and narrow the filament width, therefore making it more unstable (droplet breakup regime). However, if the fibre radii are large enough, the filament can be stabilised, therefore causing

a periodic contraction and separation of the front and the rear droplet (droplet oscillation regime).

Unlike fully and partial wetting states, the pseudo-partial wetting state is less known. In pseudo-partial wetting, both the spherical cap droplet and the thin film can coexist together, with the droplet sitting on top of the thin film. Since few numerical methods are able to simulate this quasi-statically and dynamically, in Chapter 5, I implemented long-range interactions between the fluid and solid in LBM. To show the robustness of this method, I simulated different scenarios, starting from fully and partial wetting states for simple flat surfaces. Both analytical and numerical derivations have been used and compared, and good agreement between these two implementations has been found. Next, using a different form of long-range interactions, I simulate droplet spreading on pseudo-partial wetting flat surfaces and grooved structures. I also found a good agreement of the steady state shape of droplets on grooved structures with the work of Oktasendra, et al. [184]. Finally, I simulate spreading and moving droplets along a fibre in the pseudo-partial wetting state. Both barrel and clamshell morphologies have been successfully simulated. Preliminary results showed that the relation between Bo and Ca is proportional for various droplet volumes and fibre radii, similar to the fully and partial wetting regimes.

Finally, in Chapter 6, I focussed on the dynamics of droplets impacting meshed surfaces. Inspired by the work of von Spreckelsen et al. [13], I systematically varied the impact point, trajectory, and velocity of droplets impacting square meshed surfaces. Here, I used two parameters to quantitatively characterise the interaction between the droplet and the structure: the incident rates and the interaction time. The incident rates measure the number of cases where the droplets could pass through the structure, while the interaction time measures the time differences between the droplet impact and the droplet leaving the structures. The results are rationalised by considering whether the droplet trajectory is dominated by orthogonal movement (when the direction is a multiple of 90°) or diagonal movement (when the direction is an odd multiple of 45°). Orthogonal movements tend to have a lower incident rate and a more uniform interaction time distribution. Conversely, diagonal movements are more complex with less predictability. Later, by focussing on an impact point, I compared the droplet dynamics impacting on a single-layer structure and on equivalent double-layer structures. Given the same effective pore size, a double-layer structure tends to have higher incident rates and shorter interaction times. While it performs worse for water capturing, double-layer structures offer

more flexibility with additional parameters that can be tuned, such as the separation distance and different wetting states for different layers.

7.2 Future Works

There are many directions in which this project can be taken forward. Here, I will focus on two examples where the developed numerical methods in this thesis are well-positioned to tackle: modelling pseudo-partial wetting for complex geometries and modelling meshed surfaces for oil-water separation.

7.2.1 Pseudo-partial Wetting for Complex Geometries

Presently, most of the work on long-range interactions has only been done for simple flat surfaces or surfaces with roughness much smaller than the droplet size [171, 175, 176, 235, 183, 49]. Therefore, it will be interesting to combine long-range interactions modelling with different structures. For example, Oktasendra et al. [184] have shown that when liquid is filling grooved structures, different wetting states have different filling transitions. For a fully wetting state, the thin film will first follow the grooved structures, filling the gap between the ridges, then fully submerging the groove. On the other hand, for partially wetting states, the liquid will fill the gap between the ridges, before getting pinned at the top edge of the ridge while keeping its meniscus shape. Pseudo-partial wetting shows unique filling behaviour. At the beginning, it will follow the fully wetting state, where the liquid thin film will follow the grooved structure, before filling the gap between the ridges completely. After that, the liquid will coalesce above the gap, while keeping a layer of the thin film above the ridge.

Other interesting surface structures that can be explored are post geometries and reentrant geometries. For post-like geometries [64], at least four wetting states can be observed: Wenzel, Cassie-Baxter, hemi-wicking (i.e. when a precursor film spreads first), and a mixed Wenzel and Cassie-Baxter state. Hydrophobic surfaces tend to only have Wenzel or Cassie-Baxter states, while hydrophilic surfaces tend to have Wenzel and hemi-wicking states. To understand the dynamic transition between the states, the energy loss due to dissipation needs to be considered. In Chapter 5, my preliminary data indicates that the dissipation profile of pseudo-partial wetting is different from partial wetting due to the fact that the contact line is more ambiguous; the liquid wedges merge smoothly with the thin film.

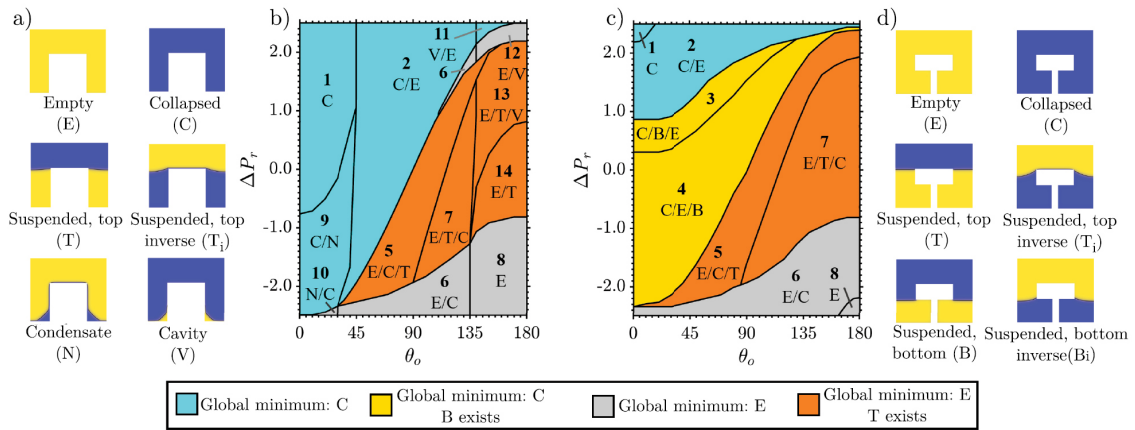


Figure 7.1: Diagonal cross-sectional images of the phase field at the free energy minima for the short post (a) and short reentrant geometry (d). The solid structure is shown in white, the liquid phase ($\phi = 1$) in blue, and the vapour phase ($\phi = -1$) in yellow. The ($\phi = 0$) interface is highlighted in black. Also shown are the phase diagrams for the post (b) and reentrant geometries (c). Numbered regions indicate the stable states, listed in order of increasing energy. Reproduced with permission from [65].

Compared to post geometries, reentrant geometries [65] have different wetting transitions from suspended (i.e. Cassie-Baxter) to collapsed (i.e. Wenzel) states (Figure 7.1). With reentrant geometries, the extra solid area introduces a higher energy barrier before the liquid is able to collapse. So far, the phase field has only been explored for the fully and partial wetting states. It will be interesting to expand this analysis by using the pseudo-partial wetting regime. Can we find new minima for pseudo-partial wetting? Also, since LBM is able to simulate dynamic systems, can we expand the previous quasi-static analysis to include liquid dynamics?

7.2.2 Meshed Surfaces for Water-Oil Separation

In Chapter 6, I have shown that LBM is able to capture the dynamics of droplets impacting meshed surfaces. As mentioned before, meshed surfaces are used for various purposes [12, 13, 14, 16, 18, 20], and one of them is for oil-water separation. For example, Gondal et al. [20] designed a gravity-driven oil-water separation system, using stainless steel meshes coated with Zinc Oxide (ZnO) and Tungsten Trioxide (WO_3). The idea is simple; a stainless steel meshed surface with pore sizes of 50, 100, 150, and 250 μm is spray-coated by ZnO or WO_3 and annealed at a temperature of 550 $^\circ\text{C}$ (Figure 7.2). After that, the mesh is prewetted by water, and then the oil-water mixture is poured onto the meshed surface. They have found that both coatings are able to separate 99% of oil when the pore size is 50 μm , while the WO_3 coating is able to do the same thing even when the pore size is increased to 150 μm .

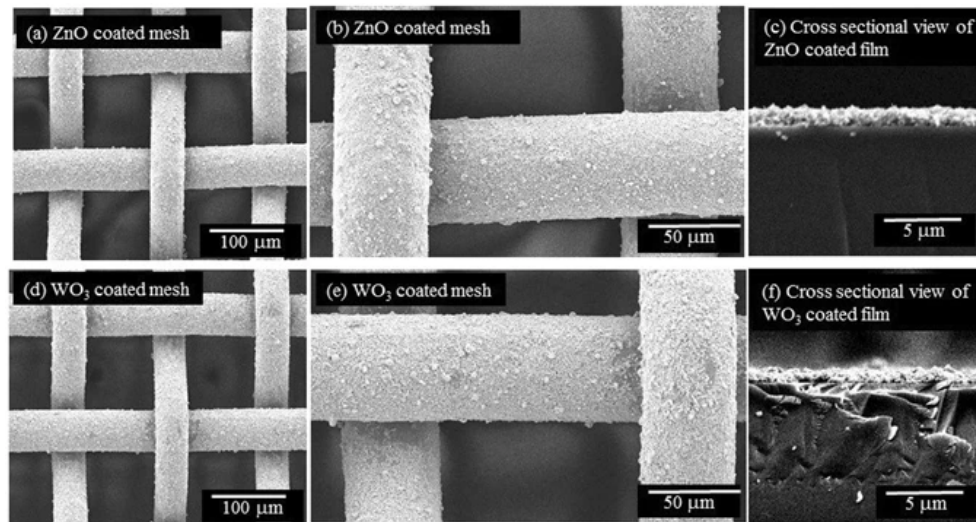


Figure 7.2: SEM image of coated stainless steel mesh with the pore size of $100\ \mu\text{m}$, ZnO coated mesh at (a) $200\times$ (b) $500\times$ magnification and (c) cross-sectional view of ZnO film at $4000\times$ magnification. WO_3 coated mesh at (d) $200\times$ (e) $500\times$ magnification and (f) cross-sectional view of WO_3 film at $4000\times$ magnification. Both WO_3 and ZnO coated surfaces have a uniformly distributed granular structure with micro and nanoscale hierarchical roughness and are free from agglomeration. The cross-sectional views further clarify the uniform distribution of the nanoparticles with an average thickness of 1 to $2\ \mu\text{m}$. Reproduced with permission from [20].

The oil-water separation is caused by the difference in the direction of the capillary forces for oil and water. First, the coated meshes have micro and nano-granular structures arranged around the mesh elements. This design causes the meshed surfaces to be superhydrophilic for water droplets surrounded by air, hydrophilic for water droplets inside the oil, and superoleophobic when the oil is submerged in water. When the mesh is pre-wetted, the water will fill the gaps caused by this granular structure and form a water film between the wires of the meshes. This water film will act as a barrier to prevent oil from the oil-water mixture from touching the meshes, inducing capillary forces in the oil whose direction is the opposite of the weight force (i.e. gravity). On the other hand, when the water part from the oil-water mixture touches the water film, it will be diffused and transferred into the other part of the mesh.

There are several open questions where modelling can aid the optimisation of the mesh design. For example, does the shape of the mesh affect the oil-water separation capability? Can we use a rhombus shape, for example? Can we change the cylindrical fibres to square fibres? Does the ratio between the fibre size and the pore size affect the water film formation? Can we mimic similar behaviour but use different structures? It will also be interesting to better understand the failure mechanism. Is the failure mode smooth or sharp? Are there

different modes of oil separation? If we introduce some movement (e.g. by shaking the tube or by using a motor), will this affect the filtering capability?

APPENDIX A

The Lattice Boltzmann Method - Code Implementation and Validation

A.1 Code Implementation

The LBM code is written in C. There are some differences in the precise implementation between the two-phase and the two-component code due to the variations between BGK and MRT. However, the general structure of the code remains the same. Figure A.1 illustrates the typical simulation cycle of my LBM code. One LB cycle usually starts at ‘compute gradients’ and ends at ‘compute momenta’.

A.1.1 Parallelisation

In both codes, the parallelisation is handled by OpenMPI. Here, I introduce (`nbPE`) to refer to the number of processors and (`myPE`) to refer to the local CPU index. The parallelisation is rudimentary. The simulation window is alongside the x -axis, and then fake (‘halo’) nodes are introduced on the left and the right of each simulation window. The neighbouring processors’ values are copied to these halo nodes, simplifying gradient calculation and the streaming process. I usually introduce two halo layers on each side, making each processor handle $[(LX/nbPE) + 4] \times LY \times LZ$ lattices. Figure A.2 illustrates this scheme.

A.1.2 Reading input file

The input file contains all the parameters needed for the simulation. Listings A.1 and A.2 show excerpts of input files for the two-phase and two-component LBM code, respectively. In

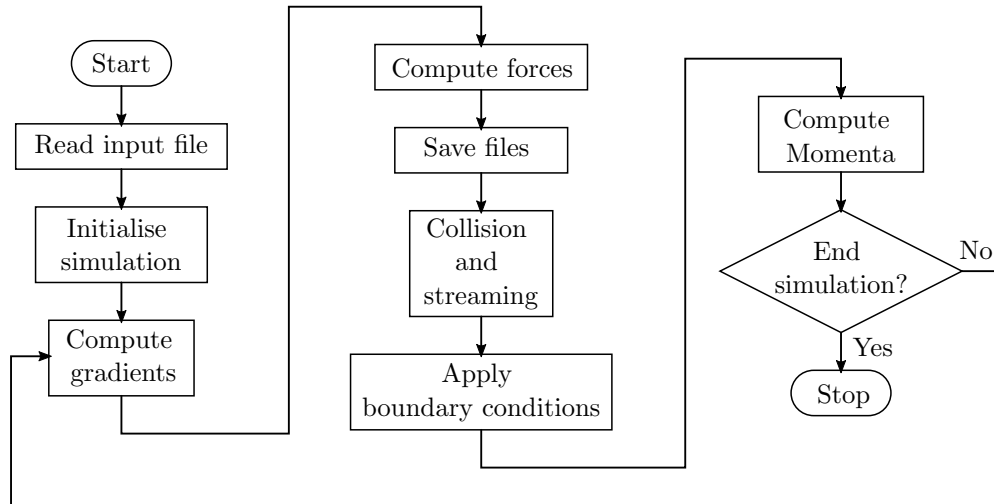


Figure A.1: A lattice Boltzmann method code cycle.

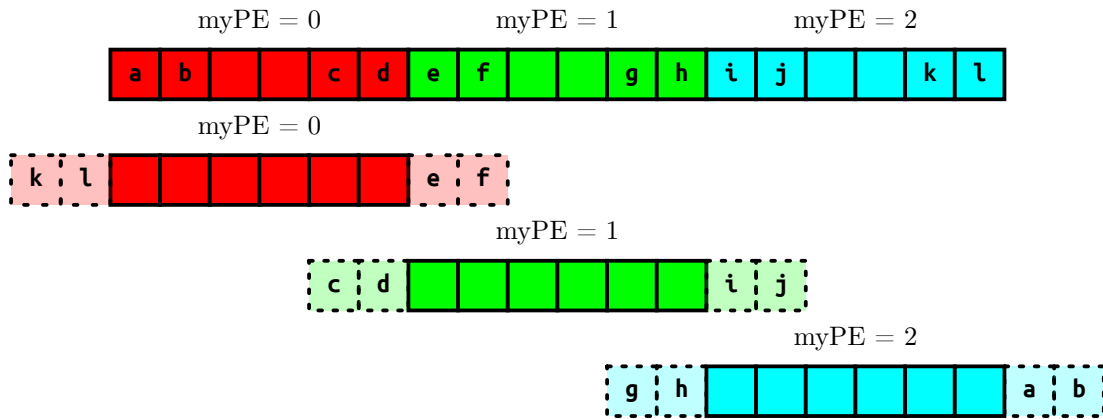


Figure A.2: An illustration of the parallelisation scheme. Different colours denote different processors. The solid line denotes real nodes, while the dashed line denotes halo nodes. During the simulation, the data from the left and right CPU neighbours will be copied to the ghost nodes.

the input file, we can set the simulation window size (LX , LY , LZ), the solid parameters (e.g. NSX , NSY , SX , SY , SZ), the initial droplet parameters (e.g., $DXC1$, $DYC1$, $DZC1$, $DR1$, g_x , g_y , g_z), the interfacial properties (λ_{ed} , κ_{hd} , κ_n), and wetting parameters (κ_w , a , b).

Listing A.1: Snippets of the input file for the two-phase code.

```

1 % SIMULATION GEOMETRY
2 240 240 50          % LX LY LZ
3 6 16               % solidconf solidconf2 - check code_initialise_geometry.cc.
4 1 1                % NSX NSY (number of pores in x and y direction)
5 200 200 10        % SX SY SZ (pore size in x, y, and z. In this case, SZ will
                    % also become the pore solid thickness.)
6 40 40 20          % dSX dSY dSZ (solid's thickness in x and y axis. Set them
                    % to SZ if using 90 degree pore. dSZ is the distance between two layer
                    % surfaces)
7 2                 % nhalo (width of the halo layer if parallel. If >0 useful
                    % for higher stencils)
8 1                 % initmode (0=serial | 1=parallel) (always use parallel

```

```

        unless need random numbers)
9  % FLUID CONFIGURATION
10 0 0          % fluidconf1 fluidconf2
11 1.5 49.5 0.0 500.0 % DXC1 DYC1 DZC1 DR1      (first drop)
12 0.0 0.0 0.0      % VX1 VY1 VZ1          (first drop)
13 0.0 0.0 0.0 -1.0 % DXC2 DYC2 DZC2 DR2      (second drop)
14 0.0 0.0 0.0      % VX2 VY2 VZ2          (second drop)

```

Listing A.2: Snippets of the input file for the two-component code.

```

1 %%%%%%%%%%%%%%%%%%%%%%%%%%%%%%%%%%%%%%%%%%%%%%%%% SIMULATION TIME INFO
2 0 % toggle_restart restart from dump? (0=no, 1=yes)
3 10000 % timedump time when to restart
4 000000 % nbEqStep number of equilibration steps
5 1 % nbIter number of iterations (added if starting from dump)
6 %%%%%%%%%%%%%%%%%%%%%%%%%%%%%%%%%%%%%%%%%%%%%%%%% SIMULATION GEOMETRY
7 1 % LX
8 1 % LY
9 25 % LZ
10 0 % nbPostX
11 0 % nbPostY
12 20 % postHeight
13 0 % postWidthX
14 0 % postWidthY

```

The input file is separated by lines, and each line can contain more than one parameter. These parameters will be read and saved into memory. Listing A.3 shows a snippet of the input file reading routine.

Listing A.3: Snippets of the input reading routine.

```

1 int readInput(){
2     std::ifstream inputFile("input.txt");
3
4     if (!inputFile) {
5         std::cout << "Can't open the input file" << std::endl;
6         return 1;
7     }
8     String endOfLine;
9
10    //%%%%%%%%%%%%%%%%%%%%%%%%%%%%%%%%%%%%%%%%%%%%%%%%%%%%%%%%%%%%
11    inputFile >> endOfLine;
12    std::cout<<"##### TIME AND SAVING INFO ##### " << std::endl;
13    //%%%%%%%%%%%%%%%%%%%%%%%%%%%%%%%%%%%%%%%%%%%%%%%%%%%%%%%%%%%%
14
15    inputFile >> toggle_restart >> endOfLine;
16    std::cout<<"toggle_restart = " << toggle_restart<<std::endl;
17
18    inputFile >> timedump >> endOfLine;
19    std::cout<<"timedump = " << timedump<<std::endl;
20
21    inputFile >> nbEqStep >> endOfLine;
22    std::cout<<"nbEqStep = " << nbEqStep<<std::endl;
23
24    inputFile >> nbIter >> endOfLine;
25    std::cout<<"nbIter = " << nbIter<<std::endl;
26    .....

```

27 }

A.1.3 Initialising the simulation

After we read the input files, the next step is to create directories for saving the dump files containing the distribution function (e.g. f_i, g_i) and the simulation output (e.g. ρ, \mathbf{v}, p). We also need to remove previous simulation results to remove clutter and reduce directory size (Listing A.4). After that, we allocate memory for different variables, including but not limited to f_i, ρ, \mathbf{v} , and \mathbf{F} . For the two-component code, we also need to create a lookup table of $\mathcal{M}^{-1}\mathcal{S}\mathcal{M}$ to reduce simulation time. See Listing A.5 for code excerpts.

Listing A.4: Snippets of the directory creation routine.

```

1 void create_folders() {
2     int systemRet;
3     .....
4     systemRet=system("mkdir full");
5     if(systemRet == -1){
6         // The system method failed
7     }
8     .....
9     systemRet=system("rm full/*.mat");
10    if(systemRet == -1){
11        // The system method failed
12    }
13    .....
14    } // end if
15 } // end function

```

Listing A.5: Snippets of the memory allocation routine.

```

1 void allocate_memory() {
2     .....
3     nn = new double*[nvel]; // f_i after streaming. nvel = q in DdQq
4     .....
5     for (int i = 0; i < nvel; i++) {
6         nn[i] = new double[N]; // N = ((LX/nbPE)+2)*LY*LZ
7         .....
8     } // end for
9     .....
10    n = new double[N]; // rho
11    .....
12    chemforce = new double*[ndim]; // F_chem
13    .....
14    for (int i = 0; i < ndim; i++) { // ndim = d in DdQq
15        chemforce[i] = new double[N];
16        .....
17    } // end allocate_memory
18
19
20 void initialise_zeros(){
21     .....

```



```

1 void initialise_new(){
2     .....
3
4     for(int k = k1; k < k2; k++) { // Loop through nodes, exclude halo.
5         .....
6         initialise_geometry(); // Solid nodes init
7         initialise_fluids();   // Fluid nodes init
8         .....
9         if (mask[k] != 28 ) { // Exclude solid nodes
10            .....
11            } else if (nvel==19) {
12                equilibriumn19(n[k],uzero,ne); // Compute  $f_i$  eq.  $n$  is  $\rho$ ,  $u$  zero
13                is initial velocity
14                .....
15                for (int i=0; i < nvel; i++) { // Distribute  $f_i$  to memory
16                    nn[i][k] = ne[i];
17                } // end for nvel
18            } // end if mask
19            .....
20        } // end for k
21    } // end function
22
23
24 void initialise_geometry(){
25     .....
26     /* Set a flat surface with thickness of SZ at the bottom */
27     case 13: std::cout << "(13) Solid at zk < " << SZ << std::endl;
28             if (zk < SZ) lmask = 28;
29             break;
30             .....
31 } // end function
32
33
34 void initialise_fluids(){
35     .....
36     case 1: std::cout << "3D droplet, R = " << DR1 << std::endl;
37     .....
38     /* Setup a 3D droplet */
39     rr1=sqrt((xk-DXC1)*(xk-DXC1)+(yk-DYC1)*(yk-DYC1)+(zk-DZC1)*(zk-DZC1));
40
41     if (rr1<=DR1) { // Inside the droplet
42         lc1 = 0.0; // Gas concentration
43         lc2 = 1.0; // Liquid concentration
44     } else { // Outside the droplet
45         lc1 = 1.0; // Gas concentration
46         lc2 = 0.0; // Liquid concentration
47     }
48
49     lv[0] = 0.0; // Set vx to 0
50     lv[1] = 0.0; // Set vy to 0
51     lv[2] = 0.0; // Set vz to 0
52     .....
53 } // end function

```

Listing A.7: Snippets of the restart simulation initialisation routine.

```

1 void initialise_resume(){
2     .....

```

```

3   read_dumps(timedump);    // Read dumps file
4   .....
5   computemomenta();       // Recover rho and v
6   .....
7 }
8
9
10 void read_dumps(long tdump) {
11   char fdump[251];        // Store dump file name
12   double *g_loc;         // Temporary array to store f_i
13   ....
14   sprintf(fdump,"dumps/dump_t%li.dmp",tdump);
15   std::ifstream fs(fdump, std::ios::in | std::ios::binary );
16   .....
17   fs.read((char *)&old_global_info_Step, sizeof(long));
18   std::cout<<"reading dump old_global_info_Step="<<old_global_info_Step<<
19   std::endl; // Previous simulation time steps
20   .....
21   for (int i=0; i < nvel; i++) { // Loop through all directions (q)
22     for (int k = 0; k < LX*LY*LZ; k++ ) { // Loop through all node
23       fs.read((char *)&g_loc[k], sizeof(double));
24     } // end for node
25   #ifdef PARALLEL
26     MPI_Scatter(g_loc ,k2-k1,MPI_DOUBLE ,&nn [i] [k1],k2-k1,MPI_DOUBLE,0,
27     MPI_COMM_WORLD); // For parallel process, scatter dump files to all
28     processors
29   #endif
30   .....
31 } // end function

```

A.1.4 Gradient calculation

Even though most calculations in LBM are done locally, both ∇ and ∇^2 calculations are needed for the computation of f_i^{eq} , g_i^{eq} , \mathbf{F}_{chem} , \mathbf{F}_{LRP} , and S_i^{Guo} . Except for \mathbf{F}_{LRP} calculation (see Section 5.3), I use a second-order central difference stencil with ten (for ∇) and nineteen points (for ∇^2) [236]. Below, ρ_i indicates the value of ρ whose location is i (see Figure 3.1(c)). Listing A.8 shows snippets of the gradient source code.

$\nabla\rho$, 10-point stencil:

$$\nabla_x \rho_0 = \frac{1}{12} [2(\rho_1 - \rho_2) + (\rho_7 + \rho_9 + \rho_{15} + \rho_{17} - \rho_8 - \rho_{10} - \rho_{16} - \rho_{18})] \quad (\text{A.1})$$

$$\nabla_y \rho_0 = \frac{1}{12} [2(\rho_3 - \rho_4) + (\rho_7 + \rho_8 + \rho_{11} + \rho_{13} - \rho_9 - \rho_{10} - \rho_{12} - \rho_{14})] \quad (\text{A.2})$$

$$\nabla_z \rho_0 = \frac{1}{12} [2(\rho_5 - \rho_6) + (\rho_{11} + \rho_{12} + \rho_{15} + \rho_{16} - \rho_{13} - \rho_{14} - \rho_{17} - \rho_{18})] \quad (\text{A.3})$$

$\nabla^2 \rho_0$, 19-point stencil:

$$\nabla^2 \rho = \frac{1}{3} [\rho_1 + \rho_2 + \rho_3 + \rho_4 + \rho_5 + \rho_6 + 6\rho_0] + \frac{1}{6} [\rho_7 + \rho_8 + \rho_9 + \rho_{10} + \rho_{11} + \rho_{12} + \rho_{13} + \rho_{14} + \rho_{15} + \rho_{16} + \rho_{17} + \rho_{18} - 12\rho_0] \quad (\text{A.4})$$

Listing A.8: Snippets of the gradient calculation routine.

```

1 void computeGradients(){
2     .....
3     /* Gradients */
4     gradn[0][k] = (2*(n[dd[1][k]] - n[dd[2][k]]) +
5                 (n[dd[7][k]] + n[dd[9][k]] + n[dd[15][k]] + n[dd[17][k]] -
6                 n[dd[8][k]] - n[dd[10][k]] - n[dd[16][k]] - n[dd[18][k]])
7                 )/12.0; // x
8     gradn[1][k] = (2*(n[dd[3][k]] - n[dd[4][k]]) +
9                 (n[dd[7][k]] + n[dd[8][k]] + n[dd[11][k]] + n[dd[13][k]] -
10                n[dd[9][k]] - n[dd[10][k]] - n[dd[12][k]] - n[dd[14][k]])
11                )/12.0; // y
12    gradn[2][k] = (2*(n[dd[5][k]] - n[dd[6][k]]) +
13                (n[dd[11][k]] + n[dd[12][k]] + n[dd[15][k]] + n[dd[16][k]] -
14                n[dd[13][k]] - n[dd[14][k]] - n[dd[17][k]] - n[dd[18][k]])
15                )/12.0; // z
16    /* Laplacian */
17    laplaciann[k] = (n[dd[1][k]] + n[dd[2][k]] + n[dd[3][k]] + n[dd[4][k]] +
18                  n[dd[5][k]] + n[dd[6][k]] - 6*n[k])/3.0 + (n[dd[7][k]] +
19                  n[dd[8][k]] + n[dd[9][k]] + n[dd[10][k]] + n[dd[11][k]] +
20                  n[dd[12][k]] + n[dd[13][k]] + n[dd[14][k]] + n[dd[15][k]]
21                  +
22                  n[dd[16][k]] + n[dd[17][k]] + n[dd[18][k]] - 12*n[k])/6.0;
23    .....
24 }
25
26 void computeGradientsLRPmu(){
27     .....
28     /* If backward difference. */
29     /* dd2 = one neighbour on the left. dd2[dd2] = two neighbours on the left */
30     gradxLRPmu[k] = 3*LRPmu[k]/2 - 2*LRPmu[dd2[k]] + LRPmu[dd2[dd2[k]]]/2;
31     .....
32     /* If forward difference */
33     gradxLRPmu[k] = -3*LRPmu[k]/2 + 2*LRPmu[dd1[k]] - LRPmu[dd1[dd1[k]]]/2;
34     /* If central difference */
35     gradxLRPmu[k] = -LRPmu[dd2[k]]/2 + LRPmu[dd1[k]]/2;
36     .....
37 } // end function

```

A.1.5 Force calculation

The computation of \mathbf{F} is straightforward. We simply sum each component (\mathbf{F}_g , \mathbf{F}_{chem} , \mathbf{F}_{LRP} , ($F_{\alpha,s}$) into a single variable. Depending on our needs, \mathbf{F}_g can either be constant forces (i.e. the acceleration is scaled to the local node density) or constant acceleration. The details of

$F_{\alpha,s}$ have been discussed in Section 3.3.3.3, while \mathbf{F}_{chem} and \mathbf{F}_{LRP} will be discussed below.

A.1.5.1 Chemical forces

To compute the chemical forces, we start by calculating the chemical potential of the system. For the two-phase code, this involves μ_ρ , ψ_{eos} , $d\psi_{eos}/d\rho$, and p in Equations 3.23, 3.24, 3.31, 3.32, and 3.33. For the two-component code, this involves μ_ϕ in Equations 3.60, 3.62, and 3.63. Listing A.9 shows snippets of this routine.

Listing A.9: Snippets of the chemical forces computation routine.

```

1 void freeenergy_carnahan_starling(){
2     .....
3     // Carnahan-Sterling EOS
4     double Psi = n[k]*csconst
5         +n[k]*(-csa*n[k]+csr*cst*logn
6         -(8*csr*cst*(-6+csb*n[k]))/((-4.0+csb*n[k])*(-4.0+csb*n[k])) )
7         -f_cs0
8     ;
9     /* First Derivative of Carnahan-Sterling EOS */
10    double dPsidRho=(1.0/( (csb*n[k]-4.0)*(csb*n[k]-4.0)*(csb*n[k]-4.0) ))
11        * (csr*cst*(-8.0+csb*n[k])*(32.0+csb*n[k]*(-4.0+csb*n[k]))
12        - ((csb*n[k]-4.0)*(csb*n[k]-4.0)*(csb*n[k]-4.0))*(2*csa*n[k]-csconst
13        )
14        + csr*cst*(-4.0+csb*n[k])*(-4.0+csb*n[k])*(-4.0+csb*n[k]) *logn)
15    ;
16    // Bulk part of chemical potential in rho
17    double murho_bulk=(lambda1/2.0)*dPsidRho;
18    // Interface part of chemical potential in rho
19    double murho_int=-kappa1*laplaciann[k];
20    // Total chemical potential
21    mun[k]=murho_bulk+murho_int;
22    // Bulk part of free energy
23    fbulk[k]= (lambda1/2.0)*Psi;
24    pbulk[k] =n[k]*murho_bulk-fbulk[k];
25    .....
26 }

```

A.1.5.2 Long-range potential forces

The long-range potential forces (\mathbf{F}_{LRP}) can be computed through two different ways. The first one is by hardcoding the equation directly. This can be in the form of Equations 5.16, 5.17, and 5.18 for flat surfaces or Equation 5.28 for fibres. Another way is by reading the value of externally generated \mathcal{V} and using it to compute μ_ϕ^{lrp} and \mathbf{F}_{LRP} . listing A.10 shows snippets of these routines.

Listing A.10: Snippets of the long range potential forces computation routine.

```

1 void LRPforces(){

```

```

2  ....
3  else if(lrp == 12) { // F = -\phi \grad\mu, with *enriching model*. Use a
   mix of quartic + exponential. Fitted for rf = 40. 2D, therefore we're in x-
   z plane.
4  ....
5  a0 = -1.416e-02;
6  a1 = -1.772e-02;
7  a2 = 5.365e-03;
8  a3 = -8.746e-03;
9  a4 = 1.679e-03;
10 a5 = 1.158e+00;
11 ....
12 uuu = a0 + a1*newr + a2*newr*newr + a3*newr*newr*newr + a4*newr*newr*newr*
   newr;
13 uuup = a1 + 2*a2*newr + 3*a3*newr*newr + 4*a4*newr*newr*newr;
14 vvv = exp(-a5*newr);
15 vvvp = -a5*exp(-a5*newr);
16 gradnewDLRP = uuup*vvv + uuu*vvvp;
17 ....
18 LRPforcey[k] = 0.0;
19 LRPforcex[k] = -p[k]*(newCLRP*gradnewDLRPx); // F = -phi * grad\mu
20 LRPforcez[k] = -p[k]*(newCLRP*gradnewDLRPz); // F = -phi * grad\mu
21 } // end if
22 ....
23 else if (lrp == 501){ // Read externally generated LRP, use simple C_phi = \
   phi+1/2.
24 LRPforcex[k] = -p[k]*gradxLRPmu[k];
25 LRPforcey[k] = -p[k]*gradyLRPmu[k];
26 LRPforcez[k] = -p[k]*gradzLRPmu[k];
27 } // end if
28 ....
29 } // end function
30
31
32 void calculateLRPmu(){
33 ....
34 Cprime_phi = 0.5;
35 LRPmu[k] = Dsolid_r*Cprime_phi;
36 ....
37 } // end function
38
39
40 void readLRP(const int num){ // Read externally generated V(r)
41 ....
42 sprintf(filename, "./mathematica/potential_%i.mat", num); // Store filename
   directory
43 checkFile(filename); // Check file existence, automatically close code if
   file not exist.
44
45 std::ifstream fs(filename, std::ios::in | std::ios::binary ); // Open file
   as fs.
46 ....
47 fs.read((char *)&lLX, sizeof(int)); // Read LX from
   potential_*.mat
48 ....
49 fs.read((char *)&lpot_tog, sizeof(int)); // Read pot_tog
50 fs.read((char *)&lpot_res, sizeof(double)); // Read pot_res
51 ....
52 for (int k = 0; k < LX*LY*LZ; k++){ // Loop through all
   nodes

```

```

53     fs.read((char *)&lA, sizeof(int));           // index of V(r)
54     fs.read((char *)&g_Dsolid_r[k], sizeof(double)); // V(r)
55 } // end for global
56     ....
57 } // end function

```

A.1.6 Saving files

This routine will save the output of the simulation (e.g. distribution function/dump file, momenta, solid structures). These files are saved as binary files containing both a header (e.g. t , ρ_l , ρ_g , β_{hd}) and the data itself. For parallel simulations, the data will first be gathered into the zeroth processor (e.g. using `MPI_Gather`) before being saved. The file size of the output is affected by the simulation window size and the number of momenta or parameters saved. For example, a 2D simulation of droplet spreading on grooved surfaces ($170 \times 1 \times 115$) will have an output size of 9.39 MB (dump) and 2.24 MB (ρ and \mathbf{v}) per time step. For a 3D simulation of a droplet moving along a fibre ($960 \times 90 \times 140$), the output size is 1.71 GB (dump), 92.28 MB (ρ), and 276.86 MB (\mathbf{v}). Listing A.11 shows an excerpt of the saving routines.

Listing A.11: Snippets of the saving routines.

```

1 void save_dumps(long tdump) {
2     ....
3     sprintf(fdump, "dumps/dump_t%i.dmp", tdump); // File name
4     std::ofstream fs(fdump, std::ios::out | std::ios::binary ); // Open file
5     /* Write header */
6     fs.write((char *)&LX, sizeof(int)); // Sim window size
7     ....
8     fs.write((char *)&global_info_Step, sizeof(long)); // Time step
9     ....
10    /* Save f_i */
11    for (int i=0; i < nvel; i++) { // Loop through 19 vectors
12        #ifdef PARALLEL
13            MPI_Gather(&nn[i][k1], k2-k1, MPI_DOUBLE, g_loc, k2-k1, MPI_DOUBLE, 0,
14                MPI_COMM_WORLD); // Gather f_i from other processors
15            ....
16            for (int k = 0; k < LX*LY*LZ; k++ ) { // Loop through sim window
17                fs.write((char *)&g_loc[k], sizeof(double));
18            }
19        }
20    }
21
22
23 void save_phase(){
24     ....
25     /* Gather rho from other processors */
26     ....
27     /* Open file */
28     ....
29     /* Write header */

```

```

30     ....
31     /* Write data */
32     for (int k = 0; k < LX*LY*LZ; k++ ) { // Loop through sim window
33         fs.write((char *)&g_n[k], sizeof(double)); // Save rho
34     };
35     ....
36 };
37
38
39 void save_mask(){
40     ....
41     /* Open file */
42     ....
43     /* Write header */
44     ....
45     /* Write solid */
46     for (int k = 0; k < LX*LY*LZ; k++ ) {
47         if(g_mask[k]==28) {
48             fs.write((char *)&k, sizeof(int)); // Save index with solid
49         }
50     }
51     ....
52 }

```

A.1.7 Collision and Streaming

The collision and streaming steps are conducted in a slightly different way between the two-phase and the two-component codes. For the two-phase model (see Listing A.12 for code excerpts):

1. Compute $f_i^{eq}(\rho, \mathbf{u} + \Delta\mathbf{u})$ and $f_i^{eq}(\rho, \mathbf{u})$ using Equations 3.10 and 3.36.
2. Using the Newton-Rhapson method, compute α_{hd} from equations 3.27 and 3.29.
3. Linearly interpolates β_{hd} if $\rho_g \leq \rho \leq \rho_l$.
4. Use equation 3.25 to do collision and streaming.

For the two-component model (see Listing A.13 for code excerpts):

1. Compute the Guo forcing term for each velocity direction using Equation 3.59.
2. Compute Equations 3.55 and 3.57 to obtain f_i^{eq} , then compute Equations 3.56 and 3.58 to obtain g_i^{eq} .
3. Collision f_i : compute Equation 3.49 by looking up at the $\mathcal{M}^{-1}\mathcal{S}\mathcal{M}$ table,
4. Collision g_i : compute Equation 3.50.

Listing A.12: Snippets of the collision and streaming of the two-phase code.

```

1 void collision_entropic(){
2     /* Swap populations. */
3     sw_nn = old_nn; old_nn = nn;   nn = sw_nn;
4     for(int k = k1 ; k < k2 ; k++){ // Exclude ghost nodes
5         ....

```

```

6   } else if (nvel==19) {
7       equilibriumn19(n[k],uufull,ne); // See Eq 3.25
8       equilibriumn19(n[k],uuzero,ne0);
9       .....
10      for (int i=0; i < nvel; i++) { // Loop through 19-directions
11          finfor[i] = ne[i]-ne0[i]; // See Eq 3.25
12      }
13      .....
14      /* Compute  $\alpha^{\{elbm\}}$  */
15      for (int ii=1; ii<=10; ii+=1) {
16          double enf=0.0;
17          double enf1=1.0;
18          .....
19          enf=entropyf19(fprime,ne,alphaentropy); // See Eq 3.27 and 3.29
20          enf1=entropyfgrad19(fprime,ne,alphaentropy);
21          .....
22          alphaentropy -= enf / enf1; // Newton-Raphson
23          if (fabs(enf)<0.000001) break;
24          .....
25      }
26      /* Interpolate beta */
27      double lc=(n[k]-densg)/deltarho; // Liquid phase has value 1
28      double betaInt=beta1*(1-lc)+beta2*lc;
29      .....
30      /* Collision combines propagation and accounts also for bounceback */
31      for (int i=0; i < nvel; i++) {
32          if(dd[i][k]>=0 && dd[i][k]<N) nn[i][dd[i][k]] = old_nn[i][k] +
33              alphaentropy*betaInt*(ne0[i]-old_nn[i][k]) + finfor[i]; // See Eq 3.25
34      } // dd[i][k] = neighbour of k at direction i
35      .....
36      } // end of collision_entropic
37
38      void equilibriumn19(double nloc,double actualuu[3],double ne[19]){
39          double ux = actualuu[0];
40          double uy = actualuu[1];
41          double uz = actualuu[2];
42
43          for(int i = 0 ; i < nvel ; i++){ // Loop through 19 directions
44              /* Slightly different form, more accurate numerically */
45              ne[i] =nloc*wei[i]*(2.0-sqrt(1+3.0*ux*ux))
46                  *(2.0-sqrt(1+3.0*uy*uy))
47                  *(2.0-sqrt(1+3.0*uz*uz))
48                  *pow(((2.0*ux+sqrt(1.0+3.0*ux*ux))/(1.0-ux)),v1[i][0])
49                  *pow(((2.0*uy+sqrt(1.0+3.0*uy*uy))/(1.0-uy)),v1[i][1])
50                  *pow(((2.0*uz+sqrt(1.0+3.0*uz*uz))/(1.0-uz)),v1[i][2])
51                  ;
52          }
53      }
54
55
56      double entropyf19(double floc[19], double feq[19], double aloc){
57          .....
58          value =
59          ((1-aloc)*floc[0]+aloc*feq[0])*log(((1-aloc)*floc[0]+aloc*feq[0])/wei[0]) -
60          floc[0]*log(floc[0]/wei[0]) +
61          ((1-aloc)*floc[1]+aloc*feq[1])*log(((1-aloc)*floc[1]+aloc*feq[1])/wei[1]) -
62          floc[1]*log(floc[1]/wei[1]) +
63          ((1-aloc)*floc[2]+aloc*feq[2])*log(((1-aloc)*floc[2]+aloc*feq[2])/wei[2]) -
64          floc[2]*log(floc[2]/wei[2]) +

```

```

65     ....
66     return value;
67 }
68
69
70 double entropyfgrad19(double floc[19], double feq[19], double aloc){
71     ....
72     value =
73     (feq[0]-floc[0])*(1+log(((1-aloc)*floc[0]+aloc*feq[0])/wei[0])) +
74     (feq[1]-floc[1])*(1+log(((1-aloc)*floc[1]+aloc*feq[1])/wei[1])) +
75     (feq[2]-floc[2])*(1+log(((1-aloc)*floc[2]+aloc*feq[2])/wei[2])) +
76     (feq[3]-floc[3])*(1+log(((1-aloc)*floc[3]+aloc*feq[3])/wei[3])) +
77     ....
78     return value;
79 }

```

Listing A.13: Snippets of the collision and streaming of the two-component code.

```

1 void collision(){
2     ....
3     for(int k = k1 ; k < k2 ; k++){
4         ....
5         /* Guo forcing related terms. See Eq 3.59.*/
6         double uxfx = ux*fx;
7         double uxfy = ux*fy;
8         double uxfz = ux*fz;
9         ....
10        fm[0] = fac* (-uf);
11        fm[1] = fac* w1 * ( (-uf+fx) + (3.0*uxfx));
12        ....
13        fm[7] = fac* w3 * ( (-uf+fx+fy) + (3.0*(uxfx+uxfy+uyfx+uyfy)));
14        fm[8] = fac* w3 * ( (-uf-fx+fy) + (3.0*(uxfx-uxfy-uyfx+uyfy)));
15        ....
16        equilibrium(k); // See Eq 3.55-3.58
17        ....
18        /* See Eq 3.49 */
19        dn[0] = (ne0-old_nn0[k]);
20        dn[1] = (ne1-old_nn1[k]);
21        ....
22        dn[10] = (ned-old_nnd[k]);
23        dn[11] = (nee-old_nne[k]);
24        ....
25        /* Collision, f_i. See Eq 3.49 */
26        /* MM, MF = M^-1 S M for f_i and S_i~{Guo} */
27        nn0[k] = old_nn0[k] + dn[0]*MM[1][0][0] + dn[1]*MM[1][0][1] + dn[2]*MM[1][0][2] + dn[3]*MM[1][0][3] + dn[4]*MM[1][0][4] + dn[5]*MM[1][0][5] + dn[6]*MM[1][0][6] + dn[7]*MM[1][0][7] + dn[8]*MM[1][0][8] + dn[9]*MM[1][0][9] + dn[10]*MM[1][0][10] + dn[11]*MM[1][0][11] + dn[12]*MM[1][0][12] + dn[13]*MM[1][0][13] + dn[14]*MM[1][0][14] + dn[15]*MM[1][0][15] + dn[16]*MM[1][0][16] + dn[17]*MM[1][0][17] + dn[18]*MM[1][0][18] + fm[0]*MF[1][0][0] + fm[1]*MF[1][0][1] + fm[2]*MF[1][0][2] + fm[3]*MF[1][0][3] + fm[4]*MF[1][0][4] + fm[5]*MF[1][0][5] + fm[6]*MF[1][0][6] + fm[7]*MF[1][0][7] + fm[8]*MF[1][0][8] + fm[9]*MF[1][0][9] + fm[10]*MF[1][0][10] + fm[11]*MF[1][0][11] + fm[12]*MF[1][0][12] + fm[13]*MF[1][0][13] + fm[14]*MF[1][0][14] + fm[15]*MF[1][0][15] + fm[16]*MF[1][0][16] + fm[17]*MF[1][0][17] + fm[18]*MF[1][0][18];
28        if(dd1[k]>=0 && dd1[k]<N) nn1[dd1[k]] = old_nn1[k] + dn[0]*MM[1][1][0] + dn[1]*MM[1][1][1] + dn[2]*MM[1][1][2] + dn[3]*MM[1][1][3] + dn[4]*MM[1][1][4] + dn[5]*MM[1][1][5] + dn[6]*MM[1][1][6] + dn[7]*MM[1][1][7] + dn

```

```

    [8]*MM[1][1][8] + dn[9]*MM[1][1][9] + dn[10]*MM[1][1][10] + dn[11]*MM[1]
    ][1][11] + dn[12]*MM[1][1][12] + dn[13]*MM[1][1][13] + dn[14]*MM[1][1][14]
    + dn[15]*MM[1][1][15] + dn[16]*MM[1][1][16] + dn[17]*MM[1][1][17] + dn[18]*
    MM[1][1][18] + fm[0]*MF[1][1][0] + fm[1]*MF[1][1][1] + fm[2]*MF[1][1][2] +
    fm[3]*MF[1][1][3] + fm[4]*MF[1][1][4] + fm[5]*MF[1][1][5] + fm[6]*MF[1]
    ][1][6] + fm[7]*MF[1][1][7] + fm[8]*MF[1][1][8] + fm[9]*MF[1][1][9] + fm
    [10]*MF[1][1][10] + fm[11]*MF[1][1][11] + fm[12]*MF[1][1][12] + fm[13]*MF[1]
    ][1][13] + fm[14]*MF[1][1][14] + fm[15]*MF[1][1][15] + fm[16]*MF[1][1][16]
    + fm[17]*MF[1][1][17] + fm[18]*MF[1][1][18];
29     ....
30     /* Collision g_i. See Eq 3.50 */
31     pp0[k] = old_pp0[k]*itaup_opp + pe0*itaup;
32     if(dd1[k]>=0 && dd1[k]<N) pp1[dd1[k]] = old_pp1[k]*itaup_opp + pe1*itaup;
33     if(dd2[k]>=0 && dd2[k]<N) pp2[dd2[k]] = old_pp2[k]*itaup_opp + pe2*itaup;
34     ....
35 }

```

A.1.8 Apply Boundary Conditions

In this routine, we can apply different boundary conditions that are not in the form of forces. For both the two-phase and the two-component models, I implement the bounce-back boundary condition (Section 3.3.3.2). A mirror boundary condition can also be applied here. See Listing A.14 for the code excerpt.

Listing A.14: Snippets of the boundary condition routine.

```

1 void bouncebackbc(){
2     for(int k = k1 ; k < k2 ; k++) { // Loop through all nodes
3         if (mask[k]==1) { // Only check boundary nodes
4             for (int i=1; i < nvel; i++) { // Check through all direction
5                 if (mask[dd[i][k]] == 28){ // Check which neighbour is solid
6                     ....
7                     /* Do bounceback. iopp is \bar{i} in Eq 3.37 */
8                     nn[iopp[i]][k] = nn[i][ dd[i][k] ];
9                     ....
10 } // end function

```

A.1.9 Compute Momenta

Here, we implement Equations 3.11, 3.48, 3.35, and 3.36 to compute ρ , ϕ (two-component only), \mathbf{u} , and \mathbf{v} . See Listing A.15.

Listing A.15: Snippets of the boundary condition routine.

```

1 void computemomenta(){
2     for(int k = k1 ; k < k2 ; k++){ // Loop through nodes
3         if (mask[k]!=28) { // Exclude solid nodes
4             ....
5             /* Exchange f_i using MPI */
6             ....
7         } else if (nvel==19) { // D3Q19

```

```

8     n[k]=momentq19(locnn);           // Compute rho
9     .....
10    velocityq19(locuu,n[k],locnn);
11    }
12    .....
13    for(int i= 0 ; i < ndim ; i++){
14        uu[i][k]=locuu[i]; // Bare fluid velocity
15        vv[i][k]=locuu[i] + 0.5*(force[i][k])/n[k]; // Real fluid velocity
16    }
17    .....
18 } // end of computeMomenta
19
20
21 double momentq19(double locnn[19]){
22     double  nloc = locnn[0]
23             +locnn[ 1]
24             +locnn[ 2]
25             +locnn[ 3]
26             .....
27             +locnn[18];
28 return nloc;
29 }
30
31
32 void velocityq19(double uuloc[3],double nloc, double locnn[19])
33 {
34     uuloc[0] = (locnn[ 1] + locnn[ 7] + locnn[ 9] + locnn[15] +
35                locnn[17] - locnn[ 2] - locnn[ 8] - locnn[10] -
36                locnn[16] - locnn[18])/nloc;
37     uuloc[1] = (locnn[ 3] + locnn[ 7] + locnn[ 8] + locnn[11] +
38                locnn[13] - locnn[ 4] - locnn[ 9] - locnn[10] -
39                locnn[12] - locnn[14])/nloc;
40     uuloc[2] = (locnn[ 5] + locnn[11] + locnn[12] + locnn[15] +
41                locnn[16] - locnn[ 6] - locnn[13] - locnn[14] -
42                locnn[17] - locnn[18])/nloc;
43
44 }

```

A.2 Typical Simulation Statistics

In this work, the simulations are conducted either on my work computer or Durham University High-Performance Computing (HPC) service, Hamilton [237]. More specifically, I am using Hamilton8, where each compute node consists of $2 \times$ AMD EPYC 7702 CPUs, with 128 CPU cores. Each node has 256GB of RAM and 400GB of local SSD storage. Below, I summarised the typical simulation statistics for the work in Chapters 4, 5, and 6 in Hamilton. LX, LY, and LZ represent the simulation window size in the x , y , and z directions, respectively. \bar{t}_{sim} represents the average simulation time for a certain number of simulation time steps, while t_{sim} represents the total simulation time.

Table A.1: Typical statistics for simulation in Chapter 4.

Fibre, 3D	$r_f = 10$		$r_f = 20$	
	LX×LY×LZ	1440 × 90 × 140		960 × 90 × 140
No. of CPU cores	24	96	24	96
\bar{t}_{sim} for 10,000 steps	8h 43m	2h 56m	5h 16m	1h 31m
RAM used	24.90 GB	32.39 GB	19.78 GB	25.43 GB

Table A.2: Typical statistics for simulation in Chapter 5.

Flat, 2D	Analytic		Numeric	
	LX×LY×LZ	180 × 1 × 65		180 × 1 × 70
No. of CPU cores	2	5	2	5
\bar{t}_{sim} for 100,000 steps	22m 2s	9m 5s	21m 54s	8m 25s
RAM used	320.53 MB	762.11 MB	324.75 MB	764.70 MB

Fibre, 3D	$r_f = 20$		$r_f = 40$	
	LX×LY×LZ	360 × 180 × 150		360 × 180 × 190
No. of CPU cores	18	72	24	72
\bar{t}_{sim} for 10,000 steps	6h 0m	1h 43m	5h 20m	2h 2m
RAM used	24.04 GB	36.48 GB	32.16 GB	44.02 GB

Table A.3: Typical simulation statistics for \mathcal{V} integration in Chapter 5. $\{T_s, q\}$ represents solid thickness and interpolation degree. Only one CPU core is used during the integration.

Flat, 2D	$\{5,2\}$	$\{5,4\}$	$\{10,2\}$
LX×LY×LZ	60 × 1 × 65		
t_{sim} total	2m 37s	37m 53s	5m 57s
RAM used	4.38 GB	12.24 GB	5.51 GB

Table A.4: Typical statistics for simulation in Chapter 6. ΔT_s is the distance between the two layers.

3D	Single-layer		Double-layer, $\Delta T_s = 40$	
LX×LY×LZ	240×240×150		240×240×190	
No. of CPU cores	12	30	12	30
\bar{t}_{sim} for 10,000 steps	14h 26m	4h 46m	16h 33m	6h 20m
RAM used	11.91 GB	16.94 GB	14.67 GB	20.39 GB

A.3 Results Validation

To validate the two-phase code, I use binary Poiseuille flow, capillary filling, and droplet-on-fibre morphology tests. The first two tests are used to validate the accuracy of the model in simulating the dynamics of a two-phase system, while the final test shows the LBM capability to simulate the droplet bistability. For the two-component code, I run the binary Poiseuille flow test only. I did not perform the capillary filling case because it is valid for partially dynamic cases, while Tanner's law comparison is ignored because I did not focus on the transient droplet spreading: during all of our tests, the liquid initially wetted the surface. The external force is applied after the liquid reaches a steady state. More validations on the two-phase code can be found in [44, 81, 238, 239], and for the two-component code can be found in [57, 142, 143, 240].

A.3.1 Binary Poiseuille Flow

Figure A.3 illustrates a 2D system to simulate Poiseuille flow. The system is bounded by solid walls on the top and bottom, where H is the distance between the walls. The system is equally divided into two parts with high-viscosity fluid on the top and low-viscosity fluid on the bottom. For the two-phase system, the kinematic viscosity (ν) is fixed, while the fluid density (ρ) is varied. For the two-component code, ρ is fixed to 1 while ν is varied. For both codes, $H = 199$ and $LX = 2$. Periodic BC is introduced on the left and right sides of the system, and a no-slip boundary condition is applied on the top and bottom. The system is initialised with $\mathbf{v} = 0$, then at $t = 0$, a constant force of $F_x = 10^{-7}$ is applied to both fluids and the simulation is run until reaching a steady state.

For an external force-driven Poiseuille flow, at steady state, the Navier-Stokes equation can be simplified into:

$$-F_x = \partial_y (\eta \partial_y v_x), \quad (\text{A.5})$$

which for a single-phase system ($\partial_y \eta = 0$):

$$v_x(y) = \frac{-F_x}{2\rho\nu} (y^2 + Hy). \quad (\text{A.6})$$

This will result in a parabolic velocity profile, with $v_x(0) = v_x(H) = 0$, and a maximum velocity at $H/2$, assuming a no-slip boundary condition.

For a two-phase system, Equation A.5 is evaluated numerically using a method introduced

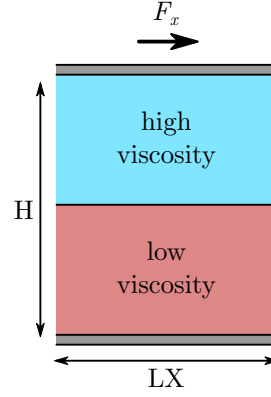


Figure A.3: Simulation setup of two plates with infinite area. For both the two-phase and two-component codes, the lower viscosity fluid is located at the bottom. The fluid-fluid interface is located at $H/2$, where H is the cavity width. F_x is the external force applied to both fluids.

in [241]. $\eta(y)$ is evaluated by using the simulated $\rho(y)$ or $\phi(y)$ as input, then Equation A.5 is solved numerically using:

$$v_x(y) = F_x \sum \frac{y}{\eta(y)} \Delta y + \mathcal{J} F_x \sum \frac{\Delta y}{\eta(y)} + \mathcal{K}, \quad (\text{A.7})$$

$$\mathcal{J} = -F_x \frac{\sum \frac{H}{\eta(H)} \Delta y}{\sum \frac{\Delta y}{\eta(H)}}, \quad (\text{A.8})$$

$$\mathcal{K} = -\mathcal{J} \frac{\Delta y}{\eta(0)}. \quad (\text{A.9})$$

This will result in a combination of two-parabolic profiles, with a higher velocity for fluid with a lower dynamic viscosity (η).

Figure A.4 shows the velocity profile for the two-phase code. Blue circles denote simulation results (printed sparsely to preserve legibility), while orange solid lines are obtained from Equation A.6 or A.7. $\eta_l = \eta_g = 0.1667$. Figure A.4(a) shows the velocity profile for a single-phase system with $\rho_l = 6.124$; Figure A.4(b) is for $\rho_l = 6.124$, and $\rho_l/\rho_g = 17.50$; while Figure A.4(c) is for $\rho_l = 7.344$, and $\rho_l/\rho_g = 126.10$. There are no significant differences between the simulation and the analytical results for all testing parameters. We can observe the parabolic profile for all cases, and the fluid with lower density is faster than the fluid with higher density. At a higher density ratio, the settling time is also longer ($\sim 2,000,000$ time steps for Figure A.4(b) and $\sim 4,000,000$ time steps for Figure A.4(c)).

Figure A.5 shows the velocity profile for the two-component code. $\rho_1 = \rho_2 = 1.0$. The heavier fluid viscosity is fixed to $\eta_1 = 0.8333$. Figure A.5(a) shows the velocity profile for a

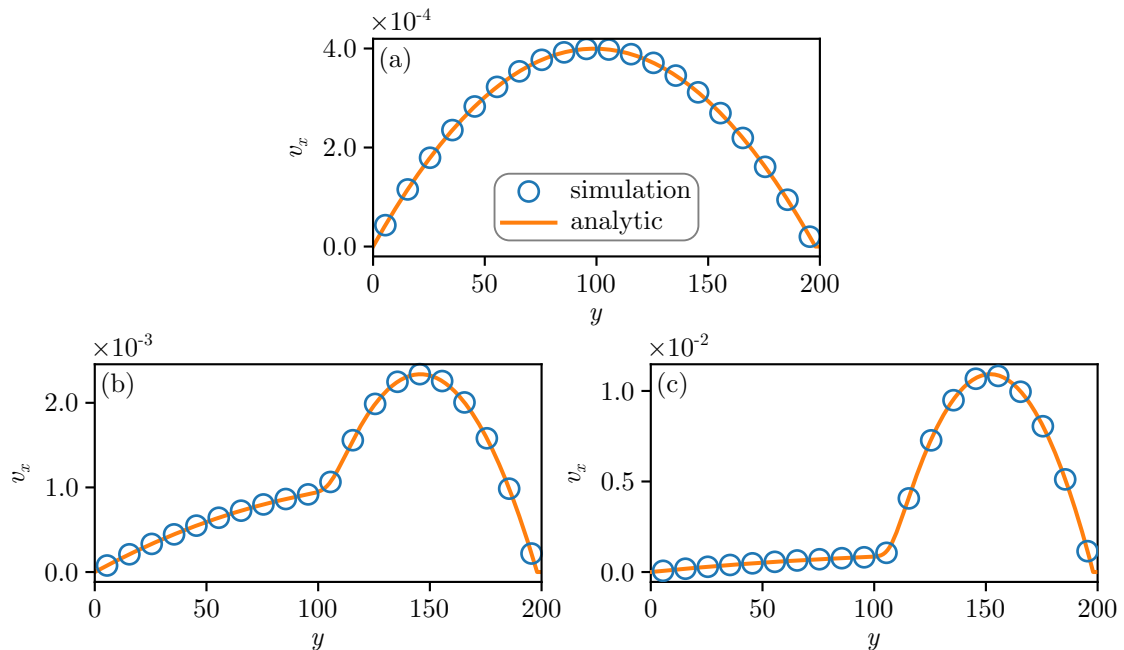


Figure A.4: The x -component of the fluid velocity (v_x) profile. $F_x = 10^{-7}$, $\eta_l = \eta_g = 0.1667$. (a) Single phase with $\rho = 6.124$. Two-phase with (b) $\rho_l = 6.124$, $\rho_l/\rho_g = 17.50$ and (c) $\rho_l = 7.344$, $\rho_l/\rho_g = 126.10$.

single-phase system; Figure A.5(b) is for $\eta_l/\eta_2 = 5$; while Figure A.5(c) is for $\eta_l/\eta_2 = 100$. Similar to the result of the two-phase code, there is no significant difference between the LBM simulation and Equation A.6 or A.7. Parabolic profiles can be observed in all cases, and the fluid with lower η also has a higher velocity.

A.3.2 Capillary Filling - Washburn's Law

Capillary filling is one of the classical benchmarks for wetting boundary conditions in LBM [81]. A non-hydrodynamic effect is happening due to the capillary forces at the contact point between the liquid, gas, and solid interfaces, balanced by the fluid viscous forces, causing liquid imbibition into a gas channel [242]. Let us consider a 2D channel with a height of H full of gas imbibed by liquid (Figure A.6). If the liquid-gas contact angle is θ , then the length of the imbibed liquid column (r) can be predicted as [240]:

$$r(t) = \left(\frac{\gamma_{lg} H \cos \theta}{3\eta_l} \right)^{\frac{1}{2}} (t + t_0)^{\frac{1}{2}}, \quad (\text{A.10})$$

where γ_{lg} is the liquid-gas surface tension and η_l is the liquid dynamic viscosity and t_0 is a constant that is an integration constant obtained by fitting the data to the equation. This equation is valid for a system with a high viscosity ratio, ignoring the dissipated energy in the

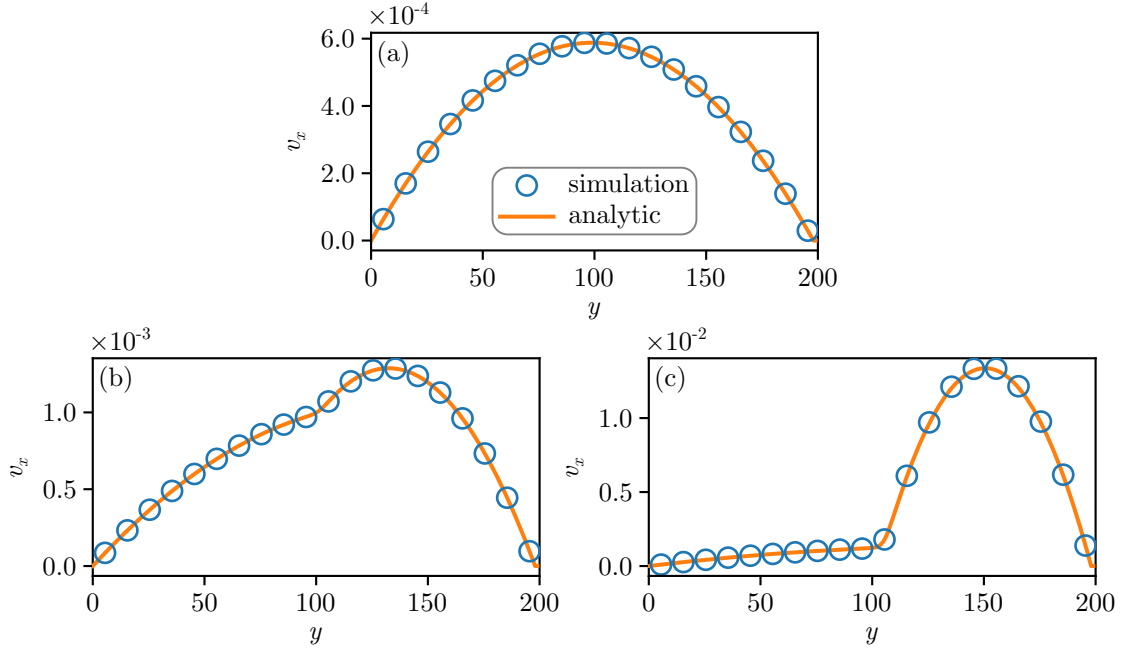


Figure A.5: The x -component of the fluid velocity (v_x) profile. $F_x = 10^{-7}$, $\rho_1 = \rho_2 = 1.0$, $\eta_1 = 0.8333$. (a) Single component system. Two-component with (b) $\eta_1/\eta_2 = 17.50$ and (c) $\eta_1/\eta_2 = 126.10$.

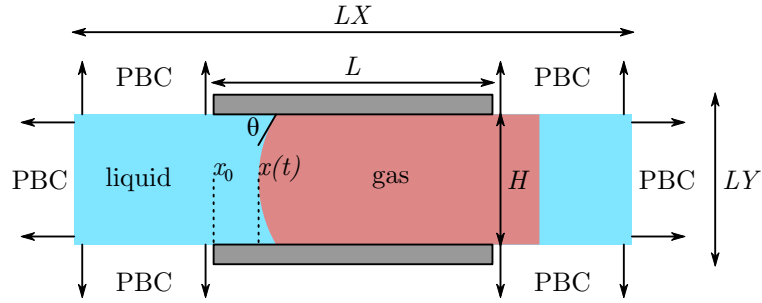


Figure A.6: The simulation setup for a capillary flow along the tube. $r = x_0 - x(t)$ is the capillary filling distance. θ is the contact angle between the liquid and gas interface. The fluid-gas interface is initiated as a flat interface, before being evolved by the LBE. This figure is adapted from [240].

gas phase.

The system is set up in Figure A.6, following the work of [240]. The grey boxes denote solid boundaries, the blue-coloured region is liquid, and the red-coloured region is gas. Outside of the solid boundary, periodic boundary conditions (PBC) are used to mimic liquid and gas reservoirs. r is defined as $r = x_0 - x(t)$. $L = 350$, $H = 39$, $LX = 700$, and $LY = 40$. $\gamma_g = 0.1837$, $\eta_l = 1.338$, with $\eta_l/\eta_g \sim 1000$. Using the fluid-solid forcing method, I set the equilibrium contact angle as $\theta_e = 37^\circ, 60^\circ, 75^\circ$. However, during the data fitting, the average local contact angle (θ) is used instead. This is obtained by fitting the liquid-gas interface to a circle with a radius of r_d which is then related via $\cos \theta = H/(2r_d)$.

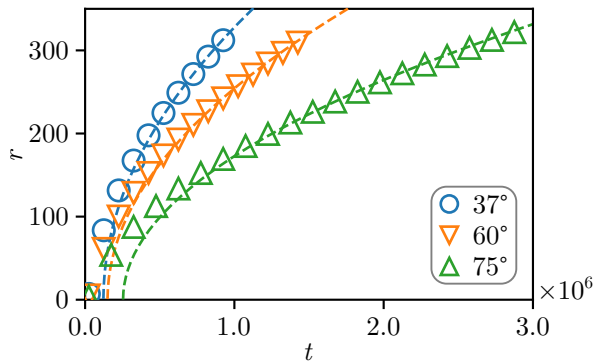


Figure A.7: The liquid column length (r) as a function of time (t). Different symbols and colours denote different equilibrium contact angles (θ_e). Dashed lines are Equation A.10. Here, θ is obtained by averaging the local contact angle, and t_0 is obtained by fitting the data to Equation A.10.

Figure A.7 shows the value of $r(t)$ for different θ_e . Different symbols denote simulation results, while dashed lines are Equation A.10. Similar to the results obtained by [81] and [240], the Washburn law only matches the simulation result during the asymptotic regime, where $t \rightarrow \infty$. In the asymptotic regime, the average θ is 46.7° , 64.8° , and 77.0° for θ_e of 37° , 60° , and 75° , respectively. This is compared to the transient regime, where θ can reach 47.8° , 73.6° , and 82.1° . As is discussed in Reference [81], the accuracy of the fluid-solid wetting interaction can be improved by using a more accurate boundary condition. However, considering the flexibility of the forcing method in modelling complex surfaces, I consider that the forcing method is satisfactory. The simulation results also confirm that lower θ will increase the imbibition speed due to the higher capillary forces, and the r profile is proportional to $t^{1/2}$.

A.3.3 Droplet Morphology

In Chapter 4, it is important to show that the LBM code can simulate the bistability of a droplet sitting on a fibre. Following the work of [76], I choose three values of $\theta_e = 45^\circ$, 51° , and 60° . $L_R = \Omega^{1/3}/r_f$ is varied from 20, 50, 100, and 600. The droplet volume is fixed at 600,000 l.u. and the fibre radius is varied. The other simulation parameters follow the results in Chapter 4.

To induce the droplet morphology, for each combination of θ_e and L_R , the droplet is initialised in four different configurations (Figure A.8). For the first configuration, a cylindrical droplet with a length of L and a droplet radius of r_d with a centre coordinate of $\{x_d^c, y_d^c\}$ is initialised such that the bottom of the fluid will touch the top of the fibre (Figure A.8(a)). In the second configuration, the fibre is moved slightly to the top, such that the centre of the fibre

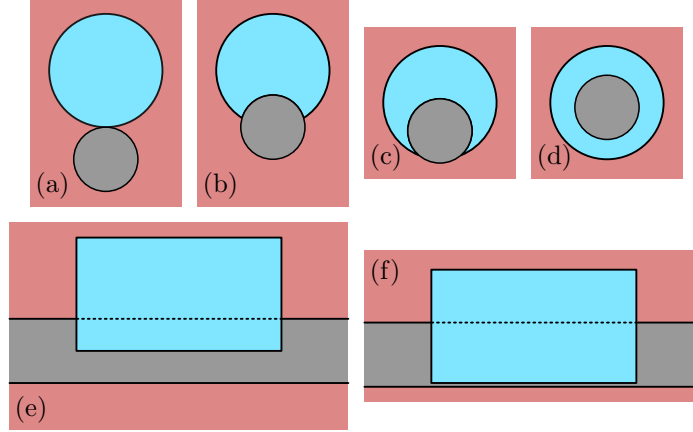


Figure A.8: Different simulation setup to obtain barrel and clamshell morphologies. Each L_R and θ combination is initialised as a cylindrical fluid in four different configurations: (a) the fibre is touching the edge of the fluid; (b, e) the centre of the fibre is equivalent to $\{x_d^c, y_d^c - r_d\}$, where x_c and y_c is the liquid centre coordinates; (c, f) the fibre centre is located at $\{x_d^c, y_d^c - r_d/2\}$; (d) the fibre centre is at $\{x_d^c, y_d^c - 5\}$. (a, b, e) are used to induce the clamshell morphology, while (c, d, f) are used to induce the barrel morphology. (a-d) The fluid cutaway in the y - z direction. (e, f) The fluid cutaway in the x - z direction.

is now $\{x_d^c, y_d^c - r_d\}$ (Figures A.8(b) and (e)). These are used to induce the clamshell morphology. The third configuration is set such that the fibre centre coordinate is $\{x_d^c, y_d^c - r_d/2\}$ (Figures A.8(c) and (f)). The final configuration is $\{x_d^c, y_d^c - 5\}$. The third and the fourth are used to induce the barrel morphology. Bistability exists if at least one of the configurations is different compared to the other one.

In Figure A.9, I overlay the simulation results (denoted by symbols) over the results from [76] (denoted by solid background colours). The data points show that a barrel-only morphology and bistability can be observed with my code. Barrel-only is observed at lower θ_e and higher L_R , similar to the observation of [76]. However, compared to Reference [76], the transition is happening at different θ_e and L_R . I hypothesise that the boundary condition in LBM that I use is the cause of this shift. As has been discussed in the text, the roughness introduced by the staircase approximation will change θ_e by $\sim 10^\circ$. This will not affect the dynamic of the droplet moving along the fibre significantly but will affect the droplet morphology transition. My primary objective is to compare the dynamics of the barrel and clamshell morphologies within the same setup and not to study the dynamics of the morphology transition. Therefore, to mitigate this boundary shift, I pick $L_R > 150$ and θ_e of 60° and 75° to simulate the bistability, $\theta_e = 28^\circ$ is picked to guarantee that the clamshell morphology is suppressed, and $\theta_e = 120^\circ$ is used to suppress the barrel morphology.

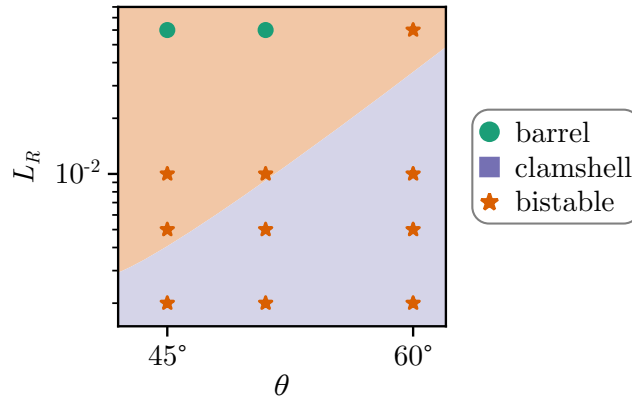


Figure A.9: Phase diagram showing different droplet morphology as a function of L_R and θ . Symbols denote simulation results while background colours are the results from [76]. Different symbols and different colour denotes different final morphology.

A.4 Grid Invariant Test

A.4.1 Modelling the Dynamics of Partially Wetting Droplets on Fibres

The so-called law of similarity states that fluid flows that share relevant dimensionless numbers provide the same physics as long as the typical scales are scaled properly [94]. To compare the effect of the simulation window, I matched the system Bond numbers to 1.211×10^{-2} , 2.506×10^{-2} , 5.186×10^{-2} , and 1.073×10^{-1} . I fixed all the physical parameters (ρ_l , ρ_g , γ_{lg} , η), then varied the fluid acceleration (g_x), and the simulation window size $\{LX, LY, LZ\}$: $1\times$ with $\{120, 45, 70\}$; $2\times$ with $\{240, 90, 140\}$; and $3\times$ with $\{360, 135, 210\}$. The droplet volume is set to 100,000, 800,000, and 2,700,000 l.u. respectively, while L_R is fixed to 4.641. θ_e is set to 75° .

Figure A.10(a) shows the droplet morphology at steady state. Dashed orange lines denote the simulation window of $1\times$, dash-dotted green lines denote $2\times$, and dotted red lines denote $3\times$. At steady state, the droplet aspect ratio increases following the simulation window size. However, the difference is not significant (0.510, 0.524, 0.583) and the droplets adopt a similar shape in the clamshell configuration.

In Figure A.10(b), I plot the droplet Capillary number versus its Bond number. Symbols denote simulation results, while solid lines are obtained by fitting Equation (4.6) to the data for each simulation window. Overall, there is no significant difference between those three simulation windows. The relation is linear, with m_1^f of 1.00, 1.00, and 1.03 for $1\times$, $2\times$, and $3\times$, respectively, and the obtained a_1^f are close to each other (-2.234, -2.377, and -1.971).

Using 20 cores, the $1\times$ simulation window used 3.15GB of RAM, with an average simulation

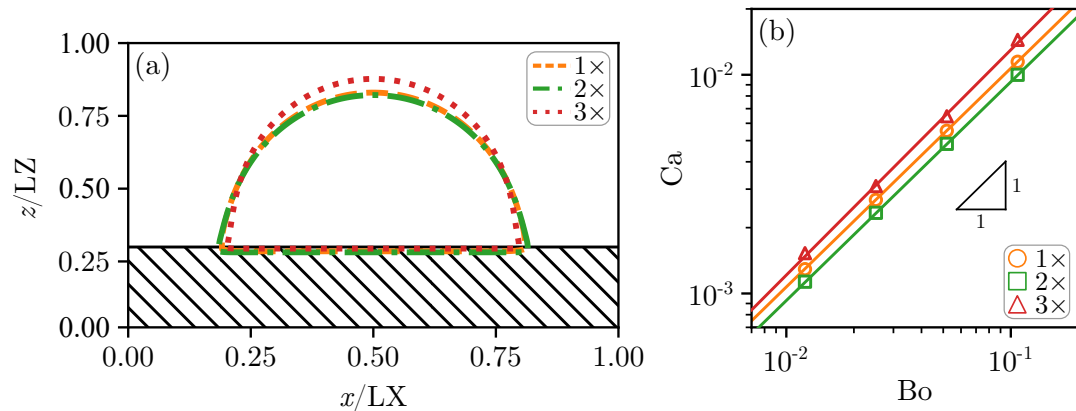


Figure A.10: (a) The droplet profile at steady state for different simulation window sizes. (b) Capillary number as a function of Bond number. For both figures, different colours and symbols denote different simulation window sizes.

time of 11m 17s per 10,000 time steps. Using 30 cores, the 2× simulation window used 8.92GB of RAM, with an average simulation time of 58m 30s per 10,000 time steps. Finally, using 45 cores, the 3× simulation window used 23.76GB of RAM, with an average simulation time of 4h 12m per 10,000 time steps. Considering the significant increase in the computational cost for 3× simulation window sizes with only a minor difference in the result, I choose $\{LX, LY, LZ\} = \{240, 90, 140\}$ for the work in Chapter 4.

A.4.2 Long-Range Fluid-Solid Interactions in Lattice Boltzmann Simulations

For this chapter, I did not perform a grid invariant test. The primary difficulty comes from the non-linearity of $\mathcal{D}(\mathbf{r})$ and $\mathcal{P}(\mathbf{r})$. In summary, for a pseudo-partial like potential, σ^{lrp} is used to control the maximum film thickness, while the apparent contact angle of the droplet is controlled by the balance between a , b , ζ^{lrp} , and f_s . Even though the attractive part of $\mathcal{P}(r)$ is linear, the repulsive part is decaying $1/r^6$, causing difficulty in increasing the film thickness while also keeping the droplet's apparent contact angle. Due to the limited scope of this work, I have not mapped the parameter space; therefore, I have not determined the exact relation between these parameters and the droplet shape.

A.4.3 Droplet Impact on Meshed Surfaces

Similar to the comparison for Chapter 4, I fix the dimensionless numbers and the physical parameters of the system and only change the system size ($LX, LY, LZ, r_d, S_s, T_s$), the external

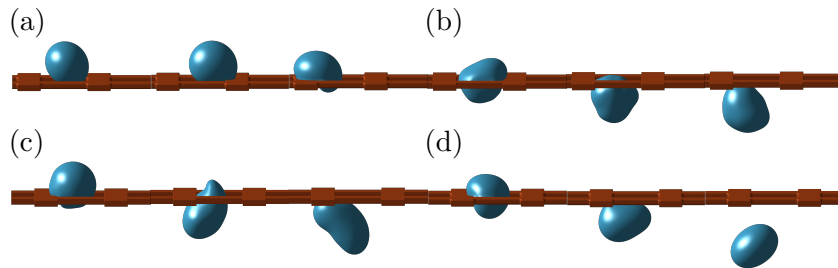


Figure A.11: Snippet of droplet hitting at $\phi_s = 90^\circ$ for (a) Simulation window $1\times$, impact point \mathcal{D} , (b) simulation window $4\times$, impact point \mathcal{D} , (c) simulation window $1\times$, impact point \mathcal{F} ; and (d) simulation window $4\times$, impact point \mathcal{F} .

acceleration (\mathbf{g}), and the droplet impact velocity (\mathbf{v}). I fix the Bond number to $\text{Bo} = 0.354$ to represent the effect of \mathbf{g} and the Weber number to $\text{We} = 2.169$ to represent the effect of \mathbf{v} . The droplet is hitting impact points \mathcal{D} and \mathcal{F} at $\phi_s = 90^\circ$. Three simulation window sizes ($\{\text{LX}, \text{LY}, \text{LZ}\}$) are compared: $1\times \{120, 120, 75\}$; $2\times \{240, 240, 150\}$; and $4\times \{480, 480, 300\}$.

At impact point \mathcal{D} , the droplet can enter the pore early when the simulation window sizes are $2\times$ and $4\times$. For the $1\times$ simulation window, the droplet still hits the edge of the solid bar, but instead of sliding into the pore, it bounces off to the other bar (Figure A.11(a)). Compared to the $2\times$ simulation window, the $4\times$ simulation window shows the droplet sticks longer to the bottom of the simulation window after entering it (Figure A.11(b)), causing a longer interaction time. The longer interaction time can be interpreted as one simulation time step is now equal to a smaller Δt in real life due to the increase in LX, LY, and LZ.

For impact point \mathcal{F} , all simulation windows show that the droplet will enter the pore relatively quickly. The $1\times$ simulation window has the shortest interaction time (3,000 time steps), followed by the $2\times$ and $4\times$ at 12,000 and $>25,000$ time steps. Similar to the impact point \mathcal{D} , at the $4\times$ simulation window, the droplet can stick to the bottom of the solid bar before leaving the structure (Figure A.11(c)), unlike at $1\times$ or $2\times$ (Figure A.11(d)) where the droplet quickly rolled into the pore.

Computational resource-wise, with 15 CPU cores, the $1\times$ simulation window used 3.50 GB RAM and took 1h 28m to run 10,000 time steps on average. Using 30 CPU cores, the $2\times$ simulation window used 16.88 GB RAM and took 6h 4m to run 10,000 time steps of simulation. Using 80 CPU cores, the $4\times$ simulation window used 137 GB RAM and took 19h 4m to run 10,000 time steps of simulation. Based on these results, I choose the simulation window size of $240 \times 240 \times 150$ to obtain the data in Chapter 6.

REFERENCES

- [1] J. Ju, H. Bai, Y. Zheng, T. Zhao, R. Fang, and L. Jiang, “A Multi-Structural and Multi-Functional Integrated Fog Collection System in Cactus”, *Nature Communications* **3**, 1–6 (2012).
- [2] H. Bai, J. Ju, Y. Zheng, and L. Jiang, “Functional Fibers with Unique Wettability Inspired by Spider Silks”, *Advanced Materials* **24**, 2786–2791 (2012).
- [3] B. J. Carroll, “Droplet Formation and Contact Angles of Liquids on Mammalian Hair Fibres”, *Journal of the Chemical Society, Faraday Transactions 1: Physical Chemistry in Condensed Phases* **85**, 3853–3860 (1989).
- [4] K. M. Takahashi, “Meniscus Shapes on Small Diameter Fibers”, *Journal of Colloid and Interface Science* **134**, 181–187 (1990).
- [5] P.-G. de Gennes, F. Brochard-Wyart, and D. Quere. *Capillarity and Wetting Phenomena: Drops, Bubbles, Pearls, Waves*. Springer Science & Business Media, (2003).
- [6] X. Chen, K. G. Kornev, Y. K. Kamath, and A. V. Neimark, “The Wicking Kinetics of Liquid Droplets into Yarns”, *Textile Research Journal* **71**, 862–869 (2001).
- [7] R. F. Lynch, “Hot-Dip Galvanizing Alloys”, *Journal of Metals* **39**, 39–41 (1987).
- [8] S. Akter and M. Hashmi, “High Speed Nylon Coating of Wire Using a Plasto-Hydrodynamic Pressure Unit”, *Journal of Materials Processing Technology* **63**, 453–457 (1997).
- [9] R. Ghosh, C. Patra, P. Singh, R. Ganguly, R. P. Sahu, I. Zhitomirsky, and I. K. Puri, “Influence of Metal Mesh Wettability on Fog Harvesting in Industrial Cooling Towers”, *Applied Thermal Engineering* **181**, 115963 (2020).
- [10] S. Ryu, P. Sen, Y. Nam, and C. Lee, “Water Penetration through a Superhydrophobic Mesh during a Drop Impact”, *Physical Review Letters* **118**, 014501 (2017).
- [11] T. Gilet, D. Terwagne, and N. Vandewalle, “Droplets Sliding on Fibres”, *European Physical Journal E* **31**, 253–262 (2010).
- [12] F. Weyer, M. Lismont, L. Dreesen, and N. Vandewalle, “Compound Droplet Manipulations on Fiber Arrays”, *Soft Matter* **11**, 7086–7091 (2015).
- [13] R. M. Von Spreckelsen, M. T. Harris, J. M. Wigzell, R. C. Fraser, A. Carletto, D. P. Mosquin, D. Justice, and J. P. S. Badyal, “Bioinspired Breathable Architecture for Water Harvesting”, *Scientific Reports* **5**, 16798 (2015).

- [14] T. Gilet, D. Terwagne, and N. Vandewalle, “Digital Microfluidics on a Wire”, *Applied Physics Letters* **95**, 014106 (2009).
- [15] K.-C. Park, S. S. Chhatre, S. Srinivasan, R. E. Cohen, and G. H. McKinley, “Optimal Design of Permeable Fiber Network Structures for Fog Harvesting”, *Langmuir* **29**, 13269–13277 (2013).
- [16] P. Brunet, F. Lapierre, F. Zoueshtiagh, V. Thomy, and A. Merlen, “To Grate a Liquid into Tiny Droplets by Its Impact on a Hydrophobic Microgrid”, *Applied Physics Letters* **95**, 254102 (2009).
- [17] D. Soto, H.-L. Girard, A. Le Helloco, T. Binder, D. Quéré, and K. K. Varanasi, “Droplet Fragmentation Using a Mesh”, *Physical Review Fluids* **3**, 083602 (2018).
- [18] F. F. Jackson, K. J. Kubiak, M. C. Wilson, M. Molinari, and V. Stetsyuk, “Droplet Misalignment Limit for Inkjet Printing into Cavities on Textured Surfaces”, *Langmuir* **35**, 9564–9571 (2019).
- [19] M. A. Gondal, M. S. Sadullah, M. A. Dastageer, G. H. McKinley, D. Panchanathan, and K. K. Varanasi, “Study of Factors Governing Oil–Water Separation Process Using TiO₂ Films Prepared by Spray Deposition of Nanoparticle Dispersions”, *ACS Applied Materials & Interfaces* **6**, 13422–13429 (2014).
- [20] M. A. Gondal, M. S. Sadullah, T. F. Qahtan, M. A. Dastageer, U. Baig, and G. H. McKinley, “Fabrication and Wettability Study of WO₃ Coated Photocatalytic Membrane for Oil-Water Separation: A Comparative Study with ZnO Coated Membrane”, *Scientific Reports* **7**, 1686 (2017).
- [21] F. Brochard-Wyart, J. M. Di Meglio, D. Quéré, and P. G. De Gennes, “Spreading of Nonvolatile Liquids in a Continuum Picture”, *Langmuir* **7**, 335–338 (1991).
- [22] É. Lorenceau and D. Quéré, “Drops on a Conical Wire”, *Journal of Fluid Mechanics* **510**, 29–45 (2004).
- [23] F. Weyer, A. Duchesne, and N. Vandewalle, “Switching Behavior of Droplets Crossing Nodes on a Fiber Network”, *Scientific Reports* **7**, 1–9 (2017).
- [24] J. Van Hulle, F. Weyer, S. Dorbolo, and N. Vandewalle, “Capillary Transport from Barrel to Clamshell Droplets on Conical Fibers”, *Physical Review Fluids* **6**, 024501 (2021).
- [25] S. Haefner, O. Bäümchen, and K. Jacobs, “Capillary Droplet Propulsion on a Fibre”, *Soft Matter* **11**, 6921–6926 (2015).
- [26] P.-B. Bintein, H. Bense, C. Clanet, and D. Quéré, “Self-Propelling Droplets on Fibres Subject to a Crosswind”, *Nature Physics* **15**, 1027–1032 (2019).
- [27] B. D. Texier and S. Dorbolo, “Droplets Climbing a Rotating Helical Fiber”, *The European Physical Journal E* **38**, 1–5 (2015).
- [28] J. Ju, K. Xiao, X. Yao, H. Bai, and L. Jiang, “Bioinspired Conical Copper Wire with Gradient Wettability for Continuous and Efficient Fog Collection”, *Advanced Materials* **25**, 5937–5942 (2013).

- [29] B. J. Mullins, R. D. Braddock, I. E. Agranovski, and R. A. Cropp, “Observation and Modelling of Barrel Droplets on Vertical Fibres Subjected to Gravitational and Drag Forces”, *Journal of Colloid and Interface Science* **300**, 704–712 (2006).
- [30] L. Rayleigh, “On the Instability of Jets”, *Proceedings of the London Mathematical Society* **1**, 4–13 (1878).
- [31] N. K. Adam, “Detergent Action and its Relation to Wetting and Emulsification”, *Journal of the Society of Dyers and Colourists* **53**, 121–129 (1937).
- [32] N. Le Grand, A. Daerr, and L. Limat, “Shape and Motion of Drops Sliding Down an Inclined Plane”, *Journal of Fluid Mechanics* **541**, 293–315 (2005).
- [33] T. Podgorski, J.-M. Flesselles, and L. Limat, “Corners, Cusps, and Pearls in Running Drops”, *Physical Review Letters* **87**, 036102 (2001).
- [34] J. C. Fernández-Toledano, T. D. Blake, L. Limat, and J. De Coninck, “A Molecular-Dynamics Study of Sliding Liquid Nanodrops: Dynamic Contact Angles and the Pearling Transition”, *Journal of Colloid and Interface Science* **548**, 66–76 (2019).
- [35] P. Zhu, R. Chen, C. Zhou, Y. Tian, and L. Wang, “Asymmetric Fibers for Efficient Fog Harvesting”, *Chemical Engineering Journal* **415**, 128944 (2021).
- [36] H. F. El-Maghraby, A. Alhumaidi, M. A. Alnaqbi, M. Sherif, Y. Tai, F. Hassan, and Y. E. Greish, “Bioinspired Asymmetric Surface Property of Functionalized Mesh to Maximize the Efficiency of Fog Harvesting”, *ChemNanoMat* **8**, e202200327 (2022).
- [37] U. Sen, T. Roy, S. Chatterjee, R. Ganguly, and C. M. Megaridis, “Post-impact Behavior of a Droplet Impacting on a Permeable Metal Mesh with a Sharp Wettability Step”, *Langmuir* **35**, 12711–12721 (2019).
- [38] Y.-Y. Tang, M.-J. Su, G.-W. Chu, Y. Luo, Y.-Y. Wang, L.-L. Zhang, and J.-F. Chen, “Impact Phenomena of Liquid Droplet Passing through Stainless Steel Wire Mesh Units”, *Chemical Engineering Science* **198**, 144–154 (2019).
- [39] G. Zhang, M. A. Quetzeri-Santiago, C. A. Stone, L. Botto, and J. R. Castrejón-Pita, “Droplet Impact Dynamics on Textiles”, *Soft Matter* **14**, 8182–8190 (2018).
- [40] K. Vontas, C. Boscariol, M. Andreadaki, A. Georgoulas, C. Crua, J. H. Walther, and M. Marengo, “Droplet Impact on Suspended Metallic Meshes: Effects of Wettability, Reynolds and Weber Numbers”, *Fluids* **5**, 81 (2020).
- [41] T. Lee and L. Liu, “Lattice Boltzmann Simulations of Micron-Scale Drop Impact on Dry Surfaces”, *Journal of Computational Physics* **229**, 8045–8063 (2010).
- [42] A. Mazloomi M., S. S. Chikatamarla, and I. V. Karlin, “Entropic Lattice Boltzmann Method for Multiphase Flows: Fluid-Solid Interfaces”, *Physical Review Energy* **92**, 023308 (2015).
- [43] K. A. Raman, R. K. Jaiman, T.-S. Lee, and H.-T. Low, “Lattice Boltzmann Simulations of Droplet Impact onto Surfaces with Varying Wettabilities”, *International Journal of Heat and Mass Transfer* **95**, 336 – 354 (2016).
- [44] M. Wöhrwag, C. Semprebon, A. Mazloomi M., I. Karlin, and H. Kusumaatmaja, “Ternary Free-Energy Entropic Lattice Boltzmann Model with a High Density Ratio”, *Physical Review Letters* **120**, 234501 (2018).

- [45] H. Huang, D. T. Thorne, M. G. Schaap, and M. C. Sukop, “Proposed Approximation for Contact Angles in Shan-and-Chen-Type Multicomponent Multiphase Lattice Boltzmann Models”, *Physical Review Energy* **76**, 066701 (2007).
- [46] L. Liu and T. Lee, “Wall Free Energy Based Polynomial Boundary Conditions for Non-ideal Gas Lattice Boltzmann Equation”, *International Journal of Modern Physics C* **20**, 1749–1768 (2009).
- [47] W. Gong, Y. Yan, S. Chen, and D. Giddings, “Numerical Study of Wetting Transitions on Biomimetic Surfaces Using a Lattice Boltzmann Approach with Large Density Ratio”, *Journal of Bionic Engineering* **14**, 486–496 (2017).
- [48] T. Akai, B. Bijeljic, and M. J. Blunt, “Wetting Boundary Condition for the Color-Gradient Lattice Boltzmann Method: Validation with Analytical and Experimental Data”, *Advances in Water Resources* **116**, 56–66 (2018).
- [49] C. E. Colosqui, M. E. Kavousanakis, A. G. Papathanasiou, and I. G. Kevrekidis, “Mesoscopic Model for Microscale Hydrodynamics and Interfacial Phenomena: Slip, Films, and Contact-Angle Hysteresis”, *Physical Review Energy* **87**, 013302 (2013).
- [50] Y. Çengel and J. Cimbala. *Fluid Mechanics Fundamentals and Applications*. McGraw-Hill US Higher Ed, third edition, (2013).
- [51] H. Y. Erbil. *Surface Chemistry of Solid and Liquid Interfaces*. Wiley-Blackwell, (2006).
- [52] E. Y. Bormashenko. *Wetting of Real Surfaces*. De Gruyter, Berlin, Boston, (2013).
- [53] B. Derjaguin, “The Definition and Magnitude of Disjoining Pressure and Its Role in the Statics and Dynamics of Thin Fluid Films”, *Kolloidnyj Žurnal* **17**, 207–214 (1955).
- [54] B. Derjaguin and N. Churaev, “Structural Component of Disjoining Pressure”, *Journal of Colloid and Interface Science* **49**, 249–255 (1974).
- [55] A. R. Herring and J. R. Henderson, “Simulation Study of the Disjoining Pressure Profile through a Three-Phase Contact Line”, *The Journal of Chemical Physics* **132**, 084702 (2010).
- [56] A. Adamson and A. Gast. *Physical Chemistry of Surfaces*. Wiley, New York, (1997).
- [57] H. Kusumaatmaja, J. Leopoldes, A. Dupuis, and J. Yeomans, “Drop Dynamics on Chemically Patterned Surfaces”, *Europhysics Letters* **73**, 740 (2006).
- [58] A. A. Darhuber, S. M. Troian, S. M. Miller, and S. Wagner, “Morphology of Liquid Microstructures on Chemically Patterned Surfaces”, *Journal of Applied Physics* **87**, 7768–7775 (2000).
- [59] S. Hu, X. Ren, M. Bachman, C. E. Sims, G. Li, and N. Allbritton, “Surface Modification of Poly (Dimethylsiloxane) Microfluidic Devices by Ultraviolet Polymer Grafting”, *Analytical Chemistry* **74**, 4117–4123 (2002).
- [60] Y. Zhao, Q. Lu, M. Li, and X. Li, “Anisotropic Wetting Characteristics on Submicrometer-Scale Periodic Grooved Surface”, *Langmuir* **23**, 6212–6217 (2007).
- [61] D. Xia, L. M. Johnson, and G. P. López, “Anisotropic Wetting Surfaces with One-Dimensional and Directional Structures: Fabrication Approaches, Wetting Properties and Potential Applications”, *Advanced Materials* **24**, 1287–1302 (2012).

- [62] C. Extrand, S. I. Moon, P. Hall, and D. Schmidt, “Superwetting of Structured Surfaces”, *Langmuir* **23**, 8882–8890 (2007).
- [63] K.-Y. Yeh, L.-J. Chen, and J.-Y. Chang, “Contact Angle Hysteresis on Regular Pillar-like Hydrophobic Surfaces”, *Langmuir* **24**, 245–251 (2008).
- [64] D. I. Yu, S. W. Doh, H. J. Kwak, H. C. Kang, H. S. Ahn, H. S. Park, M. Kiyofumi, and M. H. Kim, “Wetting State on Hydrophilic and Hydrophobic Micro-Textured Surfaces: Thermodynamic Analysis and X-Ray Visualization”, *Applied Physics Letters* **106**, 171602 (2015).
- [65] J. R. Panter and H. Kusumaatmaja, “The Impact of Surface Geometry, Cavitation, and Condensation on Wetting Transitions: Posts and Reentrant Structures”, *Journal of Physics: Condensed Matter* **29**, 084001 (2017).
- [66] J. Panter, Y. Gizaw, and H. Kusumaatmaja, “Multifaceted Design Optimization for Superomniphobic Surfaces”, *Science Advances* **5**, eaav7328 (2019).
- [67] J. Li, X. Han, W. Li, L. Yang, X. Li, and L. Wang, “Nature-Inspired Reentrant Surfaces”, *Progress in Materials Science* **133**, 101064 (2022).
- [68] K. Koch, B. Bhushan, Y. C. Jung, and W. Barthlott, “Fabrication of Artificial Lotus Leaves and Significance of Hierarchical Structure for Superhydrophobicity and Low Adhesion”, *Soft Matter* **5**, 1386–1393 (2009).
- [69] Y. Jiang, Z. Yang, T. Jiang, D. Shen, and J. Duan, “Banana Leaf Surface’s Janus Wettability Transition from the Wenzel State to Cassie–Baxter State and the Underlying Mechanism”, *Materials* **15**, 917 (2022).
- [70] Ç. Koşak Söz, S. Trosien, and M. Biesalski, “Superhydrophobic Hybrid Paper Sheets with Janus-Type Wettability”, *ACS Applied Materials & Interfaces* **10**, 37478–37488 (2018).
- [71] A. Lafuma and D. Quéré, “Slippery Pre-suffused Surfaces”, *Europhysics Letters* **96**, 56001 (2011).
- [72] T.-S. Wong, S. H. Kang, S. K. Tang, E. J. Smythe, B. D. Hatton, A. Grinthal, and J. Aizenberg, “Bioinspired Self-Repairing Slippery Surfaces with Pressure-Stable Omniphobicity”, *Nature* **477**, 443–447 (2011).
- [73] H. F. Bohn and W. Federle, “Insect Aquaplaning: Nepenthes Pitcher Plants Capture Prey with the Peristome, a Fully Wettable Water-Lubricated Anisotropic Surface”, *Proceedings of the National Academy of Sciences* **101**, 14138–14143 (2004).
- [74] C. Semprebon, G. McHale, and H. Kusumaatmaja, “Apparent Contact Angle and Contact Angle Hysteresis on Liquid Infused Surfaces”, *Soft Matter* **13**, 101–110 (2017).
- [75] M. Villegas, Y. Zhang, N. Abu Jarad, L. Soleymani, and T. F. Didar, “Liquid-Infused Surfaces: A Review of Theory, Design, and Applications”, *ACS Nano* **13**, 8517–8536 (2019).
- [76] H. B. Eral, J. De Ruiter, R. De Ruiter, J. M. Oh, C. Semprebon, M. Brinkmann, and F. Mugele, “Drops on Functional Fibers: From Barrels to Clamshells and Back”, *Soft Matter* **7**, 5138–5143 (2011).

- [77] G. McHale, M. I. Newton, and B. Carroll, “The Shape and Stability of Small Liquid Drops on Fibers”, *Oil & Gas Science and Technology* **56**, 47–54 (2001).
- [78] G. McHale and M. Newton, “Global Geometry and the Equilibrium Shapes of Liquid Drops on Fibers”, *Colloids and Surfaces A: Physicochemical and Engineering Aspects* **206**, 79–86 (2002).
- [79] R. De Ruiter, J. de Ruiter, H. B. Eral, C. Semprebon, M. Brinkmann, and F. Mugele, “Buoyant droplets on functional fibers”, *Langmuir* **28**, 13300–13306 (2012).
- [80] M. Amrei, M. Davoudi, G. Chase, and H. V. Tafreshi, “Effects of Roughness on Droplet Apparent Contact Angles on a Fiber”, *Separation and Purification Technology* **180**, 107–113 (2017).
- [81] N. Bala, M. Pepona, I. Karlin, H. Kusumaatmaja, and C. Semprebon, “Wetting Boundaries for a Ternary High-Density-Ratio Lattice Boltzmann Method”, *Physical Review Energy* **100**, 013308 (2019).
- [82] G. H. McKinley and M. Renardy, “Wolfgang von Ohnesorge”, *Physics of Fluids* **23** (2011).
- [83] H. B. Eral, D. ’t Mannetje, and J. M. Oh, “Contact Angle Hysteresis: A Review of Fundamentals and Applications”, *Colloid and Polymer Science* **291**, 247–260 (2013).
- [84] R. S. Abiev, “Effect of Contact-Angle Hysteresis on the Pressure Drop under Slug Flow Conditions in Minichannels and Microchannels”, *Theoretical Foundations of Chemical Engineering* **49**, 414–421 (2015).
- [85] O. Voinov, “Hydrodynamics of Wetting”, *Fluid Dynamics* **11**, 714–721 (1976).
- [86] R. Cox, “The Dynamics of the Spreading of Liquids on a Solid Surface. Part 1. Viscous Flow”, *Journal of Fluid Mechanics* **168**, 169–194 (1986).
- [87] D. Bonn, J. Eggers, J. Indekeu, J. Meunier, and E. Rolley, “Wetting and Spreading”, *Reviews of Modern Physics* **81**, 739 (2009).
- [88] L. Landau and E. M. Lifshitz. *Fluid Mechanics*, volume 6 of *Course of Theoretical Physics*. Pergamon Press, 2nd english edition, (1987).
- [89] C. Huh and L. E. Scriven, “Hydrodynamic Model of Steady Movement of a Solid/Liquid/Fluid Contact Line”, *Journal of Colloid and Interface Science* **35**, 85–101 (1971).
- [90] A. Mohammad Karim, “A Review of Physics of Moving Contact Line Dynamics Models and Its Applications in Interfacial Science”, *Journal of Applied Physics* **132**, 080701 (2022).
- [91] T. Blake and J. Haynes, “Kinetics of Liquid–Liquid Displacement”, *Journal of Colloid and Interface Science* **30**, 421–423 (1969).
- [92] P. Petrov and I. Petrov, “A Combined Molecular-Hydrodynamic Approach to Wetting Kinetics”, *Langmuir* **8**, 1762–1767 (1992).
- [93] F. Brochard-Wyart and P. De Gennes, “Dynamics of Partial Wetting”, *Advances in Colloid and Interface Science* **39**, 1–11 (1992).

- [94] T. Krüger, H. Kusumaatmaja, A. Kuzmin, O. Shardt, G. Silva, and E. M. Viggén. *The Lattice Boltzmann Method - Principles and Practice*. Springer International Publishing, (2016).
- [95] S. Patankar. *Numerical Heat Transfer and Fluid Flow*. Taylor & Francis, (1980).
- [96] J. H. Ferziger, M. Perić, and R. L. Street. *Computational Methods for Fluid Dynamics*, volume 3. Springer, (2002).
- [97] H. K. Versteeg and W. Malalasekera. *An Introduction to Computational Fluid Dynamics: The Finite Volume Method*. Pearson Education, (2007).
- [98] O. C. Zienkiewicz, R. L. Taylor, and P. Nithiarasu. *The Finite Element Method for Fluid Dynamics*. Butterworth-Heinemann, (2013).
- [99] C. A. Fletcher. *Computational Techniques for Fluid Dynamics: Specific Techniques for Different Flow Categories*. Springer Science & Business Media, (2012).
- [100] D. Frenkel and B. Smit. *Understanding Molecular Simulation: From Algorithms to Applications*, volume 1. Elsevier, (2001).
- [101] M. Karplus and J. A. McCammon, “Molecular Dynamics Simulations of Biomolecules”, *Nature Structural Biology* **9**, 646–652 (2002).
- [102] G. A. Bird. *Molecular Gas Dynamics and the Direct Simulation of Gas Flows*. Clarendon Press, (1994).
- [103] C. Shen. *Rarefied Gas Dynamics: Fundamentals, Simulations and Micro Flows*. Springer Science & Business Media, (2006).
- [104] P. Hoogerbrugge and J. Koelman, “Simulating Microscopic Hydrodynamic Phenomena with Dissipative Particle Dynamics”, *Europhysics Letters* **19**, 155 (1992).
- [105] P. Espanol and P. Warren, “Statistical Mechanics of Dissipative Particle Dynamics”, *Europhysics Letters* **30**, 191 (1995).
- [106] A. Malevanets and R. Kapral, “Mesoscopic Model for Solvent Dynamics”, *The Journal of Chemical Physics* **110**, 8605–8613 (1999).
- [107] A. Malevanets and R. Kapral, “Solute Molecular Dynamics in a Mesoscale Solvent”, *The Journal of Chemical Physics* **112**, 7260–7269 (2000).
- [108] S. Succi. *The Lattice Boltzmann Equation: For Fluid Dynamics and Beyond*. Oxford University Press, (2001).
- [109] S. Succi. *The Lattice Boltzmann Equation: For Complex States of Flowing Matter*. Oxford University Press, first edition, (2018).
- [110] R. R. Nourgaliev, T.-N. Dinh, T. G. Theofanous, and D. Joseph, “The Lattice Boltzmann Equation Method: Theoretical Interpretation, Numerics and Implications”, *International Journal of Multiphase Flow* **29**, 117–169 (2003).
- [111] S. Geller, M. Krafczyk, J. Tölke, S. Turek, and J. Hron, “Benchmark Computations Based on Lattice-Boltzmann, Finite Element and Finite Volume Methods for Laminar Flows”, *Computers & Fluids* **35**, 888–897 (2006).

- [112] P. L. Bhatnagar, E. P. Gross, and M. Krook, “A Model for Collision Processes in Gases. I. Small Amplitude Processes in Charged and Neutral One-Component Systems”, *Physical Review* **94**, 511 (1954).
- [113] Y. H. Qian, D. D’Humières, and P. Lallemand, “Lattice BGK Models for Navier-Stokes Equation”, *Europhysics Letters* **17**, 479–484 (1992).
- [114] D. M. Anderson, G. B. McFadden, and A. A. Wheeler, “Diffuse-Interface Methods in Fluid Mechanics”, *Annual review of fluid mechanics* **30**, 139–165 (1998).
- [115] T. E. Tezduyar, “Interface-Tracking and Interface-Capturing Techniques for Finite Element Computation of Moving Boundaries and Interfaces”, *Computer Methods in Applied Mechanics and Engineering* **195**, 2983–3000 (2006).
- [116] J. Glimm, E. Isaacson, D. Marchesin, and O. McBryan, “Front Tracking for Hyperbolic Systems”, *Advances in Applied Mathematics* **2**, 91–119 (1981).
- [117] G. Tryggvason, B. Bunner, A. Esmaeeli, D. Juric, N. Al-Rawahi, W. Tauber, J. Han, S. Nas, and Y.-J. Jan, “A Front-Tracking Method for the Computations of Multiphase Flow”, *Journal of Computational Physics* **169**, 708–759 (2001).
- [118] J. Hua, J. F. Stene, and P. Lin, “Numerical Simulation of 3D Bubbles Rising in Viscous Liquids Using a Front Tracking Method”, *Journal of Computational Physics* **227**, 3358–3382 (2008).
- [119] J. E. Welch, F. H. Harlow, J. P. Shannon, and B. J. Daly. “The MAC method—a computing technique for solving viscous, incompressible, transient fluid-flow problems involving free surfaces”. Technical report, Los Alamos National Lab.(LANL), Los Alamos, NM (United States), (1965).
- [120] S. Mckee, M. F. Tomé, J. A. Cuminato, A. Castelo, and V. G. Ferreira, “Recent Advances in the Marker and Cell Method”, *Archives of Computational Methods in Engineering* **11**, 107–142 (2004).
- [121] T. Gallouët, R. Herbin, J.-C. Latché, and K. Mallem, “Convergence of the Marker-And-Cell Scheme for the Incompressible Navier–Stokes Equations on Non-uniform Grids”, *Foundations of Computational Mathematics* **18**, 249–289 (2018).
- [122] S. Mirjalili, S. S. Jain, and M. Dodd, “Interface-Capturing Methods for Two-Phase Flows: An Overview and Recent Developments”, *Center for Turbulence Research Annual Research Briefs* **2017**, 13 (2017).
- [123] F. De Sousa, N. Mangiavacchi, L. G. Nonato, A. Castelo, M. F. Tomé, V. G. Ferreira, J. A. Cuminato, and S. Mckee, “A Front-Tracking/Front-Capturing Method for the Simulation of 3D Multi-Fluid Flows With Free Surfaces”, *Journal of Computational Physics* **198**, 469–499 (2004).
- [124] S. M. Allen and J. W. Cahn, “Mechanisms of Phase Transformations Within the Miscibility Gap of Fe-Rich Fe-Al Alloys”, *Acta Metallurgica* **24**, 425–437 (1976).
- [125] Y. Sun and C. Beckermann, “Sharp Interface Tracking Using the Phase-Field Equation”, *Journal of Computational Physics* **220**, 626–653 (2007).
- [126] M. Geier, A. Fakhari, and T. Lee, “Conservative Phase-Field Lattice Boltzmann Model for Interface Tracking Equation”, *Physical Review E* **91**, 063309 (2015).

- [127] J. W. Cahn and J. E. Hilliard, “Free Energy of a Nonuniform System. I. Interfacial Free Energy”, *The Journal of Chemical Physics* **28**, 258–267 (1958).
- [128] J. W. Cahn and J. E. Hilliard, “Free Energy of a Nonuniform System. III. Nucleation in a Two-Component Incompressible Fluid”, *The Journal of Chemical Physics* **31**, 688–699 (1959).
- [129] H. Wang, Z. Chai, B. Shi, and H. Liang, “Comparative Study of the Lattice Boltzmann Models for Allen-Cahn and Cahn-Hilliard Equations”, *Physical Review E* **94**, 033304 (2016).
- [130] A.-K. Tornberg and B. Engquist, “A Finite Element Based Level-Set Method for Multiphase Flow Applications”, *Computing and Visualization in Science* **3**, 93–101 (2000).
- [131] S. Osher and R. Fedkiw. *Level Set Methods and Dynamic Implicit Surfaces*. Springer New York, NY, (2003).
- [132] Z. Wang, J. Yang, B. Koo, and F. Stern, “A Coupled Level Set and Volume-Of-Fluid Method for Sharp Interface Simulation of Plunging Breaking Waves”, *International Journal of Multiphase Flow* **35**, 227–246 (2009).
- [133] S. Van der Pijl, A. Segal, C. Vuik, and P. Wesseling, “A Mass-Conserving Level-Set Method for Modelling of Multi-Phase Flows”, *International Journal for Numerical Methods in Fluids* **47**, 339–361 (2004).
- [134] E. Olsson and G. Kreiss, “Conservative Level Set Method for Two Phase Flow”, *Journal of Computational Physics* **210**, 225–246 (2005).
- [135] F. Gibou, R. Fedkiw, and S. Osher, “A Review of Level-Set Methods and Some Recent Applications”, *Journal of Computational Physics* **353**, 82–109 (2018).
- [136] C. K. Aidun and J. R. Clausen, “Lattice-Boltzmann Method for Complex Flows”, *Annual Review of Fluid Mechanics* **42**, 439–472 (2010).
- [137] P. Yuan and L. Schaefer, “Equations of State in a Lattice Boltzmann Model”, *Physics of Fluids* **18**, 042101 (2006).
- [138] D. C. Johnston. *Advances in Thermodynamics of the van der Waals Fluid*. 2053-2571. Morgan & Claypool Publishers, (2014).
- [139] A. Kupershtokh, D. Medvedev, and D. Karpov, “On Equations of State in a Lattice Boltzmann Method”, *Computers & Mathematics with Applications* **58**, 965 – 974 (2009).
- [140] A. J. Ladd, “Numerical Simulations of Particulate Suspensions via a Discretized Boltzmann Equation. Part 1. Theoretical Foundation”, *Journal of Fluid Mechanics* **271**, 285–309 (1994).
- [141] I. Ginzbourg and P. Adler, “Boundary Flow Condition Analysis for the Three-Dimensional Lattice Boltzmann Model”, *Journal de Physique II* **4**, 191–214 (1994).
- [142] A. Briant and J. Yeomans, “Lattice Boltzmann Simulations of Contact Line Motion. Ii. Binary Fluids”, *Physical Review Energy* **69**, 031603 (2004).

- [143] C. Semperebon, T. Krüger, and H. Kusumaatmaja, “Ternary Free-Energy Lattice Boltzmann Model with Tunable Surface Tensions and Contact Angles”, *Physical Review Energy* **93**, 033305 (2016).
- [144] H. Kusumaatmaja and J. M. Yeomans. “Lattice Boltzmann Simulations of Wetting and Drop Dynamics”. In *Simulating Complex Systems by Cellular Automata*, 241–274. Springer (2010).
- [145] D. d’Humières, “Multiple–Relaxation–Time Lattice Boltzmann Models in Three Dimensions”, *Philosophical Transactions of the Royal Society of London. Series A: Mathematical, Physical and Engineering Sciences* **360**, 437–451 (2002).
- [146] R. Benzi, S. Succi, and M. Vergassola, “The Lattice Boltzmann Equation: Theory and Applications”, *Physics Reports* **222**, 145–197 (1992).
- [147] P. J. Dellar, “Nonhydrodynamic Modes and a Priori Construction of Shallow Water Lattice Boltzmann Equations”, *Physical Review Energy* **65**, 036309 (2002).
- [148] H. Kusumaatmaja. *Lattice Boltzmann Studies of Wetting and Spreading on Patterned Surfaces*. PhD thesis, University of Oxford, (2008).
- [149] Z. Guo, C. Zheng, and B. Shi, “Discrete Lattice Effects on the Forcing Term in the Lattice Boltzmann Method”, *Physical Review Energy* **65**, 046308 (2002).
- [150] H. Huang, M. Krafczyk, and X. Lu, “Forcing Term in Single-Phase and Shan-Chen-Type Multiphase Lattice Boltzmann Models”, *Physical Review Energy* **84**, 046710 (2011).
- [151] J. Van Hulle, F. Weyer, S. Dorbolo, and N. Vandewalle, “Capillary Transport from Barrel to Clamshell Droplets on Conical Fibers”, *Physical Review Fluids* **6**, 024501 (2021).
- [152] Y.-E. Liang, H.-K. Tsao, and Y.-J. Sheng, “Drops on Hydrophilic Conical Fibers: Gravity Effect and Coexistent States”, *Langmuir* **31**, 1704–1710 (2015).
- [153] J. McCarthy, D. Vella, and A. A. Castrejón-Pita, “Dynamics of Droplets on Cones: Self-Propulsion Due to Curvature Gradients”, *Soft Matter* **15**, 9997–10004 (2019).
- [154] M. Davoudi, J. Fang, and G. Chase, “Barrel Shaped Droplet Movement at Junctions of Perpendicular Fibers with Different Orientations to the Air Flow Direction”, *Separation and Purification Technology* **162**, 1–5 (2016).
- [155] A. Sauret, F. Boulogne, D. Cébron, E. Dressaire, and H. A. Stone, “Wetting Morphologies on an Array of Fibers of Different Radii”, *Soft Matter* **11**, 4034–4040 (2015).
- [156] H. Aziz and H. V. Tafreshi, “Competing Forces on a Liquid Bridge between Parallel and Orthogonal Dissimilar Fibers”, *Soft Matter* **15**, 6967–6977 (2019).
- [157] F. Wang and U. D. Schiller, “Hysteresis in Spreading and Retraction of Liquid Droplets on Parallel Fiber Rails”, *Soft Matter* **17**, 5486–5498 (2021).
- [158] I. Peters, J. H. Snoeijer, A. Daerr, and L. Limat, “Coexistence of Two Singularities in Dewetting Flows: Regularizing the Corner Tip”, *Physical Review Letters* **103**, 114501 (2009).

- [159] S. Engelnkemper, M. Wilczek, S. V. Gurevich, and U. Thiele, “Morphological Transitions of Sliding Drops: Dynamics and Bifurcations”, *Physical Review Fluids* **1**, 073901 (2016).
- [160] J. Yang, X. Ma, L. Fei, X. Zhang, K. H. Luo, and S. Shuai, “Effects of Hysteresis Window on Contact Angle Hysteresis Behaviour at Large Bond Number”, *Journal of Colloid and Interface Science* **566**, 327–337 (2020).
- [161] T. Inamuro, S. Tajima, and F. Ogino, “Lattice Boltzmann Simulation of Droplet Collision Dynamics”, *International Journal of Heat and Mass Transfer* **47**, 4649–4657 (2004).
- [162] A. Dupuis and J. Yeomans, “Modeling Droplets on Superhydrophobic Surfaces: Equilibrium States and Transitions”, *Langmuir* **21**, 2624–2629 (2005).
- [163] S. Khirevich, I. Ginzburg, and U. Tallarek, “Coarse- And Fine-Grid Numerical Behavior of MRT/TRT Lattice-Boltzmann Schemes in Regular and Random Sphere Packings”, *Journal of Computational Physics* **281**, 708–742 (2015).
- [164] Y. Liu, M. Andrew, J. Li, J. M. Yeomans, and Z. Wang, “Symmetry Breaking In Drop Bouncing on Curved Surfaces”, *Nature Communications* **6**, 1–8 (2015).
- [165] R. N. Wenzel, “Resistance of Solid Surfaces to Wetting by Water”, *Industrial & Engineering Chemistry* **28**, 988–994 (1936).
- [166] L. Wang, H.-b. Huang, and X.-Y. Lu, “Scheme for Contact Angle and Its Hysteresis in a Multiphase Lattice Boltzmann Method”, *Physical Review E* **87**, 013301 (2013).
- [167] H. Liu, Y. Ju, N. Wang, G. Xi, and Y. Zhang, “Lattice Boltzmann Modeling of Contact Angle and Its Hysteresis in Two-Phase Flow With Large Viscosity Difference”, *Physical Review E* **92**, 033306 (2015).
- [168] H.-Y. Kim, H. J. Lee, and B. H. Kang, “Sliding of Liquid Drops Down an Inclined Solid Surface”, *Journal of Colloid and Interface Science* **247**, 372–380 (2002).
- [169] B. A. Puthenveetil, V. K. Senthilkumar, and E. J. Hopfinger, “Motion of Drops on Inclined Surfaces in the Inertial Regime”, *Journal of Fluid Mechanics* **726**, 26–61 (2013).
- [170] R. Sahu, S. Sinha-Ray, A. Yarin, and B. Pourdeyhimi, “Blowing Drops off a Filament”, *Soft Matter* **9**, 6053–6071 (2013).
- [171] L. Esibov, D. Sarkisov, U.-S. Jeng, M. Crow, and A. Steyerl, “Dynamics of Pseudo-Partial Wetting Studied by Neutron Reflectometry”, *Physica B: Condensed Matter* **241**, 1077–1079 (1997).
- [172] H. Kellay, J. Meunier, and B. Binks, “Wetting Properties of N-Alkanes on AOT Monolayers at the Brine-Air Interface”, *Physical Review Letters* **69**, 1220 (1992).
- [173] K. M. Wilkinson, C. D. Bain, H. Matsubara, and M. Aratono, “Wetting of Surfactant Solutions by Alkanes”, *ChemPhysChem* **6**, 547–555 (2005).
- [174] L. Du, H. Bodiguel, and A. Colin, “Thermally Activated Depinning Motion of Contact Lines in Pseudopartial Wetting”, *Physical Review Energy* **90**, 012402 (2014).

- [175] C. Schune, M. Yonger, B. Bresson, C. Fretigny, L. Guy, T. Chaussée, F. Lequeux, H. Montes, and E. Verneuil, “Combining Ellipsometry and AFM To Probe Subnanometric Precursor Film Dynamics of Polystyrene Melts”, *Langmuir* **35**, 7727–7734 (2019).
- [176] L. Du, H. Bodiguel, C. Cottin, and A. Colin, “Dynamics of Liquid–Liquid Menisci in Pseudo-Partial Wetting”, *Chemical Engineering and Processing: Process Intensification* **68**, 3–6 (2013).
- [177] H. Matsubara, T. Shigeta, Y. Takata, N. Ikeda, H. Sakamoto, T. Takiue, and M. Aratono, “Effect of Molecular Structure of Oil on Wetting Transition on Surfactant Solutions”, *Colloids and Surfaces A: Physicochemical and Engineering Aspects* **301**, 141–146 (2007).
- [178] J. Buehrle, S. Herminghaus, and F. Mugele, “Interface Profiles near Three-Phase Contact Lines in Electric Fields”, *Physical Review Letters* **91**, 086101 (2003).
- [179] M. Bienia, F. Mugele, C. Quilliet, and P. Ballet, “Droplets Profiles and Wetting Transitions in Electric Fields”, *Physica A: Statistical Mechanics and Its Applications* **339**, 72–79 (2004).
- [180] Y. Di and X.-P. Wang, “Precursor Simulations in Spreading Using a Multi-Mesh Adaptive Finite Element Method”, *Journal of Computational Physics* **228**, 1380–1390 (2009).
- [181] H. S. H. Mohand, H. Hoang, G. Galliero, and D. Legendre, “On the Use of a Friction Model in a Volume of Fluid Solver for the Simulation of Dynamic Contact Lines”, *Journal of Computational Physics* **393**, 29–45 (2019).
- [182] P. Van Remoortere, J. Mertz, L. Scriven, and H. Davis, “Wetting Behavior of a Lennard-Jones System”, *The Journal of Chemical Physics* **110**, 2621–2628 (1999).
- [183] C. Wu, T. Qian, and P. Sheng, “Droplet Spreading Driven by Van Der Waals Force: A Molecular Dynamics Study”, *Journal of Physics: Condensed Matter* **22**, 325101 (2010).
- [184] F. Oktasendra, A. Jusufi, A. R. Konicek, M. S. Yeganeh, J. R. Panter, and H. Kusumaatmaja, “Phase Field Simulation of Liquid Filling on Grooved Surfaces for Complete, Partial, and Pseudo-Partial Wetting Cases”, *The Journal of Chemical Physics* **158** (2023).
- [185] D. Noble and J. Torczynski, “A Lattice-Boltzmann Method for Partially Saturated Computational Cells”, *International Journal of Modern Physics C* **9**, 1189–1201 (1998).
- [186] I. Ginzburg and D. d’Humières, “Multireflection Boundary Conditions for Lattice Boltzmann Models”, *Physical Review Energy* **68**, 066614 (2003).
- [187] A. Tiwari and S. Vanka, “A Ghost Fluid Lattice Boltzmann Method for Complex Geometries”, *International Journal for Numerical Methods in Fluids* **69**, 481–498 (2012).
- [188] T. Inamuro, “Lattice Boltzmann Methods for Moving Boundary Flows”, *Fluid Dynamics Research* **44**, 024001 (2012).
- [189] T. Lee and P. F. Fischer, “Eliminating Parasitic Currents in the Lattice Boltzmann Equation Method for Nonideal Gases”, *Physical Review Energy* **74**, 046709 (2006).

- [190] C. Pooley and K. Furtado, “Eliminating Spurious Velocities in the Free-Energy Lattice Boltzmann Method”, *Physical Review Energy* **77**, 046702 (2008).
- [191] T. Seta and K. Okui, “Effects of Truncation Error of Derivative Approximation for Two-Phase Lattice Boltzmann Method”, *Journal of Fluid Science and Technology* **2**, 139–151 (2007).
- [192] J. Wigzell, R. Racovita, B. Stentiford, M. Wilson, M. Harris, I. Fletcher, D. Mosquin, D. Justice, S. Beaumont, R. Jetter, and J. Badyal, “Smart Water Channelling through Dual Wettability by Leaves of the Bamboo *Phyllostachys Aurea*”, *Colloids and Surfaces A: Physicochemical and Engineering Aspects* **506**, 344 – 355 (2016).
- [193] P. Li, B. Zhang, H. Zhao, L. Zhang, Z. Wang, X. Xu, T. Fu, X. Wang, Y. Hou, Y. Fan, and L. Wang, “Unidirectional Droplet Transport on the Biofabricated Butterfly Wing”, *Langmuir* **34**, 12482–12487 (2018).
- [194] C. Neinhuis and W. Barthlott, “Characterization and Distribution of Water-Repellent, Self-Cleaning Plant Surfaces”, *Annals of Botany* **79**, 667–677 (1997).
- [195] J. B. Boreyko and C.-H. Chen, “Self-Propelled Dropwise Condensate on Superhydrophobic Surfaces”, *Physical Review Letters* **103**, 184501 (2009).
- [196] B. K. Ahn, D. W. Lee, J. N. Israelachvili, and J. H. Waite, “Surface-Initiated Self-Healing of Polymers in Aqueous Media”, *Nature Materials* **13**, 867–872 (2014).
- [197] T. Mouterde, G. Lehoucq, S. Xavier, A. Checco, C. T. Black, A. Rahman, T. Midavaine, C. Clanet, and D. Quéré, “Antifogging Abilities of Model Nanotextures”, *Nature Materials* **16**, 658–663 (2017).
- [198] Z. Han, X. Feng, Z. Guo, S. Niu, and L. Ren, “Flourishing Bioinspired Antifogging Materials with Superwettability: Progresses and Challenges”, *Advanced Materials* **30**, 1704652 (2018).
- [199] P. Kim, T.-S. Wong, J. Alvarenga, M. J. Kreder, W. E. Adorno-Martinez, and J. Aizenberg, “Liquid-Infused Nanostructured Surfaces with Extreme Anti-ice and Anti-frost Performance”, *ACS Nano* **6**, 6569–6577 (2012).
- [200] M. Balordi, A. Cammi, G. S. de Magistris, and C. Chemelli, “Role of Micrometric Roughness on Anti-ice Properties and Durability of Hierarchical Super-Hydrophobic Aluminum Surfaces”, *Surface and Coatings Technology* **374**, 549–556 (2019).
- [201] Y. Son, C. Kim, D. H. Yang, and D. J. Ahn, “Spreading of an Inkjet Droplet on a Solid Surface with a Controlled Contact Angle at Low Weber and Reynolds Numbers”, *Langmuir* **24**, 2900–2907 (2008).
- [202] S. D. Hoath. *Fundamentals of Inkjet Printing: The Science of Inkjet and Droplets*. John Wiley & Sons, (2016).
- [203] H. Sirringhaus, T. Kawase, R. Friend, T. Shimoda, M. Inbasekaran, W. Wu, and E. P. Woo, “High-Resolution Inkjet Printing of All-Polymer Transistor Circuits”, *Science* **290**, 2123–2126 (2000).
- [204] L. Mishchenko, B. Hatton, V. Bahadur, J. A. Taylor, T. Krupenkin, and J. Aizenberg, “Design of Ice-Free Nanostructured Surfaces Based on Repulsion of Impacting Water Droplets”, *ACS Nano* **4**, 7699–7707 (2010).

- [205] C. Sodtke and P. Stephan, “Spray Cooling on Micro Structured Surfaces”, *International Journal of Heat and Mass Transfer* **50**, 4089–4097 (2007).
- [206] J.-n. Chen, Z. Zhang, R.-n. Xu, X.-l. Ouyang, and P.-x. Jiang, “Numerical Investigation of the Flow Dynamics and Evaporative Cooling of Water Droplets Impinging onto Heated Surfaces: An Effective Approach to Identify Spray Cooling Mechanisms”, *Langmuir* **32**, 9135–9155 (2016).
- [207] M. A. Hanjra and M. E. Qureshi, “Global Water Crisis and Future Food Security in an Era of Climate Change”, *Food Policy* **35**, 365 – 377 (2010).
- [208] B. Sivakumar, “Water Crisis: From Conflict to Cooperation—an Overview”, *Hydrological Sciences Journal* **56**, 531–552 (2011).
- [209] E. L. Villarreal and A. Dixon, “Analysis of a Rainwater Collection System for Domestic Water Supply in Ringdansen, Norrköping, Sweden”, *Building and Environment* **40**, 1174–1184 (2005).
- [210] D. Słyś, “Potential of Rainwater Utilization in Residential Housing in Poland”, *Water and Environment Journal* **23**, 318–325 (2009).
- [211] N. İ. Şahin and G. Manioğlu, “Water Conservation through Rainwater Harvesting Using Different Building Forms in Different Climatic Regions”, *Sustainable Cities and Society* **44**, 367–377 (2019).
- [212] L. Xu, S. Yang, Y. Zhang, Z. Jin, X. Huang, K. Bei, M. Zhao, H. Kong, and X. Zheng, “A Hydroponic Green Roof System for Rainwater Collection and Greywater Treatment”, *Journal of Cleaner Production* **261**, 121132 (2020).
- [213] Y. Tian, P. Zhu, X. Tang, C. Zhou, J. Wang, T. Kong, M. Xu, and L. Wang, “Large-Scale Water Collection of Bioinspired Cavity-Microfibers”, *Nature Communications* **8**, 1–9 (2017).
- [214] A. Yarin, “Drop Impact Dynamics: Splashing, Spreading, Receding, Bouncing”, *Annual Review of Fluid Mechanics* **38**, 159–192 (2006).
- [215] X. Li, L. Mao, and X. Ma, “Dynamic Behavior of Water Droplet Impact on Microtextured Surfaces: The Effect of Geometrical Parameters on Anisotropic Wetting and the Maximum Spreading Diameter”, *Langmuir* **29**, 1129–1138 (2013).
- [216] N. Laan, K. G. de Bruin, D. Bartolo, C. Josserand, and D. Bonn, “Maximum Diameter of Impacting Liquid Droplets”, *Physical Review Applied* **2**, 044018 (2014).
- [217] M. Abolghasemibizaki, N. Dilmaghani, R. Mohammadi, and C. E. Castano, “Viscous Droplet Impact on Nonwetable Textured Surfaces”, *Langmuir* **35**, 10752–10761 (2019).
- [218] V. Vaikuntanathan and D. Sivakumar, “Maximum Spreading of Liquid Drops Impacting on Groove-Textured Surfaces: Effect of Surface Texture”, *Langmuir* **32**, 2399–2409 (2016).
- [219] Y. Liu, L. Moevius, X. Xu, T. Qian, J. M. Yeomans, and Z. Wang, “Pancake Bouncing on Superhydrophobic Surfaces”, *Nature Physics* **10**, 515–519 (2014).
- [220] J. T. Pearson, D. Maynes, and B. W. Webb, “Droplet Impact Dynamics for Two Liquids Impinging on Anisotropic Superhydrophobic Surfaces”, *Experiments in Fluids* **53**, 603–618 (2012).

- [221] J. Xiao, F. Pan, H. Xia, S. Zou, H. Zhang, O. A. George, F. Zhou, and Y. Huang, “Computational Study of Single Droplet Deposition on Randomly Rough Surfaces: Surface Morphological Effect on Droplet Impact Dynamics”, *Industrial & Engineering Chemistry Research* **57**, 7664–7675 (2018).
- [222] N. I. Henman, F. T. Smith, and M. K. Tiwari, “Computational Study of Early-Time Droplet Impact Dynamics on Textured and Lubricant-Infused Surfaces”, *International Journal of Multiphase Flow* **161**, 104398 (2023).
- [223] A. Alizadeh, V. Bahadur, W. Shang, Y. Zhu, D. Buckley, A. Dhinojwala, and M. Sohal, “Influence of Substrate Elasticity on Droplet Impact Dynamics”, *Langmuir* **29**, 4520–4524 (2013).
- [224] J. C. Bird, R. Dhiman, H.-M. Kwon, and K. K. Varanasi, “Reducing the Contact Time of a Bouncing Drop”, *Nature* **503**, 385–388 (2013).
- [225] X. Han, J. Li, X. Tang, W. Li, H. Zhao, L. Yang, and L. Wang, “Droplet Bouncing: Fundamentals, Regulations, and Applications”, *Small* **18**, 2200277 (2022).
- [226] H. Li and S. Yu, “A Robust Superhydrophobic Surface and Origins of Its Self-Cleaning Properties”, *Applied Surface Science* **420**, 336–345 (2017).
- [227] S. Shiri and J. C. Bird, “Heat Exchange between a Bouncing Drop and a Superhydrophobic Substrate”, *Proceedings of the National Academy of Sciences* **114**, 6930–6935 (2017).
- [228] S. Luo, Z. Chen, Z. Dong, Y. Fan, Y. Chen, B. Liu, C. Yu, C. Li, H. Dai, H. Li, *et al.*, “Uniform Spread of High-Speed Drops on Superhydrophobic Surface by Live-Oligomeric Surfactant Jamming”, *Advanced Materials* **31**, 1904475 (2019).
- [229] M. Damak, M. N. Hyder, and K. K. Varanasi, “Enhancing Droplet Deposition through In-Situ Precipitation”, *Nature Communications* **7**, 12560 (2016).
- [230] X. Han, W. Li, H. Zhao, J. Li, X. Tang, and L. Wang, “Slippery Damper of an Overlay for Arresting and Manipulating Droplets on Nonwetting Surfaces”, *Nature Communications* **12**, 3154 (2021).
- [231] D. Richard, C. Clanet, and D. Quéré, “Contact Time of a Bouncing Drop”, *Nature* **417**, 811–811 (2002).
- [232] C. Lin, K. Zhang, X. Chen, L. Xiao, S. Chen, J. Zhu, and T. Zou, “Reducing Droplet Contact Time and Area by Craterlike Surface Structure”, *Physical Review Fluids* **6**, 083602 (2021).
- [233] D. Quéré, “Leidenfrost Dynamics”, *Annual Review of Fluid Mechanics* **45**, 197–215 (2013).
- [234] S. Illias, N. Rosman, N. Abdullah, S. Hussain, M. Baharudin, M. Idris, and K. Ismail, “Critical Heat Flux and Leidenfrost Temperature on Hemispherical Stainless Steel Surface”, *Case Studies in Thermal Engineering* **14**, 100501 (2019).
- [235] A. Giacomello, L. Schimmele, S. Dietrich, and M. Tasinkevych, “Perpetual Superhydrophobicity”, *Soft Matter* **12**, 8927–8934 (2016).

- [236] T. Lee and C.-L. Lin, “A Stable Discretization of the Lattice Boltzmann Equation for Simulation of Incompressible Two-Phase Flows at High Density Ratio”, *Journal of Computational Physics* **206**, 16–47 (2005).
- [237] A. R. Computing. “Advanced Research Computing : Hamilton - Durham University”. <https://www.dur.ac.uk/arc/hamilton/>, (2023). [Online; accessed 10th November 2023].
- [238] A. M. Moqaddam, S. S. Chikatamarla, and I. V. Karlin, “Simulation of Droplets Collisions Using Two-Phase Entropic Lattice Boltzmann Method”, *Journal of statistical Physics* **161**, 1420–1433 (2015).
- [239] A. M. Moqaddam, S. S. Chikatamarla, and I. V. Karlin, “Drops Bouncing off Macro-Textured Superhydrophobic Surfaces”, *Journal of Fluid Mechanics* **824**, 866–885 (2017).
- [240] C. Pooley, H. Kusumaatmaja, and J. Yeomans, “Modelling Capillary Filling Dynamics Using Lattice Boltzmann Simulations”, *The European Physical Journal Special Topics* **171**, 63–71 (2009).
- [241] S. J. Avis. *Massively Parallel Lattice Boltzmann Fluid Simulations*. PhD thesis, Durham University, (2019).
- [242] F. Diotallevi, L. Biferale, S. Chibbaro, a. Lamura, G. Pontrelli, M. Sbragaglia, S. Succi, and F. Toschi, “Capillary Filling Using Lattice Boltzmann Equations: The Case of Multi-Phase Flows”, *The European Physical Journal Special Topics* **166**, 111–116 (2009).